論文 / 著書情報
Article / Book Information

題目(和文)	
Title(English)	Recovery and recrystallization behavior of cold-rolled Al-Mn based alloy under residual stress
著者(和文)	ParkSung-Jin
Author(English)	Sung-Jin Park
出典(和文)	学位:博士（工学）, 学位授与機関:東京工業大学, 報告番号:甲第12036号, 授与年月日:2021年6月30日, 学位の種別:課程博士, 審査員:村石 信二,熊井 真次,竹山 雅夫,藤居 俊之,小林 郁夫,小林 覚
Citation(English)	Degree:Doctor (Engineering), Conferring organization: Tokyo Institute of Technology, Report number:甲第12036号, Conferred date:2021/6/30, Degree Type:Course doctor, Examiner:,,,,,
学位種別(和文)	博士論文
Type(English)	Doctoral Thesis

Recovery and recrystallization behavior of cold-rolled Al-Mn based alloy under residual stress

by

SungJin Park

DISSERTATION

Presented to
The Graduate major in Materials Science and Engineering,
The Dept. of Materials Science and Engineering,
The School of Materials and Chemical Technology
in partial fulfillment of the requirements
for the degree of

DOCTOR OF ENGINEERING

at the
Tokyo Institute of Technology
May 2021

東京工業大学
Tokyo Institute of Technology

Abstract

The purpose of the present study is to investigate the plastically deformed microstructure introduced by cold rolling and the subsequent microstructure evolution by thermal treatment in order to improve the mechanical properties and quality of cold-rolled sheets taking into account the residual stress. A commercial AA3003 alloy fabricated under different homogenization and cold rolling conditions was chosen. Considering the characteristics of microstructures such as dislocation density, distribution and size of second-phase particles, and Mn concentration in solid solution, the influence of these properties on promoting or suppressing the restoration process was investigated. The driving force associated with the dislocation density for the recrystallization increases depending on the reduction rate and the dispersoids distribution, which leads to a decrease in the recrystallized grains size. The residual stress and displacement gradients around the constituent particles predicted by the inhomogeneity problem under cold rolling conditions strongly suggests that the formation of deformation zone associated with particle stimulated nucleation (PSN) is attributed to the relaxation of disturbed stress under cold rolling. Consequently, a micromechanical-based model for the critical strain required to initiate recrystallization by the PSN effect was developed, which, to the best of the author's knowledge, is the first attempt to model the critical strain around constituent particles.

These things can be applied to the actual industry as a way to improve mechanical properties by combining experimental work and modeling techniques.

Preface

This dissertation is original and some works have been published and some are being submitted for publication.

1. SungJin Park and Shinji Muraishi,“Micromechanical analysis of residual stress around coarse precipitates under cold rolling condition”, Mechanics of material, Vol. 157, (2021) 103841.
2. SungJin Park and Shinji Muraishi,“Influence of residual stress around constituent particles on recrystallization and grain growth in Al-Mn based alloy during annealing”, Materials, 14(7), (2021) 1701.
3. SungJin Park and Shinji Muraishi,“Effect of reduction rate on the recrystallization behavior in AA3003 aluminum alloy fabricated by DC casting ”, Materials Science Forum, Vol. 1034, (2021). 17-22
4. SungJin Park and Shinji Muraishi,“Influence of different homogenization conditions on the recrystallization behavior in the cold-rolled AA3003 aluminum alloy with large magnitude of plastic strain”, The 167th conference of Japan Institute of Metals and Materials (Sept., 2020)
5. SungJin Park, Yohei Harada, Shinji Kumai and Shinji Muraishi, “Recovery behavior via triple-junction motion in cold-rolled AA3003 aluminum alloy with 90% thickness reduction”, The 138th conference of Japan Institute of Light Metals (May., 2020)
6. SungJin Park and Shinji Muraishi,“Effect of reduction rate on the recrystallization behavior in AA3003 aluminum alloy fabricated

by DC casting", ICPMAT2019, Daegu, Rep. of Korea (Sept., 2019)

The initial materials (DC-cast specimens, homogenized specimens and cold-rolled sheets) used in this study were supplied by UACJ Corp in Nagoya, Japan. The experimental and simulation work presented in this thesis has been performed in the Department of Materials Science and Engineering at the Tokyo Institute of Technology (Tokyo, Japan), where includes all the experimental design, sample preparation, annealing, microstructural characterization, convectional XRD analysis, mechanical properties and Matlab software, except: the synchrotron XRD utilized the high-intensity X-ray BL02B2 beamline ($\boldsymbol{\lambda}$=0.516Å) of the Spring-8 synchrotron radiation facility in Hyōgo Prefecture, Japan. All experimental and simulation work in this thesis was carried out by the author, SungJin Park, except: the synchrotron XRD work on diffraction pattern of AA3003 alloy was performed in Spring-8 with the help of Dr. Shogo Kawaguchi.

Contents

5 Influence of residual stress around constituent particles on recrystallization and grain growth in Al-Mn based alloy during annealing **156**

List of Tables

List of Figures

Chapter 1

General Introduction

1.1 Background

Recently, resource development and excessive use of fossil fuel caused severe environmental problems and climate change are being issued as real and serious problems. Therefore, it is necessary to reduce fossil fuel consumption and the emission of major greenhouse gases. In order to solve these problems, the development of high-efficient materials is being demanded as a major issue, and especially aluminum and its alloys are being actively developed as an alternative material.

Aluminum is one of the most abundant metals on Earth, and it is the third most common element next up oxygen and silicon, accounting for 8.1% of the crust by weight. Aluminum is a lightweight metal with a density of about 1/3 lower than that of iron and is the most widely used metal as an alternative material to steel. When the first aluminum smelting method was developed in 1886 (Lewis V. McCarty and Craig, 1997), the production of aluminum was only about 200 tonnes, but global aluminum production has increased to about 50 million tonnes in 2019, where about 20% of the production was recycled using the aluminum scrap (Association, 2019). The use of recycled aluminum is economically very efficient and is a strong environmentally competitive material. It requires about 14,000 kWh to produce 1 tonne of new aluminum, but only 5% is required to remelt and recycle 1 tonne of aluminum, resulting in an economic effect of more than 90% (Albert, 2018). In addition, there is no difference in quality between virgin and recycled aluminum alloys(Totten and Mackenzie, 2003). Therefore, the use of aluminum and its alloys is expected to continue to increase in the future due to economic efficiency.

Aluminum is one of the lightest engineering metals with a higher specific strength than steel. By applying various combinations of its beneficial properties such as strength, lightweight, corrosion resistance, recyclability and formability, aluminum is being used in more and more applications and is also a material with high potential for future development. This array of aluminum-based products is utilizing in a variety of industries such as building materials, automotive lightweight parts, aerospace materials, food and beverage packaging, and electronic materials.

Generally, aluminum alloys are composed of various types, and are classified into wrought alloy and cast alloy by manufacturing method (Totten and Mackenzie, 2003). The cast aluminum alloys can produce a wide range of the final-shape products due to their casting flexibility in the as-cast condition. Although cast alloys are less expensive to produce and have good casting flexibility compared to wrought alloys, they have a generally lower tensile strength than wrought alloys because casting defects are difficult to eliminate. Whereas, the wrought alloys have excellent mechanical properties and can be fabricated into a variety of standard and non-standard shapes. Therefore, the wrought alloys are used in various industries due to their advantages such as excellent mechanical properties, no defects from casting and ease of manufacture (ex: welding and machining)(Kaufman and Rooy, 2004). These wrought alloys are classified into heat-treated alloys (Al-Cu, Al-Mg-Si, Al-Zn) that can improve physical properties via heat treatment and non-heat-treated alloys (Al-Mn, Al-Si, Al-Mg) that cannot improve physical properties via heat treatment. Therefore, the non-heat-treated alloys are initially produced as large castings and are processed into intermediate or final products through forging, rolling, extrusion, etc. to improve mechanical properties(Davis, 2001). Further details on the manufacturing process are covered later in Section 1.2

Non-heat-treated alloys are mainly used in the form of plates (plates, sheets, foils), and 1xxx series and 5xxx series are often used by extrusion. The alloy in the form of a plate may be cold-rolled to pursue high strength, but it is used in a state with stress removed for ease of forming. The increase in free energy of wrought alloys due to plastic deformation causes defects such as dislocations inside the deformed materials. The material then becomes thermodynamically unstable due to the defect and retains an unstable defect structure. In order to reduce the level of work hardening to lower hardness and to decrease the residual stress inside the alloy to reduce the risk of stress corrosion cracking in use, the wrought alloys require further processing to eliminate defects such as annealing. Especially, the restoration mechanisms such as recovery, recrystallization, and grain growth by annealing are key to this process. The change in mechanical and microstructural properties associated with the manufacturing process of these wrought alloys are schematically shown in Fig. 1.1. The three-stage of recovery, recrystallization and grain growth during annealing are shown to occur gradually as the annealing temperature increases, assuming a certain constant annealing time at each temperature (Bhaduri, 2018)). Further details on the annealing process are covered later in Section 1.3.

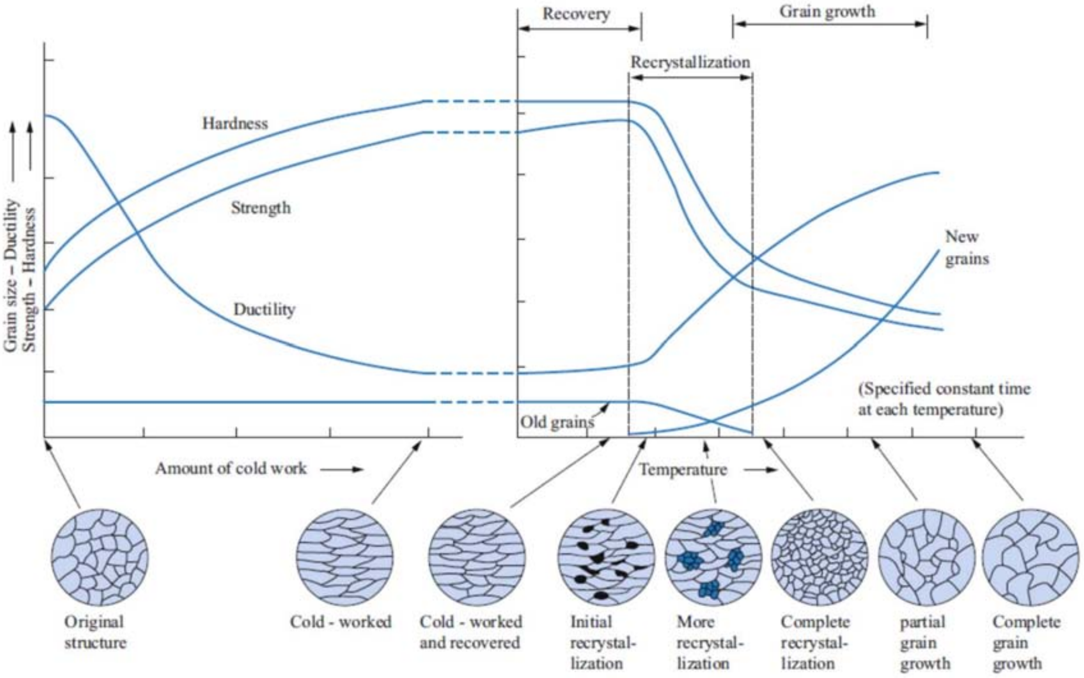

Figure 1.1: Schematic representation of the cold-work anneal cycle showing the effects on mechanical properties and microstructure (Bhaduri, 2018)

Among them, Al-Mn based aluminum alloy, which is a work hardening alloy called 3xxx-series aluminum, has moderate strength, excellent corrosion resistance and formability, and is widely used in packaging containers, beverage can body, and automobile industries (Davis, 2001). Al-Mn based alloy is fabricated through processes of manufacturing plate materials from DC-cast slabs such as casting, scalping, homogenization, hot and cold rolling, and there are various parameters (homogenization, fine and coarse precipitate, amount of reduction, annealing, etc.) in each process that can affect the microstructure. These parameters can have a significant influence on the properties of the final product. For instance, a relatively coarse grain size (about >100 μm) is preferred in most heat exchanger applications, because coarse grains provide good corrosion resistance, sagging resistance, and solderability (Tangen et al., 2010). On the other hand, the fine grain size is suitable for industrial applications such as thin can bodies where high formability is required. Considering the industrial point of view used, the grain size control during the manufacturing process is an essential and very important process for the application of aluminum materials as well as Al-Mn based alloys. A more detailed description of the Al-Mn based alloy features is covered in Section 1.1.1.

Therefore, Al-Mn based aluminum has been selected as the alloy of interest in the present study. The experimental results investigated in this study are based on homogenization conditions after casting and microstructure characteristics after cold rolling of commercial AA3003 aluminum alloys. These studies were conducted under various conditions to suppress or increase the concurrent precipitation of DC cast AA3003 alloy, and plastically deformed under various reduction ratios to control the distribution of particle-stimulated nucleation (PSN) sites. In addition, experiments are conducted in various strain regimes to understand the residual stress around precipitates, which are computed and visually implemented by Matlab based on micromechanical theory. In particular, this investigation focuses on the correlation between the stored energy associated with the dislocation density, the residual stress around coarse particles ($>1\mu m$) and the pinning effect of fine particles ($<300\ nm$). The greatest significance of this study is to appropriately integrate the experimental work and modeling technology into the structural characteristics introduced in the manufacturing conditions used in the industrial field so that it can be used in the actual industry.

1.1.1 Characteristics of Al-Mn based alloy (AA3xxx series)

When Mn is added to aluminum, the electrical conductivity is significantly lowered, and the hardness increases depending on the solubility. The addition of a small amount increases the recrystallization temperature, promotes the formation of the Fe-containing intermetallic compounds, and improves the strength without significantly deteriorating the corrosion resistance when added in a small amount (JohnE.Hatch, 1984).

This is because the secondary phase, Al_6Mn phase, is electrochemically stable in the aluminum matrix and has good corrosion resistance (Zamin, 1981). Mn element serves to increase the strength as the main alloying element of the solid solution strengthening alloy. Therefore, the size of the precipitate particles and the degree of uniform dispersion can be easily controlled by the addition of Mn, so that the microstructure and mechanical properties of the aluminum alloy can be variously controlled (Totten and MacKenzie, 2003).

Al-Mn based alloys (AA3xxx series) usually contain about 0.3-1.5 wt.% of Mn as a main alloying element in aluminum. The addition of Mn improves the strength of the aluminum alloy with maintaining the formability and corrosion resistance of pure aluminum. Mn contained in the aluminum matrix is dispersed to show the effect of improving the strength of the material, and shows various mechanical properties depending on the degree of work hardening. Work softening may occur when plastic deformation occurs due to repeated tensile and compressive stress during cold rolling (Jordon et al., 2007).

Al-Mn based is used as a beverage can body and automobile heat exchanger based on its moderate strength, excellent corrosion resistance and formability (McAlister and Murray, 1987). Recently, electric vehicles are in the spotlight due to global eco-friendly policies, and the capacity of Al-Mn based alloys is increasing as this alloy is widely used as a battery housing case for electric vehicles. The Aluminum Association (2014) reports that the average recycled content for an Al-Mn based alloy can be produced in the United States increased by 73%. These Al-Mn based alloys with high economic value are expected to increase in demand worldwide in the future. Thus, the improvement of the existing processing and heat treatment processes and the development of technologies in various fields such as multi-materialization by joining technique are very important and essential elements to preoccupy the future industrial market.

1.2 Manufacturing of Al-Mn based alloy

The composition range of alloying elements in commercial 3xxx aluminum alloys contains is 0.3∼1.5 wt.% Mn, ∼1.3 wt.% Mg, ∼0.30 wt.% Cu, 0.1∼0.7 wt.% Fe, 0.1∼0.6 wt.% Si, ∼0.1 wt.% Ti and other elements (Hirsch, 2007; Committee, 1990). Generally, the yield strength of 3xxx aluminum alloys is as low as about 20-60 MPa (JohnE.Hatch, 1984; Ryen et al., 2006). AA3003 alloy is the preferred material for automotive heat exchangers and electric vehicle battery housing case applications due to its excellent combination of strength, corrosion resistance, workability and high melting temperature. These properties make it easy to perform processes such as rolling, extrusion and brazing of alloy materials. Since the solubility of Fe and Si in aluminum is very low, the addition of Fe into the system promotes the formation of Fe intermetallic compounds. This will lead to a fine recrystallized grain structure after cold rolling and annealing (Koken et al., 1988). The presence of Mn along with Fe and Si in the Al matrix causes the formation of quaternary-phase Al-Mn-Fe-Si particles such as Al_{12}(Fe, Mn)$_3$Si, Al_{15}(Fe, Mn)$_3Si_2$ or the α-Al(Fe, Mn)Si (Davis, 2001; Eskin, 2008). The fraction of α-Al(Mn, Fe)Si phase transformed from Al_6(Mn, Fe) increases with the homogenization temperature and time (Li and Arnberg, 2003a).

After DC-cast, the Al-Mn based alloy is produced through a thermodynamic process following several process steps including homogenization, hot rolling, plastic deformation by cold rolling, and annealing. Fig. 1.2 shows a typical Al-Mn based alloy fabrication process. Many investigations have been carried out to study the plastic deformation during cold rolling and the influence of precipitation during annealing. However, quantitative studies on the dislocation density introduced by cold rolling and the residual stresses formed around the constituent particles during plastic deformation and their influence on recovery and recrystallization behavior have been still insufficient.

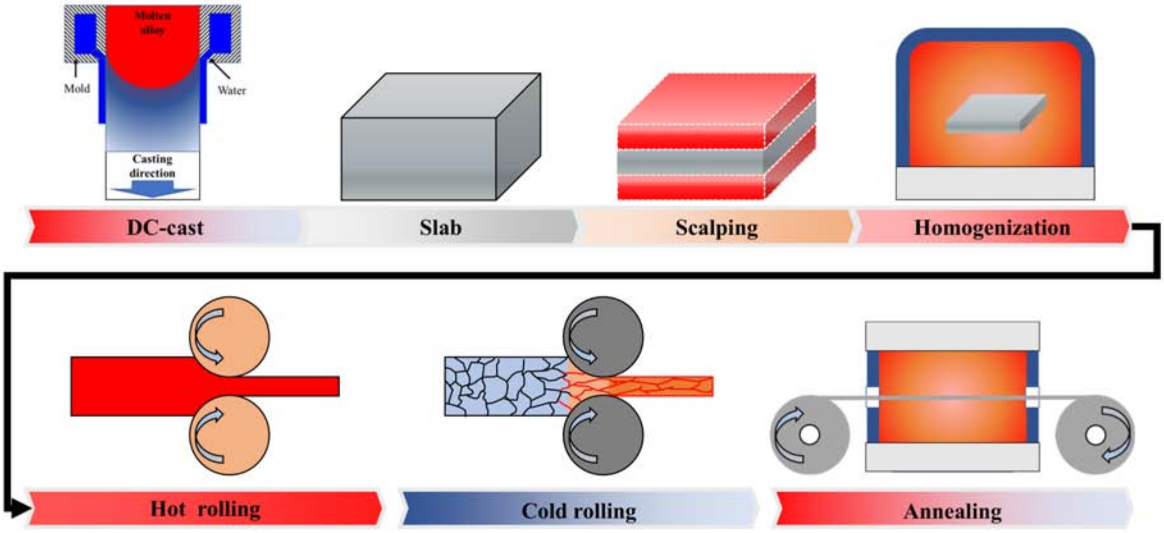

Figure 1.2: Schematic diagram of the manufacturing process for Al-Mn based alloy

1.2.1 Direct-Chill casting

The raw material for cold rolling operations is usually direct-chill (DC) cast slabs. The advantage of DC casting is that it is cost-effective due to the simplification of the process, and the surface and interior quality of the slab is excellent. The solidification of the DC-cast metal begins as it flows into a water-cooled mold composed of Al or Cu. The heat of the molten metal in the mold is transferred to the mold wall and the surface of the ingot solidifies as the primary cooling occurs, and as it exits the mold, it is directly immersed in a water tank filled with cooling water for secondary cooling (Gupta et al., 2007).

When the alloy solidifies under these conditions, equiaxed grains with a dendrites structure are produced. In Al-Mn based alloys, the main constituent particles after solidification are Al_6(Fe, Mn) and α-Al(Mn, Fe)Si. In addition, the as-cast material is supersaturated due to non-equilibrium cooling Mn and Fe at room temperature and the low solubility of these elements in aluminum (Li and Arnberg, 2003a,b). A more detailed model of the solidification behavior of Al-Mn based alloys during DC-casting is in the literature reported by Du and Jacot (2005) and Nadella et al. (2008).

The properties of the primary particles that act as nucleation sites in the recrystallization process after cold rolling are the most important factors to consider during the casting step. In addition, the evolution of the size and composition of the primary particles during homogenization is due to behaviors such as the precipitation of Mn onto particles from the supersaturated matrix and the dissolution of the dispersoids. However, the distribution of primary particles does not change even after the homogenization treatment is finished. Therefore, the Mn concentration and the distribution of the primary particles in the initial DC-cast state can be considered as one important variable in predicting the nucleation site during the recrystallization of the cold-rolled material in the future. The effect of these primary particles on the recrystallization behavior is discussed in detail later in Sections 1.3.2 and 1.5.

1.2.2 Homogenization

The size and distribution of precipitates introduced by the homogenization treatment before cold rolling can be a great influence on the microstructure during annealing after plastic deformation. Cast slabs are usually followed by a process known as homogenization treatment after casting. The homogenization treatment proceeds by holding the slab at a specific heating rate (50 °C ∼ 250 °C/h) and temperature (500 °C ∼ 630 °C) for a certain period of time, and then slowly or rapidly cooling it to room temperature (Håkonsen et al., 2002).

The entire homogenization process, including heating, holding and cooling, generally proceeds under a variety of conditions depending on the specific objectives of the final product. No change in microstructure is observed until about 400 °C, when the eutectic network of constituent particles begins to break during the temperature rising step (Li et al., 2012). At about 400 °C or higher, the Al_6(Mn, Fe) constituent particles are transformed to α-Al(Mn, Fe)Si phase according to the chemical properties of the elements constituting the 3xxx alloy Li and Arnberg (2003a). In contrast, the supersaturated Mn during the solidification process of the casting induces the precipitation of the dispersoids in the intragranular region during the homogenization treatment Li and Arnberg (2003a).

Since the solubility of Mn increases in proportion to the homogenization temperature, a complex interaction takes place between redissolution, generation of new fine secondary particles, coarsening of primary particle and diffusion of Mn into constituent particles. It is well known that the composition and crystal structure of dispersoids depends on their chemical properties of the constituent elements (McAlister and Murray, 1987). In experimental studies on the AA3003 alloy, it was found that the dispersoids was mostly composed of α-Al(Mn, Fe)Si phase (Li and Arnberg, 2003b). In addition, the α-Al(Mn, Fe)Si phase dispersoids can be coarsened to 100-200 nm size under specific homogenization and annealing conditions(Li and Arnberg, 2003b).

The DC-cast slabs used in this work were performed under various homogenization conditions to investigate the influence of change in primary particle size and dispersoids size and distribution on microstructure evolution during cold rolling. Moreover, since the Mn concentration in the aluminum matrix is different due to different homogenization conditions, the presence or absence of concurrent precipitation depending on the Mn concentration will have a great influence on the recovery and recrystallization kinetics during annealing. A more detailed description of the effects of a constituent particle associated with deformed microstructure on recovery and recrystallization behavior is covered later in Section 1.3.

1.2.3 Rolling process

Rolling is a process in which the cross-sectional area is reduced by the compressive and tensile force of the roller by passing a material between two rotating rolls. It is the most suitable process for mass production because it is the most efficient and very excellent dimensional precision among the processing methods of metal materials.

Such rolling processing can be classified into hot rolling performed at a recrystallization temperature or higher and cold rolling performed at room temperature.

Rolling is to reduce the thickness of the plate from t_0 to t_1. The reduction in sheet thickness is generally referred to as the rolling reduction, ε_t, is expressed by the following equation.

$$\varepsilon_t = \int_{t_0}^{t_1} \frac{dl}{l} = ln(\frac{t_1}{t_0}) = ln(1 + \varepsilon_n) \tag{1.1}$$

where the logarithmic strain (true strain) is ε_t, the nominal strain is ε_n, the reduced thickness of the cold rolled sheet is t_1, the initial thickness of the sheet is t_0.

The elements of the plate material undergoing deformation between the two rollers during the rolling operation, the principal axes are oriented as follows: (1) in a direction normal to the plane of the sheet, (2) in a direction parallel to the axes of the roller, and (3) in the rolling direction. The directions of the three main strain designated σ_{xx}, σ_{yy} and σ_{zz} associated with these directions are shown in Fig. 1.3. The σ_{yy} and σ_{zz} always represent compressive strain, while the σ_{xx} may be tensile strain near the entry and exit ends of the roller (Roberts, 1978).

According to Eq. (1.1), the thickness of the ideal grain boundary observed from the cross-section should decrease in proportion to the amount of reduction. However, even if the Al-Mn alloy containing constituent particles is cold-rolled under the same amount of reduction, the spacing of grain boundary in the cross-section may be different depending on the size and distribution of constituent particles. The spacing of these deformed boundaries may be attributed to residual stress around the precipitate during cold rolling and can be observed

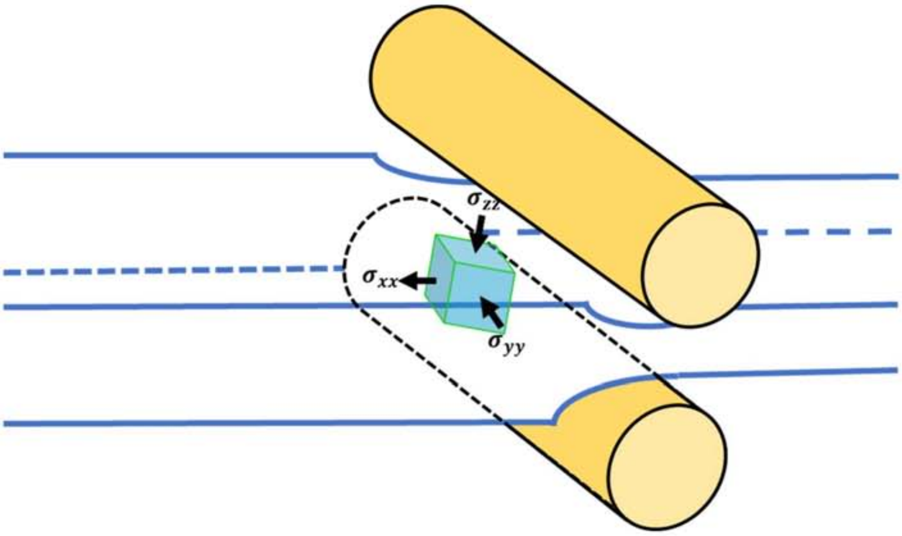

Figure 1.3: Schematic diagram of the applied strain in the workpiece during cold rolling

with high magnification equipment such as TEM.

The disturbance of stress and strain caused by precipitates during cold rolling are difficult to quantify by experimentally measuring and analyzing due to different stress directions as shown in Fig. 1.3. Therefore, a more advanced technique is needed to quantitatively analyze the residual stress around the precipitate. A more detailed description of the theoretical background for modeling and predicting residual stresses near the precipitate during cold rolling is covered later in Section 1.5.

1.3 Deformed Microstructure

Since changes in the microstructure of an alloy containing dispersed second-phase particles by cold rolling can have a significant effect on the evolution of the microstructure of the alloy during annealing, it is important to understand the work hardening phenomena and related models. In particular, the influence of the constituent particles on the characteristic microstructure, such as the dislocation density associated with the driving pressure for recrystallization, non-uniformity of deformation at the matrix boundary associated with the migration of the boundary during annealing, and the deformation structure near the coarse particles associated with PSN, is of paramount importance.

The textbook (Recrystallization and Related Annealing Phenomena) written by Humphreys et al. (2004) provides comprehensive information on the subject of this study. The following is a brief summary of the characteristics of the deformable structure introduced by cold rolling, where most of the content covered in this section was cited in the textbook written by Humphreys et al. (2004).

1.3.1 Characterization of microstructure

The FCC metals with medium or high values of stacking fault energy such as aluminum ($\sim$170 mJ/m^2) and copper ($\sim$80 mJ/m^2) are deformed by dislocation slip, where dislocation slip is accompanied with climb and cross slip. The deformation in aluminum alloy is heterogeneous, and the misoriented regions are formed due to the change in orientation inside the original grain during plastic deformation.

Pure aluminum alloys have a stacking fault energy (SFE) of 150 mJ/m^2 or more, which is higher than that of other alloys. The density and distribution of defects such as dislocations are non-uniform distributed in the case of aluminum alloys and form cellular substructures. In addition, the residual stress and dislocation density depend on several factors such as purity, grain size, distribution and size of constituent particles and deformation. Separately from the cellular substructure, pure aluminum and its alloys after deformation have remarkable heterogeneity in lattice defect distribution. This is generally referred to as a deformation band.

The main features of the microstructures in deformed metals such as aluminum and its alloys depending on the scale of the heterogeneity are summarized as follows (see textbook page 38∼39), as schematically shown in Fig. 1.4.

Dislocations

Dislocations may exist as tangles or somewhat random structures, especially after low deformation (Fig. 1.4a).

Cells and subgrains

Most of the dislocations introduced by the plastic deformation form the boundary of the cells or subgrains, where cells and subgrains are the smallest volume element in the deformed microstructure (Fig.1.4b). Some cell walls can be aligned or misoriented, which allows for further subclassification of these features.

Deformation and transition bands

Individual grains within the specimen, especially those of coarse particles, are largely subdivided into areas of different orientations during deformation. This is due to the inhomogeneous stress transmitted by adjacent grains or the intrinsic instability of the grain during plastic deformation (Fig. 1.4c). The resulting strain bands deform in different slip systems and may develop widely different orientations. The narrow area between the deformation bands that can be diffuse or sharp is called the transition band.

Shear bands

Strong shear may occur in polycrystalline samples as a result of plastic instability. Shear bands that are non-crystallographic in nature can pass through several grains and can even extend through the specimen (Fig. 1.4d).

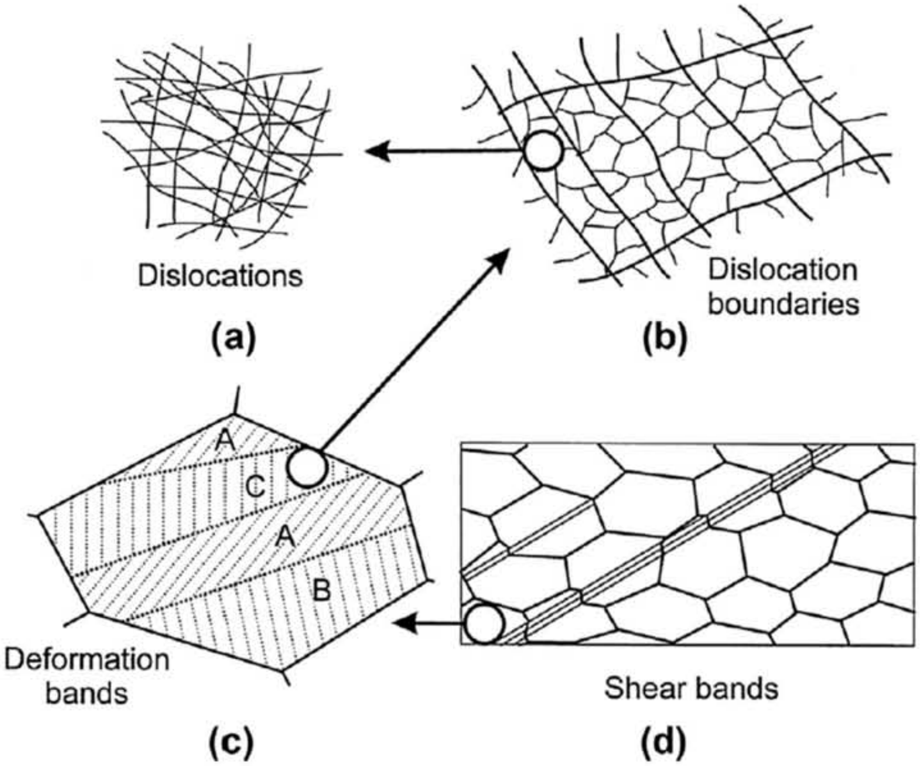

Figure 1.4: The various microstructure features in a polycrystalline metal deformed by slip : (a) dislocations; (b) dislocation boundaries; (c) deformation and transition bands within a grain; (d) specimen and grain-scale shear bands (Humphreys et al., 2004)

The various changes in the microstructure of the metal during plastic deformation are observed, such as the shape of the grain and an increase in the total boundary. However, the most important thing here is the increase in dislocation density and the microstructure evolution associated with it. In particular, the cells and sub-particles caused by the non-uniform accumulation of dislocations are the main features of microstructures generated within the grains, which can be observed at the TEM level. Cells and subgrains can be distinguished by a dislocation wall defined by geometrically necessary dislocation (GND). The size of an equiaxed shaped cell or subgrains decreases in inverse proportion to the increasing strain during plastic deformation at room temperature. Thus, the level of stored energy introduced by cold rolling can be inferred qualitatively by measuring the size of the cell or sub-particle.

Many experimental studies have been conducted to analyze the driving force for the recovery and recrystallization, but most of them have been qualitative analysis by indirect measurements such as resistance, microhardness and changes of flow stress. In addition, although a lot of quantitative research have been conducted on the dislocation density by direct transfer observation by TEM, there is a problem that it is difficult to measure dislocation density by TEM observation due to variables such as overlapping of dislocations. In order to solve this problem, it is necessary to investigate for more accurate dislocation density measurement through X-ray peak profile analysis. In particular, more accurate results can be obtained by using high-intensity synchrotron XRD.

A more detailed description of the annihilation and absorption of dislocation during the recovery and recrystallization behavior is covered in Section 1.4.

1.3.2 Deformation zone around precipitate

The metal alloys containing second phase particles develop gradients of strain and crystal orientation in the vicinity of the particle with high elastic modulus during plastic deformation. Thus, more complex dislocation structures are formed around second phase particles during plastic deformation. This results in localized lattice rotation around the particles, and these regions are commonly called the particle deformation zone (Humphreys, 1977). This deformation zone acts as a nucleation site for new grains for recrystallization known as particle stimulated nucleation (PSN) during annealing. In addition, the PSN is useful for controlling the texture anisotropy and recrystallized grain size of a product. This PSN effect is known to occur around coarse particles of about $1\mu m$ or more (Humphreys et al., 2004), whereas the fine secondary particles at the level of about $200nm$ can pin and delay the migration of dislocations and boundary (Nes et al., 1985). This section describes a model for the formation of deformation zones around particles during plastic deformation.

Fig. 1.5 shows the effect of particle in a matrix containing spherical particle during the plastic deformation. In the initial undeformed state, spherical particles are contained in the matrix as shown in Fig. 1.5a. When the deformation occurs due to shear stress, the matrix and deformable particles are deformed equally by the applied strain as shown in Fig. 1.5b. Whereas, assuming that the particle is non-deformable, the gap between the undeformed particle (circle indicated by black line) and deformed particle (circle filled in blue), and eventually, the mismatch of plastic deformation occurs locally by this difference (Fig. 1.5c).

According to Ashby (1966), this local strain incompatibility can be achieved by the generation of a dislocation around the particle or by activation of another slip system around the particle. It can be accommodated by the generation of dislocations at the interface of the matrix surrounding the undeformed particles, which leads to an

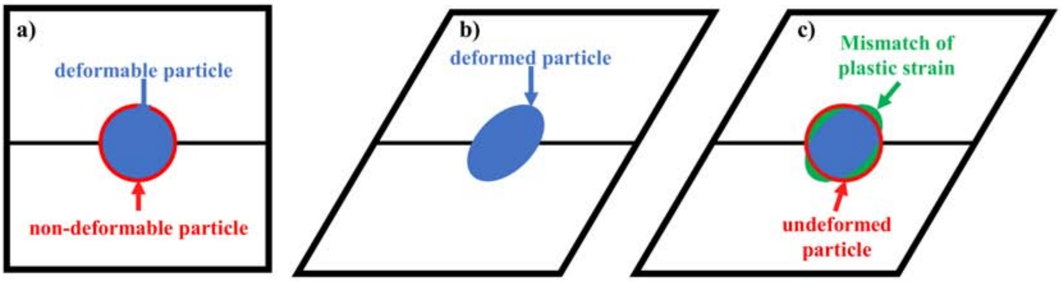

Figure 1.5: The incompatibility between a deformable matrix and a non-deformable particle. (a) Undeformed state, (b) with deformed particle, (c) with undeformed particle

increase in dislocation density around the particle by promoting dislocation generation and interfering with the migration of dislocations (Muraishi, 2014). This is known by Ashby (1970) as a Geometrically Necessary Dislocation (GND).

The deformation zone of the cold-rolled alloy generally extends in the rolling direction as shown in Fig. 1.6. The shape and distribution of these dislocation structures in the vicinity of the particle mainly depend on the strain and particle size, but other factors such as shape, interfacial strength and matrix are also known to be important. The transition from a dislocation structure that is considered "non-rotating or laminar plastic flow" to the deformation zone around particle, which can be considered to contain "rotating plastic flow" is difficult to predict. These phenomena are theoretically a scale in the middle between dislocation and continuum mechanics.

Various models have been proposed for the formation process of the deformation zone caused by the interaction of particles and the surrounding matrix. First, the formation of the deformation zone may be the result of plastic relaxation of dislocation arrays, such as Orowan loops or prismatic dislocation loops (Humphreys, 1985; Muraishi, 2014). Fig. 1.7 schematically shows a model of this process. When dislocations

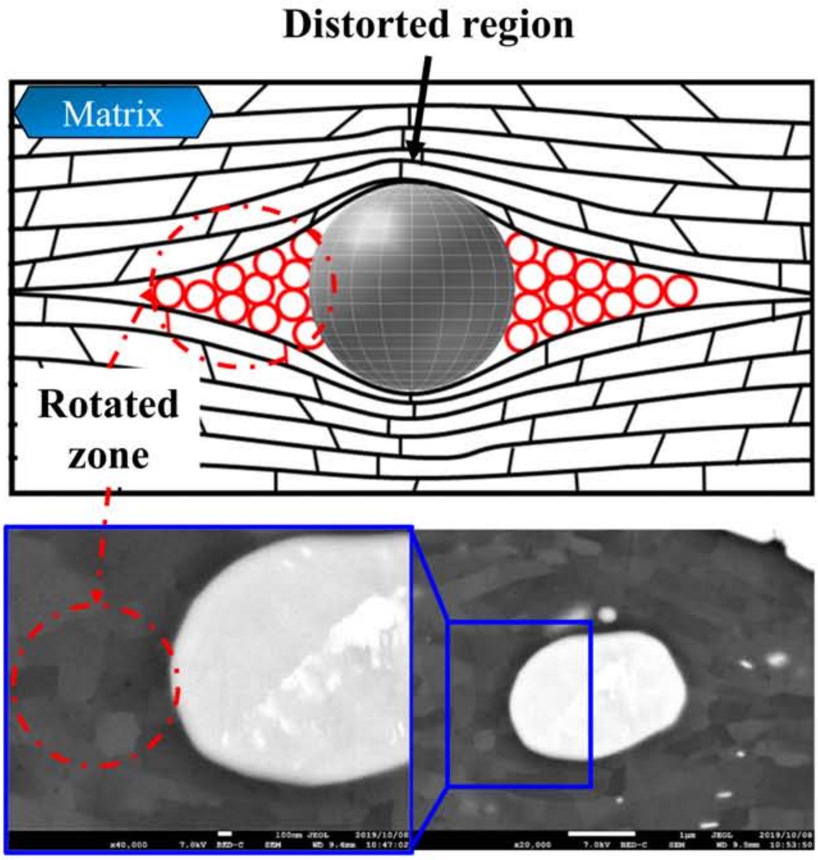

Figure 1.6: Schematic diagram of the development of a deformation zone

are accumulated by the particles, they form Orowan loops as shown in Fig. 1.7a. The increase in the interface stress due to the accumulated dislocations will lead to plastic relaxation (Hazzledine and Hirsch, 1974; Muraishi, 2014) and rotation of the particle and generation of secondary dislocations (L. M. Brown and Stobbs, 1971) as shown in Fig. 1.7b. As the deformation progresses, the dislocation accumulated around the particle increases, and the further glide dislocation makes it difficult to access the particle, which will lead to increase the effective particle size as shown in Fig. 1.7c. Therefore, further relaxation will occur in the matrix and in the impermeable zone near the particle, which diffuses outward from the particle surface as shown in Fig. 1.7d.

Moreover, the rotation of the non-deformable particle will occur due to the deformation mechanism (Humphreys and Kalu, 1990). This will eventually result in an orientation gradient outward from the surface of particle as schematically shown in Fig. 1.7e.

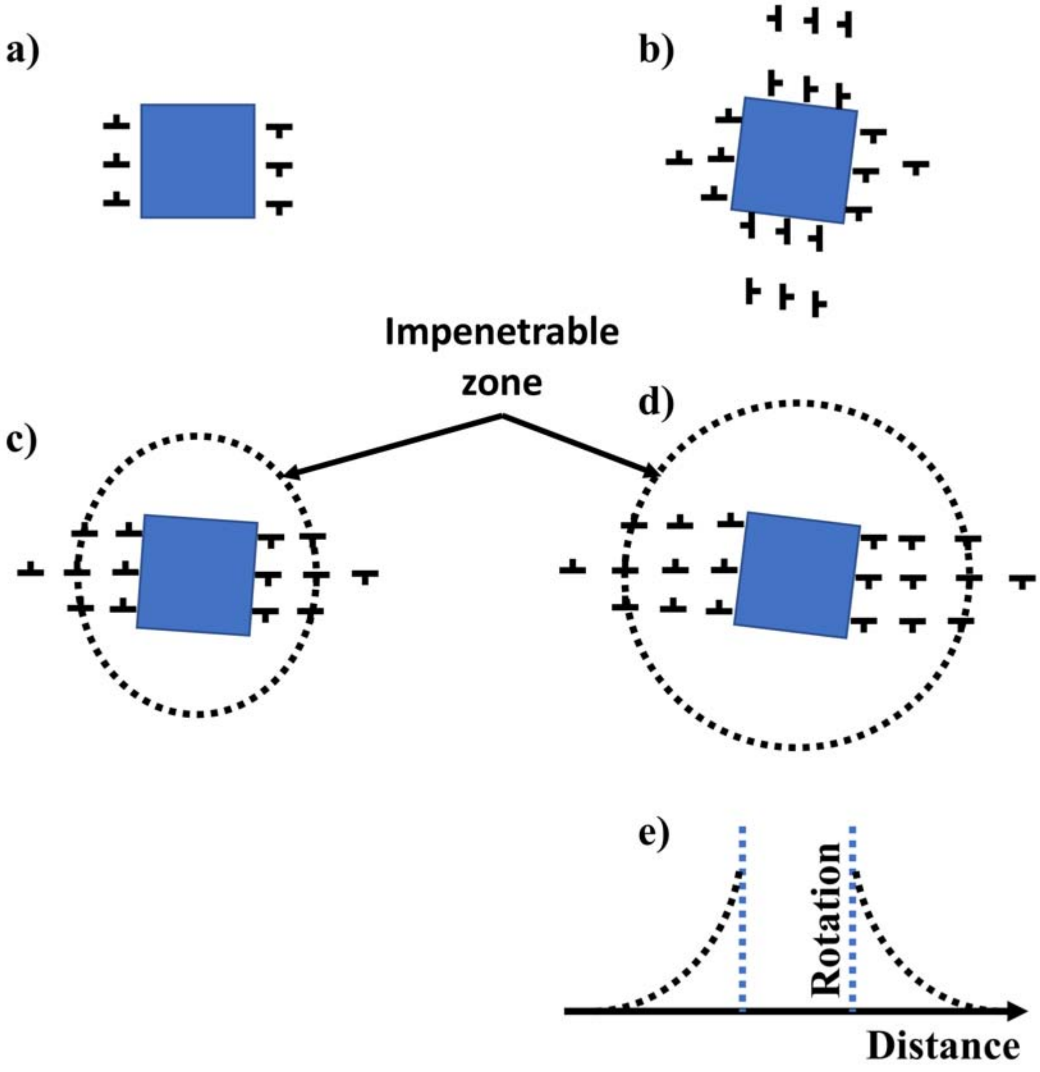

Figure 1.7: Schematic diagram of the development of a deformation zone (Humphreys and Kalu, 1990)

Recalling the first model, the movement of the dislocation near the particle is either stopped or bypassed. However, since the matrix far away from the particle is not affected by the it, it can be ideally deformed as shown in Eq. (1.1) by various slip systems. Therefore, the gradient of strain is formed from the non-deformable particle ($\varepsilon_t = 0$) to the matrix ($\varepsilon_t = t_1$) that is not affected by the particle.

Fig. 1.8 shows the second model in which the deformation zone is developed by the shadows of various slip systems across the non-deformable particle proposed by Humphreys and Ardakani (1994), where the matrix near particles with various slip system traces (S1 and S2) is indicated by dotted lines. The matrix in region-A, which is considered unaffected by the presence of particle, will be similar to the typical slip activity of single-phase metals with same orientations (Fig. 1.8a). However, in region-B, the dislocation slip will be suppressed due to the presence of particle. Eventually, the accumulation of dislocations creates back stresses at the particle and impedes further slip activity in the system. On the other hand, in region-C away from the particle, the slip becomes relatively free as the particle influence decreases. Thus, the particle is considered to shadow a local region in the vicinity of the particle due to the operation of a certain slip system Humphreys and Ardakani (1994). Slip system S2 is also slip limited in this way (Fig. 1.8b). Considering both slip systems S1 and S2 as shown in Fig. 1.8c, the three regions denoted D, E and F are important in this model, except for the regions far away from the particles. Regions D and E are limited in the slip activity by slip systems S1 and S2, respectively, and in the region-F, the activity is more complexly restricted by the both slip systems (Humphreys and Ardakani, 1994). Therefore, the slip activity in the vicinity of the particle behaves in a variety of ways, and this strain incompatibility causes plastic relaxation and crystal rotation, which leads to the development of lattice misorientations with the matrix that is not restricted by the particles.

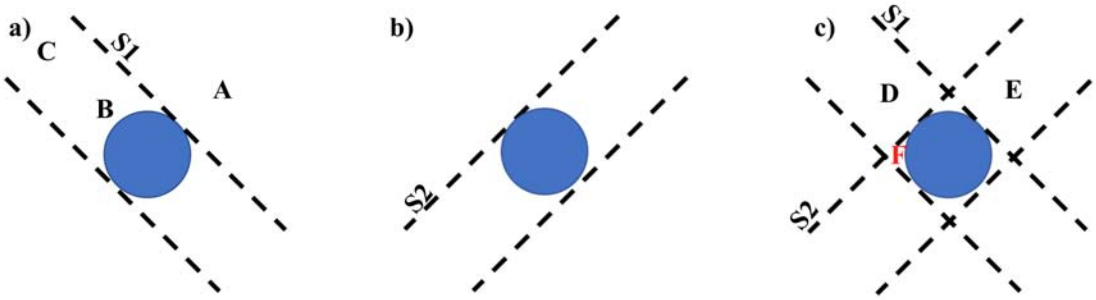

Figure 1.8: Schematic diagram of the slip shadowing model for the deformation zone. (a) Slip on system S1 is restricted by the particle, (b) Slip on system S2 is restricted by the particle, (c) Slip restriction on both systems S1 and S2 (Humphreys and Ardakani, 1994)

Although little research has been done on the misorientations around the particle, it is generally reported that the misorientation between the matrix and the deformation zone is around 30∼40 degrees even after a large deformation (Bay and Hansen, 1979; Humphreys, 1977; Liu et al., 1989). Due to the symmetry of the cubic crystal, this is not necessarily the same as the physical misorientation that occurred during deformation, and the mean misorientation of ∼40 degrees are occurred by randomly oriented crystals.

Most of the deformation regions around the particles have been studied using EBSD and TEM, but when variables such as the elastic modulus of the particle and matrix and the shape of the particle are changed, experimental measurement and analysis of the deformation zone around particle will become difficult. If the plastic relaxation region and strain gradient around the particle can be predicted through modeling, recrystallization by PSN can be more easily controlled by computing the magnitude and region of the misorientation within the deformation region. Therefore, the modeling based on micromechanics is suggested to solve this problem in this study, and the related theory is covered in Section 1.5.

1.4 Annealing after cold rolling

The free energy associated with the dislocations and boundaries in the crystalline material increases due to plastic deformation during the cold rolling, and the processed material containing these defects is thermodynamically unstable. These thermodynamically unstable defects should theoretically be removed naturally, but since such a mechanism lacks the energy to remove defects at room temperature, the structure including unstable defects is maintained even after plastic deformation.

When the plastically deformed material is further annealed at a specific temperature, the thermal activation processes such as diffusion in the solid-state provide enough energy to remove the defects, therefore, providing a mechanism to alternatively arrange them in a lower energy configuration. The evolution of the microstructure of the specimen with plastic deformation during annealing is shown in Fig. 1.9.

Fig. 1.9a schematically shows the retention of an unstable defect structure after plastic deformation. When the annealing process is started, subgrains are formed inside the original grains due to the annihilation and rearrangement of some dislocations during the recovery process (Fig. 1.9b). Subsequently, a recrystallized nucleation site is partially formed in the deformed or recovered structure, which leads to the generation of new dislocation-free grains (Fig. 1.9c). When recrystallization is complete, completely new recrystallized grains with a low dislocation density are formed (Fig. 1.9d), and then the grain growth occurs to lower the interfacial energy (Fig. 1.9e). In addition, partial growth of several large grains may occur under certain circumstances (Fig. 1.9f), which is called abnormal grain growth or secondary recrystallization.

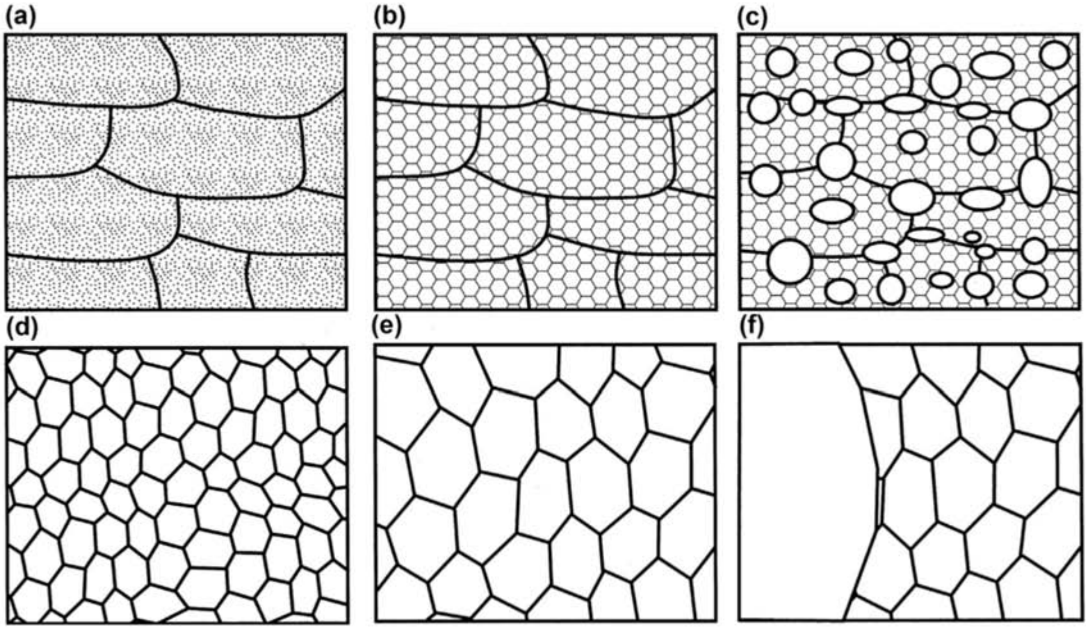

Figure 1.9: Schematic representation of the continuous static recrystallization during the annealing in the plastic deformed metal. (a) formation of subgrain and (b) recrystallized grains growth suppressed by fine particles

According to the textbook written by Humphreys et al. (2004), the borderlines between the microstructure evolution during annealing are unclear, and the restoration process such as recovery, recrystallization, and grain growth occurs in two ways: 1) The restoration process during annealing occurs heterogeneously throughout the deformed material and can be formally distinguished in the nucleation and growth stages, which phenomenon is called a discontinuous process. 2) On the other hand, when microstructures evolve gradually and uniformly without discernible nucleation and growth stages, this phenomenon is called a continuous process. Note that these classifications do not imply behavior by a specific micro mechanism, it is only a classification from a phenomenological point of view. The continuous and discontinuous processes to be considered for the static annealing phenomenon is represented in Table 1.1. The continuous process includes recovery, continuous recrystallization and normal grain growth due to subgrain growth, and the discontinuous process includes discontinuous subgrain growth, primary recrystallization and abnormal grain growth.

Table 1.1: Classification of static annealing phenomenon (Humphreys et al., 2004)

	Continuous	Discontinuous
Recovery	Subgrain growth	Discontinuous subgrain growth
Recrystallization	Continuous recrystallization	Primary recrystallization
Grain growthl	Normal grain growth	Abnormal grain growth

For the lower deformation, the low driving force associated with the dislocation density will lead to discontinuous static annealing behavior. Whereas, the continuous and discontinuous static recovery and recrystallization behavior of largely plastically deformed metal is difficult to distinguish because the borderlines are unclear, but the continuous and discontinuous recovery and recrystallization can be identified in specific regions. For instance, the recrystallization that occurs preferentially by the PSN effect in the deformation region around coarse second phase particles with high dislocation density can be classified as discontinuous recrystallization. In addition, localized discontinuous recrystallization may occur at certain locations within the dispersoids regions, but continuous recrystallization usually occurs in this region (see Fig. 1.11). The new grains generated by this discontinuous recrystallization cause abnormal grain growth, resulting in inhomogeneous grain size. However, assuming that the migration of boundary and the grain growth is delayed by the uniformly distributed fine particles, it can be considered that uniform grain size is obtained overall.

Although continuous and discontinuous static annealing behavior can be observed through TEM, it is difficult to analyze these phenomena because only very local regions can be observed. Therefore, the continuous and discontinuous static recovery and recrystallization behaviors should be distinguished by EBSD analysis, and the effect of these behaviors on the recrystallized microstructure can be analyzed.

The following is a brief summary of the phenomena of microstructure evolution during the recovery and recrystallization, where most of the content covered in this section was cited in the textbook written by Humphreys et al. (2004).

1.4.1 Recovery

Recovery refers to the change in properties of the deformed material that occurs first in the restoration process during annealing. In addition, the recovery can occur not only in plastically deformed materials, but also in any crystals in which non-equilibrium, high concentrations of point or line defects have been introduced. This recovery behavior is limited to the local process and is mainly due to changes in the dislocation structure of the material (Beck, 1954; Bever et al., 1973; Furu et al., 1995).

Dislocation recovery is not a single microstructural evolution process, it is a series of micro-mechanisms schematically shown in Fig. 1.10. Whether some or all of these behaviors represented in Fig. 1.10 occur during recovery will depend on a number of parameters such as alloy type, material purity, strain, heat treatment temperature, etc. Although the recovery stages tend to occur in the order shown, there may be significant overlap between them.

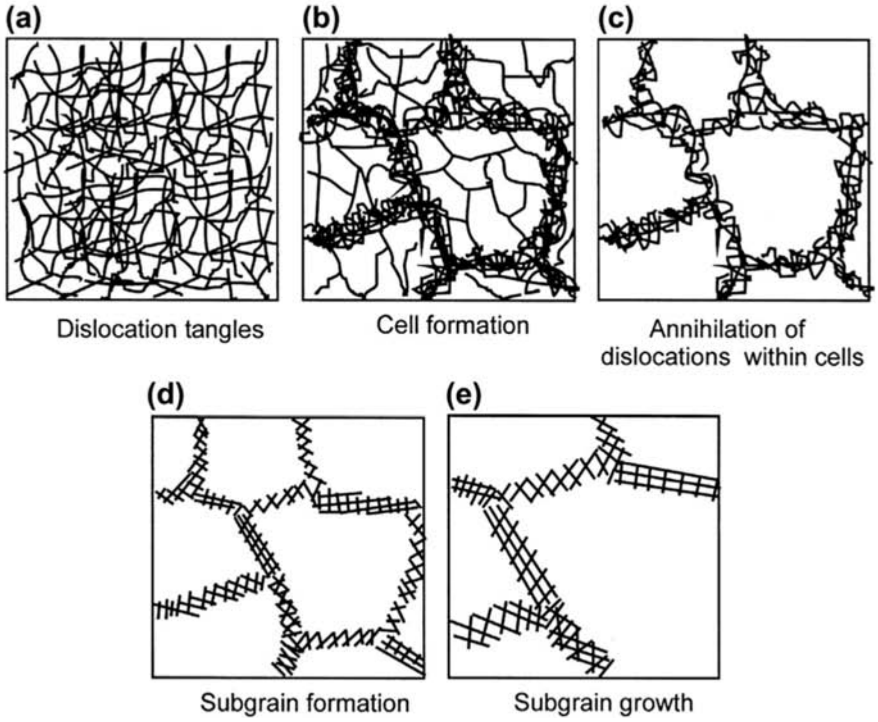

Figure 1.10: Schematic diagram for each step during the recovery in the plastically deformed material (a) dislocation tangles, (b) cell formation, (c) annihilation of dislocations within cells, (d) subgrain formation, (e) subgrain growth (Humphreys et al., 2004)

Dislocation migration and annihilation during recovery are the two main processes that lead to the rearrangement of dislocations into lower-energy configurations. These processes are achieved by glide, climb, and cross-slip of the dislocation. For example, the dislocation with opposite signs on the same glide plane annihilate by gliding towards each other, which can also occur at low temperatures. In addition, the combination of ascent and glide cancels the translocation of the opposite Burgers vector in the other glide plane. Since the dislocation climb requires thermal activation, this process can only occur at high homologous temperatures. These microstructure changes in the recovery stage of the deformed material occur subtly on a very small scale. Therefore, microstructure analysis for the recovery process is observed using TEM with a high-magnification, or some physical and mechanical properties are indirectly measured through changes in electrical conductivity and hardness.

1.4.2 Recrystallization

The process in which deformed grains with defects such as dislocations due to plastic deformation are replaced with new grains without internal defects is recrystallization behavior, and the driving force for recrystallization is energy accumulated by plastic deformation. These recrystallization behaviors are classified into two types: 1) static recrystallization that occurs when a material deformed by cold working receives heat from outside, and 2) dynamic recrystallization that occurs when a material undergoes plastic deformation at above the recrystallization temperature. Therefore, the driving force for static recrystallization is determined by the combination of the energy accumulated by plastic deformation and the additional energy obtained from the outside depending on the annealing temperature.

The plastically deformed metals have greater internal energy than the undeformed state. The cell structure associated with dislocation inside deformed material is a thermodynamically unstable structure. When annealing is performed at or above the recrystallization temperature, sufficient energy to activate the recrystallization is supplied from the outside, so that the annihilation of dislocations occurs due to dislocations climb inside the material, which leads to the creation of new particles with low dislocation density.

Fig. 1.11 schematically shows the discontinuous static recrystallization occurring inside the material when the plastically deformed metal undergoes an annealing process. Fig. 1.11a shows that the dislocation introduced by plastic deformation is accumulated inside the deformed grain. Then, the subgrains are formed inside the deformed grains by rearrangement of the dislocations, and the nucleation site for recrystallization occurs in a local region with higher energy, resulting in new recrystallized grains (Fig. 1.11b). When recrystallization is complete, the new recrystallized grain growth occurs to lower the interfacial energy as shown in Fig. 1.11c.

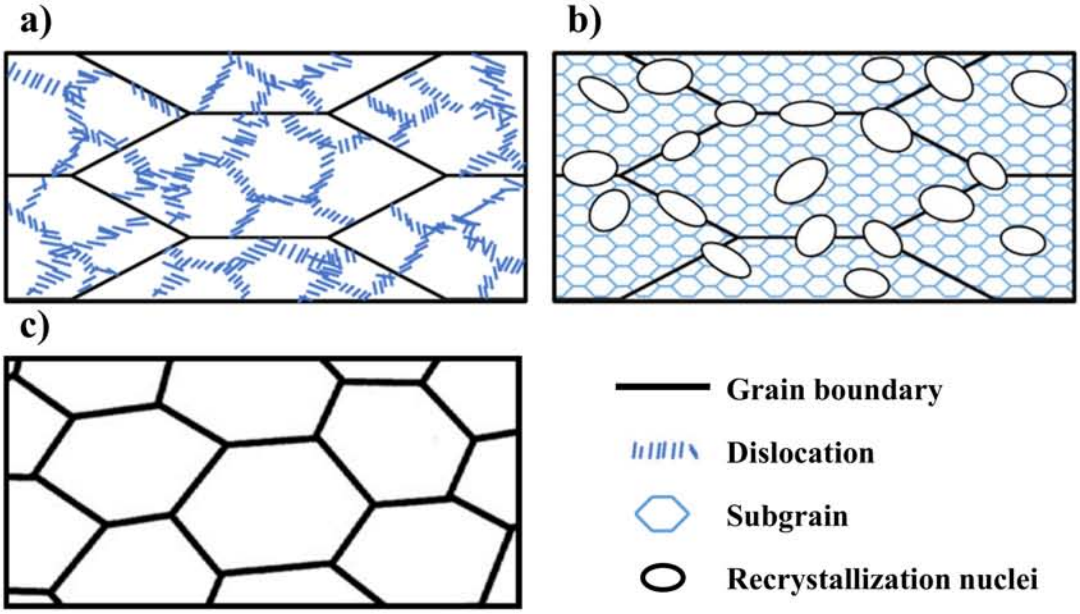

Figure 1.11: Schematic representation of the discontinuous static recrystallization during the annealing in the plastic deformed metal. (a) deformed state, (b) nucleation for recrystallization and (c) grain growth after recrystallization complete

Fig. 1.12 shows a schematic diagram of a continuous static recrystallization in which grain coarsening is controlled by dispersed fine particles during recrystallization. The subgrains formed inside the deformed grains are gradually developed by increasing the misorientation until the LAGB evolves to HAGB. Since the borderlines between the discontinuous and continuous static recrystallization are unclear, the static annealing phenomenon shown in Table 1.1 should be considered.

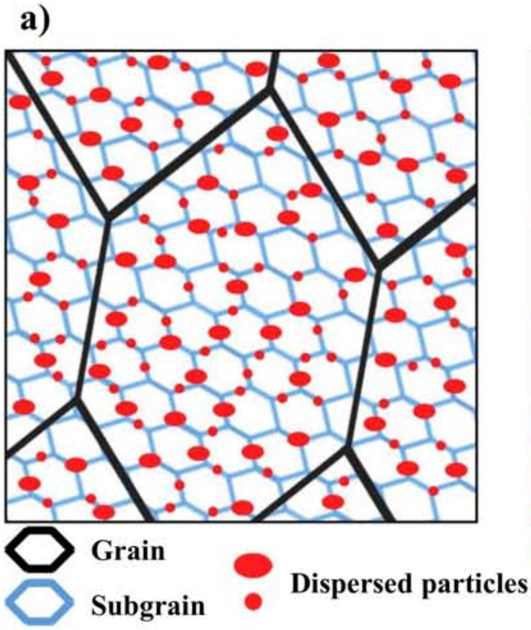

Figure 1.12: Schematic representation of the continuous static recrystallization during the annealing in the plastic deformed metal. (a) formation of subgrain and (b) recrystallized grains growth suppressed by fine particles

Factors affecting the recrystallization behavior in Al-Mn based aluminum alloys include the grain size, the levels of Mn concentration, and the precipitate size and distribution. The distribution of precipitates depending on the heat treatment conditions before cold rolling is the most important factor in forming the dislocation distribution associated with the nucleation for recrystallization. Recovery and recrystallization behavior are basically caused by the migration of grain boundaries. Nucleation sites for recrystallization are generated by the growth of subgrains or migration of grain boundary. In addition, the migration of grain boundaries and subgrains can be disturbed by the existence of particles, concurrent precipitation, and segregation of atoms into grain boundaries, which will delay recovery and recrystallization.

Fig. 1.13 shows a schematic TTT curve for a material rapidly heated to the annealing temperature, where the interaction points between precipitation and recrystallization are indicated by A and B. The temperature T_A and T_B and the corresponding time depend on the specific alloy, and the T_A of Al-Mn alloy is ~400 °C and T_B is ~350 °C (Somerday and Humphreys, 2003). In regime−I ($T < T_B$), although the coarsening of the precipitate and recrystallization can simultaneously occur, this process would be extremely slow for Al-Mn alloys with T_A and T_B below 400 °C. Thus, significant precipitation occurs before recrystallization, and recrystallization is inhibited. For regime−II ($T_A > T > T_B$), the recrystallization begins before precipitation, but subsequent precipitation occurs during recrystallization and will eventually prevent the completion of recrystallization. In regime−III ($T > T_A$), since the recrystallization is completed before precipitation, there is no delay in recrystallization behavior due to precipitation, but precipitation may subsequently occur in the recrystallized state.

The velocity, v, of grain boundary for recrystallization can be expressed as

$$v = M \sum P_i = MP \tag{1.2}$$

where, the M is mobility of the boundary, and the P is net pressure.

The driving force is generally introduced by the reduction of free energy due to the removal of lattice defects during the migration of boundary. Dislocation density increased by plastic deformation is an important energy source for driving force during the annealing. In addition, the disappearance of grain boundaries is an important driving force during grain growth and secondary recrystallization. Therefore,

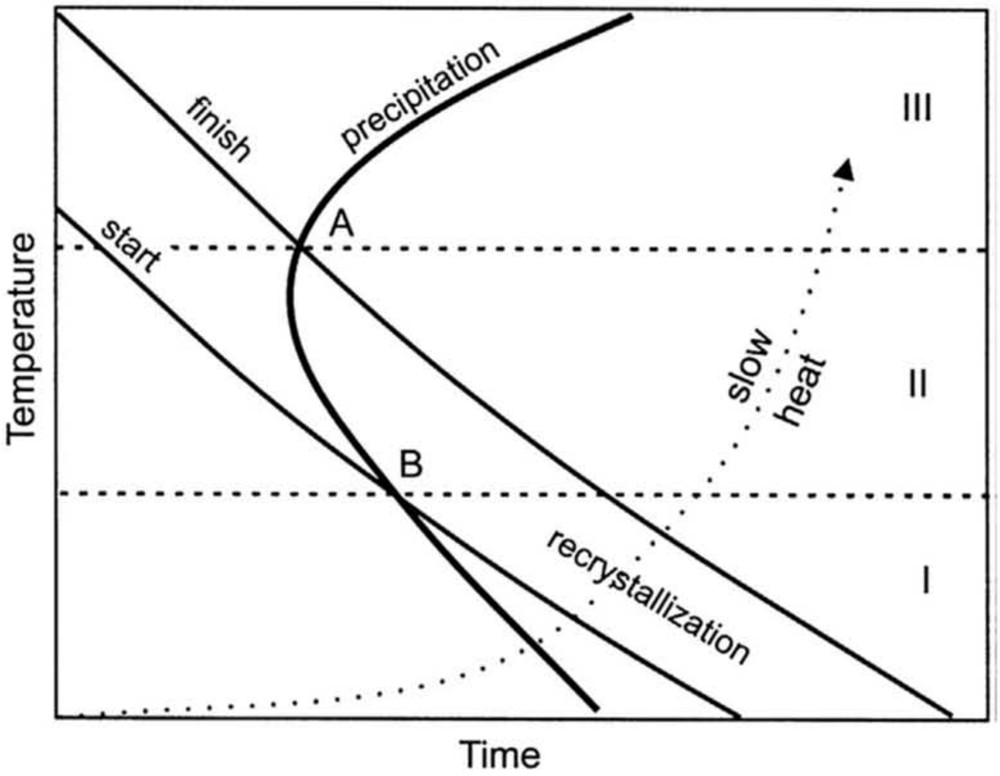

Figure 1.13: Schematic TTT diagram for recrystallization and precipitation in cold rolled supersaturated aluminum alloys, rapidly heated to temperature (Humphreys et al., 2004)

when the average grain size is small, the driving force associated with the decrease in grain boundaries increases, and the nucleation sites for recrystallization increase, which will eventually lead to refinement of the recrystallized grain.

As mentioned in the previous Section 1.3.2, it is also necessary to take into account the deformation zone due to the increase in dislocation density and stress disturbance around the second phase particles. These deformation zones are covered in the next Section 1.5.

1.5 Modelling of residual stress around precipitate

Cold rolling is an operation of physically reducing the cross-section of the cast material, and compressive and tensile stress are simultaneously applied to the specimen. According to Baldwin (1949), the typical distribution of residual stress occurring in cold-rolled sheets is classified into two main types. When the rolling reduction is small by using a relatively small roller of a thick plate, the deformation is mainly concentrated near the surface. Therefore, since the large deformation of the surface is constrained by the small deformation area inside, compression stress occurs on surface and tensile stress occur inside the material. On the other hand, when a large amount of strain is applied to a thin plate with a large roller, the deformation in the thickness direction becomes more uniform. At this time, since the metal in contact with the roller rapidly develops flow stress in the center and the surface is constrained by friction, tensile stress occurs on the surface and compressive stress occurs inside the material. These two cases are implemented by the macroscopic residual stress which is acting on the plate during general cold rolling. However, the distribution and magnitude of residual stress in the alloy containing the inhomogeneous inclusion are largely dependent on the distribution and size of the inclusion locally from the viewpoint of micro-residual stress.

In the region with inhomogeneous inclusion, the mismatch of plastic strain occurs between the inclusion and matrix with a different modulus of elasticity. When the compressive or tensile stress occur in the matrix during plastic deformation, the residual stress is generated around the inhomogeneity because the opposite stress acts on the precipitate. Residual stress formed around these inhomogeneous precipitates may be a great influence on nucleation during recrystallization.

Considering the strain (or stress) acting on the material during cold rolling, the tensile strain is applied in the x_1-axis direction and the compressive strain is applied in the x_3-axis direction (Fig. 1.14). When the cold rolling is initiated, the strain distribution of the specimen creates a steep displacement gradient from the surface to the inside. The residual stress introduced by the mismatch of plastic strain during cold rolling can be approached in three consecutive stages, as shown in Fig. 1.14. Note that the arrows only indicate the direction of the plastic flow. Assuming in 2-dimension to simplify the analysis for the residual stress around the inhomogeneity introduced by the mismatch of plastic strain during cold rolling, it can be distinguished by an inner inhomogeneity and an outer matrix (Fig. 1.14a). Since the matrix is deformation faster than inhomogeneity at the start of cold rolling, the inhomogeneity and the matrix are subjected to opposite elastic strains in the same direction, which is tensile and compressive in a direction parallel to the x_1-axis, respectively, as shown in Fig. 1.14b. Assuming that the external strain is high enough for the matrix to allow plastic deformation, the matrix becomes a plastic state and eventually plastic deformation occurs in the same direction as the applied external strains, while the inhomogeneity is still in an elastic state. In order to undergo plastic deformation by cold rolling, the strain in the matrix and inclusions will change in opposite directions, as shown in Fig. 1.14c. At this stage, even if both the matrix and the inhomogeneity reach the plastic state, the matrix will deform much more than the inhomogeneity because the matrix has a lower modulus of elasticity than the inhomogeneity. Therefore, disturbance of strain introduced by the mismatch of the plastic strain between the matrix and the inhomogeneity will occur around the inhomogeneity.

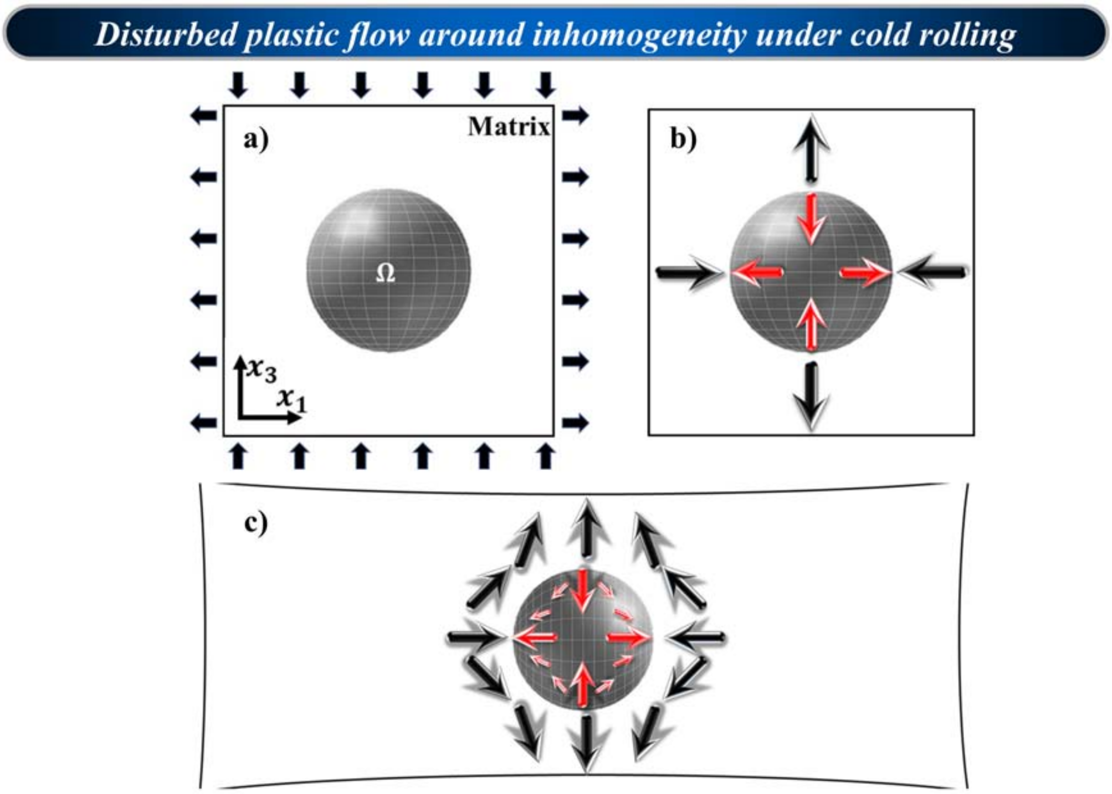

Figure 1.14: Simplified diagram showing the strain evolution in the specimen during cold rolling (the arrows represent the strain direction acting on each section)/ (a) applied strain (or stress) under cold rolling, (b) regime-1: both the outer matrix and the inhomogeneity are in elastic state and (c) regime-2: the outer matrix is in plastic state while the inhomogeneity is still in elastic state.

Analysis of these strain fields around inhomogeneous inclusions has little quantitative data for polycrystalline due to the difficulty of experimental measurement. Region of highly misoriented small equiaxed grains less than $0.1nm$ in diameter are found near the inhomogeneous particle parallel to the rolling direction, but further away from the inhomogeneity, the subgrains become elongated and distorted due to the presence of the particles (Humphreys, 1977; Hansen and Bay, 1981).

Therefore, in this study, the inhomogeneity problem based on micromechanics is adopted to investigate the deformation zone formed around the precipitates. The following is a brief summary of the Eshelby inclusion problem (J. D. Eshelby, 1957, 1959), where most of the contents are cited in the textbook written by T. Mura (1987) (Micromechanics of Defects in Solids).

1.5.1 General Eshelby's inclusion problem

Micromechanics is a subject that deals with the mechanics associated with the microstructure of materials, where the method used is the continuum theory of elasticity, and its applications cover wide fields related to the microstructure and mechanical behavior of materials. Eshelby's inclusion method plays an essential role as a fundamental theory in the field of modern micromechanics and has been widely applied to evaluate the effective strain, stress, and displacement fields of heterogeneous media, where these subjects are handled by means of a powerful and unified method that is called the "*eigenstrain*" defined by T. Mura (1987). Eigenstrain is denoted by ε_{ij}^{*} and means strain when the stress is zero, which includes inelastic strains associated with thermal expansion, phase transformation, initial strain, plastic strains, and mismatch strain.

Considering an infinitely homogeneous linear elastic solid (matrix), D, and an inclusion, Ω, embedded in a matrix, Eshelby's inclusion problem is solved by a series of cutting and combining as shown in Fig. 1.15. Assuming that no force is applied to the inclusion nor to the matrix and both inclusion and matrix have the same elastic constant, the initial strain and stress fields are 0 in the matrix and inclusion (Fig. 1.15a). When the inclusion is removed from its surrounding matrix (Fig. 1.15b), the inclusion undergoes a uniform strain, ε^*_{ij}, to reach its an unconstrained state and the stress is zero (Fig. 1.15c). Thereafter, the inclusions are restored to their original shape by applying appropriate surface traction (Fig. 1.15c), and then put the inclusion back to the matrix where it was cut off from the matrix and combine the interface between the inclusion and the matrix (Fig. 1.15d). Finally removing the surface traction of the inclusion, the equilibrium between the inclusions and the matrix is reached at a constrained strain, ε^c_{ij} (Fig. 1.15e), eventually returning to the original inclusion problem as shown in Fig. 1.15a.

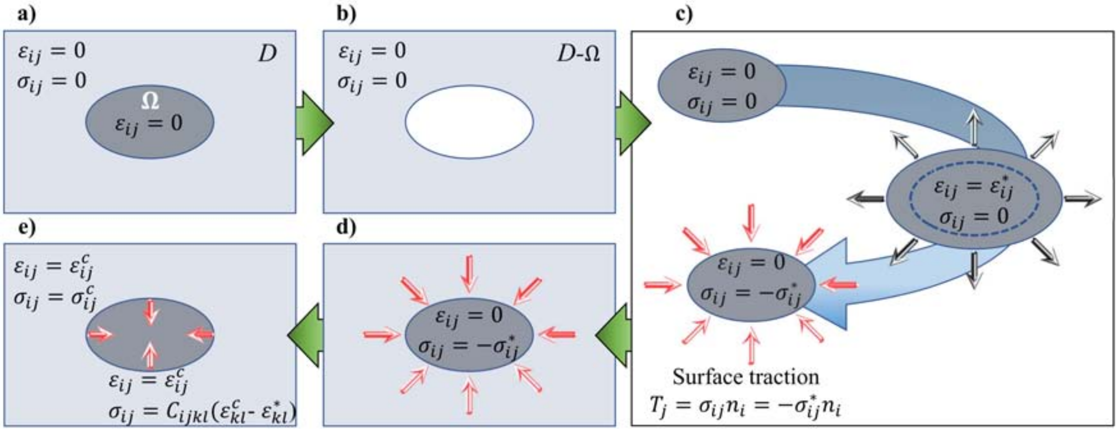

Figure 1.15: Schematic diagram of Eshelby inclusion problem.

As a result, the strain and stress in the inclusion and matrix will deform as follow.

$$\varepsilon_{ij} = \begin{cases} \varepsilon^c_{ij} & in \ \ D - \Omega \\ \varepsilon^c_{ij}(= S_{ijkl}\varepsilon^c_{ij}) & in \ \ \Omega \end{cases} \quad \sigma_{ij} = \begin{cases} C_{ijkl}\varepsilon_{kl} & in \ \ D - \Omega \\ C_{ijkl}(\varepsilon_{kl} - \varepsilon^c_{ij}) & in \ \ \Omega \end{cases} \tag{1.3}$$

with $\varepsilon_{ij}= e_{ij}+\varepsilon^*_{ij}$
where C_{ijkl} denotes the elastic moduli, ε_{ij} is the total strain, e_{ij} is the elastic strain, and ε^*_{ij} is the eigenstrain. In addition, a fourth-

order rank tensor S (S_{ijkl}=S_{jikl}=S_{ijlk}) is referred to as Eshelby's tensor that relates the constrained strain, ε^c_{ij}, inside the inclusion to its eigenstrain, ε^*_{ij}.

The internal stress due to the inhomogeneity is explicitly computed by Green's function. For isotropic materials, elastic Green's function is given

$$G_{ij}(x-x^{'}) = \frac{1}{16\pi\mu(1-\nu)|x-x'|}\left((3-4\nu)\delta_{ij} + \frac{(x_i-x_i^{'})(x_j-x_j^{'})}{|x-x'|^2}\right) \tag{1.4}$$

where, ν is the Poisson ratio, μ is the shear modulus, x is the coordinates for the inclusion in an infinite isotropic elastic matrix, and δ_{ij} is the Kronecker delta. The Eshelby tensor for the interior and exterior points can be solved by integral with respect to $|\Omega|$ as follows,

$$\begin{aligned}\varepsilon_{ij}(x) =& S_{ijkl}(x)\varepsilon^*_{kl}\\ =& \frac{1}{2}\int_{|\Omega|}\big\{C_{klmn}\varepsilon^*_{mn}(x')G_{ik,l}(x-x')n_j\\ &+ C_{klmn}\varepsilon^*_{mn}(x')G_{jk,l}(x-x')n_j\big\}dS(x')\end{aligned} \tag{1.5}$$

where $G_{ij,k}$ is first derivative of Green's function, n_i is outward normal vector of the surface $|\Omega|$.

For example, Eshelby's tensor S_{ijkl} for the sphere shape of inclusion is simply given by

$$\begin{aligned}S_{1111} =& S_{2222} = S_{3333} = \frac{7-5\nu}{15(1-\nu)},\\ S_{1122} =& S_{2233} = S_{3311} = S_{1133} = S_{2211} = S_{3322} = \frac{5\nu-1}{15(1-\nu)},\\ S_{1212} =& S_{2323} = S_{1313} = \frac{4-5\nu}{15(1-\nu)}\end{aligned} \tag{1.6}$$

As for the point on the outside of the inclusion, the stress and strain are nonuniform and quite different from the inside. In an infinite isotropic elastic body, coordinate of an ellipsoidal inclusion with half axis, $a_i = (i = 1, 2, 3)$ parallel to x_1, x_2 and x_3 axis, is mentioned by the following elliptic equation

$$\frac{x_1^2}{a_1^2} + \frac{x_2^2}{a_2^2} + \frac{x_3^2}{a_3^2} \leq 1 \tag{1.7}$$

The solution of the Eshelby tensor is named as the interior point Eshelby tensor when the evaluation point is located inside the inclusion, e.g., the value of the elliptic equation is less than 1.0. In the meanwhile, the solution is named as the exterior point Eshelby tensor when the evaluation point is located outside the inclusion (Fig. 1.16).

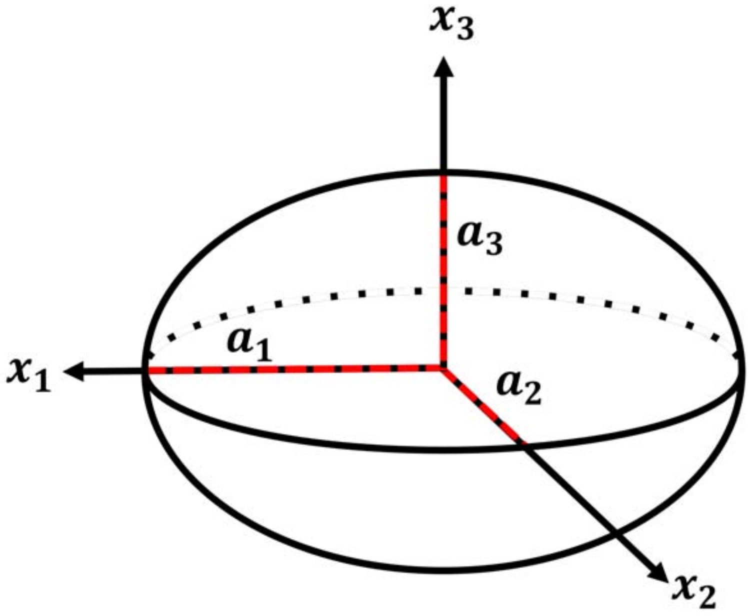

Figure 1.16: Schematic diagram of ellipsoidal inclusion aligned with semi-axes a_1, a_2 and a_3 parallel to coordinates, x_1, x_2 and x_3, respectively.

1.6 Methodology

The main purpose of this experiment is to collect a series of data to investigate the recovery and recrystallization behavior of Al-Mn based alloys under residual stress. The initial material subjected to a series of processes was provided by UACJ Corp. The various equipment used for the microstructure characterizations, the sample preparations and the measurement conditions for the entire experiment are briefly described in this section.

1.6.1 Sample preparation

The chemical composition of AA3003 aluminum alloy in this study is listed in Table 1.2. The initial as-cast alloy (200 *mm* in length, 80 *mm* in width, 155 *mm* in thick) was fabricated by DC cast. Fig. 1.17. schematically shows the dimension and orientation of DC-cast Fig. 1.17a) and cold-rolled (Fig. 1.17c) AA3003 aluminum alloy. The as-cast AA3003 (Al-1.05Mn in wt.%) alloy was homogenized under different conditions; 580 °C for 8h with a heating rate of 50 °C/h (RA), 580 °Cfor 16h with a heating rate of 500 °Ch (RB), and then immediately quenched in the water at room temperature (R.T). All homogenized specimens were processed by cold-rolling with a reduction ratio of 90%. The cold-rolled sheets were isothermally annealed at 220 °C to 400 °C for 2s to 24h in salt-bath, and then immediately quenched into the water at R.T.

Table 1.2: Chemical composition of AA3003 aluminum alloy used in this study

	Mn	Cu	Fe	Si	Ti	Al
AA3003	1.15	0.16	0.52	0.28	0.01	bal.

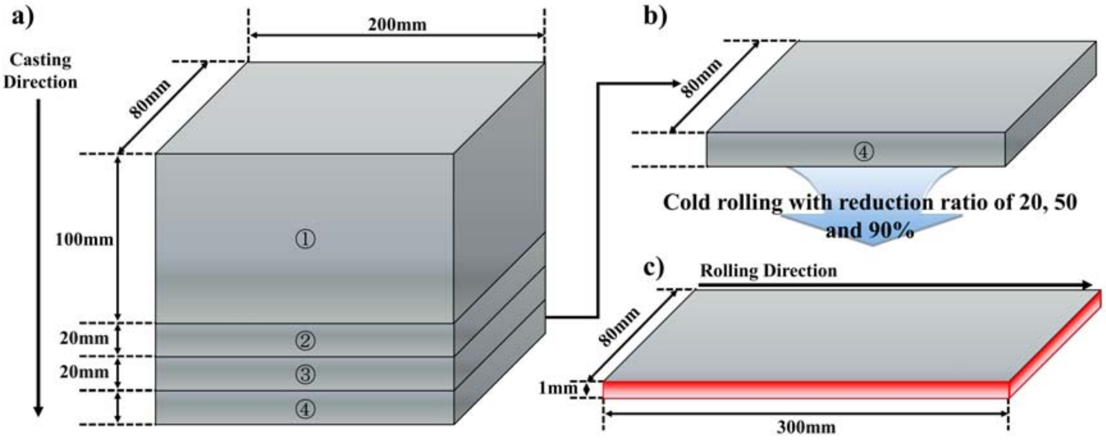

Figure 1.17: (a) Schematic diagram of DC casting direction and dimensions, (b) positions of a sample taken from the ingots for a test, and (c) dimensions of cold-rolled sheets

The homogenization treatment (as-homo) was conducted at 580 °C for 8h with a slow heating rate of 50 °C/h (RA), and then immediately quenched into the water at room temperature (R.T). Then the as-homo specimens were processed by cold-rolling with a reduction ratio of 20% (AM2), 50% (AM5), and 90% (AM9). The cold-rolled sheets were isothermally annealed in a salt bath at 300 °C, 350 °C, 375 °C and 400 °C for times ranging from 2s to 24h, and then immediately quenched into the water at R.T.

1.6.2 Microstructural characterization

The evolution microstructure of deformed and annealed specimens was mainly observed by optical microscope (OM, BX51M, Olympus, Tokyo, Japan) and field-emission scanning electron microscopy (FE-SEM, JSM7200F, JEOL Ltd., Tokyo, Japan), in which the center of the longitudinal section containing the rolling direction (RD) and the normal direction (ND) were chosen for the observation area.

The polished specimens for OM were anodized at 40 V within 2 min using Baker's reagent (aqueous solution of 3.3% HBF_4). The grain size measurement was carried out in accord with the linear intercept method based on ASTM-E1382 (ASTM, 1997). The number density and area fraction constituent particles of the polished specimen were measured by FE-SEM image analysis using the Image-J program. Primary particles and dispersions were measured separately in each cluster region.

The measurement of crystalline orientation and grain boundary misorientation was conducted by FE-SEM equipped with electron backscatter diffraction (EBSD, DVC5, EDAX, AMETEK Inc., Berwyn, PA, USA), in which the data was treated by TSL orientation imaging microscopy (OIM, Analysis8, EDAX, AMETEK Inc., Berwyn, PA, USA) analysis software and MTEX toolbox for MATLAB (Hielscher et al., 2019) (R2019a). EBSD analysis was performed with an acceleration voltage of 15 keV, a working distance of 18 mm, and a step size of 0.025∼0.1 μm at a samples tilt of 70 °.

In order to examine detailed microstructure, transmission electron microscopy (TEM, JEM-3010, JEOL Ltd., Tokyo, Japan) observation was carried out for as-rolled and annealed specimens with operation voltage of 300 kV. The foil specimen preparation suitable for TEM was made by twin jet polishing technique in a 20% HNO_3 methanol solution under the condition of about $-20\,^{\circ}C$ or less.

The change in crystallite size and dislocation density was measured and analyzed by synchrotron and conventional XRD. We utilized the high intensity X-ray BL02B2 beam line (λ=0.516Å) of SPring-8 synchrotron radiation facility (JASRI, Hyogo, Japan) for this study. The time resolution of this experiment was 10s. The conventional XRD measurement was carried out by convergent beam method with Cu-Kα (λ=1.540Å) radiation (RINT-2100, Rigaku Co. Ltd., Tokyo, Japan).

1.6.3 Vickers hardness

The microhardness was measured at location along the center line of RD plane by the Vickers hardness tester (MMT-X, Matsuzawa Co. Ltd., Akita, Japan) under a load of 100 gf for 15s, where the hardness value was determined as the average value measured at least 5 times for each sample. These microhardness results are used to obtain the apparent activation energy for the restoration process. The apparent activation energy for each restoration process of cold-rolled specimens was estimated by using the modified JMAK-microhardness model.

1.6.4 Electrical conductivity

The electric conductivity was measured by eddy current inspection at room temperature using an exclusive 500 kHz dedicated inspection probe (SIGMA 3000 tester, GE Inspection Technology), where the electrical conductivity was normalized by the unit in %IACS (International Annealed Copper Standard). The unit used for the analysis was calibrated using a standard sample before each measurement. The electrical conductivity measured for the different conditions (as-cast, as-homo and cold-rolled specimens before/after annealing) were represented by the average electrical conductivity, where the measurements were carried bout at least 5 times on the ND plane of each specimen. The unit of %IACS can be converted to an electrical resistivity, ρ_{elec}, as follows

$$\%IACS = \rho_{elec}/n\Omega m \tag{1.8}$$

The concentration of Mn in a solid solution was determined by following formula,

$$Mn(mass\%) = (\rho_{measure} - \rho_{pure\,Al}/\Delta\rho_{Mn\,in\,Al\,alloy} \tag{1.9}$$

Where, $\rho_{measure}$ is the electrical resistivity converted by Eq. (1.8), $\rho_{pure\,Al}$ is the electrical resistivity of pure aluminum (26.5 $n\Omega m$ at room temperature (Komatsu and Fujikawa, 1997)) and $\rho_{Mn\,in\,Al\,alloy}$ is the electrical resistivity contribution for Mn solute atom in Al matrix (31 $n\Omega m$ mass%$^{-1}$ at room temperature (Komatsu and Fujikawa, 1997)).

1.6.5 Modelling

All computational work for residual stress around the constituent particles were performed by coding in MATLAB developed by MathWorks, and visualization work was also implemented by using the plot functions provided by MATLAB. Note that the license for MATLAB was used by acquiring an "*Individual License*" supported by Tokyo Institute of Technology.

1.7 Purpose of the present study

The objective of the present study is to obtain a fundamental understanding of the plastically deformed microstructure of the cold rolled sheet containing the second particles and the subsequent microstructure evolution by thermal treatment under the residual stress. For this purpose, a commercial AA3003 aluminum alloy was selected for investigation in this work. The following objectives are sought in this thesis:

- After homogenizing the cast material under two conditions with different heating rates and holding temperatures, the influence of the distribution and size of the precipitate on the specimen during plastic deformation is investigated. In addition, using an alloy homogenized under the same conditions, the characteristics of the plastic deformation microstructure according to the cold rolling reduction are evaluated.

- Regarding the microstructural changes during annealing, evaluation of the decisive factors affecting the recovery and recrystallization with simultaneous precipitation behaviors of cold-rolled specimens is carried out. Specifically, this work investigates the influence of microstructures such as dislocation density, number density of primary and secondary particles, level of Mn supersaturation in Al matrix, etc., which serves to promote or suppress the overall restoration behaviors.

- A theory based on micromechanics is introduced to quantitatively evaluate the residual stress induced around the constituent particles, which are computed and visually implemented by the MATLAB. The shape of the constituent particles and the disturbance of strain and stress around the constituent particles are quantitatively investigated under actual applied cold rolling conditions, and the critical strain required to initiate recrystallization by PSN is described.

- The validation of predicted model is verified by comparing the EBSD results around the α-Al(Mn, Fe)Si precipitate in cold-rolled AA3003 alloy with different reduction ratios.

1.8 Outline of the present thesis

The present thesis is entitled “Recovery and Recrystallization behavior in the cold-rolled Al-Mn based alloy considering residual stress”. This work focuses on the field experimental analysis of microstructure behavior occurring during cold rolling and annealing, as well as the analysis of residual stress around the precipitate based on the Eshelby inclusion problem. The plastic deformation behavior is analyzed in terms of initial grain size and dislocation density. The driving force and other variables for recrystallization are explained through the JMAK model and dislocation density. The effect of cold rolling and the shape of the precipitate on the deformed zone around the precipitate is analyzed by the residual stress around the precipitate in terms of mismatch of plastic strain between matrix and precipitate with a different modulus of elasticity. By comparing the EBSD analysis results and the computation results based on micromechanics, the influence of the precipitate on the deformation zone around the precipitate is evaluated. The outline of the present thesis consisting of 6 chapters is shown in Fig. 1.18.

In Chapter 1 “General introduction”

Background, literature review and purpose of the present study are introduced.

In Chapter 2 “Recrystallization kinetics and microstructure evolution of cold-rolled AA3003 aluminum alloy with various reduction ratio”

To investigate the influence of cold rolling reduction ratio on recrystallization kinetics, the cold-rolled AA3003 aluminum alloy was fabricated with a reduction ratio of 20%, 50% and 90%, and then the cold-rolled sheet was subjected to isothermal annealing in a salt bath ranging from 300 °C to 400 °C. The evolution of the microstructure in the cold-rolled specimen was investigated based on the change in the number fraction of the LAGBs and HAGBs, and the electric conductivity associated with the concurrent precipitation. The relaxation and recrystallization kinetics under different annealing conditions were characterized in terms of the Johnson–Mehl–Avrami–Kolmogorov (JMAK) model, where micro-hardness tests were conducted for estimation of mechanical energy stored in cold rolled specimens.

***In Chapter 3* "Influence of constituent particles on restoration behavior in cold-rolled AA3003 aluminum alloy"**

This chapter focused on investigating the microstructure evolution of the severely deformed AA3003 alloys during annealing with the different level of Mn supersaturation and the constituent particle distribution. In order to examine the influence of the number density and area fraction of constituent particles on work hardening and restoration behavior, the amount of Mn supersaturation in the Al matrix was controlled by different homogenization conditions. The effect of constituent particles on the dislocation density as well as the activation energy for recovery and recrystallization was also discussed.

***In Chapter 4* "Micromechanical analysis of residual stress around coarse precipitate under cold rolling condition"**

In this chapter, the influence of the constituent particle on the deformed microstructure induced by the cold rolling was estimated by adopting a micromechanical-based model, where the stress and strain disturbance around the coarse particle were quantitatively analyzed by solving Eshelby inhomogeneous inclusion problem. The residual stress inside and outside the coarse particle were explicitly computed by using the analytical solution of the interior and exterior points Eshelby tensor. The residual stress dependent on the aspect ratio of the coarse particle and its restoration process was also discussed.

In Chapter 5 **"Influence of residual stress around constituent particles on recrystallization and grain growth in Al-Mn based alloy during annealing"**

A comprehensive experimental study on the influence of constituent particles on the restoration behavior after cold rolling was investigated in chapter 5, and the residual stress and deformation zone formed around the constituent particles were analyzed by the micromechanics theory. The process of nucleation and growth depending on the reduction ratio was experimentally determined in accord with the change in dislocation density under the constant volume fraction of constituent particles. The deformation zone formed around the precipitate was characterized by the misorientation measured by the EBSD analysis and the residual stress predicted by the Eshelby method.

In Chapter 6 **"General conclusion"**

This chapter summarized the overall conclusion of the present study and future work is proposed.

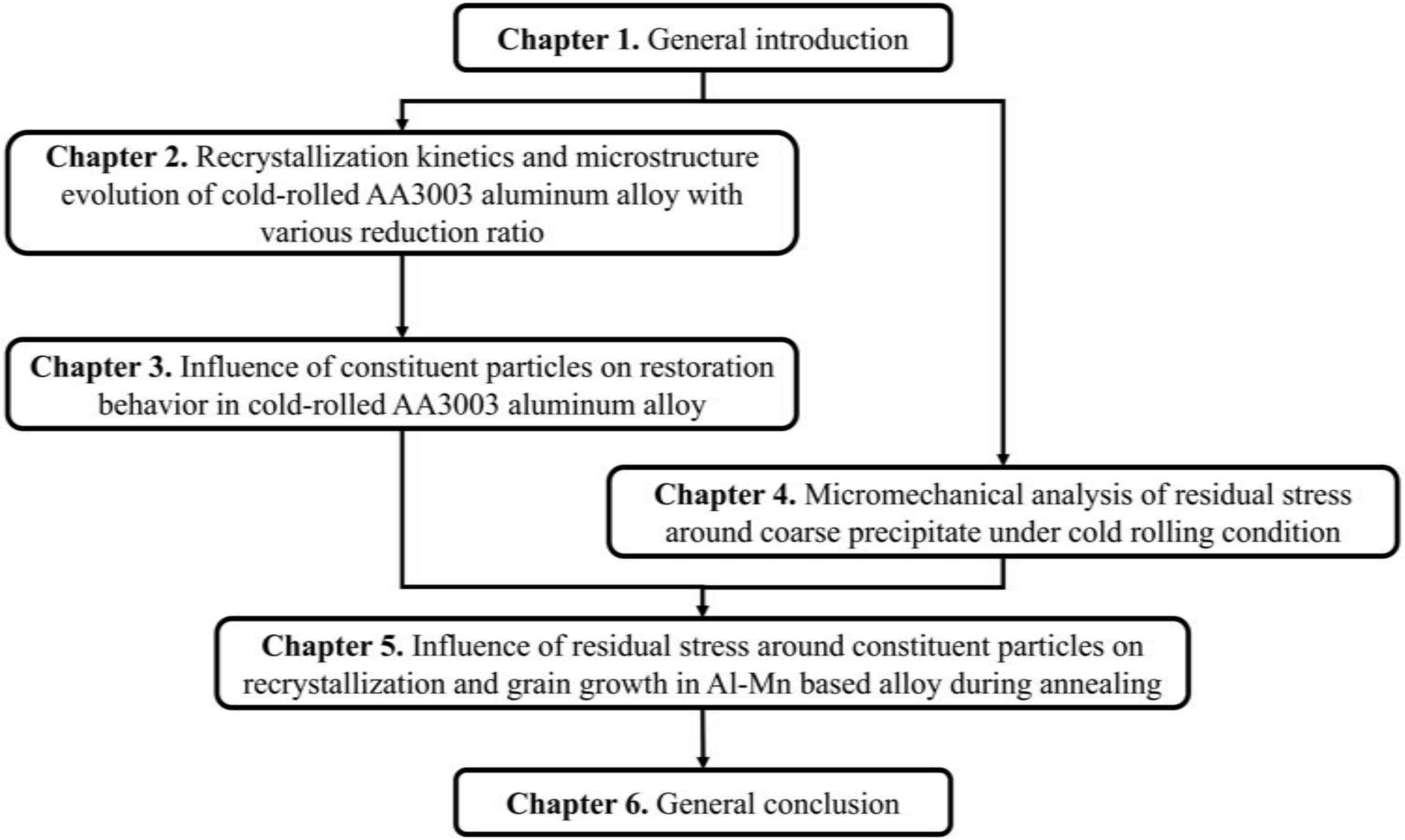

Figure 1.18: Outline of the present thesis

Chapter 2

Recrystallization kinetics and microstructure evolution of cold-rolled AA3003 aluminum alloy with various reduction ratio

2.1 Introduction

The Al-Mn based alloys with moderate strength, excellent formability and corrosion resistance, etc are widely used in heat exchangers, beverage cans and other industries (Poole et al., 2012). The production process to commercialize this alloy is usually produced by direct-chill (DC) casting of large products, and followed by scalping, homogenization, hot rolling and cold rolling to manufacture the products.

The cold-rolled sheets produced through this process become thermally unstable as free energy associated with dislocations and boundaries increases proportionally to the reduction rate (Humphreys et al., 2004). Since the cold-rolled sheets with thermodynamically unstable structures lack the energy to remove the defects on their own at room temperature, the cold-rolled sheet necessarily requires an additional process to remove the unstable structure such as annealing (Humphreys, 1977).

Generally, the annealing procedure is involved in the fabrication process of Al-Mn alloy, where the sequential processing of heating and cold rolling to control the microstructure greatly influences the evolution of microstructure and mechanical properties of the material. The thermal activation processes, such as the diffusion of the solid-state caused by annealing at a specific temperature, provide enough energy to remove the defects, thus providing an effective mechanism to lead to lower energy structures. Alteration in the sequence or employed procedure in the processing is used to control the microstructure which in turn affects the properties of the material.

The change of microstructure that occurs during annealing depends on the degree of the restoration mechanism such as recovery, recrystallization and grain growth. The second-phase particle of Al-Mn based alloy is an important factor affecting recovery and recrystallization behavior. The deformation zones formed around coarse primary particles ($> 1 \mu m$) during plastic deformation may accelerate the recrystallization behavior by particle-stimulated nucleation (PSN) (Humphreys, 1977, 1997). Whereas, both the low-angle grain boundary (LABG) and high-angle grain boundary (HABG) migration is delayed by fine secondary particles (Zener pinning) (Nes et al., 1985; Smith, 1945). In addition, the recovery and recrystallization behavior in deformed and supersaturated AA3003 alloy during annealing can be affected by a phenomenon commonly referred to as concurrent precipitation (Jr et al., 1986; Nagahama and Miki, 1974). In order to improve the characteristics of these microstructures in the homogenization step, studies have been conducted to suppress the concurrent precipitation or increase the distribution of coarse particles and dispersoids to increase the PSN site and suppress the growth of recrystallized grains (Sun et al., 2006, 2008). Since the driving force generated by correlation between the constituent particles and the amount of plastic deformation significantly affects the restoration behavior during subsequent annealing, it is important to study the residual stress generated by the constituent particles. However, the critical strain associated with the residual stress introduced by plastic deformation to promote PSN around coarse particles is not yet clearly known.

The fundamental process of recovery and recrystallization behavior is the migration of grain boundaries associated with the dislocation migration. Recrystallization nucleation occurs due to sub-grain coarsening and grain boundary migration (H, 1978). The coarsening of sub-grain occurs in the process of primary recrystallization nucleation and continuous recrystallization during recovery behavior (Rios et al., 2005). The migration of the HAGBs occurs in the primary recrystallization and recrystallized grain growth due to the strain-induced grain boundary migration (Paggi et al., 2015). The motion of these grain boundaries is interrupted by the already existing particles, particles generated by concurrent precipitation, Mn segregating to a stationary boundary, and Mn segregating to a moving grain boundary (Chen et al., 2003; Du and Jacot, 2005; Tangen et al., 2010). However, the details of the constituent particle interaction with the change in LAGBs and HAGBs during annealing are still unclear.

In this study, the cold-rolled Al-Mn based alloy was fabricated with a different reduction rate and investigated the effect of reduction rate on the recovery and recrystallization behavior under the certain volume fraction of constituent particle in AA3003 alloy. In addition, the evolution of the microstructure in the cold-rolled specimen is analyzed based on the change in the number fraction of the LAGBs and HAGBs, and electric conductivity associated with the concurrent precipitation as well as the apparent activation energy for recrystallization.

2.2 Experimental Procedure

A commercial AA3003 (Al-1.15Mn-0.52Fe-0.28Si-0.16Cu in wt.%) alloy was used in this study. The initial as-cast alloy (200 mm in length, 80 mm in width, 155 mm in thick) was fabricated by DC cast. The homogenization treatment (as-homo) was conducted at 580 °C for 8h with a heating rate of 50 °C/h, and then immediately quenched into the water at room temperature. Then the as-homo specimens were processed by cold-rolling with the reduction rate of 20% (AM2), 50% (AM5), and 90% (AM9). The cold-rolled sheets were isothermally annealed in a salt bath at 300 °C, 350 °C, 375 °C and 400 °C for times ranging from 2s to 24h, and then immediately quenched into the water at room temperature.

The microstructure at the thickness center of the deformed and annealed specimens were characterized in the longitudinal section, containing the rolling direction (RD) and the normal direction (ND) by optical microscope (OM) and field-emission scanning electron microscopy (FE-SEM). The measurement of crystalline orientation and grain boundary misorientation was conducted by FE-SEM equipped with EBSD, in which the data was treated by TSL OIM analysis software and MTEX toolbox for MATLAB (Hielscher et al., 2019). The misorientation of grain boundaries of less than 2 degrees were neglected due to significant orientation noise in the deformed and annealed specimens. Generally, a low angle grain boundary is defined as boundaries with misorientation between 2 and 15 degrees, and boundaries exceeding 15 degrees are defined as high-angle grain boundaries

(Jazaeri and Humphreys, 2009). All specimens were examined in the TD (ND-RD) plane, and ND is vertical in all figures.

The microhardness was measured by the Vickers hardness test under a load of 100 gf for 15 seconds. The apparent activation energy for recrystallization of cold-rolled specimens was estimated by using the modified JMAK-microhardness model. The electric conductivity was measured by eddy current inspection at room temperature using 500kHz dedicated inspection probe.

2.3 Results

2.3.1 Effect of homogenization treatment

The typical solidification microstructure of the DC-cast (as-cast) and the homogenized (as-homo) commercial AA3003 aluminum alloy are shown in Fig. 2.1. The microstructure of as-cast specimen was equiaxed in shape, and the grain size and the area fraction of primary particle were amounted to be 88 μm and about 9.2%, respectively (Fig. 2.1a and b). Whereas, the grain size in the as-homo specimen was increased to about 160 μm and the area fraction of primary particle decreased to 4.2% with spheroidization by homogenization (Fig. 2.1c and d). The electrical conductivity of the as-homo specimen is increased from 30 to 43.5 %IACS, which reflects the differences in solute level on Mn. A large number of fine secondary particles in the as-homo specimen was formed in the aluminum matrix by homogenization treatment (Fig. 2.1d). The change in electrical conductivity is due to the secondary particles occurred by homogenization, which means that the solubility of Mn in the aluminum matrix decreases. Thus, the potential ability of concurrent precipitation in the recovery and recrystallization process during annealing will be significantly reduced.

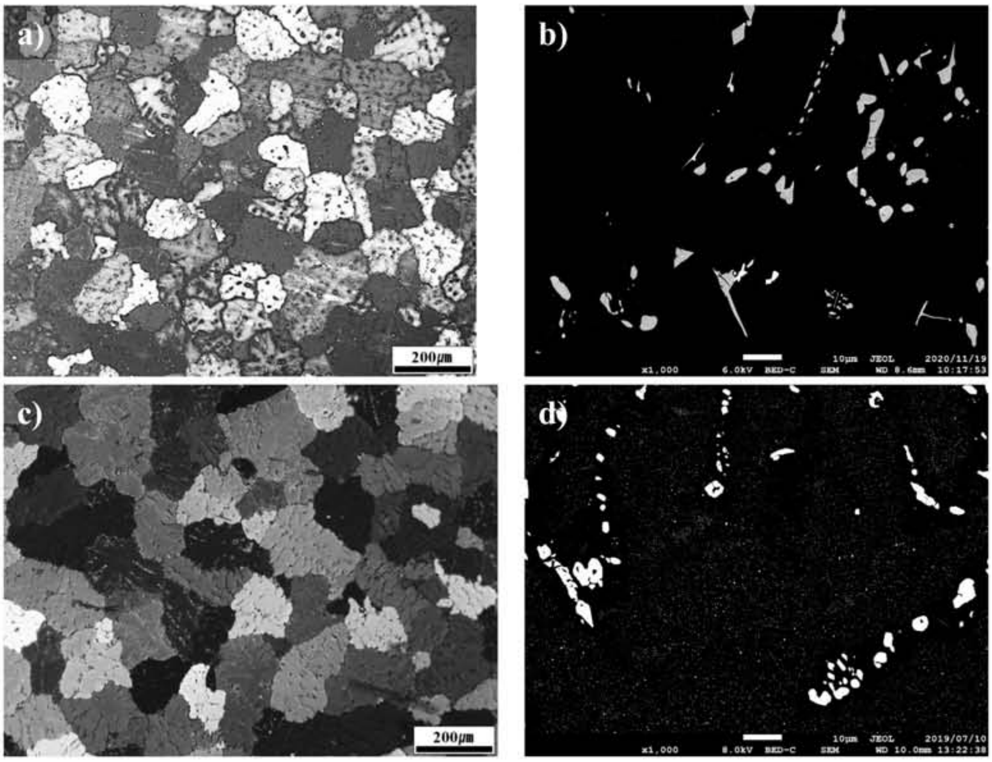

Figure 2.1: The typical microstructure of (a and b) as-cast and (c and d) as-homo AA3003 aluminum alloy

2.3.2 Effect of reduction rate on microstructure and orientation

The microstructure and inverse pole figure (IPF) map measured by EBSD in the cross-section of a cold-rolled specimen are represented in Fig. 2.2, where the white regions are constituent particles. Since the AM9 is severely deformed, the Kikuchi pattern and confidence index (CI) obtained at large step size (1 μm) was unclear. Therefore, these analyzes were measured in the size of 100 μm × 200 μm with a step size of 1 μm for (a) AM2 and (b) AM5, and 50 μm × 100 μm size with a step size of 0.1 μm for (c) AM9. The respective IPF maps for AM2, AM5 and AM9 show the evolution of the deformed microstructure with an increase of the plastic strain. It can be seen that as the strain increases, the thickness of grains decreases, and the shape of grains is elongated along the parallel to the RD. In addition, the microstructure of the cold-rolled specimen significantly changes its crystallographic texture due to the rotation of grain and the formation of sub-grain within the deformed grains during plastic deformation (Harris et al., 1998). A relatively coarse sub-grain is observed in AM2, while fine sub-grain is formed in AM9 with an increase in reduction rate.

The triangular IPF plot in Fig. 2.2 represents the color codes that can be used to qualitatively interpret the distribution of crystal orientations in the IPF map. Considering these IPF plots, AM2 indicates that the pink color corresponding to $< 112 > \parallel$ ND crystal direction occupies the majority, and AM9 occupies a large part of the orange color, which is close to $< 013 > \parallel$ ND crystal direction. Although the crystal direction of AM9 is distributed randomly, it is relatively largely distributed in $< 111 > \parallel$ ND crystal direction indicated in blue color. This means that AM2 with low strain has a lower volume fraction of the brass and goss components, and as the reduction ratio increases, a well-developed the copper rolling texture components increases. These textures are commonly formed from aluminum with high stacking fault energy (Donadille et al., 1989).

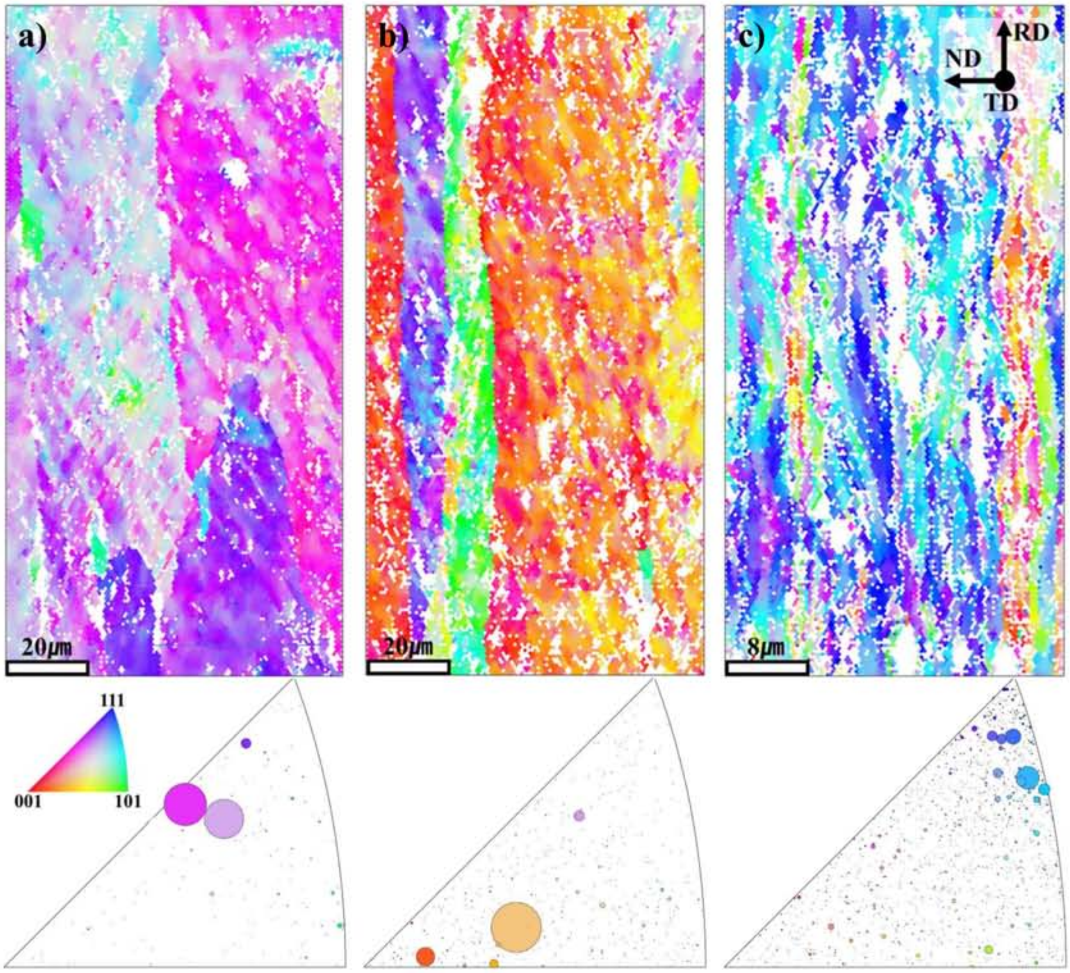

Figure 2.2: EBSD map in the longitudinal section of (a) AM2, (b) AM5 and (c) AM9. The inverse pole figures (IPF) indicate the color key of the crystal direction parallel to the normal direction (ND)

The kernel average misorientation (KAM) approach simply represents the quantified local misorientation. This map can qualitatively evaluate the dislocation density introduced by plastic deformation, taking into account the relationship between the dislocation and the local crystal misorientation calculated using the MTEX toolbox for Matlab (Hielscher et al., 2019). Fig. 2.3 shows the KAM map in the same area as the IPF map measured in Fig. 2.2, where the black region represented the constituent particles.

AM2 with a low strain rate shows a similar local misorientation distribution in region of both coarse particles and dispersoids, and the shear band inclined about 63 degrees perpendicular to the ND in the dispersoids region is clearly identified. As the strain increases, local high misorientation associated with dislocation density is generated around the coarse particles (Fig. 2.3b), where may lead to preferential recrystallization around the coarse particle due to the locally high dislocation density during subsequent annealing. When the strain is increased to 0.9, the high misorientation is formed around the coarse constituent particle as well as in the dispersoids region, where the misorientation is quite homogeneously distributed, as shown in Fig. 2.3c. Considering the correlation between this local misorientation associated with dislocations, the high dislocation density is homogeneously formed by increasing the strain, which will provide a high driving force for recrystallization in subsequent annealing. In addition, in this study, note that the critical strain for the initiation of recrystallization due to the PSN effect around the coarse particles during annealing can be estimated as 0.5 as will be discussed in Section 2.3.3.4.

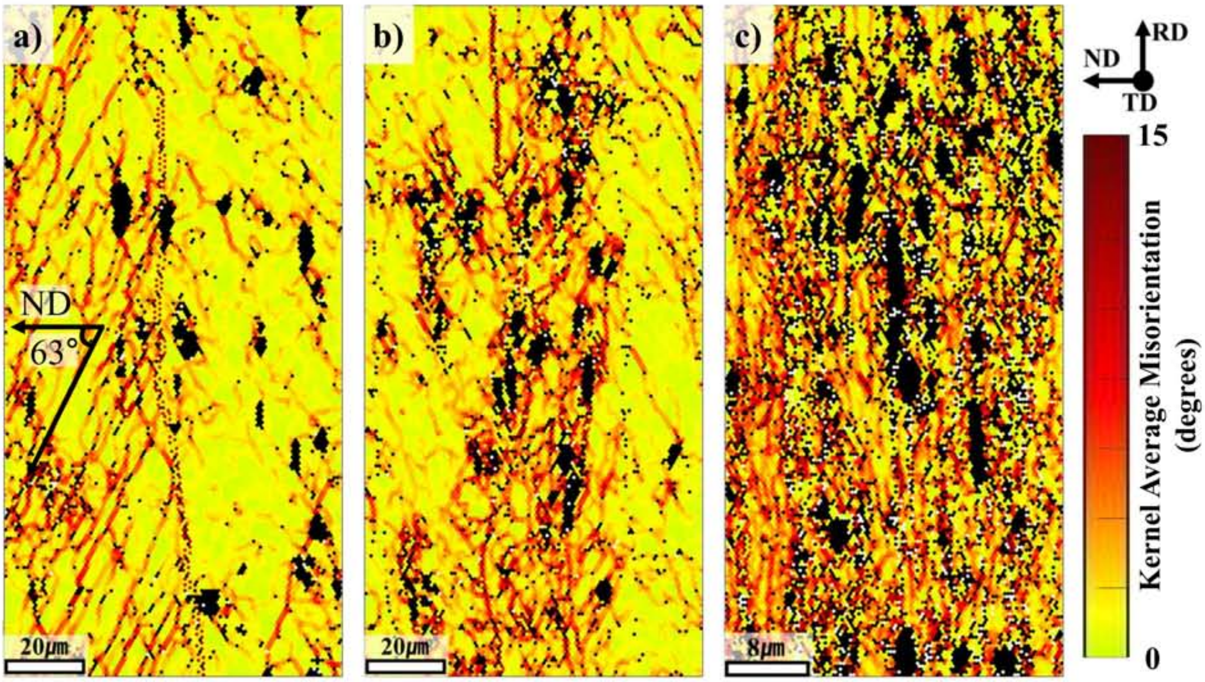

Figure 2.3: Kernel average misorientation map in longitudinal section of (a) AM2, (b) AM5 and (c) AM9

The effect of magnitude of plastic strain on the number fraction of the LAGBs and HAGBs are shown in Fig. 2.4. The number fraction of LAGBs and HAGBs are indicated by the red and black lines, respectively. Note that the number fraction of LAGBs and HAGBs were evaluated by TSL OIM analysis software from the EBSD maps in the longitudinal section of the cold-rolled AA3003 aluminum alloy.

The number fraction of LAGBs is dropped with increasing the plastic strain, while the fraction of HAGBs increases in inverse proportion to the number fraction of LAGBs. Accounting that the profile of Vickers hardness as indicated by the blue line shows similar increasing profile as compared with the number fraction of HAGB, the fraction of HAGBs becomes sufficient to proceed the recrystallization when the fraction of HAGBs is reached to 60∼70%, which is a well-known fact pointed out by Humphreys (1999). The number fraction of HAGBs in the cold-rolled specimens show a parabolic increase with plastic strain, which is measured to be 7% for AM2, 57% for AM5 and 81% for AM9. The number fraction of HAGBs in the as-homo is measured to be 2.4%. Therefore, the recrystallization in the AM9 during annealing is easily occurred with the large number fraction of HAGBs as compare with the AM2 and AM5 when the same annealing temperature is assumed.

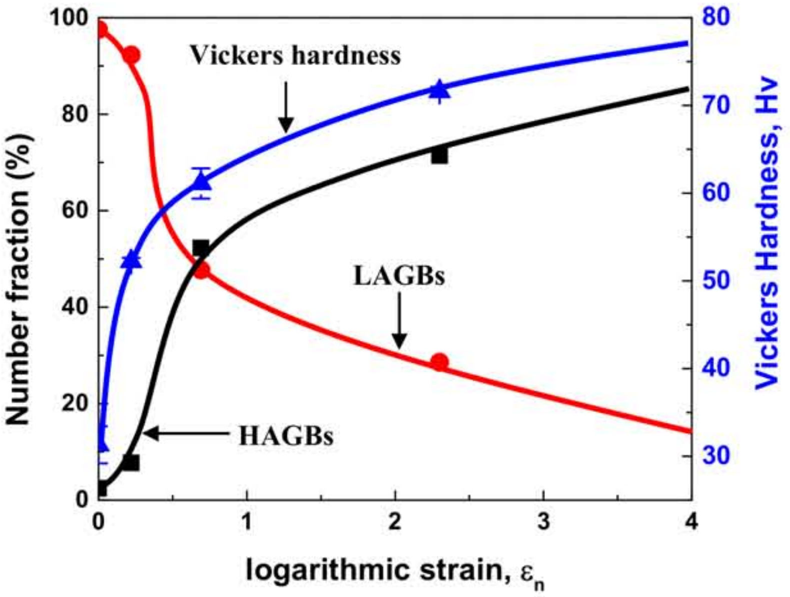

Figure 2.4: Changes in the number fraction of the LAGBs and HAGBs, and Vickers hardness with reduction rate in the AA3003 aluminum

The nucleation sites for recrystallization of cold-rolled specimens during annealing are generally controlled by particle-stimulated nucleation (PSN) and grain boundary nucleation. Therefore, in order to study the nucleation effects of PSN, the deformed structure surrounding the coarse primary particles can be considered as the nucleation site (Humphreys, 1977; Tangen et al., 2010). Fig. 2.5 shows the deformed structure around the primary constituent particles after cold rolling for (a) AM2, (b) AM5 and (c) AM9. The white dotted lines in the figure demonstrate the extension of the deformation zone, which surrounds the particle after plastic deformation by cold rolling. In particular the flow pattern was clearly distinguished to form at larger reduction rate and around the undeformed primary particle (Fig. 2.5c). According to Humphreys (1977), the deformed microstructure is characterized by the distorted zones parallel to ND, and the rotated zone parallel to TD around the coarse particle. These rotated regions with refined sub-grain structure and high lattice rotation provide a high local stored energy, which is important for nucleation of recrystallization.

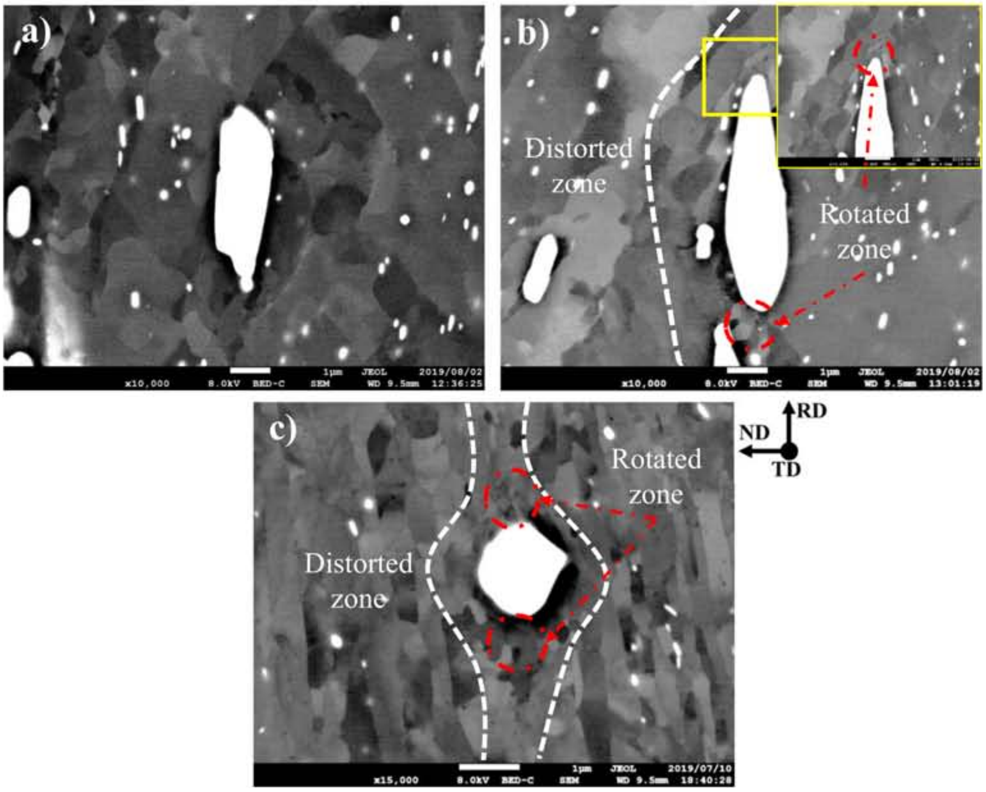

Figure 2.5: Deformation zone around a large primary particle of (a) AM2, (b) AM5 and (c) AM9

2.3.3 Recovery and recrystallization behavior during annealing

2.3.3.1 Evolution of microstructure

Fig. 2.6 shows the evolution of microstructure in (a) AM2, (b) AM5 and (c) AM9 after annealing at 400 °C for each time. The microstructures of cold-rolled specimens were elongated in the rolling direction, and the thickness of grains in the TD plane decreased in proportion to the reduction rate. The recrystallized grains start to be generated with increasing annealing time, where the recrystallization can be identified via the evolution of microstructure. The AM2 specimen clearly shows primary recrystallization after 10 seconds (Fig. 2.6a), where partially equiaxed grains occurring near the grain boundary. Although equiaxed shape grains with a size of about 73 μm recrystallized by subsequent annealing are produced and grown, some of the grain grows in a direction parallel to RD. This means that specimens with low strain were partially recrystallized and relaxation occurred.

On the other hand, the AM9 with large strain was recrystallized under annealing at 400 °C within 2 seconds, and the size of the recrystallized grains was about 6.7 μm (Fig. 2.6c), which was very small compared to AM2 and AM5 specimens. It can be seen that large deformed specimen with fine recrystallized grain are recrystallized faster than low deformed specimen with coarse grains. In general, the metal materials cause an increase in dislocation density and a decrease in crystallite (cell and sub-grain) size during plastic deformation (Humphreys et al., 2004; Ungár et al., 1998), and a large number of HAGBs are generated as the reduction rate increases (Fig.2.4).

As the recrystallization is complete, collisions between these new particles occur with increasing frequency, and the specimen is entirely replaced by new recrystallized grains. After primary recrystallization is completed, the structure is still unstable, and the recrystallized grains can grow further by grain boundaries migration using the grain boundary free energy as the driving force. Since the grain boundary interfacial free energy is much lower than the stored strain energy (Kalu and Waryoba, 2007), the migration of the grain boundaries due to the grain boundary interfacial free energy has a lower reaction order than that of the first recrystallization, which contributes to the abnormal grain growth and secondary recrystallization after the completion of the primary recrystallization.

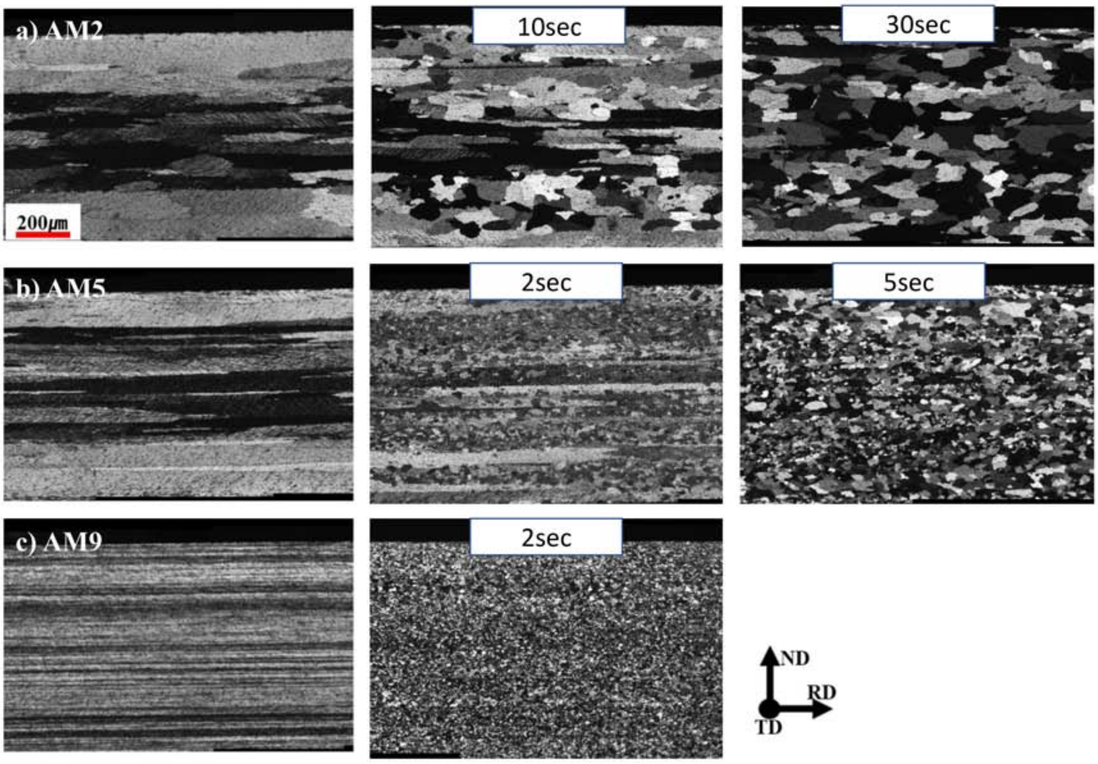

Figure 2.6: Evolution of the recrystallization microstructure for the (a) AM2, (b) AM5 and (c) AM9 at 400 °C for different holding time

2.3.3.2 Change in microhardness during annealing

Fig. 2.7 shows the results of the Vickers hardness test of (a) AM2, (b) AM5 and (c) AM9, where three distinct regions were identified clearly on the microhardness graph. In the early stage of annealing, the microhardness of cold-rolled specimens was relatively insensitive to annealing temperature, which corresponds to the recovery stage. In the second stage, the hardness decreased rapidly in a very short time, and it was attributed to recrystallization, which resulted in drastic softening of the cold-rolled specimens. For the final stage, the hardness decreased slightly with annealing, and its mechanism was considered to be grain growth. The annealing time required for the restoration process strongly depends on the reduction rate and the annealing temperature. The critical transition time from recovery to recrystallization was 1800s, 30s, and 10s for AM2, AM5, and AM9 at 350 °C, respectively. On the other hand, when annealed at 400 °C, recrystallization was completed in a very short time of 30s, 10s, 2s, respectively. Obviously, the transition time decreases as the reduction rate and the annealing temperature increases, which is closely related to the size of the recrystallized grain.

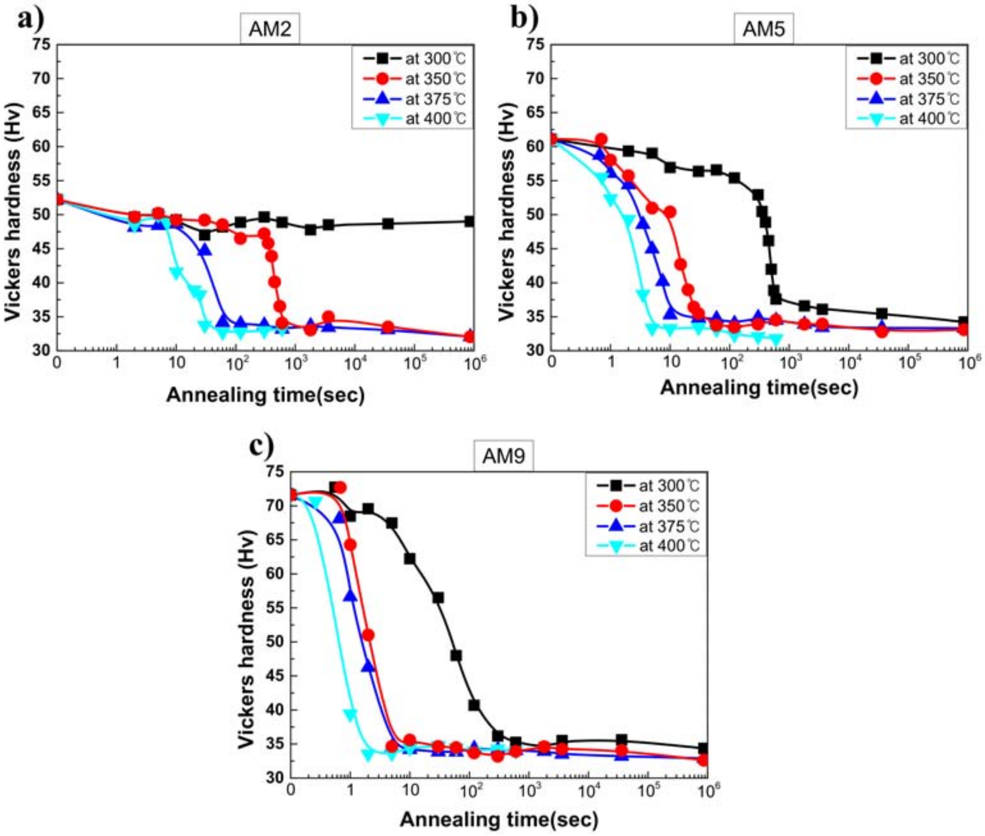

Figure 2.7: Relationship between Vickers hardness and the annealing time at each temperature of AM2, AM5 and AM9

2.3.3.3 JMAK-microhardness model

The microstructural change associated with restoration process during annealing is classified into 3 stages, recovery, recrystallization and grain growth. Among them, recrystallization mechanism can be treated and analyzed by Johnson-Mehl-Avrami-Kolmogorov (JMAK) model as

$$X_v = 1 - exp[-kt^n] \tag{2.1}$$

Where X_v is volume fraction of recrystallized grains, n is the order of the reaction, k is the reaction rate constant, and t is the annealing time. The modified JMAK model was proposed by Kalu and Waryoba

(2007), where the fractional change of recrystallized grains is substituted by softening behavior associated with recovery, recrystallization and grain growth. This can be expressed in terms of microhardness as:

$$X_v = \frac{HV_{RV} - HV_t}{HV_{RV} - HV_{RX}} \tag{2.2}$$

where HV_{RV} is the microhardness for cold-rolled specimen, HV_t the microhardness for annealed specimen at time t and HV_{RX} is the microhardness for a fully recrystallized specimen.

Fig. 2.8 shows the change in the volume fraction of recrystallized grain which is translated from Vickers hardness for AM2, AM5 and AM9 with annealed at different temperatures. It can be seen that the fraction transformed X_v from the onset of annealing to the 0.2 point is the recovery stage, and the curve increases gradually as the annealing time increases. At the onset of recrystallization, the slope of the curve increases sharply, indicating an increase in the proportion of recrystallized grains with dislocation free. The grain growth begins after the transformed fraction is 1.0, and the slope of the curve gradually increases. The completion time for recrystallization of AM2 annealed at 350 °C, 375 °C and 400 °C is attained at 600s, 120s and 60s, respectively. The transformed fraction curve for AM9 indicates that recrystallization behavior was completed immediately at all temperature. It can be seen that the restoration behavior during annealing of plastically deformed specimens strongly depends on the reduction rate and the annealing temperature.

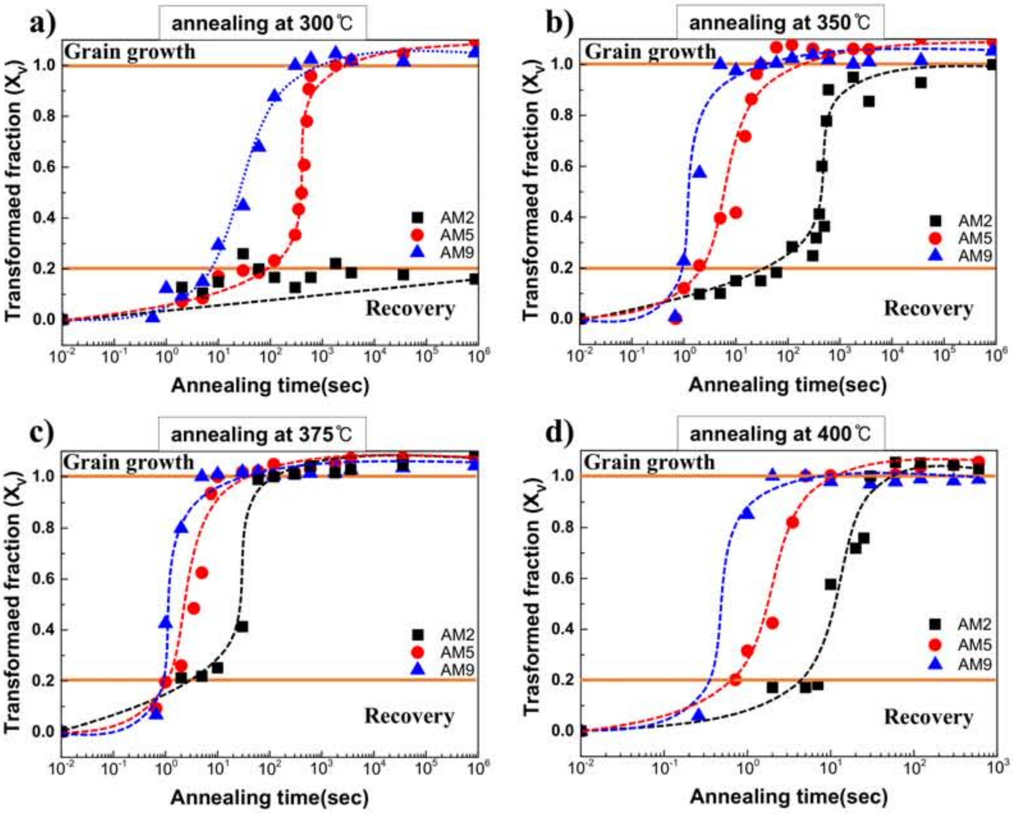

Figure 2.8: The transformed volume fraction vs annealing time for the specimens AM2, AM5 and AM9; at (a) 300 °C, (b) 350 °C, (c) 375 °C and (d) 400 °C

Taking logarithm twice in Eq. (2.1), the JMAK exponent, n, and the temperature-independent constant, k, can be analyzed from JMAK plots as shown in Fig. 2.9. The JMAK exponent, n, reflects the nucleation rate and growth morphology, which is a kinetic parameter depending on the annealing temperature, nucleation rate and growth rate. The JMAK exponent is typically $1 \leq n \leq 2$ for 1-D growth, $2 \leq n \leq 3$ for 2-D growth, and $3 \leq n \leq 4$ for 3-D growth (Christian, 1975). The JMAK exponent is amounted to be about 1.3 at 350 °C and 375 °C and 1.9 at 400 °C for the recrystallization of AM2, and about 1.5 at 300 °C and 350 °C and 2.1 at 375 °C and 400 °C for the recrystallization of AM5, respectively. In the case of AM9, the JMAK exponent is changed from 1.0 to 2.9 with increase of annealing temperature.

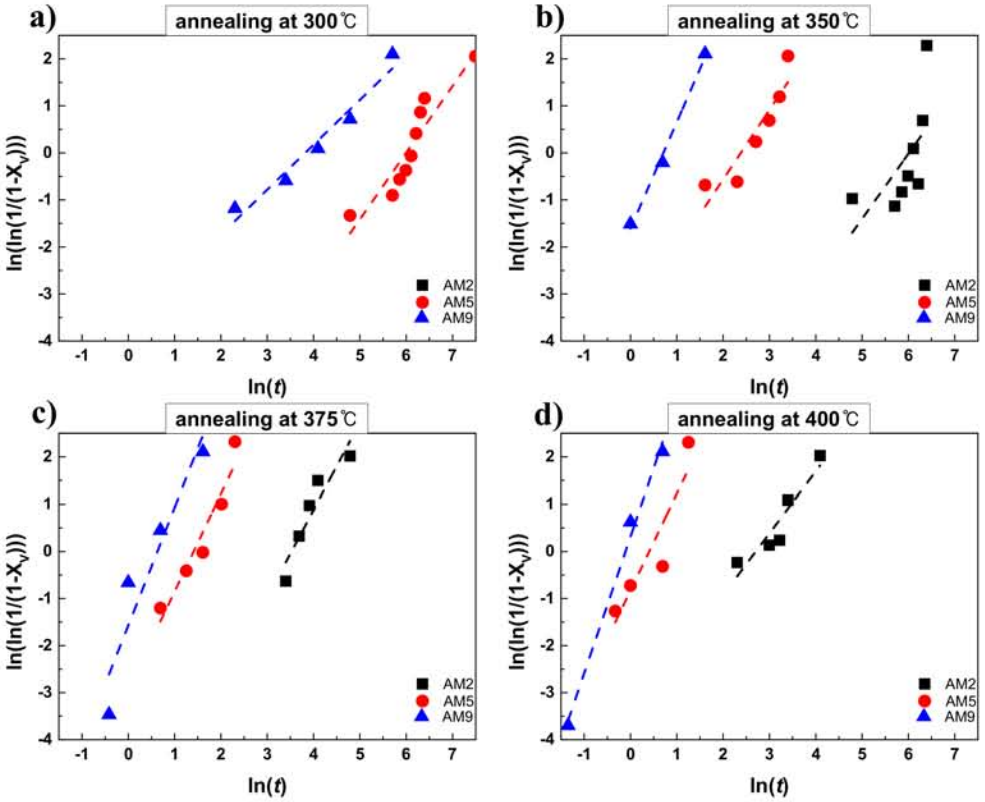

Figure 2.9: JMAK plots for recrystallization kinetics for the AM2, AM5 and AM9 annealed at (a) 300 °C, (b) 350 °C, (c) 375 °C and (d) 400 °C

The apparent activation energy, Q, for the recrystallization can be determined by an Arrhenius equation. The temperature dependence, k, of the recrystallization is described in the form of Eq. (2.1), which can also be expressed as:

$$\ln k = \ln k_0 - \frac{Q}{RT} \tag{2.3}$$

Temperature dependence of rate constant is plotted in Fig. 2.10 and activation energy for recrystallization is evaluated. The apparent activation energies for recrystallization of AM2, AM5 and AM9 is amounted to be 332KJ/mol, 239KJ/mol and 115KJ/mol, respectively.

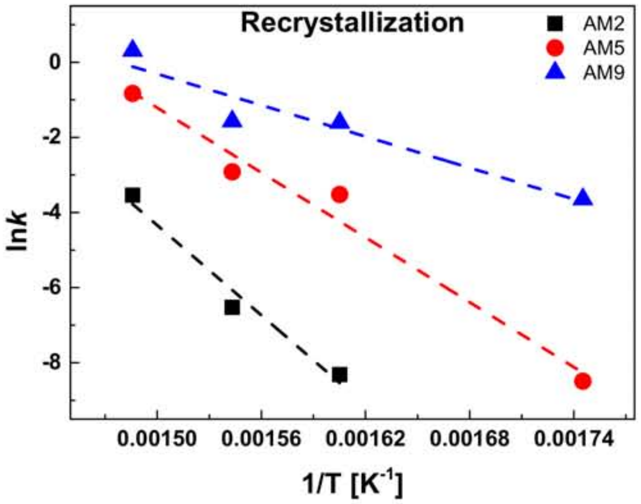

Figure 2.10: A plot of ln(k) vs 1/T for (a) recovery and (b) recrystallization

2.3.3.4 Sub-grain growth and recrystallization

Fig. 2.11 shows the IPF and KAM maps of (a and b) AM2 and (c and d) AM5 measured at the point of transition from recovery to recrystallization during annealing at 350 ℃. These analyzes were measured in the size of 20 μm × 20 μm with a step size of 0.1 μm for (a) AM2 and (b) AM5. The AM2 partially formed an equiaxed sub-grain, but a deformed grain elongated in the RD was still observed (Fig. 2.11a), which means that partial recovery and relaxation are in progress due to low plastic deformation. Considering the microstructure deformed by cold rolling, a clearly distinguished shear band in AM2 deformed with low plastic strain formed fine sub-grains with low misorientation boundary throughout the specimen due to rearrangement of dislocations during annealing (Fig. 2.11b). It should be taken into account that the fine secondary particles strongly inhibit the migration of dislocation and boundary by pinning effect during recovery

(Humphreys and Martin, 1968; Jones et al., 1979). This phenomenon is more pronounced due to the low driving force for recovery in the specimens with low strain. The dispersion of fine particles exerts a stronger pinning effect on the sub-grain of AM2 in the dispersoids region. The fine secondary particles prevent the sub-grain growth from reaching the critical size for recrystallization nucleation, which eventually leads to preventing the recrystallization. On the other hand, AM5 shows that the equiaxed sub-grain microstructure is well-developed among the elongated grains along rolling direction, which is formed by dislocation rearrangement and annihilation during the recovery stage (Fig. 2.11c). The size of sub-grain surrounded by the local misorientation is found to be significantly smaller in the dispersion region than around the coarse particles (Fig. 2.11d).

AM2 shows an overall lower KAM angle than AM5, which can be considered in terms of the development of cell wall (or dislocation wall) associated with the dislocation density of the initial cold-rolled specimen. In addition, the concentration of misorientation due to localized increase in dislocation density and fine secondary particle can lead to an increase of the non-indexed region around the equiaxed grain. The increase in this area during annealing may be a hint as to the onset of recrystallization of the annealed specimen (De Vincentis et al., 2017). Since the growth of sub-grain associated with the rearrangement of dislocations during the recovery depends on the dislocation density in the initial specimen before annealing, the dislocation structure is formed more densely at large strain, as shown in Fig. 2.3c. Although the size of the sub-grain cannot be determined with certainty on this KAM map, the approximate size of the sub-grain can be deduced from the distribution and magnitude of the KAM angle. At the point of transition from recovery to recrystallization, the sub-grain size is amounted to be about 0.6 μm for AM2 and about 0.4 μm for AM5, where the sub-grain size considered only the dispersoids regions. In addition, the distribution of local misorientation in the AM2 shows similar trends for the value of KAM angle around the precipitate and in the dispersoids region.

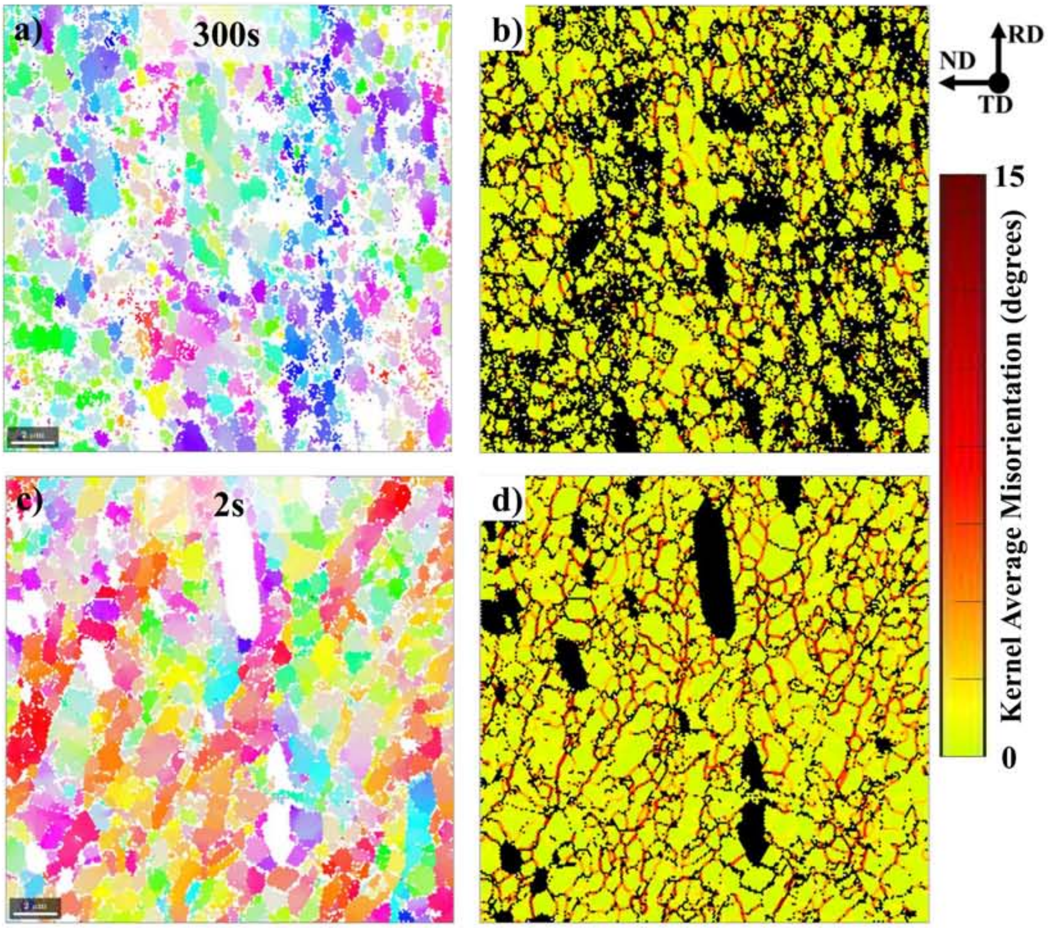

Figure 2.11: (a and c) EBSD map and (b and d) KAM maps in longitudinal section of (a and b) AM2 and (c and d) AM5 at the point of proximity transition from recovery to recrystallization during annealing at 350 °C. The inverse pole figures (IPF) indicate the color key of the crystal direction parallel to the normal direction (ND).

Recalling the change in the volume fraction of recrystallized from Fig. 2.8, it can be seen that the recrystallization behavior is strongly dependent on the annealing temperature and the reduction rate, indicating that the low strain and annealing temperature are not sufficient to complete the recrystallization quickly. This can be considered in terms of the sub-grain growth associated with the dislocation migration and the boundaries migration within the locally plastically deformed grains, and these recrystallization behaviors can be analyzed simply through the KAM map. The change in the KAM angle of (a and b) AM2, (c and d) AM5 and (e and f) AM9 during recrystallization at 350 °C for each time is presented in Fig. 2.12, where (a), (c), and (e) are about 50% recrystallization progressed, and (b), (d), and (f) are completely recrystallized.

For the AM2 with low plastic strain, the local plastic strain in the grains shows to decrease during the partial recrystallization process, but there exists localized misorientation throughout the specimens even after the prolonged annealing (Fig. 2.12a and b). On the other hand, in case of the AM5 and AM9, the local misorientation was preferentially eliminated around coarse particles, and misorientation also decreased in the dispersoids region, as shown in Fig. 2.12c and e. After recrystallization is completed, the local misorientation is hardly observed in the dispersoids region as well as around the coarse particles (Fig. 2.12d and f). This clearly emphasizes that the recrystallization kinetics increases in proportion to the reduction rate. In addition, it is evident that recrystallization of cold-rolled specimens with strains greater than 0.5 occurs preferentially near coarse particles.

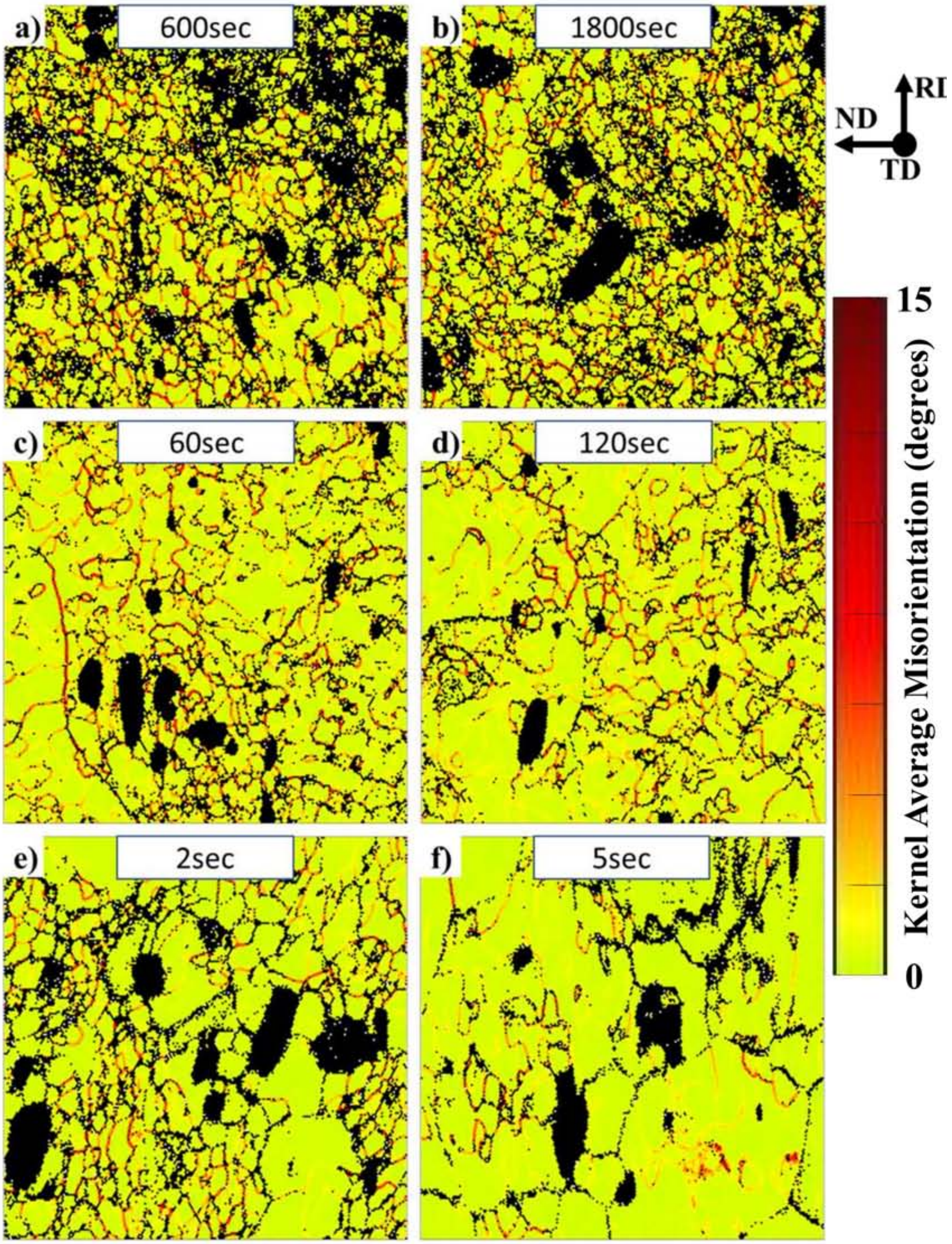

Figure 2.12: Kernel average misorientation map of (a and b) AM2, (c and d) AM5 and (e and f) AM9 at the point of (a, c and e) 50% recrystallization and (b, d and f) completed recrystallization during annealing at 350 °C for each time

2.4 Discussions

2.4.1 Mn micro-segregation

The difference in amount of reduction does not have a significant effect on the volume fraction of the constituent particles in the equilibrium state, but annealing after the cold rolling may affect the nucleation of the precipitate and the diffusion rate of the solute.

Generally, when the casting material is plastically deformed, the electrical conductivity will be inversely proportional to the rolling reduction rate, ie., the increase in the internal defect density by cold rolling may be attributed to the amount of strain. The conductivity of the 20% cold-rolled specimens increased from 43.4 to 48.6 %IACS in the present experiment (see Section 3.3.1 and Fig. 2.13), which corresponds to a decrease of 0.13 wt.% Mn concentration in solid solution. Recalling the fact that electrical conductivity is greatly influenced by solid solution of Mn element (JohnE.Hatch, 1984), the micro-segregation of Mn solute between the dislocation wall and cell interior formed during deformation can be increased local supersaturation (Chen et al., 2003), which leads to a decrease of Mn concentration in Al matrix, thereby an increase of conductivity. As the amount of reduction increases, the electrical conductivity gradually decreased and was found to be 46.7 %IACS in 90% cold-rolled specimens. This means that the electrical conductivity is no longer dependent on the segregation of manganese and is dominated by defects introduced by cold rolling.

Fig. 2.13 shows the variation of electrical conductivity and Mn concentration for AM2 AM5 and AM9 under different annealing temp. Since electrical conductivity is sensitive to the degree of Mn solid solution and the dislocation density, the former and latter part of conductivity increase indicates the annihilation of dislocations and the precipitation starts, respectively.

For the annealing at 350 °C, the conductivity of AM5 and AM9 specimens increases with increasing the annealing time. Such increase can be corresponded to the annihilation of dislocation density in the Al matrix and boundary owing to the nucleation and growth of new recrystallized grains (Fig. 2.7). Whereas the conductivity in the AM2 specimen was increased after 400s, it indicates that the precipitation is facilitated by dislocation networks at low-temperature annealing. This can be clearly identified with a profile of the Mn concentration annealed at 350 °C (Fig. 2.13c).

For the annealing temperature at 400 °C, all cold-rolled samples are completely recrystallized within 100s regardless of the strain, and the conductivity profiles indicating the precipitation start is clearly distinguished from recrystallization as compared with the case of 350 °C (Fig. 2.7). Therefore, the annihilation of dislocations microstructure and recrystallization at 400 °C is completed prior to the precipitation. Such results correspond to the evolution of microstructure and electrical conductivity results during annealing (Fig. 2.5 and 2.7).

Supposing that the solid solubility of Mn is enhanced at the moving boundary under cold rolling condition as comparison with that at the static boundary (Chen et al., 2003), since grain size and morphology of AM2 were hardly changed by annealing in present study, Mn segregation at grain boundaries and dislocation walls is responsible for the higher electrical conductivity of AM2. In the meanwhile, as the reduction rate is increased to AM9, the electrical conductivity tends to be lower level regardless of the annealing temperature, which is due to the microstructural change in terms of dislocation cells and sub-grains. Since the larger density of dislocations introduced by cold rolling leads to the formation of finer dislocation cells and sub-grains, the amount of Mn segregation would be reduced at the large numbers of dislocation cell boundaries, which leads to the lower conductivity of AM9 in average.

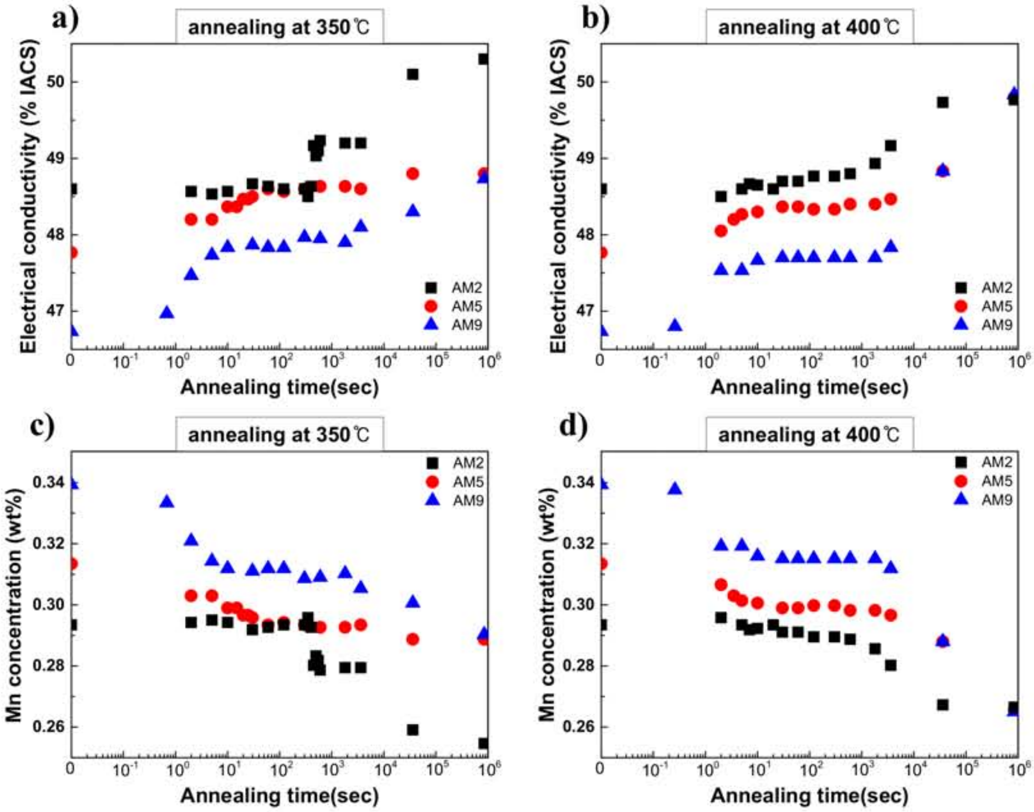

Figure 2.13: Change in the electrical conductivity as a function of annealing time for the cold-rolled AA3003 aluminum alloy; at (a, c) 350 °C and (b, d) 400 °C

2.4.2 Change in number fraction of the LAGBs and HAGBs

As it can be seen in Fig. 2.2, the deformed microstructure of cold-rolled specimens is consisted of the sub-grains and grain with a thin thickness along the rolling direction with an increase of reduction rate. Since the HAGBs tend to increase in proportion to the reduction rate, the restoration process is considered as the development of sub-grain microstructure, which is associated with the rearrangement of dislocations in regions with local orientation gradients (Doherty and Cahn, 1972). Deformed grains with lower strain produced relatively coarse sub-grain microstructures with lower local misorientation, whereas the specimens with a strain of 0.9 produced well-developed sub-grains with higher local misorientation to increase the number fraction of HAGBs significantly. In addition, the HAGBs increase intensively in the local deformation zone around the coarse constituent particles, which leads to an increase in dislocation density (Ashby, 1966; Humphreys et al., 2004). According to Jazaeri and Humphreys (2009), the transition between discontinuous and continuous recrystallization was discussed in terms of the change in number fraction of HAGB during annealing. Since the deformed sub-grain is consumed by the recrystallized grains, the discontinuous recrystallization changes the HAGBs relatively rapidly, whereas the continuous recrystallization results in little change in HAGB.

Fig. 2.14 shows the change in the number fraction of LAGBs and HAGBs of the (a) AM2, (b) AM5 and (c) AM9 during annealing at 350 °C. The AM2 with low strain increased the number fraction of HAGB significantly at the beginning of annealing, and then the HAGB remains at nearly 40% until recrystallization begins (Fig. 2.14a). The number fraction of HAGB in the AM5 increases gradually in the recovery stage and then increases to about 70% as recrystallization begins (Fig. 2.14b). In contrast, AM9 shows little change during recovery and recrystallization (Fig. 2.14c). After recrystallization is completed, all specimens show about 70% of the number fraction of HAGB. The decrease in LAGB at the beginning of annealing suggests the growth of more developed sub-grains due to dislocation rearrangement and absorption into the boundary or cell wall during recovery. The sub-grain boundary (or cell wall) composed of low-angle misorientation gradually develops due to the migraion of dislocation, which means that sub-grain with high misorientation are formed locally.

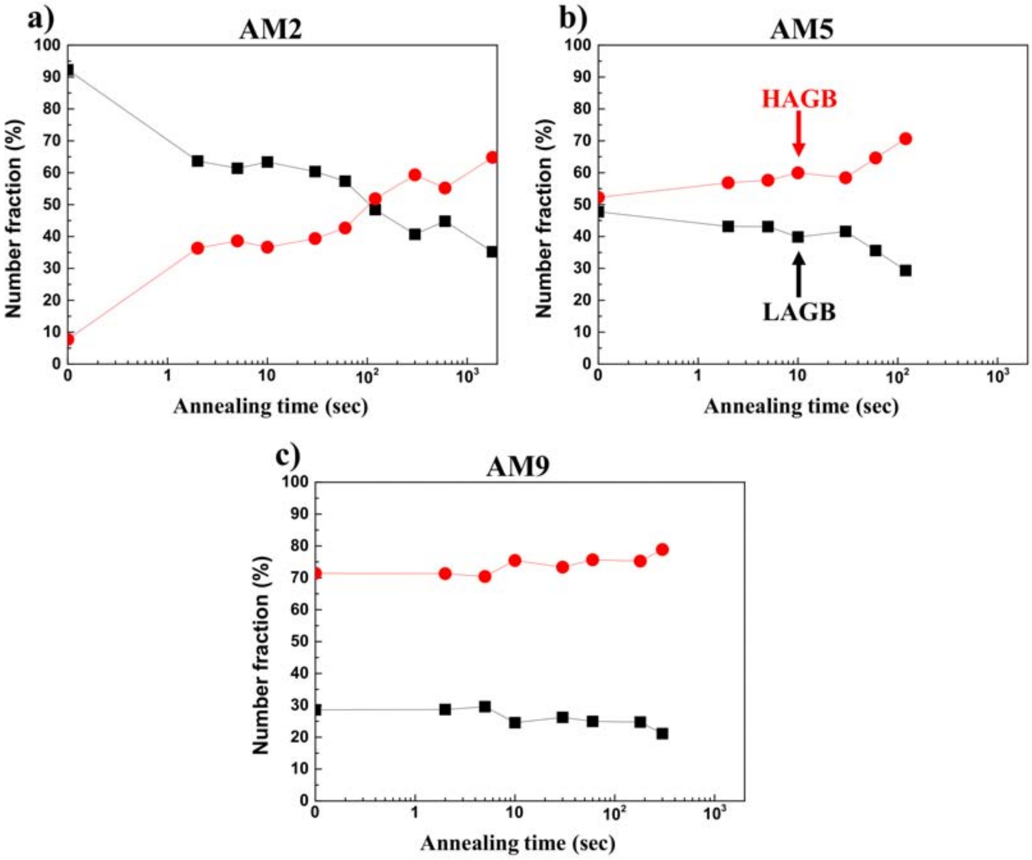

Figure 2.14: Changes in the number fraction of the LAGBs and HAGBs during annealing at 350 °C

Comparing the change in HAGBs and the transformed volume fraction during annealing (Fig. 2.8), AM2 containing a large amount of LAGB showed a large change from LAGB to HAGB at the beginning of annealing, but there is almost constant when the percentage of HAGB reaches 70-80% by subsequent annealing. This phenomenon can be considered a decrease in LAGBs in terms of sub-grains growth due to rearrangement of dislocations during recovery.

The changes in LAGBs and HAGBs during plastic deformation and annealing are schematically shown in Fig. 2.15. Specimens with low plastic deformation generate LAGBs within deformed grains with entangled dislocations in a large proportion. When the plastic strain increases to 0.5, HAGB is created inside the grains, but the grain shape still remains the initial lath shape. These low-deformed specimens increase HAGB and decrease the proportion of LAGB due to the migration and absorption of dislocations during annealing.

On the other hand, in severely deformed specimens, the lamellar boundary distortion occurs due to the influence of constituent particles during plastic deformation, and as the decrease of the gap between the boundary, the boundary of the dislocation interconnecting the lamellar boundary is gradually developed and the HAGB increases with the decrease of the gap between the boundary. The increased HAGBs produces equiaxed grains due to the movement of boundaries at the beginning of annealing, where the lamellar structure containing the LAGBs is retained in some regions. When recrystallization is completed, the fine recrystallized grains are formed, and some LAGB may exist near the boundary and constituent particles. This reflects that once HAGBs reaches a certain number fraction, the ratio of HAGBs and LAGBs can depend on the annihilation of LAGBs.

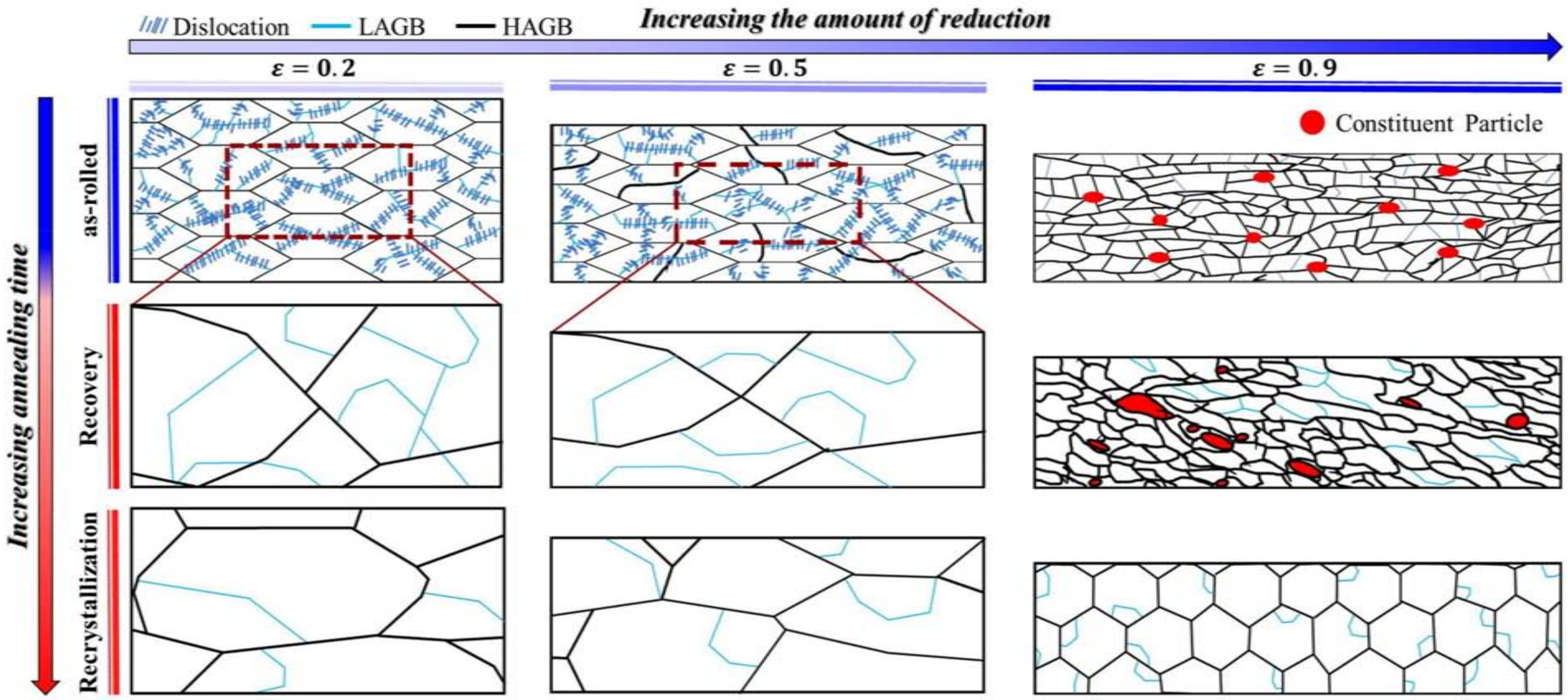

Figure 2.15: Schematic diagram of the change in the number fraction of HAGBs during the cold rolling and subsequent annealing

The recrystallization by PSN occurred preferentially in the deformation zone formed around the coarse particles, where the orientation of the nucleus does not differ significantly from that of the conventional grain (Bieda et al., 2010; Humphreys et al., 2004). When recrystallization begins, some nucleation is created and grown in the deformation zone around the coarse constituent particles by the migration of HAGB, where the number fraction of HAGB decrease locally and rapidly (Fig. 2.11 and 2.12). According to Sztwiertnia et al. (2013), the HAGBs decreases significantly in the region around coarse particle after the primary recrystallization, while the HAGBs in the dispersoids region remains at the level of number fraction before annealing. This suggests that recrystallization occurs preferentially due to the increase in residual stress caused by local plastic deformation around the coarse grains at the beginning of recrystallization, while the recrystallization has not yet progressed in the dispersion region.

2.4.3 Apparent activation energy for recrystallization

According to literatures, the activation energy for migration of the low angle boundary in aluminum alloys depends on the activation energy for lattice-diffusion of the main additive element (Mn=217kJ/mol (Bakker et al., 1990)), while the activation energy for migration of HAGBs in the aluminum alloy is close to the value for grain boundary diffusion (84 kJ/mol) reported by Balluffi (1970). The Al-Mn based alloys containing alloying elements such as Mn, Si and Fe can cause precipitation of second-phase particles during recrystallization behavior, which will significantly exert the effect in the pinning of grain boundaries and the retarding the migration of grain boundaries.

Significant pinning effects were found in the annealed specimens on recovery and recrystallization, which is attributed to the presence of the dispersoids precipitated under homogenization at the low and high angle grain boundaries introduced during plastic deformation. The apparent activation energies for recrystallization of AM2, AM5 and AM9 were determined to be 332KJ/mol, 239KJ/mol and 115KJ/mol, respectively, where the apparent activation energy for recrystallization of AM9 is almost similar to the activation energy for self-diffusion in the aluminum (Balluffi, 1970). Therefore, the recrystallization kinetics for AM9 is attributed to the stored energy associated with dislocation density. This means that since the strain energy is large enough for the recrystallization, therefore the effects of the precipitates and solid solution atoms on the recrystallization rate can be negligible.

Although the activation energy for recrystallization in the AM5 specimen is similar to the activation energy for Mn diffusion (217 kJ/mol (Bakker et al., 1990)) in aluminum, since the concurrent precipitation did not occur during recovery and recrystallization in the present study (see Section 3.4.1), the activation energy for recrystallization of AM2 and AM5 may be influenced by pinning effect of fine secondary particles. In particular, accounting the crystallite size of AM2 is hardly changed during recovery, driving pressure for recrystallization and migration might be insufficient against the considerable pinning effect of fine particles on LAGB and HAGB. Hence, the fine secondary particle on LAGB and HAGB is responsible for the significant delay in recovery and recrystallization of AM2 and AM5.

2.5 Conclusions

The effect of reduction rate on the recrystallization behavior of the cold-rolled AA3003 aluminum alloy was investigated in this chapter.

The EBSD map show that the recrystallization preferentially occurs at the rotation zone around the coarse particles for AM5 and AM9 specimens, which suggests that the PSN effect on the recrystallization requires a critical strain of about 0.5. Analysis of the thermal activation process by JMAK theory reveals that the apparent activation energy for the recrystallization of AM9 is close to the activation energy for self-diffusion in the aluminum. In the meanwhile, activation energies of AM2 and AM5 exhibit higher values, which is attributed to the Zener pinning effect of the fine secondary particle to retard the restoration process. During recrystallization at 350 °C, the Mn concentration in AM2 decreased by 0.015 wt% within the interval between the 300s and 600s, which implies that recrystallization and precipitation occurred simultaneously. On the other hand, the electrical conductivities of AM5 and AM9 were lowered depending on the amount of the cold rolling, which were gradually increased to the constant values irrespective to the reduction ratio in the recrystallization stage. The number fraction of HAGBs increases in proportion to the amount of reduction, which yield about 8% for AM2, 52% for AM5 and about 72% for AM9. During the recovery and recrystallization, the number fraction of HAGBs of AM2 and AM5 increase significantly at the beginning of annealing and remain almost constant when the number fraction of HAGBs reaches 70-80%.

Chapter 3

Influence of constituent particles on restoration behavior in cold-rolled AA3003 aluminum alloy

3.1 Introduction

In Chapter 2, the effect of the cold rolling reduction on the recrystallization kinetics of commercial AA3003 aluminum alloy was investigated. In the absence of concurrent precipitation during annealing, the recrystallization kinetics is changed depending on the amount of plastic deformation, in which the number fraction of high-angle grain boundary and low-angle grain boundary is varied with the reduction ratio.

The presence of the fine secondary particle generated by homogenization treatment delays the formation of the low-angle grain boundary (LAGB) and the migration of the dislocations, which is due to the pinning effect during subsequent annealing. In particular, the dispersoids have a great influence on the restoration rate of cold-rolled specimens with lower plastic strain. Regarding the specimens with the large plastic strain, the recrystallization around the coarse constituent particles is promoted by particle-stimulate nucleation (PSN) and the migration of HAGB is inhibited by the presence of fine secondary particles, which leads to the refinement of the recrystallized grains. These results imply that the deformed microstructure composed of the constituent particles have a significant influence on the recrystallization kinetic associated with the formation of LAGB, HAGB and the migration of dislocations.

The hardening of the metal is accompanied by the structural refinement of dislocation microstructure, where the tangled dislocations would be developed into the dislocation boundaries and HAGBs under the certain level of plastic deformation. Due to the accumulation of dislocations, the stored energy is increased to acts as the driving force for the recovery and recrystallization during annealing. It should be noted that, recalling the fact that the recovery rate increases in proportion to the amount of reduction in the previous Chapter 2, large plastic deformation leads to a significant reduction in thermal stability from the viewpoint of the annihilation of dislocation microstructure, which is an important issue in terms of the structural stability of the cold-rolled sheet at low temperature.

In the case of the severe plastic deformation, lamellar microstructure of elongated grains are often found as the strait boundaries parallel to the rolling direction, and a region with a low dislocation density exists between the dislocation boundaries (Hughes and Hansen, 2000; Liu et al., 2002). The annihilation and rearrangement of dislocation introduced by cold rolling is an important mechanism in the initial recovery stage in prior to the coarsening of the sub-grain (Humphreys et al., 2004). The initial stage of recovery exhibits limited influence on the deformed microstructure and its mechanical properties, which is phenomenologically dominated by the triple junction motion. For instance, the triple junction motion increases the spacing of the lamellar boundary and gradually decreases the hardness (Yu et al., 2011). The grain shrinkage also occurs at the triple junction where the three boundaries are connected, leading to an increase in the spacing of the adjacent lamella boundaries (Yu et al., 2013). The recovery behavior caused by this mechanism is commonly referred to as the triple junction motion, and this behavior leads to a significant increase in lamella spacing before recrystallization begins. Therefore, the triple junction motion in the recovery stage is an important mechanism for specifying the spacing of the lamella boundaries closely related to the size of the recrystallized grain.

It should be noted that the mechanism of the triple junction motion in the pure metals during the recovery process has been extensively studied over the last few decades (Gottstein and Shvindlerman, 2009; Vandermeer and Hansen, 2008; Yu et al., 2013) and that polycrystalline metals have indicated unique characteristics (Chaix et al., 2010; King, 1999). The boundaries composed of triple junctions can possess higher energy than adjacent boundaries (Chaix et al., 2010; Shekhar and King, 2008), which may provide sites for the promotion of the concurrent precipitation and nucleation of recrystallization (Brechet, 2010; Lefevre-Schlick et al., 2009). Although the kinetics of triple junction motion for pure metals has been studied through experimental (Yu et al., 2012) and simulation analysis (Thomas et al., 2019), the investigation of the difference in stored energy of the alloy due to the correlation between the distribution of constituent particles and certain plastic deformation is still insufficient. Since the constituent particles generated under different homogenization conditions have a great influence on the density and structure of dislocations during cold rolling, the thickness of the elongated grains and their curvature may vary depending on the number density and interspacing of the constituent particles.

In the Al-Mn system, the constituent particles composed of the orthorhombic $Al_6(Fe, Mn)$ and cubic α-Al(Mn, Fe)Si phase mainly would be formed as the primary particles during solidification and the fine secondary particles during heat treatment (e.g., homogenization and annealing). The precipitation of fine secondary particle in supersaturated DC-cast Al-Mn alloy occurs in the temperature range of 300°C to 530 °C (Li and Arnberg, 2003a). In addition, the dissolution of the dispersoids and diffusion of Mn into the constituent particles during homogenization at high temperature act an important role in the evolution of the size and composition of the primary particles (Li and Arnberg, 2003b, 2002). The constituent particles formed under the different homogenization conditions can affect the recovery and recrystallization microstructure because the residual stress around the particles would be different even at the same reduction ratio. In particular, the supersaturated Mn in the cold-rolled Al-Mn based alloys can simultaneously progress the recrystallization and precipitation during annealing, and the temperature at which simultaneous precipitation occurs is known to be in range of 350 °C to 400 °C (Somerday and Humphreys, 2003). In addition, segregation of solute atoms may occur during cold rolling, which locally increases the Mn concentration around the dislocation wall (and/or cell wall) and grain boundaries. Thus, the driving force for precipitation will be locally varied with the Mn supersaturation during the annealing (Chen et al., 2003).

Therefore, the present chapter focused on the correlation between the constituent particles and microstructure evolution during annealing under a large amount of plastic strain (90% thickness reduction). To this end, the amount of Mn supersaturation in the Al matrix was controlled by different homogenization conditions, and the effect of volume fraction and number density of primary and secondary particles on the work hardening and the recovery and recrystallization behaviors was investigated.

3.2 Experimental Procedure

A commercial AA3003 (Al-1.15Mn-0.52Fe-0.28Si-0.16Cu in wt.%) alloy was used in this study. The as-cast materials were homogenized under different conditions; route-A (RA) 580 °C for 8h with a heating rate of 50 °C/h and route-B (RB) 580 °C for 16h with a heating rate of 500 °C/h, and then immediately quenched in the water at room temperature. All homogenized specimens were processed by cold-rolling with strain rate of 0.9. The cold-rolled sheets were isothermally annealed at 220 °C to 400 °C for 2s to 24h in salt-bath, and then immediately quenched into the water at room temperature.

The microstructure evolution of all the specimens was observed by OM and FE-SEM. Electric conductivity was measured by eddy current inspection (using SIGMA tester). Back-scattered electron imaging (BEI) mode was used to capture the microstructural characteristics of the constituent particles in all samples. The measurement of crystalline orientation and grain boundary misorientation was conducted by FE-SEM equipped with EBSD, in which the data was treated by TSL OIM analysis software and MTEX toolbox for MATLAB (Hielscher et al., 2019). In order to examine detailed microstructure, transmission electron microscopy (TEM) observation was carried out for as-rolled and annealed specimens with an operation voltage of 300 kV (JEOL, JEM-3010). The foil sample preparation suitable for TEM was made by twin jet polishing technique in a 20% HNO3 methanol solution under the condition of about $-20\,^{\circ}\mathrm{C}$ or less.

The microhardness was measured by Vickers hardness tester with an interval of 50 μm at a load of 100 gf for 15s. The apparent activation energy for recrystallization of cold-rolled specimens was estimated by using the modified JMAK-microhardness model. The dislocation density was measured and analyzed by synchrotron XRD. The high-intensity X-ray BL02B2 beamline (λ=0.516Å) of the SPring-8 synchrotron radiation facility is utilized in this study. The time resolution of this experiment was 10s.

3.3 Results

3.3.1 Effect of homogenization conditions

The constituent particles characterized by the Al_6(Fe, Mn) and α-Al(Mn, Fe)Si phase are the main intermetallic compounds in the Al-Mn based alloys. Since these constituent particles have a great influence on the evolution of dislocation density and microstructure during plastic deformation and annealing, the microstructure observation was performed for the change in the characteristics of constituent particles by the homogenization treatment. The microstructure of as-cast specimen and the homogenized RA and RB specimens are shown in Fig. 3.1. The grain of each specimen was observed by OM for each anodized specimen (Fig. 3.1a, c and e), the images observed by FE-SEM/BEI show microstructure characteristics in the (b, d and e) primary particles and (b, d and e) dispersoids region. The size and distribution of constituent particles were obtained from FE-SEM/BEI images using the Image-J program, where the images observed at the magnification of 1000 for primary particles and the magnification of 10000 for fine secondary particles were used.

The as-cast specimen shows an equiaxed grain microstructure with a typical dendrites structure fabricated by DC-casting, where the average grain size is amount to be 148 μm (Fig. 3.1a). The constituent particles after solidification consist of most of Al_6(Fe, Mn) phase (yellow arrow) and a trace amount of α-Al(Mn, Fe)Si phase (white arrow), and no fine secondary particles are observed (Fig. 3.1b). The aluminum at room temperature becomes supersaturated with Mn and Fe due to its low solubility (Li et al., 2012; Li and Arnberg, 2003a,b; Ryen et al., 2006), and the electrical conductivity of as-cast specimen was as low as 30 %IACS. The grain size of RA (Fig. 3.1c) and RB (Fig. 3.1f) are amounted to be 160 μm and 178 μm, respectively, which are varied depending on the holding time of homogenization. Although the heating rate did not affect the grain growth, the properties of the constituent particles were varied with the homogenization conditions.

It can be seen that the RA specimens shows the spheroidization and coarsening of primary particles (Fig. 3.1b and d), and the number density was reduced as compared with the as-cast specimen (Fig. 3.1b and d). On the other hand, the number density of the primary particles of the RB specimen was significantly increased inside the grain, and their size was reduced to be about 1.8 μm, which is smaller than that of the as-cast specimen (Fig. 3.1g).

In addition, the particle-free zone (PFZ) was formed in the clustered region of the primary particles by homogenization, and the PFZ spacing was about 11 μm and 25 μm in RA and RB9, respectively (Fig. 3.1d and g). The fine secondary particles show a markedly different trend. A large number of dispersoids in RA were precipitated, and it was observed that the number density and size of RB were significantly smaller than that of RA (Fig. 3.1e and h). The change in quantitative values of the grain size, primary particle size and area fraction, dispersoids size and area fraction, and electrical conductivity by homogenization are listed in Table 3.1. The Al_6 (Mn, Fe) constituent particles were transformed to a large number of α-Al (Mn, Fe) Si phase, which can be clearly identified in the BEI image of the as-cast specimen and the homogenized specimens (Fig. 3.1b, d and g) . The α-Al (Mn, Fe) Si phase appears brighter than the Al_6 (Mn, Fe) particles in the BEI image, which due to the lighter contrast caused by the higher average atomic number (Dehmas et al., 2013).

Since the modulus of elasticity of this α-Al(Mn, Fe)Si phase is much larger than that of Al_6(Mn, Fe)particles, the residual stress will increase due to the mismatch of plastic strain between the aluminum matrix and the constituent particles during cold rolling. In particular, the mismatch of plastic strain around coarse particles can lead to deformation zone formed by the accumulation of dislocations, which is more effective in promoting PSN. Therefore, the transformation from Al_6(Mn, Fe) to α-Al(Mn, Fe)Si phase is important in cold rolling processes it can increase the dislocation density associated with the driving force for recrystallization. Details of the residual stress around the constituent particles will be discussed in Chapters 5 and 6.

3.3.2 Plastic deformation characteristics

3.3.2.1 Effect of second-phase particles

The typical longitudinal microstructure of the 90% cold-rolled RA and RB specimens is shown in Fig. 3.2, which are referred to as (a-b) RA9 and (c-d) RB9, respectively. Fig. 3.2a and c are observed by BEI,

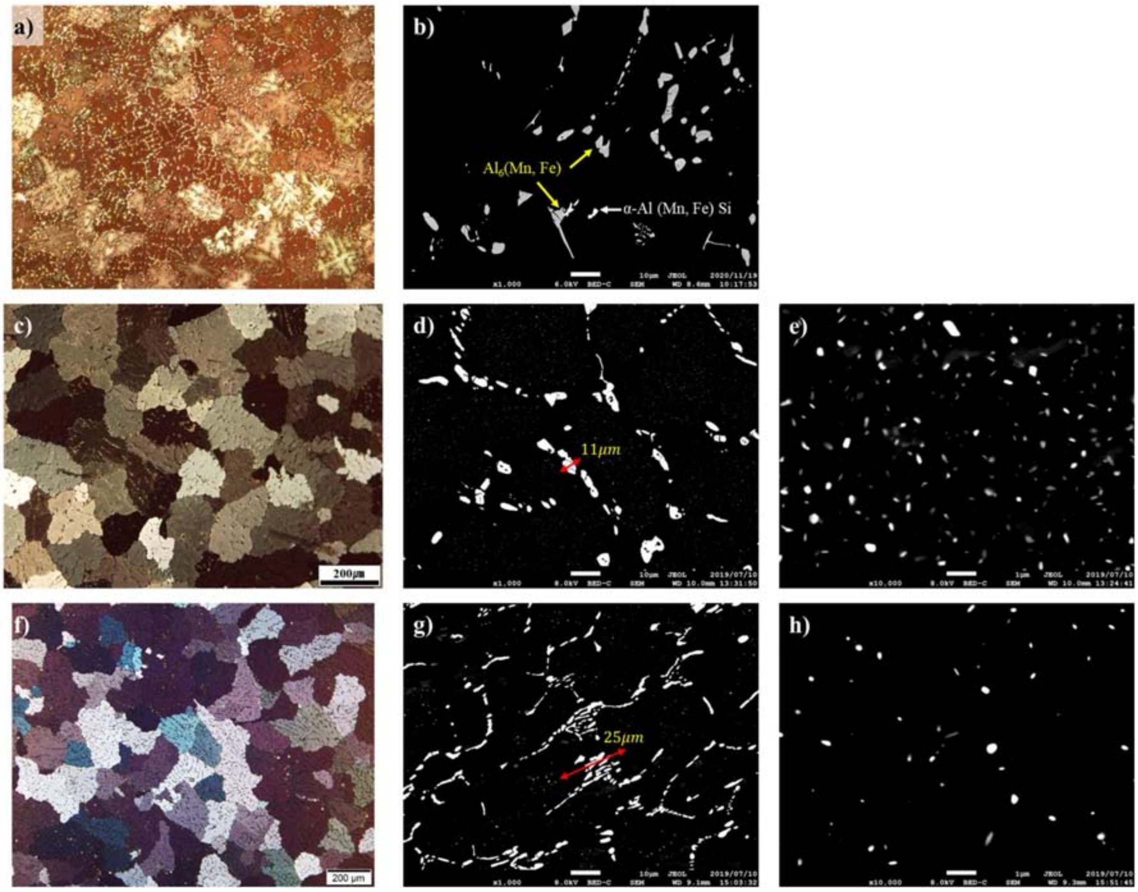

Figure 3.1: Microstructure characteristics of (a, b) as-cast, (c-e) RA and (f-h) RB; (a, c and f) typical OM image and (b, d and e) BEI image in coarse particle region and (e and h) BEI image in dispersoids region

where the dispersoids are mainly distributed around the boundaries of deformed grains. The RA9 specimen is composed of a large number of dispersoids that precipitated during homogenization, where the lamella grains are distorted due to the existence of the fine secondary particles (Fig. 3.2a). In the meanwhile, the RB9 specimen shows a relatively flat lamella microstructure with very a few numbers of dispersoids overall the specimen (Fig. 3.2c).

The boundaries introduced by cold rolling can be classified into two categories. The first is a lamellar boundary, which is approximately

Table 3.1: Change in grain size, area fraction and size of constituent particles and electrical conductivity by homogenization

		as-cast	RA	RB
Grains	size(μm)	88	160	178
Primary particles	size(μm)	3.5	2.5	1.8
	area fraction (%)	14.2	4.2	4.8
Dispersoids	size(μm)	-	0.171	0.145
	area fraction (%)	-	2.6	0.17
Electrical conductivity	(%IACS)	29.6	43.5	39.9

parallel to the RD, and the other one is an interconnected boundary that is approximately perpendicular to the RD (Fig. 3.2b and d). The average lamellar boundary spacing of RA9 and RB9 specimens was measured to be approximately 175 nm and 239 nm, respectively (Fig. 3.2b and d). The measurement of the lamella spacing was performed at a position that maintains a straight-line shape while excluding the boundary distorted around the triple junction points and constituent particles as much as possible. This difference in boundary spacing can be considered in terms of the distribution of constituent particles. That is, the accumulation of dislocations is changed depending on the distribution of the constituent particles, therefore the lamella boundaries tend to be more distorted as shown in Fig 3.2a. Generally, the large particles have a significant effect on the deformed microstructure, where the high-angle boundaries will be introduced by the large local lattice rotations in the vicinity of the particles (Humphreys and Hirsch, 1976). In addition, the fine secondary particles locally increase the density of dislocations by accumulating dislocations around them (Ashby and Johnson, 1969). Assuming that the residual stress under the same cold rolling condition is changed with the distribution manner of the dispersoids, the presence of a large number of dispersoids acts as a strong barrier to dislocation migration during cold rolling, which leads to an increase in dislocation density associated with the residual stress. Therefore, even if the same reduction ratio is applied for the different conditions of homogenized specimens, the RA9 with a higher area fraction of constituent particles show thinner lamella spacing than RB9, which will result in a higher dislocation density.

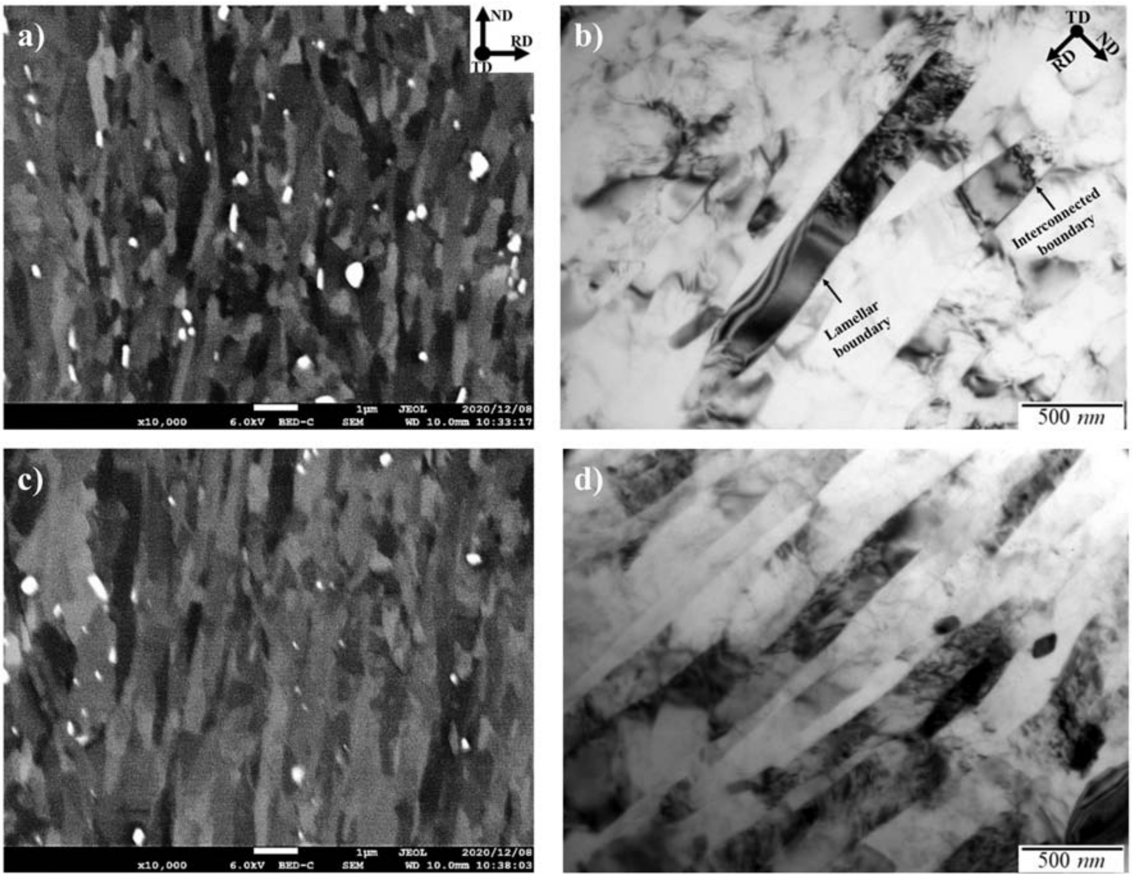

Figure 3.2: Deformed microstructure of (a, b) RA9 and (c, d) RB9

3.3.2.2 Evolution of dislocation density with increasing strain

As mentioned in 3.3.2.1, the deformed microstructure of RA9 and RB9 were largely changed with the homogenization conditions, which is attributed to the different size and distribution manner of dispersoids. In order to estimate the effect of homogenization condition on the stored energy of cold-rolled Al-Mn alloy sheets, the dislocation density of RA9 and RB9 were measured by synchrotron X-ray.

The effect of homogenization condition on the (111) diffraction peaks of RA9 and RB9 measured by synchrotron XRD is shown in Fig. 3.3. The diffraction angle of RA9 and RB9 is shifted slightly toward the lower angle compare to the as-cast. This shift of diffraction angle implies an increase of d-spacing in ND direction as a result of residual strain. The profile of RA9 shows the broadening of a diffraction peak at a similar peak position of RB9. Accounting that the same amount of plastic strain was induced for RA9 and RB9, the broadening of a diffraction peak for RA9 is attributed to the decrease in the crystallite size and the local residual stress influenced by the presence of constituent particles under cold rolling.

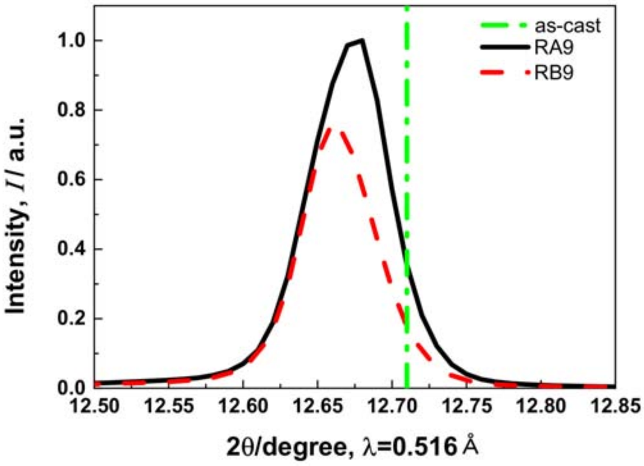

Figure 3.3: (111) diffracted peak at different homogenization condition for the RA9 and RB9

The residual stress associated with the dislocation density can be quantitatively analyzed by the Williamson-Hall plot, where the crystallite size and lattice strain can be estimated from the shift of the peak and the variation of the width (Williamson and Hall, 1953). The change in dislocation density with increase of the reduction ratio was evaluated using the profiles of (1 1 1), (2 0 0), (2 2 0), (3 1 1) and (2 2 2) reflections of the aluminum phase in this analysis. The effect of lattice strain, ε_L, on the full width at half maximum (FWHM) value obtained at each peak can be expressed by the Williamson-Hall equation as follows (Williamson and Hall, 1953)

$$\Delta 2\theta \cos\theta = (0.9\lambda/D) + 2\varepsilon_L \sin\theta \tag{3.1}$$

where $\Delta 2\theta$ is the FWHM of diffraction peak, θ is the Bragg diffraction angle, λ is the wavelength of X-ray (λ=0.516Å) and D is the average crystallite size.

The FWHM values for each specimen are shown in Fig. 3.4a in the form of a linear equation in the Williamson-Hall plot. According to the first and second terms of the Williamson-Hall plot of Eq. (3.1), the crystallite size and lattice strain are determined from the intercept and slope of the linear regression profile, respectively. The slope of the profile shows almost similar values in both specimens. This means that the average elastic strain is not significantly affected by the properties of the precipitate.

Fig. 3.4b shows the change in crystallite size and lattice strain evaluated from XRD profile analysis. The crystallite sizes of RA9 and RB9 are amounted to be 237 nm and 256 nm, respectively. It can be clearly seen that the crystallite size obtained by Eq. (3.1) decreases as the area fraction of the constituent particles increases, which indicates a correlation with the constituent particles such as the spacing of the lamellar boundary obtained by TEM observation. According to Ungár et al. (2001), the crystallite size calculated through X-ray diffraction analysis by Eq. (3.1) can be regarded as the average size of sub-grains and dislocation cells due to the coherently scattered X-rays.

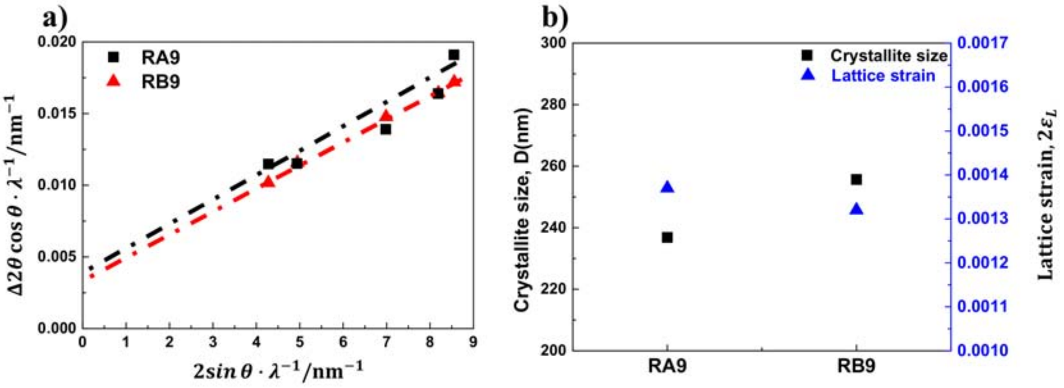

Figure 3.4: (a) Williamson-Hall plots and (b) Crystallite size and lattice strain for the RA9 and RB9 measured by XRD

The change in the dislocation density induced by constituent particle characteristics can be also determined from X-ray diffraction by assuming the lattice strain caused by dislocation lines. According to the relationship between the crystallite size and lattice strain obtained by Eq. (3.1), the dislocation density, ρ, is given by Williamson and Smallman as follows (Williamson and Smallman, 1956),

$$\rho = \frac{(3nK/F)^{1/2} < \varepsilon_L^2 >^{1/2}}{Db} \tag{3.2}$$

where n is the number of dislocations on each face of matrix, K is constant depending on the strain distribution around the dislocation line, F is an interaction parameter, $< \varepsilon_L^2 >^{(1/2)}$ is root mean square strain, b is Burgers vector. In literature(Williamson and Smallman, 1954), the constant of K assumed by the Cauchy strain distribution is amounted to be $K = 25$, whereas that by Gaussian strain distribution is nearly $K = 4$. In the absence of the extensive polygonization in dislocation arrangement, the dislocation density is calculated by assuming $n \approx F$, and $K = 4$. Thus, the Eq. (3.2) can be simply given as

$$\rho = \frac{2\sqrt{3} < \varepsilon_L^2 >^{1/2}}{Db} \tag{3.3}$$

The dislocation densities of RA9 and RB9 were evaluated as 3.87×10^{14} m^{-2} and 3.24×10^{14} m^{-2}, respectively. The change in dislocation density is due to the change in crystallite size as shown in Fig. 3.4b. Considering the similar slope for the lattice strain in Fig. 3.4a and the linear relationship between the crystallite size and lattice strain in Eq. (3.3), the difference in dislocation densities of RA9 and RB9 specimens with the same amount of reduction depends on changes in lamella spacing and crystallite size, as shown in Figs. 3.2 and 3.4.

Taking into account the residual stress caused by the constituent particles during plastic deformation, the dislocation density will be changed depending on the shape, size and number density of the particles. The influence of the number density of constituent particles in RA and RB obtained through BEI image analysis on the dislocation density calculated by Eq. (3.3) is shown in Fig. 3.5, where the primary particles is indicated by the black line and the fine secondary particles are indicated by the red line. Assuming that the dislocation density should be proportionally increased by an increase of the number density of the particles in the matrix phase, the large numbers of fine secondary particles for RA9 is naturally responsible for the larger dislocation density in Fig. 3.5. This can be separately considered in terms of the distribution of the primary and secondary particles in the matrix phase. Basically, as the spacing between constituent particles becomes narrower, the larger external stress is necessary for the motion of dislocations. Therefore, the relaxation of the residual stress around the constituent particles would be easily occurred by the plastic deformation around the larger constituent particles under the lower stress level. Recalling the facts that the distribution of the primary and secondary particles as shown in Fig. 3.1, the different number density of primary particles can be seen with similar area fraction in Fig. 3.1 (d) and (g), while the distribution of the secondary particles in (e) and (h) are apparently different. This indicates that, although the dislocation density in the primary particle cluster region might be proportionally changed with the size and the shape of the particle, the migration of dislocations is more suppressed by the large numbers of secondary particles during the plastic deformation, which leads to the dislocation accumulation around the secondary particles in view of total dislocation density as shown in Fig. 3.5. Therefore, the dislocation density increases mainly depending the number density of the fine secondary particles.

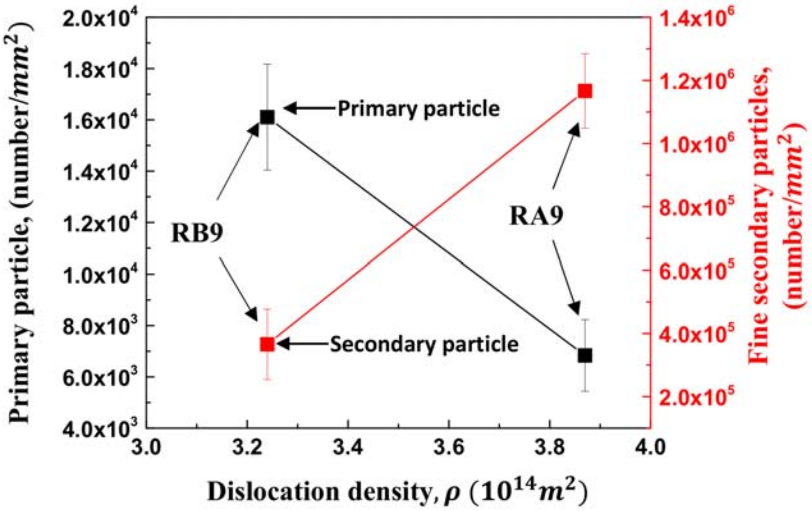

Figure 3.5: Relation between dislocation density and number density of constituent particles.

As Ashby (1966, 1970) first reported, the presence of dispersed second-phase particles causes to the generation of dislocations and retards the migration of dislocation. This will eventually lead to an increase in the total dislocation density as dislocations accumulate around the particles during plastic deformation. In a similar way, the constituent particles can pin the boundaries of cells and sub-grain. Therefore, the distribution of the dispersoids under the same cold rolling conditions can be expected to affect the size of the dislocation cells and sub-grains, which is supported by the change in crystal size obtained from Eq. (3.1) and the lamella spacing measured in the TEM image.

3.3.3 Annealing behavior

3.3.3.1 Softening behavior at low temperature

In the literature (Kalu and Waryoba, 2007), the consumption of dislocations in the cold-rolled specimen was amounted to be about 10% during the recovery, which corresponds to a decrease of about 10% in microhardness. The transition from recovery to recrystallization is distinguished by the decrease in Vickers hardness. The Vickers hardness profiles after isothermal annealing are shown in Fig. 3.6, where the point at which the hardness decreased by 10% was defined as the transition from recovery to recrystallization and indicated by a dotted line. The decrease in microhardness as a function of annealing time indicates the softening behavior of the cold-rolled specimen. After the prolonged annealing at low temperature annealing, the hardness reaches the point of transition from recovery to recrystallization. With a higher driving force for softening associated with dislocation density, the RA9 reaches the recrystallization process in a shorter time than RB9. Even if the dislocation density is taken into account, the softening behavior of RB9 with high Mn concentration proceeds very slowly, which may be due to the drag effect of the Mn atom in aluminum.

As mentioned in Chapter 2, the apparent activation energy for the recovery mechanism was measured from the JMAK microhardness model. The apparent activation energies for recovery of RA9 and RB9 are 124 kJ/mol and 193 kJ/mol, respectively. Accounting for the fact that the activation energy for grain migration and coarsening during the recovery depends on the purity of the material, the RB9 with high Mn concentration will lead to significant solute drag. Therefore, the solute drag effect on the recovery rate may be significantly reduced for the dissipation of the stored energy, which is responsible for the increase of the activation energy of RB9.

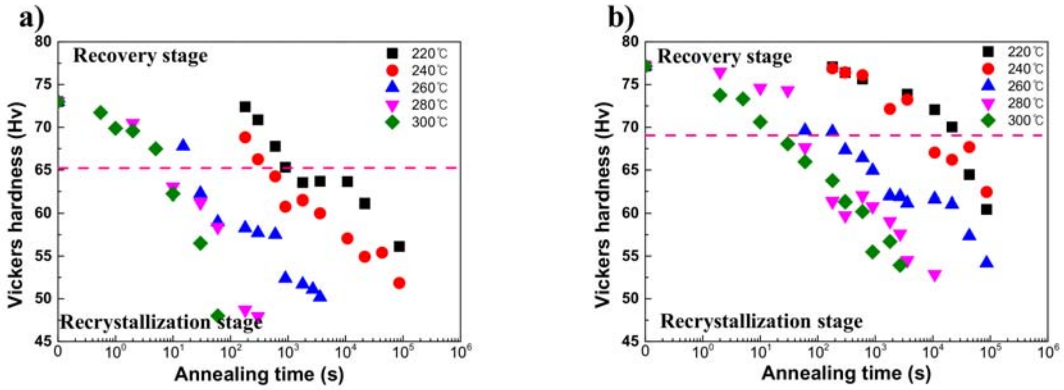

Figure 3.6: (a) Change in Vickers hardness as a function of annealing time at range of 220 to 300 °C in (a) RA9 A and (b) RB9

Fig. 3.7 shows the IPF maps of (a-c) RA9 and (d-f) RB9 measured to the point of transition to recrystallization during recovery at 280 °C. Although EBSD maps are difficult to measure the spacing of lamellar structure accurately than TEM images, IPF maps have the advantage of being able to handle recovery behavior over a larger area. The EBSD analysis was measured in a size of 7 μm × 14 μm with a step size of

0.07 μm for as-rolled and a size of 50 $\mu m \times 100$ μm with a step size of 0.1 μm for annealed specimens.

When RA9 is annealed at 280 °C for 10s, some equiaxed sub-grains appear within the lamella grain as shown in Fig. 3.7b, but these sub-grains are not larger than the surrounding boundary and remain the initial lamella shape. The spacing of the lamella boundary is dominated by the triple junction motion and increases rapidly, but the growth of the equiaxed grain boundary parallel to the rolling direction operates very slowly in the recovery stage. This triple junction motion accompanied by shrinkage and expansion progressively reduces the aspect ratio of the lamellar structure, which gradually evolves into an equiaxed structure, as shown in Fig. 3.7c. However, the microstructure of RB9 does not evolve into equiaxed grains during annealing at 280 °C for 60s (Fig. 3.7d-f), and shows a lamellar structure with an extended boundary spacing than the initial rolled material.

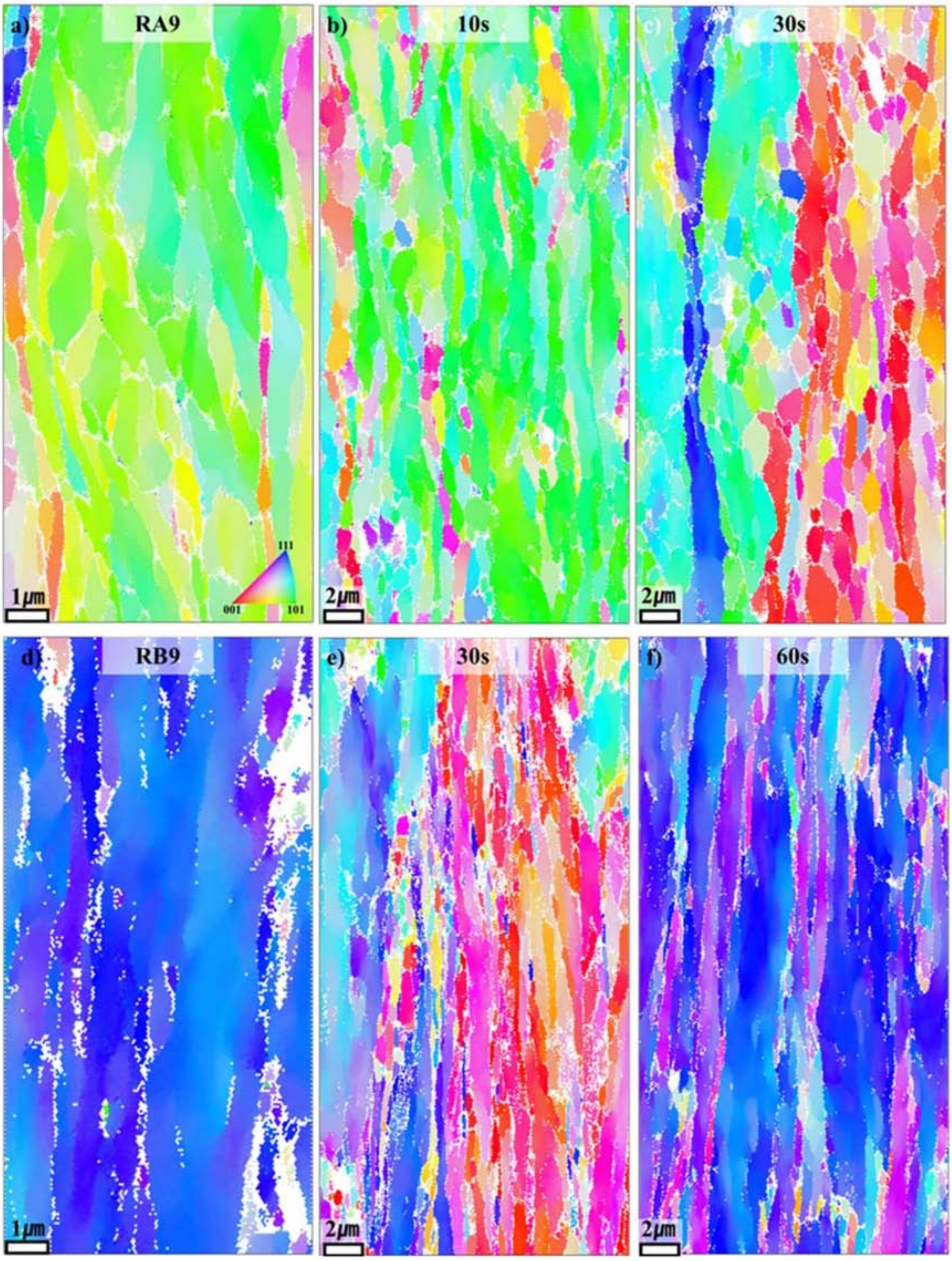

Figure 3.7: EBSD map in longitudinal section of (a-c) RA9 and (d-f) RB9 from cold-rolled state to the near point where recovery behavior ends during annealing at 280 °C. The inverse pole figures (IPF) indicate the color key of the crystal direction parallel to the normal direction (ND)

TEM observation was conducted for the RA9 and RB9 annealed at a lower temperature of 220 °C in order to observe the evolution microstructure associated with the dislocation migration within lamellar grains during the recovery process more clearly. TEM dark-field images for RA9 and RB9 annealed at 220 °C are shown in Figs. 3.8 and 3.9, respectively.

The RA9 annealed for 30 min shows a very high dislocation density boundary interconnected with lamella boundaries, as shown in Fig. 3.8a. This shows a dislocation structure with a similar tendency to that of the initially as-rolled specimen (Fig. 3.8b), but a relatively dislocation-free region appears in the upper region of the lamellar structure and in the adjacent grains. By subsequent annealing, the interconnected dislocation inside the lamella forms a higher misorientation due to the accumulation by rearrangement of the dislocation, which leads to a decrease in the aspect ratio of the lamella structure (Fig. 3.8b). However, there are still some dislocations inside the grain, and it can be seen that the dislocation is pinned by the fine secondary particles (indicated by the yellow arrow in Fig. 3.8b.). After annealing for 24 hours (Fig. 3.8c), little dislocation was observed inside the grain, and the lamellar structure is separated by the development of sub-grain along with the increase of the lamellar spacing by the triple junction motion. This can be considered as the rearrangement of dislocations inside the lamellar structure during annealing and absorption into the interconnect boundary, whereby the interconnected dislocation boundary is strengthened and developed into an independent grain.

Fig. 3.9 shows the evolution of the dislocation structure of RB9 with a relatively high concentration of Mn. After annealing for 3 hours (Fig. 3.8a), the dislocation inside the lamellar structure is almost sim-

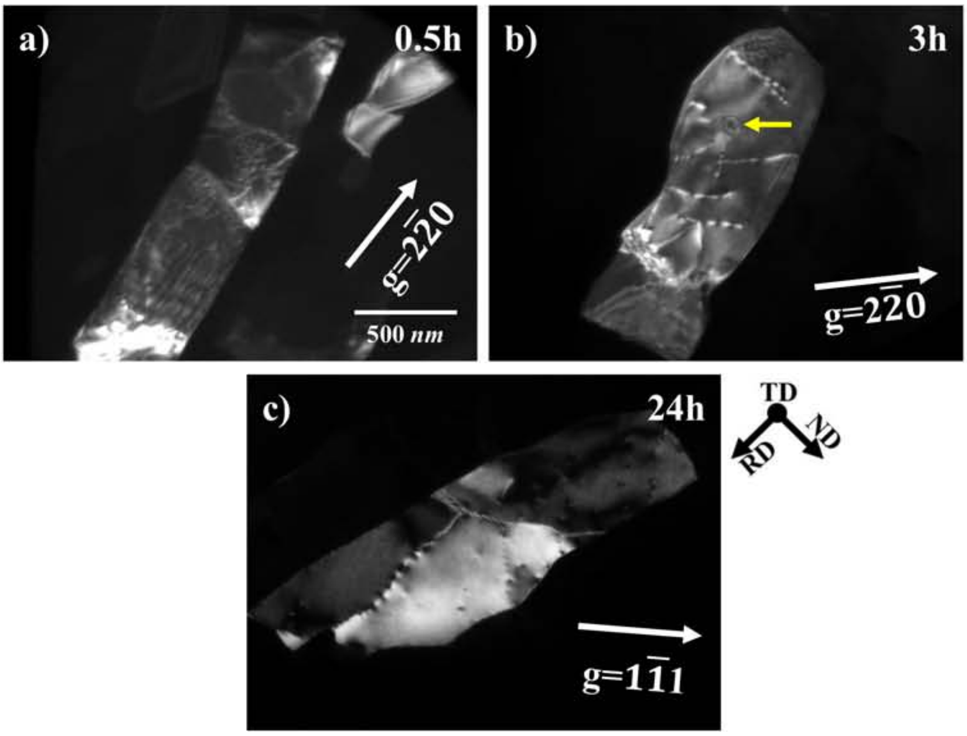

Figure 3.8: Microstructure evolution of the RA9 annealed at 220 °C for (a) 0.5h, (b) 3h and (c) 24h

ilar to that of the initial specimen. It can be seen that the dislocation migration at 220 °C is very slow compared to RA9. With the increase of the annealing time, the dislocation-free regions are shown locally inside the lamellar structure due to the gradual migration of dislocations, but a complex entangled dislocation is still observed inside the grain and at the boundary (Fig. 3.8b). When annealed for 24 hours (Fig. 3.8c), the most dislocations are localized at the interconnected dislocation boundaries due to the dislocation migration, and relatively dislocation-free regions are observed above and below these interconnection boundaries. In addition, the dislocation is pinned at the lamella boundary so that a dislocation line linking from the boundary to the inside is observed. This may be due to the inhibiting effect of the dislocation movement of high concentrations of solute atoms at the boundary.

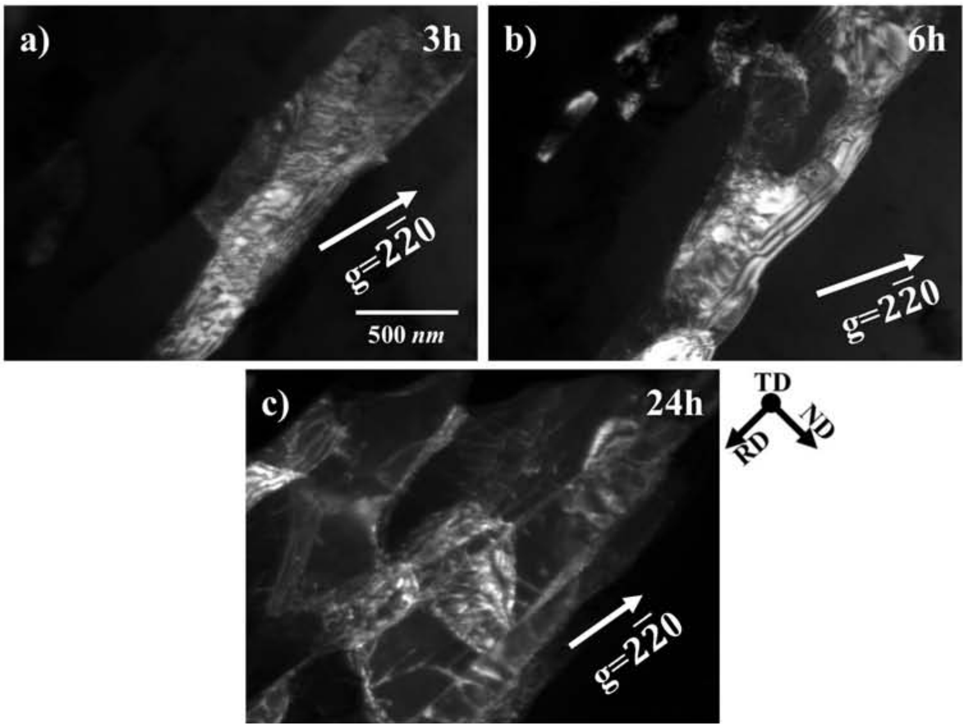

Figure 3.9: Microstructure evolution of the RB9 annealed at 220 °C for (a) 3h, (b) 6h and (c) 24h

By comparing RA9 and RB9, it can be clearly seen that the aspect ratio of lamellar grains in the RA9 decreases due to the expansion of the boundary and the development of the interconnection dislocation with an increase in the annealing time. However, RB9 shows that the aspect ratio as well as the spacing of the lamella boundaries is almost similar to that of the specimens in the initial rolled state, despite increasing the annealing time. It can be seen that the recovery behavior through the triple junction motion is highly dependent on the concentration of Mn solute.

The triple junction motion increases the lamella boundary spacing rapidly, but the boundary along the rolling direction increases slowly.

These coarsening patterns gradually reduce the aspect ratio of the microstructure, gradually transitioning from a lamellar structure to a more equiaxed structure, as shown in Fig. 3.7c. Despite this transition, the microstructure of RB9 is still mostly lamellar structure during annealing at 220 °C for up to 24 hours, as can be seen in the TEM images in Fig. 3.7a–c.

The schematic diagrams and TEM observation results for triple junction motion mechanism are represented in Fig. 3.10, where the process of coarsening and shrinking of interconnected boundaries with increase of annealing time are illustrated. Assuming that the distortion caused by the constituent particles does not occur at the initial lamella boundary, the boundary generally forms a flat boundary, where the lamellar grain with a low radius of curvature will shrink in triple-junction point during annealing. During the coarsening of the lamella grain through triple junction motion, the boundary is connected to the interconnection dislocation boundary and can be deflected in the direction of the neighboring boundary (Yu et al., 2011). When the triple-junction motion is finally terminated, the shrunken grain ends at the triple-junction point and forms a fine equiaxed crystal structure. In addition, as the annealing time is increased, the straight boundary is gradually changed into the curved boundary, which is possible by the boundary migration via triple junction motion.

3.3.3.2 Recrystallization behavior

The change in the Vickers hardness for RA9 and RB9 under the annealing temperature at 300 °C, 350 °C and 400 °C are represented in Fig. 3.11, where the recovery, recrystallization and grain growth stages are clearly distinguished on the microhardness profiles. As mentioned

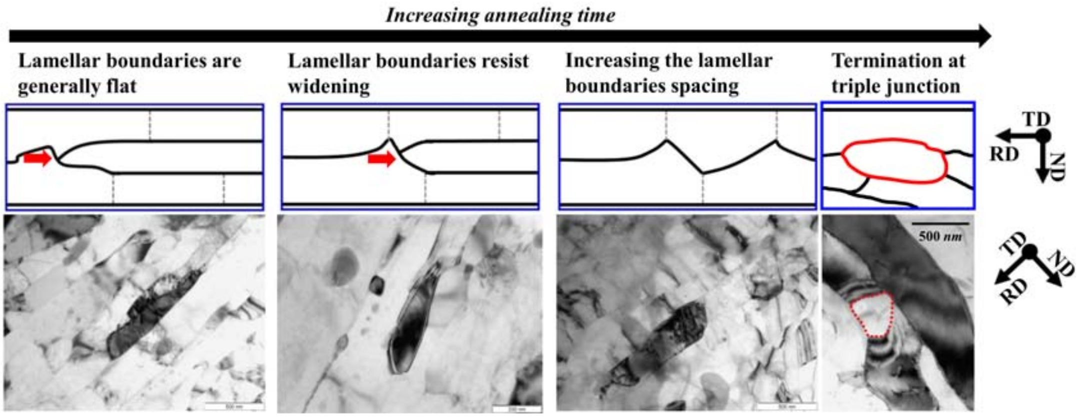

Figure 3.10: Schematic diagram and TEM images of triple junction motion in the large deformation AA3003 Aluminum alloy during the recovery process

in the previous Chapter 2, the restoration rate is basically highly dependent on the reduction ratio and the annealing temperature. Since the specimens used in this chapter have the same reduction ratio, the recrystallization behavior may be delayed due to the occurrence of concurrent precipitation due to the relatively high concentration of Mn. The time to reach the point where the recrystallization during annealing at 300 °C was completed by about 50% was 30s and 2700s for RA9 and RB9, respectively. As the annealing temperature increases, the recrystallization rate gradually increases, and the recrystallization of RA9 and RB9 annealed at 400 °C is completed after 2s and 100s, respectively. It can be clearly seen that the recrystallization behavior is highly dependent on the concentration of Mn in the Al matrix, which is associated with concurrent precipitation. In addition, the delayed recrystallization behavior by concurrent precipitation can have a significant effect on the size and shape of the recrystallized grains, which will be discussed in later section.

The apparent activation energy for the recrystallization was estimated by the JMAK microhardness model (see Chapter 2). The apparent activation energies for recrystallization of RA9 and RB9 are 115 kJ/mol and 195 kJ/mol, respectively. Considering that microsegregation and dislocation clusters due to solute diffusion during recovery act as nucleation sites for precipitation, the RB9 with a relatively high Mn concentration may experience significant concurrent precipitation delays during recrystallization. Therefore, microsegregation of the recrystallization behavior and precipitation nucleation may generate preferentially than recrystallization nucleation at the boundary with a locally high dislocation density. This can significantly delay recrystallization by the dissipation of stored energy and increased dispersoids, which is responsible for the increase in the activation energy for the recrystallization of RB9.

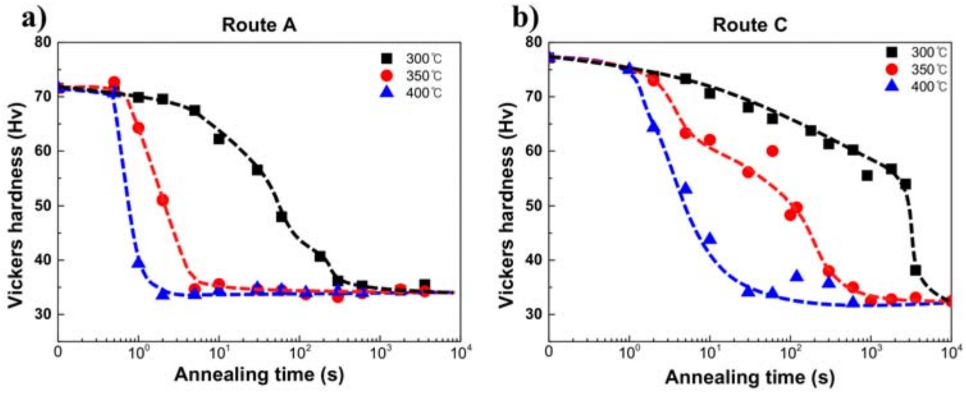

Figure 3.11: Change in Vickers hardness as a function of annealing time at range of 300 °C, 350 °C to 400 °C in (a) RA9 A and (b) RB9

Figs. 3.12 and 3.13 show the (a) grain orientation spread (GOS) map overlaid with IPF map, the (b, d) kernel average misorientation (KAM) map and (c) grain map of RA9 and RB9 measured at (a and b) 50% recrystallization and at (c and d) recrystallization completed during annealing at 350 °C. The GOS map indicates that the orientation of the aluminum is less than 3 degrees, which indicates the recrystallized grain (Sridharan et al., 2016). The KAM maps were calculated considering only neighbors with a specified small threshold angle of 2.5 ° and a misorientation angle less than the threshold angle. Therefore, the KAM map is no longer related to the sub-grain boundary and the local dislocation structure of the annealed specimen can be observed (Lopez-Sanchez et al., 2020). Considering that the annihilation and migration of dislocations associated with boundary migration dominate the recrystallization behavior, this analysis can effectively analyze the local dislocation distribution due to the annihilation and migration of dislocation during annealing. Note that the constituent particles are represented in white for GOS and grain maps, and in black for KAM maps.

EBSD analysis for RA9 was measured in a size of 20 μm × 20 μm with a step size of 0.1 μm (Fig. 3.12). After annealing at 350 °C for 2s, RA9 reached 50% recrystallization fraction in a very short time, which was obtained from the recrystallization fraction calculated from the JMAK plot in Chapter 2. The recrystallized grain in the GOS map is mainly observed around the coarse constituent particles (Fig.3.12a), which clearly shows that the recrystallization proceeded preferentially to the particle stimulated nucleation (PSN) effect. In addition, recrystallized grains are observed in regions where coarse constituent particles are clustered. It can be seen that the accumulation of dislocations due to the interaction between coarse particles increases during plastic deformation, and recrystallization begins rapidly in the coarse particle cluster region during annealing. On the other hand, in the dispersoids region, grains that are stretched in some rolling direction are observed, and a well-developed equiaxed sub-grain is shown due to the rearrangement of dislocations and absorption into the boundary. These sub-grains can serve as nucleation sites for recrystallization by subsequent annealing. Regarding the behavior of these dislocations, the local dislocation distribution is shown in the KAM map (Fig. 3.12b). The distribution of local dislocations is hardly observed around the coarse particles, while dislocation structures with high local density can be seen in the dispersoids region. The grain map at the point of completion of recrystallization after 5 seconds shows that the grains of the elongated shape in the rolling direction are no longer observed, and recrystallized grains with an average size of 8 μm are formed. In addition, a dislocation structure with a relatively low dislocation distribution density is observed, where dislocations pinned by the dispersoids appear to be connected to the boundaries of the recrystallized grains.

The EBSD analysis for RB9 was measured in a size of 30 μm × 60 μm with a step size of 0.3 μm. After annealing at 350 °C for 100s, the RB9 reached a recrystallization fraction of 50 % wiwh a relatively very slow recrystallization rate. The primary recrystallized grains are preferentially occurred by the PSN effect around coarse constituent particles, which can be clearly identified in the GOS map (Fig. 3.13a). In addition, the size of recrystallized grain was formed to significantly larger than RA9. It is considered that the primary recrystallized grains generated around the coarse particles grew in the rolling direction due to the expansion of the particle-free zone (PFZ) around the coarse particles by homogenization and the delay of boundary migration by the solute drag and concurrent precipitation in the region of dispersoids during annealing. The local dislocation distribution significantly decreased in the density of dislocations due to recrystallization around coarse particles, but dislocation structures with high density are very dense throughout the dispersoids region. It is believed that this was caused by the disturbance of the dislocation migration by the solute

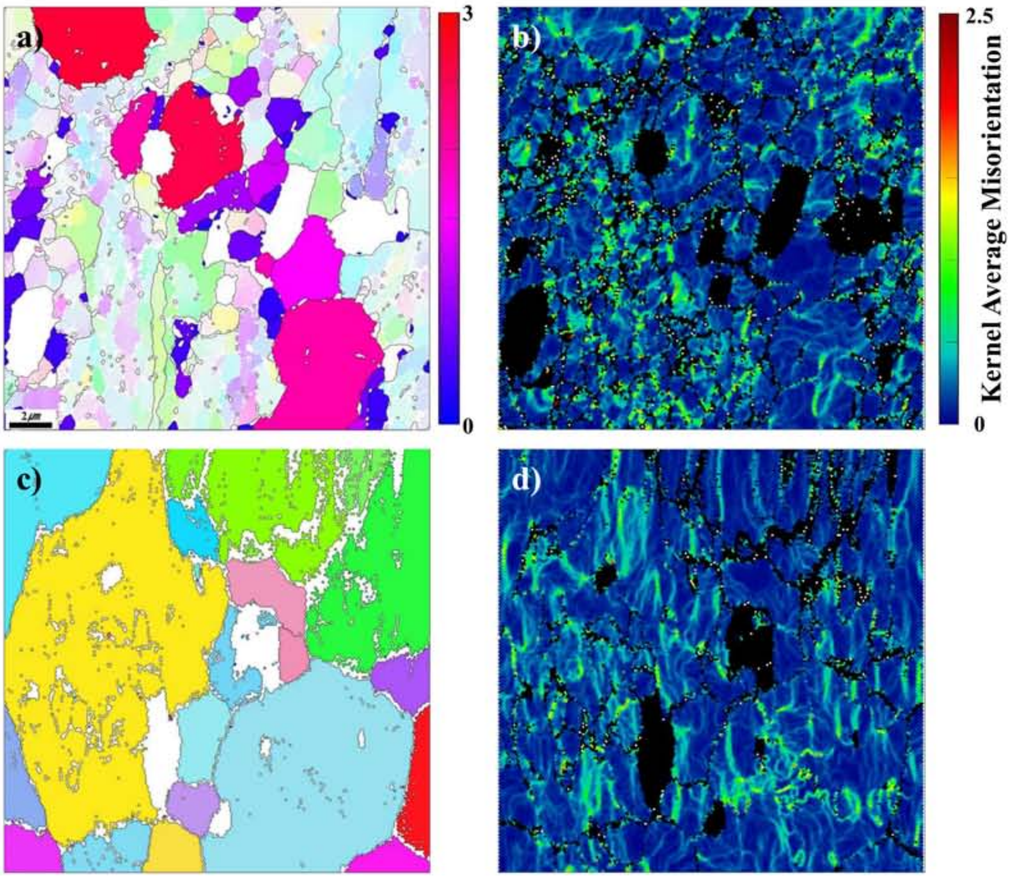

Figure 3.12: (a) Grain orientation spread (GOS) map overlaid with IPF map, (b, d) kernel average misorientation to the 1st neighbor with 2.5 ° threshold angle and (c) grain map in RA9 annealed at 350 °C for (a, b) 2s and (c, d) 5s

in the dispersoids region. The dislocations accumulated at such a high density can act as a nucleation site for precipitation of dispersoids rather than recrystallization during subsequent annealing.

The grain map at the point of completion of recrystallization after 1000s shows the recrystallized grains in the shape of elongated in the rolling direction observed in the initial rolled material, where the recrystallized grains size is amounted to be 21 μm (Fig. 3.13c). It can be seen that the grains recrystallized in the expanded PFZ grow in the rolling direction and are formed into grains of a coarse and elongated shape than RA9. The shape of these recrystallized grains is considered to grow into coarse and elongated grains by growing in the rolling direction of the primary recrystallized grains in the expanded PFZ. In addition, consumption of more dislocations than RA9 is expected due to the influence of concurrent precipitation and recrystallization during the annealing, which is clearly identified in Fig. 3.13d. The distribution of dislocation shows a significantly lower distribution of the local dislocation compared to RA9. However, the dislocations from fine secondary particles to grain boundaries show locally in the dispersoids regions formed inside the particles.

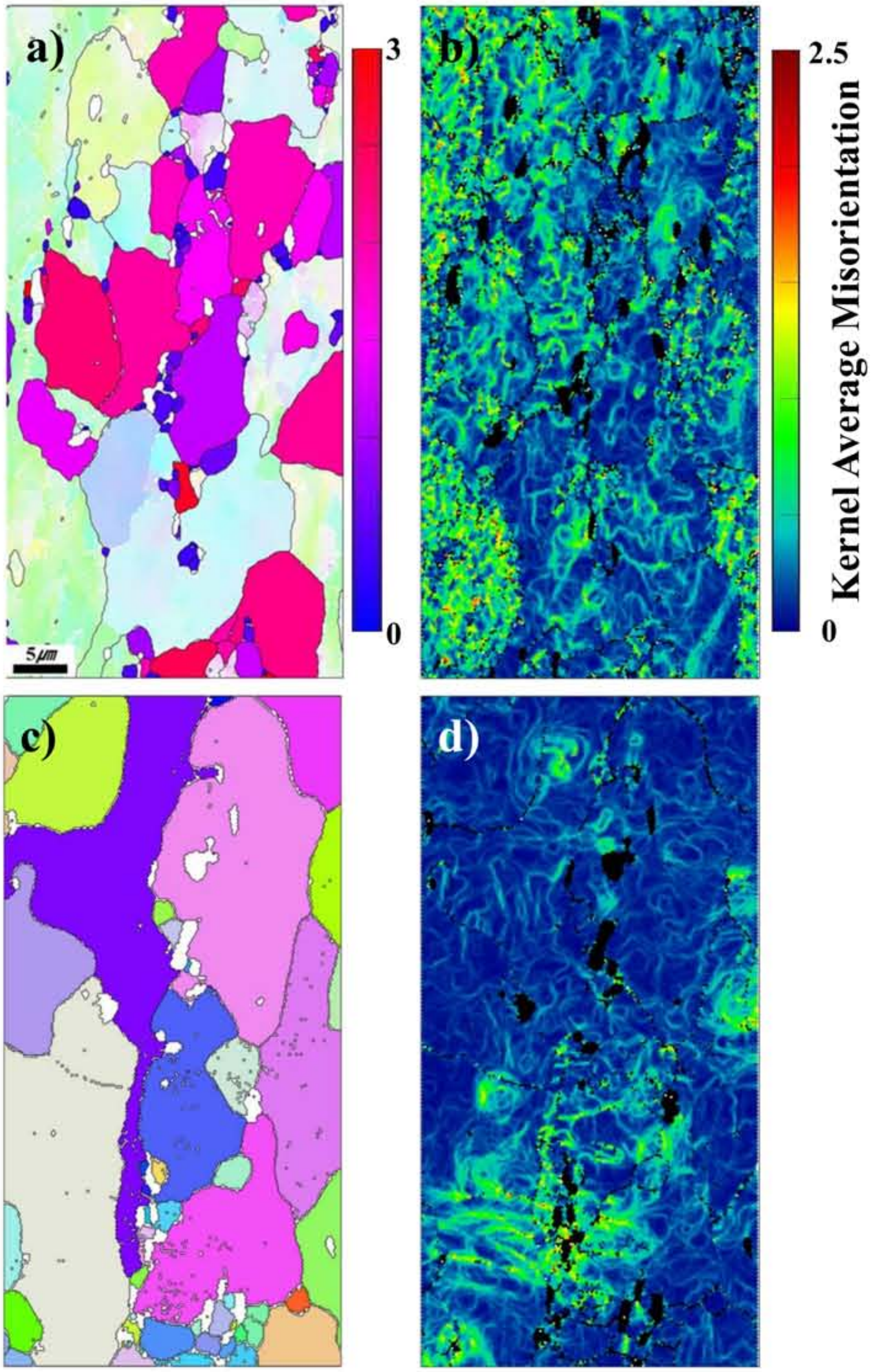

Figure 3.13: (a) Grain orientation spread (GOS) map overlaid with IPF map, (b, d) kernel average misorientation to the 1st neighbor with 2.5 ° threshold angle and (c) grain map in RB9 annealed at 350 °C for (a, b) 100s and (c, d) 1000s

3.4 Discussions

3.4.1 Effect of homogenization conditions

Homogenization treatment is generally conducted for improvement of the precipitation microstructure by controlling the size and distribution of constituent particles as well as the Mn supersaturation in the Al matrix, in which the coarse primary particles (>1 μm) promote recrystallization (Humphreys, 1977), while the dispersoids precipitated during homogenization suppresses recovery and recrystallization (Nes et al., 1985; Smith, 1945). When the higher level of Mn supersaturation is remained in the Al matrix after the homogenization, the precipitation and recrystallization would occur simultaneously during the annealing after cold rolling, which leads to the delay of recrystallization behavior. In the present study, two homogenization conditions were conducted in order to control the number density of constituent particles which influenced by different heating rates and holding times. The primary particles in the RA specimen homogenized at a slow heating rate of 50 °C/h increase in size with a decrease in number density, whereas the RB homogenized at a heating rate of 500 °C/h increased in the number density of primary particles by breaking up for spheroidization.

According to Li and Arnberg (2003a), the number density of the dispersoids increases with the heating temperature and reaches its maximum value at about 530 °C. The precipitation rate of the dispersoids is much faster than the growth rate of the primary particles, and a large number of dispersoids generated during heating have been found to decrease their volume fraction during holding at high temperatures (Li and Arnberg, 2003b). The constituent particles in the

AA3003 alloy show little change in the shape and size when heated below 300 °C, but the eutectic network of primary particles begins to break up above about 400 °C (Li and Arnberg, 2003b). Simultaneously, the supersaturated solid solution decreases the solubility of Mn in the matrix by precipitating the dispersoids of α-Al (Mn, Fe) Si phase when Mn begins to decompose (Li and Arnberg, 2003b; Song et al., 2018). Supersaturated Mn is expected to precipitate a significant dispersoids during heating under homogenization conditions of RA. Some of these dispersoids diffuse Mn into the primary particles due to re-dissolution during homogenization at high temperatures, which leads to the growth of the primary particles. On the other hand, the RB specimen is expected to significantly suppress the precipitation of dispersoids during heating due to the fast-heating rate of 500 °C/h. It is judged that this led to the destruction and size reduction of the primary particles during prolonged homogenization at high temperatures. Therefore, the change in the size and area fraction of constituent particles during homogenization occurs due to the precipitation of Mn in the supersaturated matrix during heating and re-dissolution of the dispersoids during homogenization at high temperatures, where the coarsening of the primary particles is greatly dependent on the precipitates generated during heating.

Fig. 3.14 shows a schematic model for precipitation and evolution of constituent particles under different homogenization conditions used in this work. Initial as-cast specimen is assumed to be rich in the supersaturated Mn atoms for precipitation, and the same distribution of Mn atoms. Supersaturated cast specimen can provide a large number of nucleation sites for precipitation under slow heating conditions (Fig. 3.14a). This is contrary to the fast-heating rate. The commercial as-cast AA3003 alloy containing Mn-bearing constituent particles is known to precipitate in the range of 350 °C to 530 °C during heating (Li and Arnberg, 2003a). Thus, a fast-heating rate will inhibit nucleation for precipitation. The particles precipitated by nucleation grow and rearrange at increased heating temperature, where the fine secondary particle evolve by dissolution and growth regardless of the heating rate. Therefore, when the homogenized at a slow heating rate, a large number of fine secondary particle can be generated, and they grow into various shapes including circular and long rod-shaped particles. On the other hand, when the homogenization temperature is reached by a fast-heating rate, the evolution microstructure consists of a few fine secondary particles, and most of the particles are dissolved and spheroidized (Fig. 3.1h).

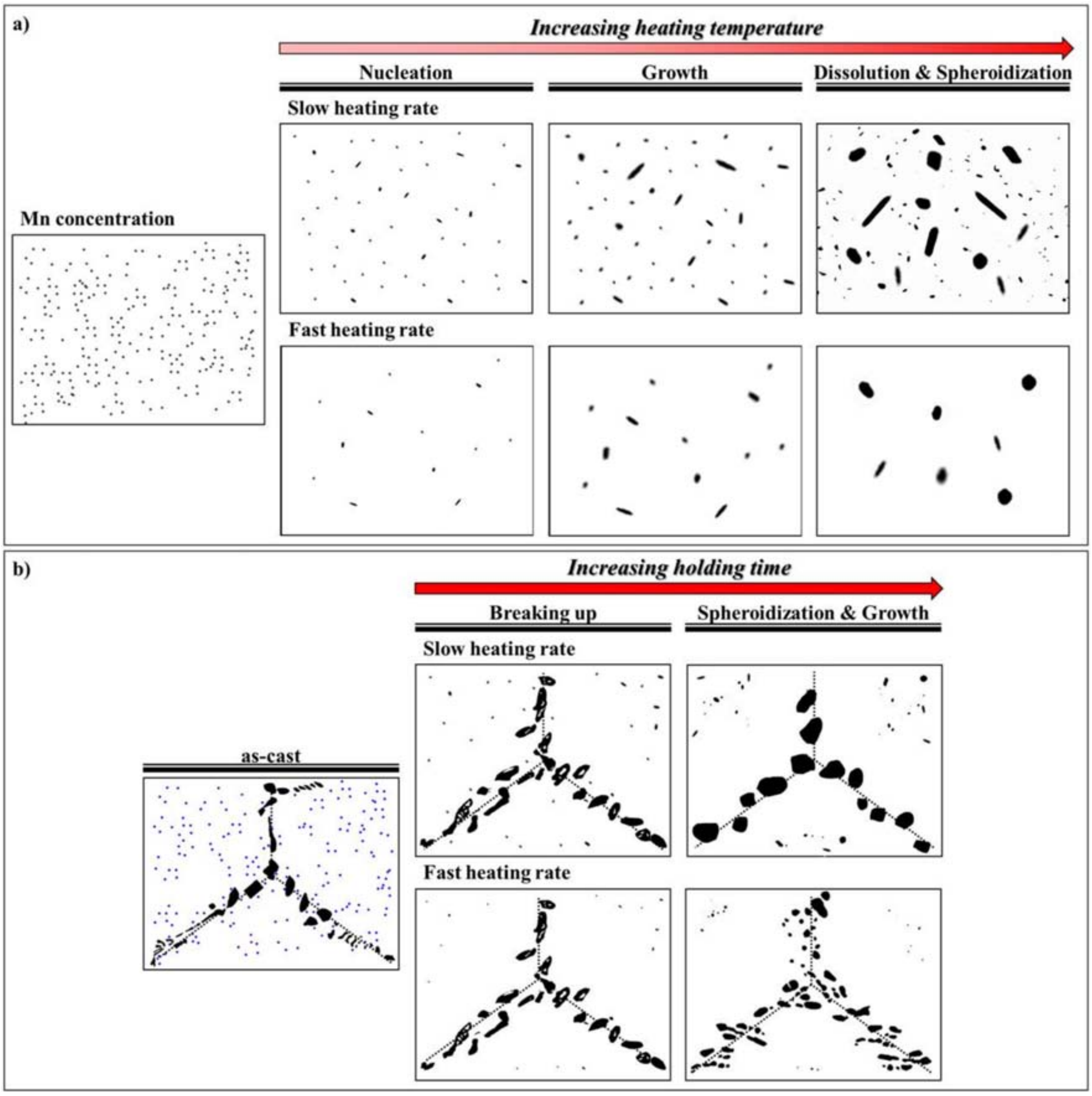

Figure 3.14: Schematic diagram of secondary particles precipitation and evolution of primary particles behavior during heating and holding

Considering the microstructure evolution by the fast-heating rate and long-term homogenization treatment, the homogenized RB specimen has a significant potential of precipitation due to the Mn diffusion during the annealing after cold rolling. Since the diffusion of solute and the precipitation of fine secondary particles can occur in preference to dislocation and boundary migration, the restoration process of the RB with relatively higher Mn concentrations may require greater thermal activation energy than that of the RA specimen.

Fig. 3.15 shows the dispersion structure in the fine dispersoids region of RA9 and RB9 during annealing at low temperature. Comparing the microstructure before/after annealing, RA9 shows almost the same distribution and size of secondary particles irrespective to the annealing process. On the other hand, RB9 clearly shows that the number density of very fine dispersoids increased due to the precipitation at the grain boundaries. In addition, the bright contrast of boundaries (white arrows) observed in Fig. 3.15b may be solute-rich regions. Therefore, the grain boundary has a role of the sink of supersaturated Mn atoms due to total energy reduction. Furthermore, by assuming the diffusion of the Mn solutes along the boundary, the Zener drag can also occur in LAGBs associated with the dislocation boundary during recovery, and HAGBs containing locally high concentrations of Mn can cause the greatest drag during recovery (Tangen et al., 2010). Due to the existence of the boundary with large misorientation angle, Zener drag effect is more enhanced at this boundary with the locally concentrated Mn atoms, which delays the recovery process. It is reported that the boundary composed of these high concentrations of Mn will delay recrystallization by acting as a nucleation site for the precipitation of fine particles during recrystallization (Chen et al., 2003). As a consequence, RB9 with the higher level of the Mn supersaturation exhibited a strong Zener drag effect during the recovery process and eventually resulted in the retardation of the recrystallization process by the precipitation of Mn-contained dispersoids at the boundary.

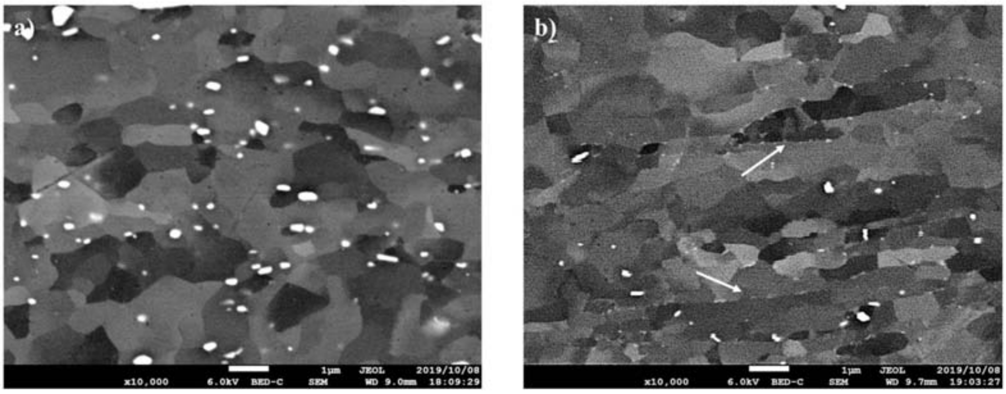

Figure 3.15: Microstructure evolution of the (a) RA9 and (b) RB9 annealed at 260 °C for 6h

3.4.2 Activation energy and triple junction motion

The largely deformed AA3003 alloys with different Mn concentrations and constituent particle characteristics differ in apparent activation energy due to different mechanisms operating during recovery. The initial recovery state is mainly accomplished by the annihilation and rearrangement of dislocations and boundary dislocations in the deformed grain, and the activation energy for this behavior is about 80 kJ/mol (Liu et al., 2002). The triple junctional motion that dominates the subsequently recovery behavior causes the migration of boundary for coarsening of the lamella structure, which can increase the activation energy due to the influence of the Zener drag effect by constituent particles and solutes.

The apparent activation energy for coarsening of the lamellar structure largely depends on the purity of the material, and high purity aluminum is known to be about 73 kJ/mol (Haessner and Schmidt, 1993). However, the AA3003 alloys containing Mn segregate the solute at the boundary during recovery and generate solute drag during boundary migration. Thus, the apparent activation energy can increase during recovery (Kuhlmann, 1948). The lattice and boundary diffusion of Mn solutes during annealing is generally considered the mechanisms for the mobility of the boundary (Humphreys et al., 2004). These mechanisms can be rationalized based on the high stored energy associated with dislocation density and microstructure characteristics of RA9 with low activation energy during recovery and recrystallization. Since the increase in dislocation density due to the area fraction, triple junction, and high-density constituent particles of HAGB is lead to the short diffusion distance and high driving force, the solute drag in the RA9 will be lowered during recovery compared to RB9. This can be supported by the resulting apparent activation energy for recovery. RA9 is about 124 kJ/mol, which is similar to the activation energy for self-diffusion of aluminum (Balluffi, 1970). whereas, the activation energy for recovery of RB9 is 193 kJ/mol, which is similar to the diffusion energy of manganese in aluminum (Bakker et al., 1990).

The triple junction motion during recovery behavior is the initial behavior to eventually reach recrystallization. A schematic diagram of continuous decrease in microhardness associated with annihilation and rearrangement of dislocations during annealing is shown in Fig. 3.16, where also shows a gradual evolving microstructure from lamellar structures to equiaxed crystal shapes through triple junction motion prior to nucleation for recrystallization. In this model, the triple junction connecting the three lamellar boundaries can increase the spacing of the boundary of adjacent lamellar. It can be seen that a gradual transition from the lamellar to equiaxed morphologies can be possible when the formation of the recrystallized nucleus is preceded.

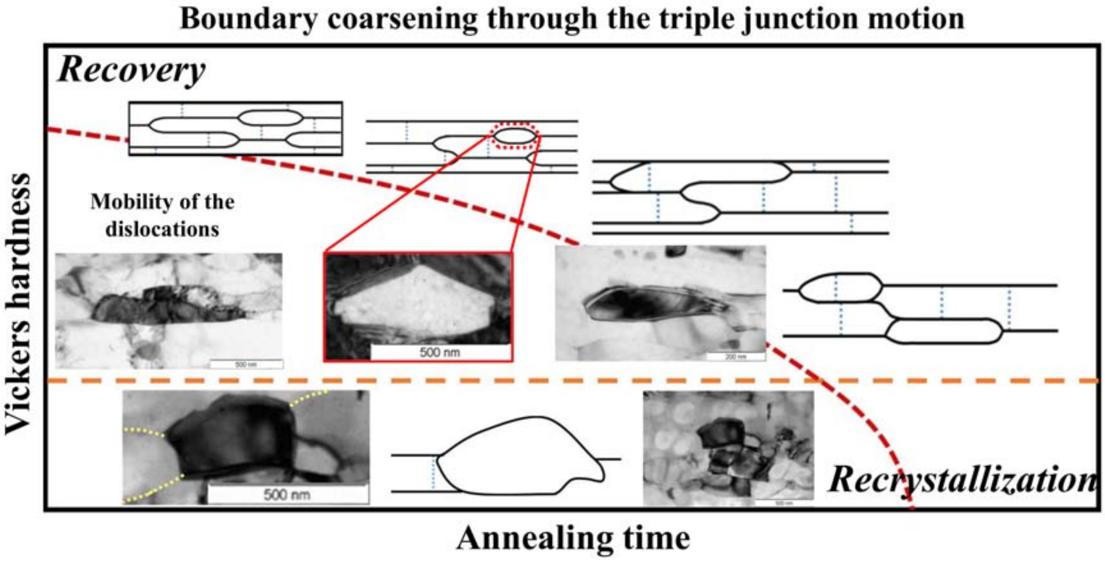

Figure 3.16: Schematic diagram showing a continuous decrease in the Vickers hardness and a gradual transition in the structure morphology during annealing of cold-rolled AA3003 aluminum alloy

3.4.3 Simultaneous recrystallization and precipitation

As compared with the relatively supersaturated RB9 specimens, large number density of dispersoids was observed in RA9 specimens by homogenization treatment with a smaller size of equiaxed recrystallized grain microstructure (Figs. 3.11 and 3.12). In addition, the time to complete the recrystallization of the RB9 specimen was considerably longer, which is caused by the segregation of Mn solute element and the concurrent precipitation.

Regarding the size of the recrystallized grain, the recrystallization is preferentially nucleated around the coarse constituent particles by PSN and grows to solute-free regions. Since the region of the recrystallized grains generated by PSN grow within the PFZ, growth of the recrystallized grains into the dispersoids region formed by homogenization is strongly suppressed (Fig. 3.11a). The growth of this primary recrystallization is believed to depend on the PFZ introduced by homogenization before cold rolling, where the shape and size of the recrystallized grains are due to the significantly wider PFZ and fewer dispersoids in RB9 than in RA9. In addition, it should be taken into account that the total driving pressure of RB9 for recrystallization associated with the dislocation density may be lower due to concurrent precipitation during recrystallization.

Fig. 3.17 shows the change in the area fraction of (a) primary particles and (b) fine secondary particle of the RA9 and RB9 during annealing at 350 °C, where the RA9 and RB9 are indicated by square and circle, respectively. When the recrystallization is completed, the primary particle fractions of RA9 and RB9 remain almost constant, as shown in Fig. 3.17a. This means that the growth of primary particles does not occur in the recrystallization regime due to solute depletion in the PFZ by homogenization. On the other hand, the changes in fine secondary particles show opposite trends in RA9 and RB9 (Fig. 3.17b). The RA9 sufficiently precipitated during the homogenization showed a constant area fraction until recrystallization was completed. This indicates that no precipitation occurred during the recrystallization. Whereas, the supersaturated RB9 maintains a constant at the beginning of annealing, and gradually increases in volume ratio at the point where recrystallization begins near the coarse precipitate (Fig. 3.13a). This means that recrystallization occurs in the area where the primary particles are clustered, while the precipitation behavior occurs preferentially in the region of the fine secondary particles prior to recrystallization. An area fraction of fine secondary particle similar to that of RA9 is reached by subsequent annealing, and recrystallization is completed at a similar point.

According to Somerday and Humphreys (2003), the temperature at which the supersaturated Al-Mn alloy recrystallization and precipitation occurs simultaneously was found to be between 350 °C and 400 °C. In this temperature range, primary recrystallization can be begun by PSN, but precipitation may simultaneously occur in the supersaturated region. Therefore, the recrystallization behavior may be inhibited in the dispersoids region during subsequent annealing. Although both precipitation kinetics and recrystallization kinetics are controlled by diffusion, they have different temperature dependences, and the driving force of precipitation at high temperatures decreases.

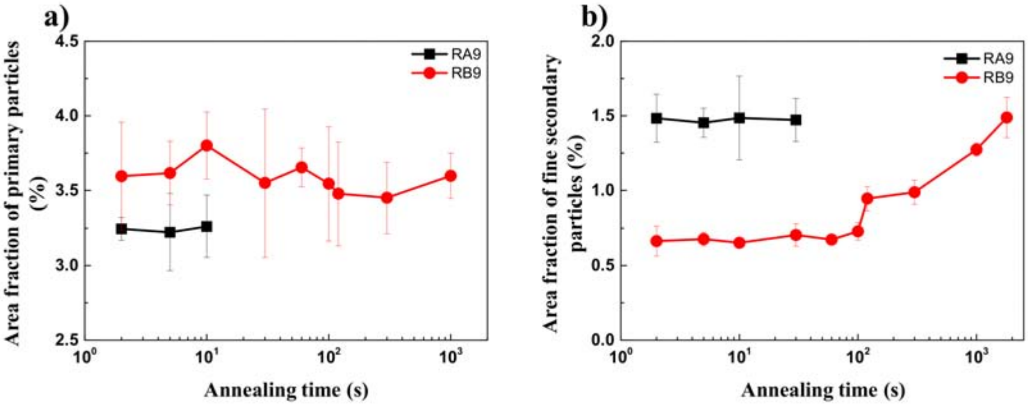

Figure 3.17: Area fraction of the (a) primary particles and (b) fine secondary particles of RA9 (square symbol with black color) and RB9 (circle symbol with red color) during annealing at 350 °C

The dislocation density introduced by cold rolling depends not only on the amount of plastic strain but also on the distribution and size of the constituent particles. Due to the presence of constituent particles, the migration of dislocations is prevented and dislocations accumulate locally around the particles, which leads to an increase in dislocation density (Ashby and Johnson, 1969; Humphreys et al., 2004). The accumulated dislocation provides energy for nucleation of recrystallization and precipitation during annealing.

Considering the restoration behavior in the PFZ and the dispersoids region, the recrystallization occurs preferentially in PFZ formed by the growth of coarse particles, but the precipitation behavior can occur first in the dispersoids region by supersaturated solutes and locally stored energy associated with the accumulated dislocation. This is evident when comparing the recrystallization behavior results of RA9 and RB9, and the difference in recrystallization kinetics between the two specimens from the change in Vickers hardness can be clearly identified.

The driving pressure for recrystallization is provided from the stored energy associated with the dislocation density, and the precipitation prior to recrystallization creates a Zener boundary pinning pressure. Precipitation occurs in the supersaturated matrix area, and sub-grains develop around the precipitated dispersoids. This phenomenon is observed in relatively supersaturated RB9, and the recrystallized grain grows in the rolling direction and appears as an elongated shape. Since the PFZ in the RB9 is wide, the degree of accumulation of dislocations around the primary particles is weak and the stored energy is in a low state. Consequently, Mn segregation acts strongly at the dislocation boundary, and boundary migration by the triple junction motion in the fine dispersoids region is suppressed. Considering that the magnitude of the residual stress occurring around the particle depends on the size and area fraction of the constituent particle (T. Mura, 1987), the supersaturated RB9 will have low stored energy even under the same reduction ratio conditions.

3.5 Conclusions

The effect of the homogenization condition on the microstructure evolution and kinetics during the recovery and recrystallization behavior of cold-rolled AA3003 alloy were investigated. The RB specimen homogenized with a fast-heating rate shows a significant lower number density of secondary particles, which is due to the suppression of the precipitation during homogenization as compared with the RA specimen with a slow heating rate. Electrical conductivity measurement revealed that the difference of the Mn supersaturation in RA9 and RB9 corresponds to a concentration of 0.11 wt.%Mn. The dislocation density introduced by cold rolling depends strongly on the size and the number density of constituent particles, where the number density of fine secondary particles has a significant effect on the inter-particle spacing and local dislocations of the lamella structure in the dispersoids region. These results suggest that the deformed microstructure as well as the magnitude of residual stress around the constituent particles can be controlled by homogenization conditions. By conducting annealing, the transition behavior from the recovery to the recrystallization in RA9 and RB9 was varied depending on the level of the Mn supersaturation, in which the recovery kinetics by triple junction motion was greatly retarded in RB9 due to the concurrent precipitation preferentially occurred at the dislocation boundary. Furthermore, accounting that the PFZ formed around the coarse primary particle in RB9, the dislocation density and the residual stress was locally changed to reduce the driving pressure for recrystallization in RB9, eventually, the recrystallization by PSN begins with the slower rate in RB9.

Chapter 4

Micromechanical analysis of residual stress around coarse precipitates under cold rolling condition

4.1 Introduction

In Chapter 3, the effect of the homogenization condition on the restoration behavior of commercial AA3003 aluminum alloy cold-rolled to a large strain was investigated. The microstructure controlled by the homogenization conditions, e.g., area fraction, number density and size of the constituent particles have a significant influence on the evolution of the dislocation and precipitation microstructure under the same magnitude of plastic strain. This reflects the suppression of the recovery and recrystallization kinetics due to the micro-segregation of Mn and the concurrent precipitation during annealing.

Supposing that the homogenized specimens were cold-rolled under the same reduction ratio, the increased number of the fine secondary particles formed during the homogenization with the slow heating rate enables to increase the magnitude of the stress disturbance around the constituent particles during the plastic deformation, which leads to the increase of the dislocation density and the formation of a thinner lamellar structure along the rolling direction. In addition, the spheroidized primary particles inhibiting the dislocation motion can also act as the accumulation site of the local dislocation density. During the recovery, the lamellar microstructure induced by the severe plastic deformation will be changed into the fine equiaxed one through the triple junction motion mechanism, where the migration of the boundary is delayed by the supersaturated Mn in Al matrix. Although the primary recrystallization preferentially would occur around the coarse particles by particle stimulation nucleation (PSN) at the particle-free zone (PFZ), the recrystallization would be delayed at the region of the dense dispersoids. These results implies that the microstructure evolution during the plastic deformation and subsequent annealing is strongly dependent on the homogenization condition. That is, both of the Mn supersaturation and the distribution of the constituent particles changes the work hardening and the restoration process of dislocations.

In Chapter 2, the influence of the cold rolling on the recrystallization behavior of commercial DC-cast AA3003 aluminum alloys is discussed, where the microstructure change associated with the reduction rate was discussed in terms of dislocation density. The region of the recrystallization introduced by particle-stimulated nucleation (PSN) was mostly investigated through the observation of the texture by EBSD (Nes and Embury, 1975) and the surrounding deformed microstructure and dislocation density by FE-SEM/BEI and TEM (Tangen et al., 2010). Humphreys (1979a) and Huang et al. (2000) studied the influence of coarse precipitates on the recrystallization behavior of aluminum and its alloys during isothermal annealing and reported that the deformed structures around the coarse particles can be classified into two categories. The characteristic deformed microstructures observed around precipitates in cold-rolled AA3003 aluminum alloy are shown in Fig. 4.1. The first type of structure consists of distorted zones formed above and below the coarse particles, which are generally observed as an elongated shape almost parallel to the rolling direction. The second type of microstructure is the rotated zone, which is observed in fine equiaxial shapes on the left and right sides of coarse particles. Such rotated zone induced by high level of locally stored energy are accompanied by a refined sub-grain structure and high lattice rotation. Rotated zones associated with the PSN effect are expected to exhibit a rapid migration of dislocations and boundaries during annealing at certain temperatures, leading to the relaxation of residual stress and the nucleation of recrystallization. De Siqueira et al. (2013) revealed that the PSN effect caused by rotated zones occurs not only in aluminum alloy, but also in stainless steels. Because residual stress analyses based on the Eshelby tensor model enables one to determine the disturbance of the external/internal strain (or stress) field around an inhomogeneity (Shibata et al., 1992; Muraishi and Taya, 2020), the behavior of deformed zone under cold rolling can be discussed in terms of the local plastic strain around the coarse precipitate. Such a theoretical assessments based on the inhomogeneity problem can be extended to clarify the effect of PSN on the recrystallization behaviors in aluminum alloys (She et al., 2019; Humphreys, 2000) and steel materials (De Siqueira et al., 2013).

The Eshelby inclusion method (J. D. Eshelby, 1957, 1959) or elastic fields inside and outside ellipsoidal inclusions has been widely accepted in materials science and engineering; in particular, this method has been principally used to solve the inclusion and inhomogeneity problems in metal matrix composites (Sharma, 2000; Garces et al., 2006; Li et al., 2007), and structural and nanostructured materials (Patton et al., 1998; Muraishi, 2016; Muraishi and Taya, 2019). Eshelby found that the elastic strain (and stress) inside the ellipsoidal inclusions is uniform when a homogeneous eigenstrain is applied to an inclusion, indicating that the disturbance of the stress and strain inside and outside the inhomogeneity can be solved via the Eshelby tensor when the fictitious eigenstrain is determined under external loading conditions. According to the micromechanical theory presented by T. Mura (1987), Eshelby tensors provide an explicit solution for the internal stress field of various morphology of ellipsoidal inclusions with various morphologies when the eigenstrain is correctly chosen. Numerous studies have explored the morphology of ellipsoidal inclusions in terms of the Eshelby tensor for inclusions associated with particles (Robson, 2016), fibers (Joffre et al., 2014), pores (Chiang, 2007), and cracks (Healy et al., 2006), where the elastic constants differ from those of the matrix phase. In addition, the Eshelby tensors for non-ellipsoidal inclusions, such as helical (Muraishi and Taya, 2019) or star-shaped inclusion (T. Mura., 1997), have been reported in recent papers.

In this study, in order to estimate the stress disturbance around an inhomogeneity under cold rolling process, the internal stress and strain around an inhomogeneity under external cold rolling conditions are explicitly determined by means of the Eshelby method. The computed elastic fields inside and outside the inhomogeneity were compared with the deformed microstructure around an α-Al(Mn, Fe)Si precipitate in cold rolled AA3003 aluminum alloys. The strain inside the α-Al(Mn, Fe)Si particle was determined by applying the interior-point Eshelby tensor, S, proposed by T. Mura. (1997), and the strain outside the precipitate was analytically computed by the exterior point Eshelby tensor derived by Ju and Sun (1999, 2001).

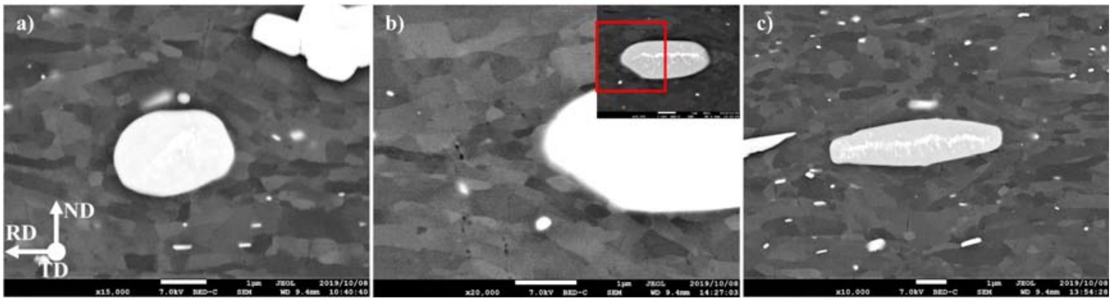

Figure 4.1: Micrograph showing a deformation zone around an α-Al(Mn, Fe)Si particle with an aspect ratio of approximately (a) 1.0, (b) 2.0 or (c) 4.0 formed during cold rolling in the AA3003 aluminum alloy. The nominal strain of the cold rolled specimen is assumed to be 0.9.

4.2 Geometry of inhomogeneity

To theoretically assess the spatial distribution of internal stress around an inhomogeneity under cold rolling conditions, an Al-Mn alloy system was chosen as the model case. Although the Al_6Mn phase is stable in binary Al-Mn system, the Al_6Mn phase (orthorhombic) can be transformed into α-Al(Mn, Fe)Si (cubic structure) in Al-Mn-Si alloy system during homogenization treatment (Li and Arnberg, 2003a). Therefore, α-Al(Mn, Fe)Si particles are the major precipitates in cold-rolled AA3003 aluminum alloy.

As shown in Fig. 4.1, the shape of the α-Al(Mn, Fe)Si precipitate can be approximated by an ellipsoidal inhomogeneity in order to apply the analytical solution of the Eshelby model. The computation model for ellipsoidal inhomogeneities in a x_1-x_2-x_3 coordinate system is illustrated in Fig. 4.2. To compute the Eshelby tensor, ellipsoidal inhomogeneities are distinguished by the aspect ratio, $\alpha = a \;/\; c$. The semi-axis lengths a, b and c of the ellipsoids are defined in the direction parallel to the x_1, x_2 and x_3 axes, respectively. The length of semi-major axis for the prolate spheroid, a, is perpendicular to the compressive strain axis of the cold rolling.

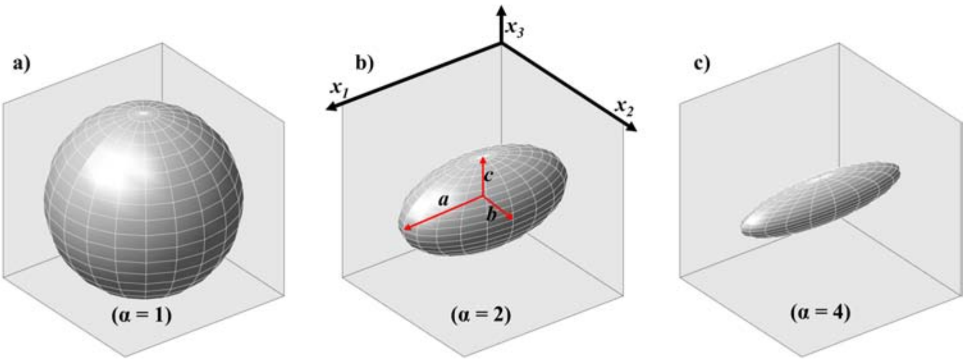

Figure 4.2: Three types of ellipsoidal precipitates aligned with semi-axes a, b and c parallel to coordinate axes x_1, x_2 and x_3, respectively. (a) Sphere with a / c = 1.0 ($a = b = c$), and Prolate spheroid with a / c = 2.0 (b) and 4.0 (c) ($a > b = c$)).

4.3 Eshelby inhomogeneity problem under external strain

Let us consider a region of ellipsoidal inhomogeneity **Ω** embedded in an infinite elastic solid matrix D, where the stiffness of the inclusion differs from that of the matrix phase. Assuming that the external strain is applied at an infinitely far point (remote strain), the stress and strain disturbances around the inhomogeneity **Ω** can be solved by the equivalent inclusion method, where the stress inside **Ω** for the inhomogeneity and the equivalent inclusion can be expressed as follows

(Ju and Sun, 1999):

$$\sigma_{ij} = C^*_{ijkl}(\varepsilon^0_{kl} + \tilde{\varepsilon}_{ij}) = C^*_{ijkl}(\varepsilon^0_{kl} + S_{klmn}\varepsilon^*_{mn}) \tag{4.1}$$

$$\sigma_{ij} = C_{ijkl}(\varepsilon^0_{kl} + \tilde{\varepsilon}_{ij} - \varepsilon^*_{kl}) = C_{ijkl}(\varepsilon^0_{kl} + S_{klmn}\varepsilon^*_{mn}) \tag{4.2}$$

where, ε^0_{ij} is the applied strain, $\tilde{\varepsilon}_{ij}$ is the disturbed strain caused by the inhomogeneity, S_{klmn} is the Eshelby tensor, ε^*_{mn} is a fictitious eigenstrain for equivalent inclusion system, and C_{ijkl} and C^*_{ijkl} are the stiffness of the matrix and the inhomogeneity, respectively. Based on the equality of the stress in Eq. (4.1) and (4.2), a relationship between the eigenstrain and the applied strain is obtained:

$$(S_{klmn} + (C^*_{klij} - C_{klij})^{-1}C_{ijmn})\varepsilon^*_{mn} = -\varepsilon^0_{pq} \tag{4.3}$$

In general, the Eshelby tensor for interior and exterior points can be solved by integrating with respect to $|\Omega|$ as follows (J. D. Eshelby, 1959; Muraishi, 2016; Muraishi and Taya, 2019; T. Mura, 1987):

$$\begin{aligned}\tilde{\varepsilon}_{ij}(x) =& S_{ijmn}(x)\varepsilon^*_{mn} \\ =& \frac{1}{2}\int_{|\Omega|}\{C_{pqmn}\varepsilon^*_{mn}(x')G_{ip,q}(x-x')n_j \\ &+ C_{pqmn}\varepsilon^*_{mn}(x')G_{jp,q}(x-x')n_j\}dS(x')\end{aligned} \tag{4.4}$$

where $G_{ij,k}$ is first derivative of Green's function, n_i is outward normal vector of the surface $|\Omega|$.

According to the theory of micromechanics (T. Mura, 1987, p.74), the strain and stress inside $|\Omega|$ becomes uniform inside the ellipsoidal inclusion when a homogenous eigenstrain is assumed in D, where the analytical solution of the interior-point Eshelby tensor $\boldsymbol{S}$ for the ellipsoidal inclusion depends on the inclusion shape and Poisson's ratio. For a field point x outside Ω, the solution of the exterior-point Eshelby tensor in Eq. (4.4) becomes a field function, which is distinguished from the interior-point Eshelby tensor, $\boldsymbol{S}$. In the present study, the analytical solution of the Eshelby tensor was adopted to compute of the stress strain at the exterior-point (Ju and Sun, 1999). To avoid the confusion between the analytical solutions, the interior- and exterior-point Eshelby tensors are denoted as $\boldsymbol{S}$ (T. Mura, 1987) and $\overline{\boldsymbol{G}}$ (Ju and Sun, 2001), respectively.

Once the eigenstrain under the external strain condition is solved in Eq. (4.3), the strain field outside the inclusion can be derived from the exterior-point Eshelby tensor as follows:

$$\varepsilon_{ij}(x) = \varepsilon^0_{ij} + \overline{G}_{ijmn}(x)\varepsilon^*_{mn}, \qquad x \in D - \Omega \tag{4.5}$$

Explicit expressions of the exterior-point Eshelby tensors $\overline{\boldsymbol{G}}$ have been given by Ju and Sun (1999, 2001).

In present study, the strain fields inside and outside a precipitate embedded in an aluminum matrix were computed by analytical solutions of the Eshelby tensor (T. Mura, 1987; Ju and Sun, 1999, 2001)to demonstrate the disturbance of the external elastic field around the precipitate. Because precipitates in AA3003 aluminum alloy are generally observed as the spheres or prolate spheroids, this work considers two types of ellipsoidal inclusion models; one for a sphere (semi-axis, a = b = c) and one for a prolate spheroids (semi-axis, $a > b = c$), where the semi-major axis a is aligned in the x_1 axis direction (Fig. 4.2). The elastic properties of the materials are listed in Table 4.1. Data for the elastic strain components were calculated under an applied strain, with $\varepsilon^0_{11} = -\varepsilon^0_{33} = 1.0$, $\varepsilon^0_{22} = 0$ as the representative value. The external strain field around the precipitates was computed using three-dimensional (3D) Eshelby inclusion model proposed by Healy et al. (2006).

The strain field distributions for ε^0_{11}, ε^0_{33} and ε^0_{12} on the cross-section of the precipitate (x_1-x_3 plane) were obtained as density plots. For 3D strain fields, the isosurfaces of the strains normalized by the absolute values of positive (red) and negative (blue) strain were represented by 3D graphics using MATLAB surface and patches function.

Table 4.1: Young's modulus and Poisson's ratio for an aluminum matrix with an α-Al(Mn, Fe)Si precipitate. The subscripts m and p indicate the matrix phase and the precipitate, respectively.

Constant	Value	Source
E_m	69.0GPa	Kaufman (1999)
ν_m	0.33	
E_p	175.0GPa	Chen et al. (2010)
ν_p	0.28	assumed

4.4 Results

4.4.1 Estimation of fictitious eigenstrain under external strain

When considering the plastic deformation of a sheet material under the cold rolling, the magnitude of the applied strain along the transvers direction (ε_{22}) can be regarded as zero (plane strain condition). Therefore, the applied strains in the rolling direction (ε_{11}) and normal direction (ε_{33}) satisfies, $\varepsilon_{11} + \varepsilon_{33} = 0$, due to the conservation of volume. The other strain components can be expressed as $\varepsilon_{23} = \varepsilon_{13} = \varepsilon_{12} = 0$, on average. The strains components in x_1-x_2-x_3, coordinates are illustrated in Fig. 4.3a.

The change in fictitious eigenstrain inside the precipitate is presented in Fig. 4.3b as a function of the aspect ratio, where the fictitious eigenstrain components were computed by Eq. (4.3) under an applied strain of $\varepsilon_{11}^{0} = -\varepsilon_{33}^{0} = 1.0$, $\varepsilon_{22}^{0} = 0$. The absolute value of the eigenstrain ε_{mn}^{*} tends to increase with increasing aspect ratio, particularly for ε_{11}^{*}, which influences the values of the shape-dependent Eshelby tensor for a prolate spheroid. The values of the fictitious eigenstrains yield $\varepsilon_{33}^{*} = -\varepsilon_{11}^{*} = 0.9266$, ε_{22}^{*} as zero. When the aspect ratio is increased to 10.0, the magnitude of the eigenstrain associated with the long axis of the prolate spheroid, ε_{11}^{*}, increases to -1.4802, while that for the prolate short axes vary depending on the orientation of the prolate spheroid, with $\varepsilon_{22}^{*} = 0.2352$ and $\varepsilon_{33}^{*} = 1.0472$. The detailed cold rolling conditions used in this study are discussed in the next section.

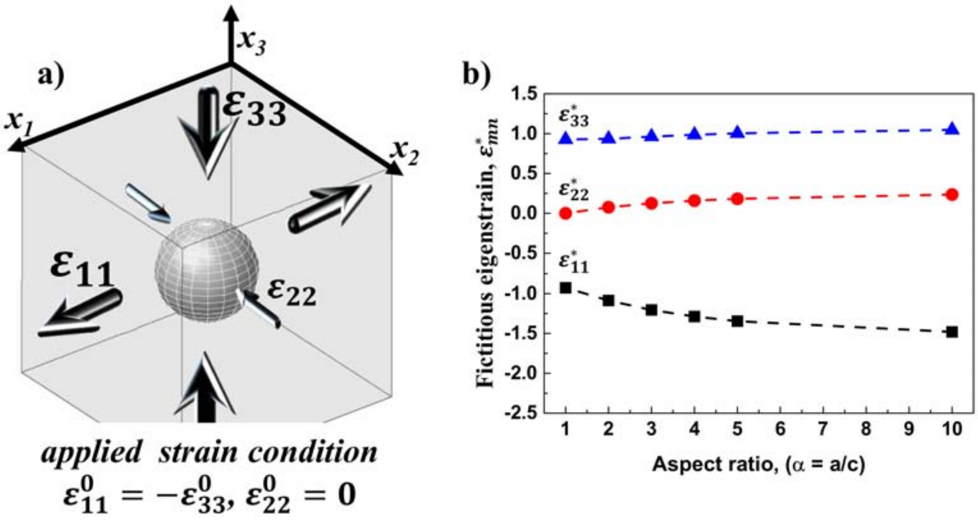

Figure 4.3: (a) Schematic of ellipsoidal inhomogeneity and applied strains assumed in present study ($\varepsilon_{11}^{0} = -\varepsilon_{33}^{0}$, $\varepsilon_{22}^{0} = 0$), (b) Change in the fictitious eigenstrains as a function of aspect ratio, α (a / c).

4.4.2 Disturbance of stress and strain inside inhomogeneity

The stress σ_{ij} and disturbed strain $\tilde{\varepsilon}_{ij}$ inside inhomogeneity Ω were computed for the different inhomogeneity shapes, as shown in Fig. 4.4. The condition of applied strain is similar to that for Fig. 4.3: $\sigma^0_{11} = -\sigma^0_{33} = 1.0$, $\sigma^0_{22} = 0$. The stress disturbance can be regarded as the residual stress since the applied strain σ^0_{ij} in matrix phase is plastic strain. The strain components determined for the spherical precipitate are given in Table 4.2. The stress and strains inside the precipitates are obtained for a sphere and prolate spheroid, where the values are shown by squares for σ_{11} and ε_{11}, circles for σ_{22} and ε_{22}, triangles for σ_{33} and ε_{33}, respectively. The stress and the disturbed strain inside inhomogeneity Ω were computed by Eq. (4.1).

Table 4.2: Stress and strain components computed for the spherical precipitate ($\alpha = 1.0$) under cold rolling condition, $\varepsilon^0_{11} = -\varepsilon^0_{33} = 1.0$, $\varepsilon^0_{22} = 0$. Fictitious eigenstrain, ε^*_{mn} (Eq. (4.3)), the disturbed strain inside Ω, $\tilde{\varepsilon}_{ij} = S_{klmn}\varepsilon^*_{mn}$ (Eq. (4.1)) and stress inside Ω, σ_{ij}, (Eq. (4.1)) are represented.

Fictitious eigenstrain, ε^*_{mn}		
ε^*_{11}	ε^*_{22}	ε^*_{33}
-0.9266	$<10^{-16}$	0.9266
Strain disturbance, $\tilde{\varepsilon}_{ij}$		
$\tilde{\varepsilon}_{11}$	$\tilde{\varepsilon}_{22}$	$\tilde{\varepsilon}_{33}$
-0.4334	$<10^{-16}$	0.4334
Stress inside inhomogeneity, σ_{ij} / GPa		
σ_{11}	σ_{22}	σ_{11}
77.47	$<10^{-14}$	-77.47

Fig. 4.4 clearly shows that the stress and strain are strongly influenced by the inhomogeneity aspect ratio. For a spherical precipitate ($\alpha = 1$), $\tilde{\varepsilon}_{11}$ and $\tilde{\varepsilon}_{33}$ have the same magnitude with opposite signs,

which is due to the fictitious eigenstrain under the applied strain, as mentioned for Fig. 4.3. As the aspect ratio increases, the magnitude of $\tilde{\varepsilon}_{11}$, which is associated with the long axis of the prolate spheroid, decreases to zero, implying that the prolate spheroid is forcibly confined by the matrix phase. In contrast, the values of $\tilde{\varepsilon}_{22}$ and $\tilde{\varepsilon}_{33}$, which are associated with the prolate short axes, decrease slightly as the aspect ratio increases. Consequently, as shown in Fig. 4.4b, the stress inside the inhomogeneity deduced from Eq. (4.1) suggests the presence of plane stress with respect to the transverse-direction cross section (σ_{22} = 0), where the tensile stress of σ_{11} is continuously increases with increasing of aspect ratio under cold rolling conditions.

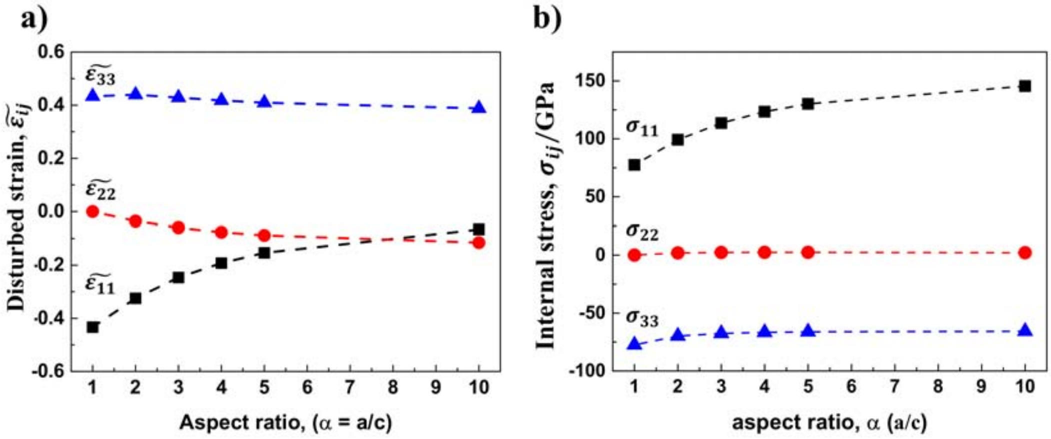

Figure 4.4: Respective strain disturbance (a) and stress (b) inside Ω as a function of aspect ratio under cold rolling conditions.

4.4.3 Elastic strain field around an isolated precipitate

The effect of the aspect ratio on the elastic field outside an α-Al(Mn, Fe)Si precipitate embedded in an aluminum matrix was investigated under plane strain compression conditions. The disturbance of normal and shear strains ($\tilde{\varepsilon}_{11}$, $\tilde{\varepsilon}_{33}$ and $\tilde{\varepsilon}_{12}$) are shown in Fig. 4.5, 4.6, and 4.7, respectively. The strain fields were computed from Eq. (4.5) for an applied strain of $\varepsilon^0_{33} = \varepsilon^0_{11} = -1.0$, $\varepsilon^0_{22} = 0$. Three models with different aspect ratios ($\alpha = 1$, 2 and 4) were used, where the inclusion geometry is consistent with that represented in Fig. 4.2. Because the magnitudes of the stresses and strains inside inhomogeneity are proportional to the applied strain in Eq. (4.3), the computed results are plotted as normalized values, $\varepsilon_{ij}/\varepsilon^0_{11}$. Tensile and compressive strain fields near the ellipsoidal precipitates are indicated in red and blue, respectively.

The effect of the aspect ratio on the strain field for $\tilde{\varepsilon}_{11}$ around the precipitate is shown in Fig. 4.5 as two-dimensional (2D) contours (a, b, and c) and 3D isosurface plots (d, e, and f). The isosurfaces for a given magnitude of compressive and tensile strain are indicated by blue and red, while that for zero strain is distinguished by hyperbolas (yellow) in the 3D plot (d, e, and f). Notably, the values of the strain disturbance inside the inhomogeneity in Fig. 4.5 are consistent with that presented in Fig. 4.4a. The 2D and 3D plots show that the external strain fields are disturbed by the precipitates, in which the tensile strain (indicated by red) appears in the vicinity of the precipitate along the x_1 axis. A high-magnitude of tensile strain with a penny shaped symmetry appears at a point slightly away from the precipitate parallel to x_3 axis, which is only observed for the spherical precipitate (Fig. 4.5a and d). Compressive strain (blue) appears at both ends of the ellipsoid precipitate parallel to the x_3 axis (Fig. 4.5a, b and c); specifically, the compressive strain exhibits a donut-shaped symmetry surrounding the surface of the ellipsoid precipitate with respect to the x_3 axis (Fig. 4.5d, e and f). The maximum strain magnitude is observed for the sphere ($\alpha = 1$), which decreases as α increases. The tensile component becomes dominant in the strain disturbance as the aspect ratio increases over the entire volume, and the region of high-magnitude tensile strain is concentrated at both ends of the ellipsoidal precipitate parallel to the x_1 axis (Fig. 4.5c).

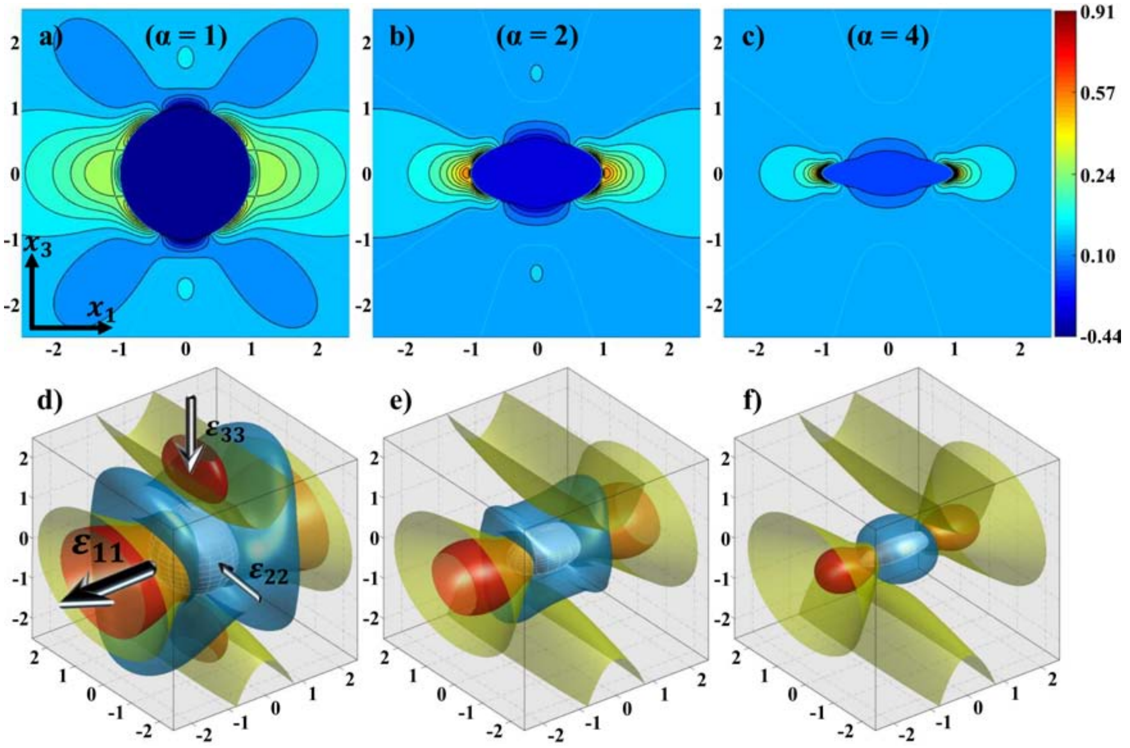

Figure 4.5: Strain disturbance, $\tilde{\varepsilon}_{11}$, around an inhomogeneity under cold rolling conditions for an aspect ratio of $\alpha = 1.0$ (a, d), 2.0 (b, e), or 4.0 (c, f).

The strain disturbance around the precipitate under applied strain along the x_3 axis is important when considering the stress accumulation and relaxation around precipitate in a cold-rolled specimen. The strain disturbance for $\tilde{\varepsilon}_{33}$is represented in 2D contour plots (Fig. 4.6a, b, and c) and 3D isosurface plots (Fig. 4.6d, e, and f). Notably, the strain disturbance values inside the inhomogeneity in Fig. 4.6 are consistent with those presented in Fig. 4.4a.The tensile strain is substantially lower, as indicated in red (positive), and its magnitude decreases with increasing aspect ratio, as shown in Fig. 4.6a-c. In particular, when the aspect ratio is increased to 4.0, the strain gradient and its magnitude around the precipitate (indicated in yellow in Fig. 4.6) disappear, as shown in Fig. 4.6c, even though the tensile strain is concentrated at both sides of the precipitate on the x_1 axis.

The 3D isosurface plots show that the maximum values of the tensile and compressive strain occur for the spherical precipitate. A donut-shaped (Fig. 4.6d and e) and lip-shaped (Fig. 4.6f) region of tensile strain appear around the equator of the ellipsoidal precipitate, while the compressive strain exhibits a penny shape at the ends of the precipitate along the x_1 axis, which becomes smaller as the aspect ratio increases (Fig. 4.6c and f). For the ellipsoidal precipitate with the same semi-axis lengths, shown in Fig. 4.6, an increase in the aspect ratio along the x_1 direction ($\alpha > 1$) resulted in a lower strain magnitude around the precipitate (Fig. 4.6e and f). The stress disturbance along the longitudinal direction of the inhomogeneities is discussed in greater detail in Section 4.4.4

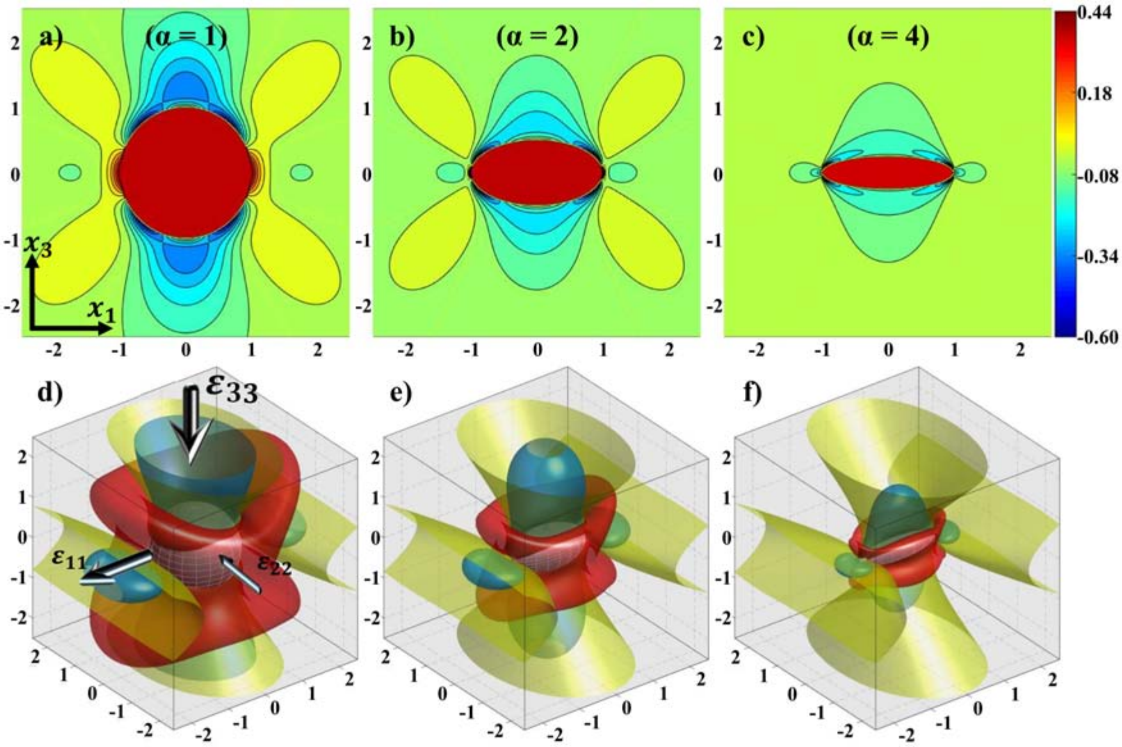

Figure 4.6: Strain disturbance, $\tilde{\varepsilon}_{33}$, around the inhomogeneity under cold rolling conditions for an aspect ratio of α = 1.0 (a, d), 2.0 (b, e), or 4.0 (c, f).

Although the applied strains for shear components can be assumed as zero on average, shear strain appears locally around the inhomogeneity, even for normal applied strains. This fact may be important when considering the deformation zone that accompanies lattice rotation and dislocation accumulation near the precipitate in later sections. The shear strain disturbance for $\tilde{\varepsilon}_{13}$, around a precipitate under cold rolling conditions is shown in 2D (Fig. 4.7a, b and c) and 3D (Fig. 4.7d, e and f) plots. The maximum strain disturbance is observed for the spherical precipitate, where a high-magnitude shear strain with a negative sign appears at both ends of the precipitate, as shown in blue; moreover, the magnitude of the shear strain decreases with increasing aspect ratio (Fig. 4.7b and c). In the 3D isosurface plots, a negative shear strain is distributed around the precipitate with a cubic shape (Fig. 4.7d and e). When the aspect ratio is increased to $\alpha = 4.0$, the region of compressive strain becomes smaller and the compressive strain magnitude is decreased, while the tensile strain is dominant around the prolate precipitate (Fig. 4.7c and f).

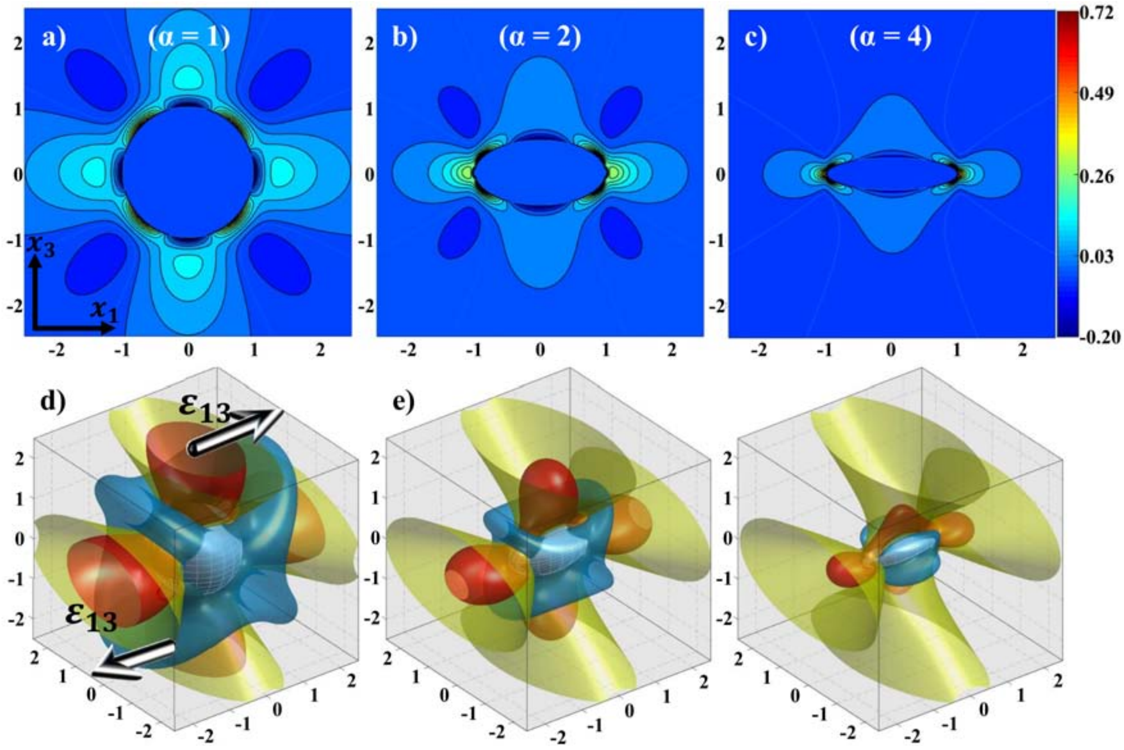

Figure 4.7: Strain disturbance, $\tilde{\varepsilon}_{13}$, around an inhomogeneity under cold rolling conditions for an aspect ratio of $\alpha = 1.0$ (a, b), 2.0 (b, e), or 4.0 (e, f).

4.4.4 Line profiles of strain disturbance inside and outside the precipitate

As shown by the 2D contour plots in Figs. 4.5–4.7,the normal and shear strains inside the precipitate are uniform and vary with the aspect ratio (α) of the precipitate. Based on the 2D results computed for the x_1-x_3 plane (Section 4.4.3), the local strain disturbance on the x_1

axis ($x_2 = x_3 = 0$) is plotted for inhomogeneities with different aspect ratios in Fig. 4.8. The applied strain condition is the same as that for Figs. 4.3–4.7: $\varepsilon^0_{11} = \varepsilon^0_{33} = 1.0$, and $\varepsilon^0_{22} = 0$. It has been shown that the strain magnitude outside the precipitate increases as the observation point approaches the interface (—x_1 / a— = 1.0), where the maximum normal strains values are $\tilde{\varepsilon}_{11} = 0.326$ $\tilde{\varepsilon}_{22} = -0.129$ and $\tilde{\varepsilon}_{33} = 0.433$ for a spherical precipitate (Fig. 4.8a). However, the values of $\tilde{\varepsilon}_{11}$ and $\tilde{\varepsilon}_{22}$ decrease to 0.063 and -0.011, respectively, at the interface between the matrix and precipitate. As the aspect ratio increases from a sphere to a prolate shape, the strain magnitude is greatly increased to $\tilde{\varepsilon}_{11} = 0.908$ and $\tilde{\varepsilon}_{22} = -0.313$, as shown in Fig. 4.8c. Compared with the strain disturbance shown in Fig. 4.8a and c, the maximum value of $\tilde{\varepsilon}_{11}$ is higher for the prolate spheroid, which is consistent with the results shown in Fig. 4.3a. It should be noted that although the Eshelby tensor is shape-dependent and the stress distributions outside the inhomogeneity are similar, the strain for the prolate spheroid increase sharply at the interface because the strain gradient is proportional to the length of the inhomogeneity.

For the shear strain, the maximum values for a sphere are $\tilde{\varepsilon}_{23} = -0.209$, $\tilde{\varepsilon}_{13} = -0.172$ and $\tilde{\varepsilon}_{12} = 0.227$ (Fig. 4.8d). When the aspect ratio increased to $\alpha = 4$, the shear strain magnitude increased to $\tilde{\varepsilon}_{23} = -0.167$, $\tilde{\varepsilon}_{13} = 0.508$ and $\tilde{\varepsilon}_{12} = 0.606$ (Fig. 4.8f). Clearly, the sign of $\tilde{\varepsilon}_{13}$ changes to positive at the interface of the inhomogeneity as the aspect ratio increases.

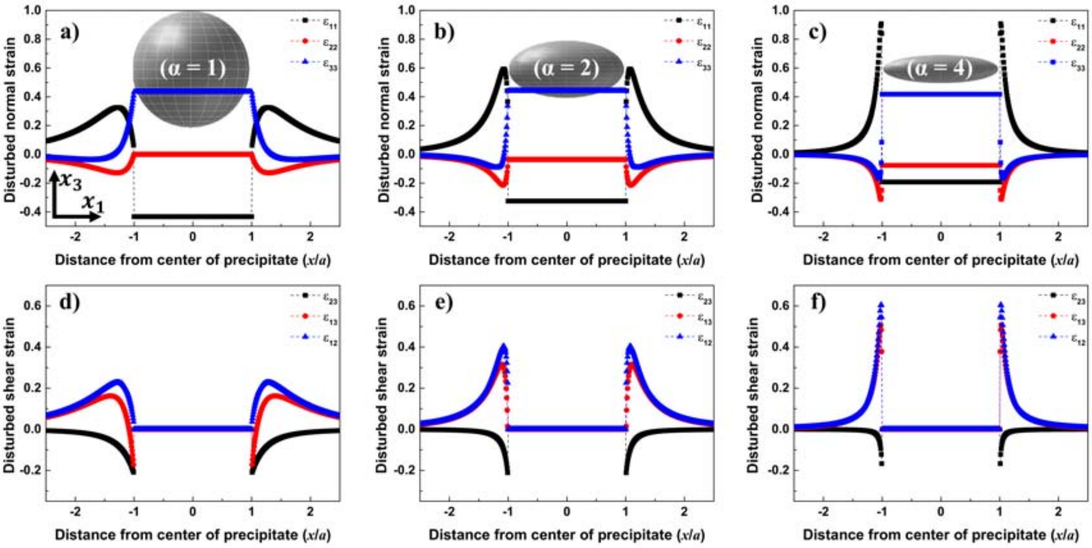

Figure 4.8: Line profiles for normal and shear strain disturbances along x_1 direction for an aspect ratio of $\alpha = 1.0$ (a, d), 2.0 (b, e), or 4.0 (c, f).

4.4.5 Equivalent stress around an isolated precipitate

To predict the region of a deformation zone near a precipitate, the residual stress is evaluated by the equivalent stress, σ_{eqv}, which is defined as follows:

$$\sigma_{eqv} = \sqrt{\frac{1}{2}[(\sigma_{11} - \sigma_{22})^2 + (\sigma_{22} - \sigma_{33})^2 + (\sigma_{33} - \sigma_{11})^2 + 6(\sigma_{12}^2 + \sigma_{23}^2 + \sigma_{31}^2)]} \tag{4.6}$$

The equivalent stress, σ_{eqv}, for a spherical precipitate is 134.18GPa.When the aspect ratio is increased to $\alpha = 4.0$, σ_{eqv} increases to 166.60GPa. Consequently, σ_{eqv} increased substantially with the normal stress σ_{11} associated with the x_1 direction as the aspect ratio increased.

The computed equivalent stress around the precipitate is shown in 3D plots (Fig. 4.9). TThe region of the equivalent stress is extended to be approximately twice the length of the precipitate from the interface of the ellipsoid precipitate (x_1/a— $= 1.0$), as shown in Fig. 4.9a.

Although the equivalent stress increases with increasing aspect ratio, the region of stress disturbance caused by inhomogeneous precipitate is greatly reduced; therefore, the stress and strain gradients are much larger for a higher aspect ratio.

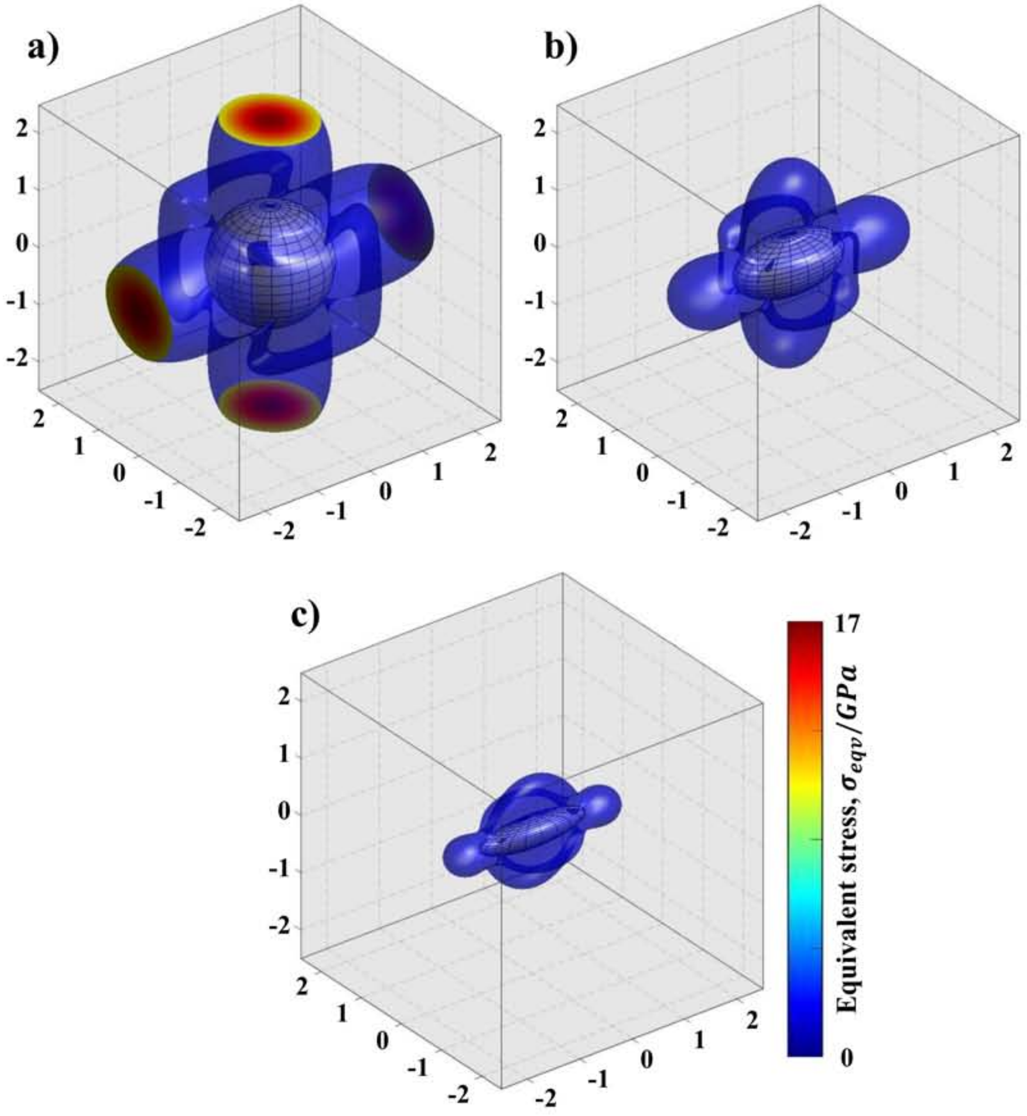

Figure 4.9: Disturbance of σ_{eqv} around an inhomogeneity under cold rolling conditions with an aspect ratio of $\alpha = 1.0$ in (a), 2.0 (b), or 4.0 (c).

Table 4.3: Comparison of the stress inside an inhomogeneity for different aspect ratios under cold rolling conditions ($\varepsilon^0_{33} = -\varepsilon^0_{11} = -1.0$, $\varepsilon^0_{22} = 0$). The equivalent stress σ_{eqv} was calculated from Eq. (4.6).

	σ_{ij} / GPa			
α	σ_{11}	σ_{22}	σ_{33}	σ_{eqv}
1.0	77.47	0.0	−77.47	134.18
2.0	99.19	2.0	−69.79	146.89
4.0	123.38	2.47	−66.65	166.60

4.5 Discussions

4.5.1 Dislocation distribution around the precipitate

According to Ashby (1966, 1970), a matrix containing an inclusion (precipitate) experiences a strain incompatibility between two phases when the elastic properties are different. This mismatch in plastic strain can be accommodated by the dislocations generated at the precipitate-matric interface (Ashby and Johnson, 1969), denoted as “geometrically necessary dislocations (GNDs)” by Ashby (1970).

Humphreys and Hirsch (1976) and Lewis and Martin (1963) found that the dislocation density introduced by external loads (tensile loads, compressive loads, shear loads, etc.) can increase when the precipitates are embedded in a matrix phase. Therefore, the accumulation of dislocations based on the precipitate shape must be considered.

As mentioned in Section 4.4.4, as the aspect ratio increases, the maximum disturbed strain and stress occur in a region adjacent to the precipitate. This finding suggests that the aspect ratio of the precipitate is strongly correlated to the local dislocation density. A previous report (Muraishi, 2014)showed that the local dislocation density around ellipsoidal precipitates in an aluminum matrix can be increased by promoting dislocation generation and interfering with dislocation migration. As discussed in Sections 4.4.3 and 4.4.5, as the aspect ratio increased, the region of maximum disturbed strain and stress gradually decreased at both ends of the precipitate along x_1 direction. Accordingly, for a spherical precipitate (α=1), the largest region of elastic stress is attained due to a greater level of complex rotational dislocation (disclination) around the precipitate (T. Mura, 1987, p.117), which is associated with local lattice rotation (lattice bending) in the vicinity of the precipitate (Humphreys, 1979a). These characteristics reflects the microstructure around the precipitate, which is commonly termed the deformation zone (Fig. 4.1).

4.5.2 Deformation zone around precipitate

As shown in Fig. 4.1, fine equiaxial grains are exclusively formed at both ends of the precipitate along the rolling direction, which suggests that the density and distribution of dislocations under cold rolling conditions change locally around the precipitate, depending on the precipitate shape. In general, the deformed microstructure in a cold-rolled sheet is elongated in the same average direction due to dislocation slip along the rolling direction. However, because the plastic deformation under external loading is significantly disturbed by the existence of the precipitates, sub-grains of a fine equiaxial shape with high misorientation were found at the both sides of the precipitate parallel to the rolling direction. In a previous study (Humphreys, 1979b), local lattice rotation around a spherical precipitate was shown to occur for the $< 112 >$ rotation axis perpendicular to both Burger's vector and the normal vector of the primary slip plane. Generally, when the precipitate stiffness is sufficient to prevent dislocation migration, a high dislocation density arises with exclusive deformation of the matrix phase, which leads to the local plastic deformation and relaxation to release the elastic stress around the inhomogeneity. Therefore, as discussed for the stress and strain disturbance in Sections 4.4.3 and 4.4.5, the dislocation microstructure evolves around the precipitates in order to cancel the local mismatch of plastic strain around the inhomogeneity. For instance, the region of disturbed strain around the inhomogeneity decreases with increasing aspect ratio, as shown in Figs. 4.5–4.7, because the increased longitudinal length of the inhomogeneity along x_1 direction is strongly constrained by the matrix phase. This behavior implies that the deformation zones with local lattice rotation are strongly influenced by the aspect ratio parallel to x_1 axis of the precipitate.

Considering that a larger plastic zone is observed for spherical precipitates, as shown by the equivalent stress (Fig. 4.9),a rotated zone nucleus should form at both ends of the spherical precipitate to activate the PSN effect. This assumption is strongly supported by observation and prediction results reported in the literature, the plastic relaxation induced by the generation of prismatic loops (Humphreys, 1979b; Muraishi, 2014), the local lattice rotation observed under the relatively large plastic deformations (Humphreys, 1979a; Humphreys and Bate, 2003).

4.5.3 Residual stress of inhomogeneous precipitates

When plastic strain is exclusively introduced in the matrix phase, the mismatch in plastic strain should be treated as a prescribed eigenstrain inside the inhomogeneity, which can be treated by the inhomogeneous inclusion problem under applied loading conditions (T. Mura, 1987, p.177). Therefore, the stress disturbance changes with the mismatch in plastic strain, ε^P_{ij}, as follows:

$$\begin{aligned}\sigma_{ij} &= C^*_{ijkl}(\varepsilon^0_{kl} + \tilde{\varepsilon}_{kl} - \Delta\varepsilon^P_{kl}) \\ &= C^*_{ijkl}(\varepsilon^0_{kl} + S_{klmn}\varepsilon^*_{mn} + S_{klmn}\varepsilon^P_{mn} - \Delta\varepsilon^P_{kl}) \\ &= C^*_{ijkl}(\varepsilon^0_{kl} + S_{klmn}\varepsilon^*_{mn} * -\Delta\varepsilon^P_{kl}) \qquad (4.7)\\ \sigma_{ij} &= C_{ijkl}(\varepsilon^0_{kl} + \tilde{\varepsilon}_{lj} - \varepsilon^*_{kl} - \Delta\varepsilon^P_{kl}) \\ &= C_{ijkl}(\varepsilon^0_{kl} + S_{klmn}\varepsilon^*_{mn} * -\varepsilon^{**}_{kl}) \qquad (4.8)\end{aligned}$$

with

$$\varepsilon^{**}_{mn} = \varepsilon^*_{mn} - \Delta\varepsilon^P_{mn} \qquad (4.9)$$

where ε^{**}_{mn} is the total eigenstrain, $\Delta\varepsilon^P_{mn}$ is the mismatch in plastic strain, ε^*_{mn} is the equivalent (fictitious) eigenstrain as defined in Eqs. (4.1) and (4.2). In the absence of an applied strain, the residual stress, $\Delta\sigma_{ij}$, can be simply expressed by setting the external strain to zero ($\varepsilon^0_{ij} = 0$) (T. Mura, 1987, p.181),

$$\Delta\sigma_{ij} = C^*_{ijkl}(S_{klmn}\varepsilon^{**}_{mn} - \Delta\varepsilon^P_{kl}) = C_{ijkl}(S_{klmn}\varepsilon^{**}_{mn} - \varepsilon^{**}_{kl}) \qquad (4.10)$$

Hence, the relation between the total eigenstrain and the mismatch in plastic strain is given as (Muraishi and Taya, 2019),

$$\varepsilon^{**}_{mn} = ((C^*_{ijkl} - C_{ijkl})S_{klmn} + C_{ijkl}I_{klmn})^{-1}C^*_{ijkl}\Delta\varepsilon^P_{kl} \qquad (4.11)$$

Because the plastic deformation is assumed to occur in the matrix phase, the mismatch in plastic strain inside the inhomogeneity can be defined as $\Delta\varepsilon^P_{kl} = -\varepsilon^0_{kl}$. This assumption is easily verified by the fact that the elastic stress strain is not influenced by the homogeneous plastic strain in the body. Moreover, considering that the residual stress magnitude varies in proportion to the mismatch in plastic strain, as shown by Eqs. (4.10) and (4.11), high-magnitude residual stress around the inhomogeneity should be compensated for by local plastic deformation, which may cause the resultant microstructure of a rotated zone around inhomogeneous precipitates.

Residual stresses inside an inhomogeneity were computed for aspect ratios of $\alpha = 1.0$, 2.0 and 4.0 using Eq. (4.10), as shown in Table 4.4. The condition for plastic strain mismatch is, $\Delta\varepsilon_{33}^{P} = -\Delta\varepsilon_{11}^{P} = 1.0$, $\Delta\varepsilon_{22}^{P} = 0$. For comparison, the stress under external loading conditions, as computed by Eq. (4.1), is represented as $\varepsilon_{33}^{0} = -\varepsilon_{11}^{0} = -1.0$, $\varepsilon_{22}^{0} = 0$. It has been shown that the residual stress for σ_{11} and σ_{33}, in a spherical precipitate are approximately 50% lower than the total stress inside the inhomogeneity computed by Eq. (4.1). In contrast, when the aspect ratio is increased to 4.0, the stress σ_{11} values computed by Eqs. (4.1) and (4.10) are similar, while the magnitude of σ_{33} decreases. This finding indicates that stress relaxation under cold rolling conditions is more effectively achieved by a spherical inhomogeneity than a prolate inhomogeneity for a given plastic strain magnitude in the matrix phase.

It is important to note that, the predicted stress values in Table 4.4 are extremely large, even when a plastic strain mismatch under the cold rolling is assumed, with $\Delta\varepsilon_{33}^{P} = -\Delta\varepsilon_{11}^{P} = 0.9$ (reduction ratio: 90%). This result implies that the stress relaxation is caused by crystal dislocations during cold rolling. Assuming the flow stress of $\sigma = 0.1$ 0.2 GPa for aluminum alloy, the corresponding strain for the initiation of a deformation zone is estimated as $\Delta\varepsilon_{33}^{P} = 0.0013$, which shows good agreement with the yielding behavior of aluminum alloy. As the stress field of inhomogeneity can be exactly demonstrated by GND arrangements (Muraishi, 2014), the stress level predicted by the present work would be reduced by the introduction of the crystal dislocations if the dislocations are arranged such that the fictitious eigenstrain listed in Table 4.2 is cancelled at the inhomogeneity interface. Simultaneously, during the process of the stress relaxation caused by crystal dislocations, a deformation zone accompanied by a large misorientation angle would form around the inhomogeneity based on the conservation of the total sum of Burger's vector. Although a detailed calculation for the deformation zone produced by GNDs is not presented here, a theoretical assessment of the equilibrium position of a deformation zone boundary has been discussed in terms of the dislocation punching model by Shibata et al. (1992).

Table 4.4: Comparison of the stress computed by Eq. (4.1) and the residual stress deduced from the mismatch in plastic strain by Eq. (4.10) under cold rolling conditions, $\varepsilon^0_{33} = -\varepsilon^0_{11} = -1.0$, $\varepsilon^0_{22} = 0$.

	α=1.0		α=2.0		α=4.0	
	Eq. (4.1)	*Eq.* (4.10)	*Eq.* (4.1)	*Eq.* (4.10)	*Eq.* (4.1)	*Eq.* (4.10)
σ_{11}	77.47	41.24	99.19	76.24	123.38	115.23
σ_{22}	0.0	0.0	2.00	3.22	2.47	3.98
σ_{33}	−77.47	−41.24	−69.79	−28.87	−66.65	−23.80

Nevertheless, considering the fact that the effect of the aspect ratio on the stress computed by Eqs. (4.1) and (4.10) show similar tendencies in Table 4.4; here, the σ_{11} value associated with the long axis of the prolate spheroid increased greatly as the aspect ratio increased from $\alpha = 1.0$ to 4.0. Thus, the residual stress and strain outside the inhomogeneity can be expressed by the disturbed strain under external loading conditions, as predicted in Figs. 4.5–4.9, where the applied strain inside the matrix phase is assumed to be plastic as follows:

$$\sigma_{ij}(\text{outside}) = C_{ijkl}\overline{G}_{ijmn}\varepsilon^{**}_{mn} \tag{4.12}$$

Here, $\overline{G}_{ijmn}$ is the exterior point Eshelby tensor and ε^{**}_{mn} is deduced from the mismatch in plastic strain by Eq. (4.10).

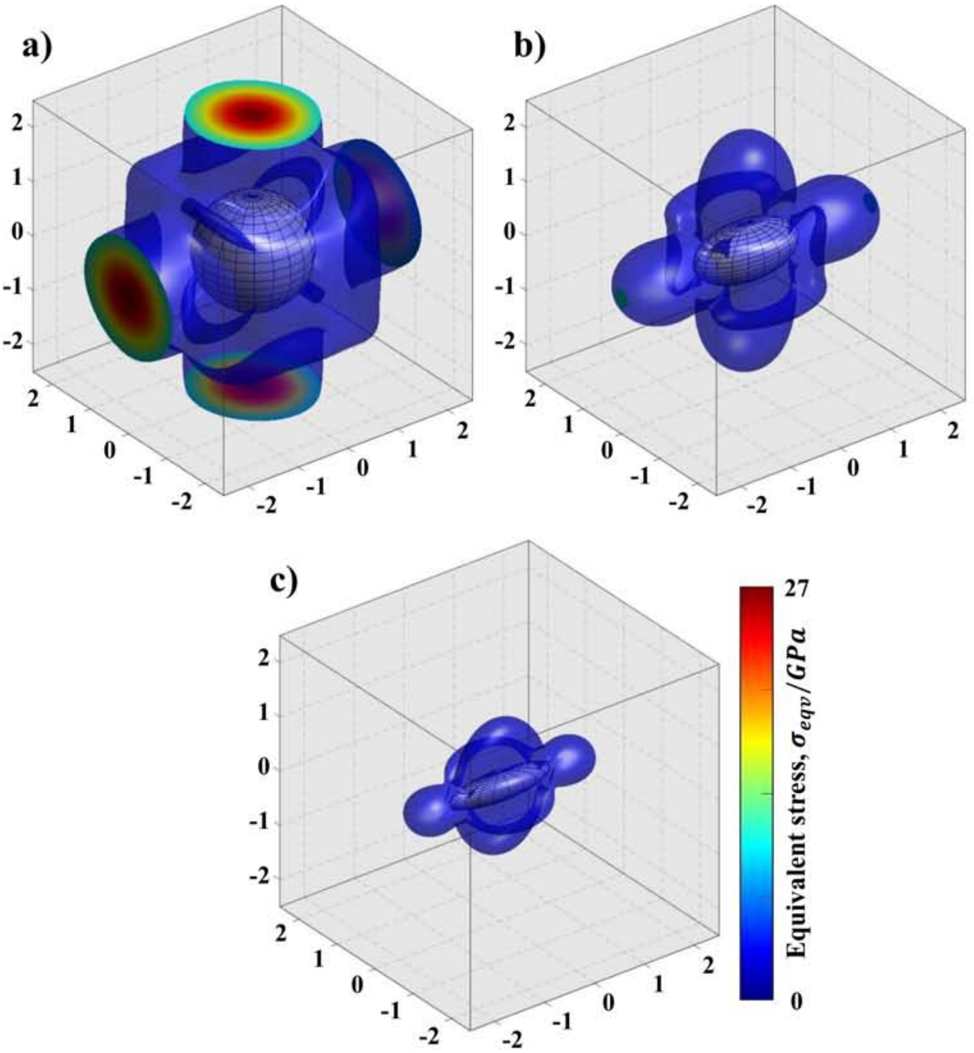

Figure 4.10: Residual stress around an inhomogeneity under cold rolling conditions for an aspect ratio of α =1.0 (a), 2.0 (b) and 4.0 (c). The equivalent stress outside the inhomogeneity is deduced from Eq. (4.12).

As shown in Fig. 4.10, the distribution of equivalent stress around the inhomogeneity is similar to that computed by Eq. (4.1) under external loading conditions, as shown in Fig. 4.9. Based on the above prediction results, the precipitate shape has a significant impact on the stress relaxation caused by dislocations, because the region of high-magnitude internal stress tends to be plastically deformed to accommodate dislocations with a higher orientation gradient. This finding can be supported by EBSD analysis results, where the maximum misorientation angle in the rotated zone near the precipitate was measured to be 39 degrees for a nominal strain rate of 0.5. This angle also increased in proportion to the amount of reduction (approximately 30 and 61 degrees for nominal strain rates 0.2 and 0.9, respectively).

4.6 Conclusions

The strain disturbance and residual stress around a coarse precipitate in a matrix phase were predicted by solving an inhomogeneity problem under cold rolling conditions in a manner analogous to the Eshelby method. The present study has demonstrated that the strain disturbance inside and outside an ellipsoidal precipitate is greatly influenced by the applied strain and the short-axis length. Residual stress analysis revealed that as the aspect ratio of the precipitate increases, the region of the equivalent stress around the precipitate is localized by the prolate shape, with a higher-magnitude stress gradient. Based on the residual stress value, the formation of the rotated zone around the coarse precipitate would be influenced by the stress relaxation mediated by GNDs. This trend also implies that the effect of PSN on the recrystallization of the cold-rolled sheets is effectively caused by spherical precipitate.

Chapter 5

Influence of residual stress around constituent particles on recrystallization and grain growth in Al-Mn based alloy during annealing

5.1 Introduction

In Chapter 4, the strain disturbance and the residual stress around the coarse precipitate in the matrix phase were investigated by solving the inhomogeneity problem under cold rolling conditions by means of the Eshelby method. The region of residual stress caused by inhomogeneous precipitate depends on the aspect ratio of the precipitate, and the large magnitude of the stress is found in the case of the spherical precipitate. Although the magnitude of the residual stress is predicted by linear elasticity, c.f. the strain disturbance inside and outside the inhomogeneity is proportional to the applied strain, the residual stress is strongly influenced by the short axis length of the ellipsoidal precipitates, where the value of the residual stress is increased with increasing aspect ratio and the region of the stress disturbance around the inhomogeneous precipitate is greatly reduced in its area. Assuming that the residual stress around the coarse precipitate would be relaxed by introduction of the dislocations, the value and the region of the residual stress predicted by the present study may implement the deformed zone frequently observed around the coarse precipitate. In another words, the particle-stimulated nucleation (PSN) effect on recrystallization can be effectively occurred as a result of the stress relaxation around the coarse spherical particle.

The optimum microstructure and mechanical properties of commercial AA3003 aluminum alloy are chosen by consecutive reduction and heat treatment, where concurrent precipitation would greatly influence the recovery and recrystallization at a certain temperature. It is well known that stored elastic energy by cold working process are the most important factor in the recrystallization of rolled aluminum alloys (Humphreys et al., 2004), however, recrystallization behavior is greatly influenced by concurrently existing particles and precipitates. Whether concurrent precipitation would occur or not during the homogenization and subsequent heat treatment, fine secondary particle causes a significant effect on recovery and recrystallization phenomena. Many researchers proved that promotion or suppression of concurrent precipitation occurred during annealing when correct homogenization conditions were selected (Lloyd and Kenny, 1980). Therefore, the initial microstructure introduced by homogenization treatment is an important factor for cold rolling and subsequent annealing treatment, where the volume fraction, size, shape and inter-spacing of the particles can be varied to influence stored energy and recrystallization phenomena (Gil Sevillano et al., 1980; Gholinia et al., 2002). In Chapter 2, the recrystallization of cold-rolled AA3003 aluminum alloy during annealing is reported, where the change in electric conductivity associated with the concurrent precipitation as well as the apparent activation energy for recrystallization was discussed. It has been demonstrated that cold-rolled sheets homogenized by a certain temperature before cold rolling exhibited a negligible level of concurrent precipitation during annealing. Regarding the effect of second particles on recrystallization, many types of research have been carried out such as delay of the restoration behavior due to concurrent precipitation(Nes et al., 1985; Zhao et al., 2018), and the promotion of recrystallization by particle-stimulated nucleation (PSN) (Simonovic and Sluiter, 2009; Humphreys, 1982).

Humphreys (1979a) have studied the influence of coarse precipitate on the recrystallization behavior of aluminum and its alloys during isothermal annealing, and the deformed structure around the coarse particles can be classified into two types: the distorted zones formed perpendicular to rolling direction and rotated zone formed parallel to rolling direction. This deformation zones formed by an accumulation of dislocation around the coarse particles are particularly important because it provide a PSN effect of recrystallization, which leads a strong impact on recrystallized grain size and structure (Humphreys et al., 2004). PSN is generally known to occur only in particles larger than about $1 \mu m$ in diameter. Since the probability of PSN is strain dependent, the resultant grain size as well as the texture orientation is possibly controlled by the distribution and the number of potential nucleation sites around the particle, in which the higher magnitude of the residual strain would be expected by the larger second particles.

The change of microstructure that occurs during annealing depends on the degree of the restoration mechanism such as recovery, recrystallization and grain growth. The deformation zones formed around coarse primary particle (>1μm) during plastic deformation may accelerate the recrystallization behavior by PSN (Humphreys, 1997). Whereas, the fine secondary particles suppress both the migration of low-angle grain boundary (LABG) and high-angle grain boundary (HABG) in Al-Mn-based alloy (Zener pinning) (Smith, 1945). More importantly, the recovery and recrystallization kinetics are significantly retarded by large amounts of Mn supersaturation in Al-Mn-based alloy, which is commonly referred to as concurrent precipitation (Nagahama and Miki, 1974; Liu and Radhakrishnan, 2010). Therefore, in order to suppress the concurrent precipitation, microstructure controlling by homogenization treatment prior to the cold rolling and subsequent annealing is an important issue in advanced engineering processing in Al-Mn-based alloy (Sun et al., 2006, 2008).

The increase in the dislocation density during the cold rolling has the greatest influence on the driving force of the recrystallization and the velocity of boundary migration under subsequent annealing. Although the kinetics of the recrystallization accompanied with the concurrent precipitation during annealing depends on the activation energy of Mn diffusion in Al matrix (Vernon-Parry et al., 1996; McQueen et al., 2016), detail of the dislocation interaction with the constituent particles is still unclear, especially, the quantitative/macroscopic model for the evolution of dislocation microstructure associated with dislocation density during annealing is limited. In Chapter 4, the micromechanics-based analysis of the residual stress around the coarse particles under cold rolling condition has been proposed.

In this study, therefore, the effect of the amount of reduction and the subsequent annealing treatment on the recrystallization phenomena under the certain volume fraction of primary particle in AA3003 alloy was investigated by means of the dislocation density measurement by synchrotron X-ray, the crystallite size and orientation measurement by EBSD analysis, where the nucleation and growth associated with the restoration of dislocation microstructure around the constituent particles was discussed. In addition, the recrystallization behavior near the coarse particle is analyzed in terms of the residual stress around the α-Al(Mn, Fe)Si particle by solving an inhomogeneous inclusion problem under cold rolling condition.

5.2 Experimental Procedure

A commercial AA3003 (Al-1.15Mn-0.52Fe-0.28Si-0.16Cu in wt%) alloy was used in this study. The initial as-cast alloy (200 mm in length, 80 mm in width, 155mm in thick) was fabricated by DC cast.

With the aim of reduction of concurrent precipitation during subsequent annealing, the homogenization treatment (as-homo) was conducted at 580 °C for 8h with a slow heating rate of 50 °C/h, and then immediately quenched into the water at room temperature (R.T). Then the as-homo specimens were processed by cold-rolling with the reduction rate of 20% (AM2), 50% (AM5), and 90% (AM9). In order to analyze the temperature dependency of the effect of concurrent precipitation on the recrystallization, the cold-rolled sheets were isothermally annealed at 300 °C, 350 °C, 375 °C and 400 °C for 2s to 24h in salt-bath, and then immediately quenched into the water at R.T.

The grain microstructure for the deformed and annealed specimens at the center of the thickness were characterized by optical microscope (OM) and field-emission scanning electron microscopy (FE-SEM), in which the longitudinal section is composed of the rolling direction (RD) and the normal direction (ND). The measurement of crystalline orientation and grain boundary misorientation was conducted by FE-

SEM equipped with electron backscatter diffraction (EBSD), in which the data was treated by TSL orientation imaging microscopy (OIM) analysis software and MTEX toolbox for MATLAB (Hielscher et al., 2019). The misorientation of grain boundaries of less than 2 degrees was neglected due to significant orientation noise in the deformed and annealed specimens. Generally, a low angle grain boundary (LAGB) is defined as boundaries with misorientation between 2–15 degrees, and boundaries exceeding 15 degrees are defined as high-angle grain boundary (HAGB) (Zhou et al., 2019). In order to examine dislocation microstructure, transmission electron microscopy (TEM) observation was carried out for as-rolled and annealed specimens with an operating voltage of 300 kV (JEOL, JEM-3010). The preparation of TEM foils were made by twin jet polishing technique in a 20% HNO_3 methanol solution under the condition of about $-20\,°C$ or less.

Electric conductivity was measured by eddy current inspection (using SIGMA tester), which is expressed in terms of %IACS. The microhardness was measured by Vickers hardness tester with an interval of 50 μm under a load of 0.98 **N** for 15s. The change in dislocation density was measured and analyzed by synchrotron and conventional XRD. The high-intensity X-ray BL02B2 beamline (λ=0.0516 nm) of the SPring-8 synchrotron radiation facility is utilized in this study. The time resolution of this experiment was 10s. The conventional XRD measurement was carried out by convergent beam method with Cu-Kα (λ=0.1540 nm) radiation.

The residual stress field in/outside the precipitate embedded in the aluminum matrix was computed by analytical solutions of the Eshelby tensor (T. Mura, 1987; Ju and Sun, 1999, 2001), where the PSN effect on the deformation zone around the spherical inhomogeneity is assumed by mismatch of plastic strain between the α-Al(Mn, Fe)Si particle and Al matrix. The elastic properties used for the matrix and precipitate are given in Table 5.1. The displacement and equivalent stress field around the α-Al(Mn, Fe)Si precipitate are represented as density plots using MATLAB.

Table 5.1: Young's modulus and Poisson ratio for aluminum matrix and α-Al(Mn, Fe)Si precipitate. The subscripts m and p indicate matrix phase and precipitate.

Constant	Value	Source
E_m	69.0GPa	(Kaufman, 1999)
ν_m	0.33	
E_p	175.0GPa	(Chen et al., 2010)
ν_p	0.28	assumed

5.3 Results

5.3.1 Microstructure of homogenized specimen

The typical microstructure and distribution of primary and secondary particles in the as-homo specimen are shown in Fig. 5.1. The as-homo specimen shows characteristic equiaxed grain microstructure with average grain size of $160\mu m$ (Fig. 5.1a). In order to distinguish the primary particle Al_6(Mn, Fe) and α-Al(Mn, Fe)Si, the backscattered electron image is presented in Fig. 5.1b. A large quantity of primary particles with rod-like, plate-like and network eutectic shape is distributed in the grain boundaries and inside of inter-dendritic area (Fig. 5.1a and b), where, primary particles consists of α-Al(Mn, Fe)Si phases and less amount of Al_6(Mn, Fe) phases with an average size of 2.5 μm. A large number of fine secondary particles were homogeneously formed in the Al matrix due to the effect of the homogenization treatment. It is noted that dislocation networks were frequently observed around the smaller precipitate with a diameter of 459 *nm* at the interior of the grain, which is enclosed by the dislocation walls (Fig. 5.1c). The quantitative values of grain size, primary particle size and electric conductivity are listed in Table 5.2. Since the electric conductivity of as-homo specimen was significantly increased as compared to that of as-cast specimen, the amount of concurrent precipitation during the recovery and recrystallization stages is potentially reduced by homogenization treatment.

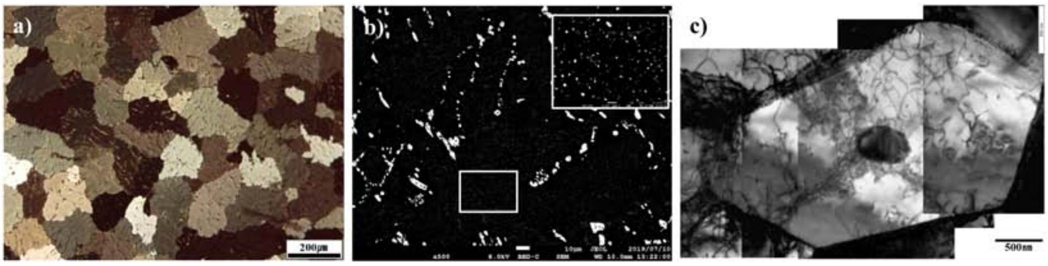

Figure 5.1: The typical microstructure of homogenized AA3003 aluminum alloy.

Table 5.2: Change of grain size, primary particle size and electrical conductivity in the DC cast AA3003 aluminum alloy by homogenization

	Grain size (μm)	Primary particle size (μm)	Electric conductivity (%IACS)
as-cast	140	2.85	30
as-homo	160	4.1	43.5

5.3.2 Change in microstructure with increase of strain

TEM images of cold-rolled specimens for AM2, AM5 and AM9 are shown in Fig. 5.2. Relations between specimen orientation and viewing direction are indicated by TD, ND and RD. It is apparent that, as the reduction rate increases from AM2 to AM9, the cold-rolled specimens show elongated grain microstructure parallel to the RD. As the rolling reduction increases, the microstructure of the cold-rolled specimens show elongated grains with the straight grain boundaries parallel to the rolling direction.

The ideal plastic strain of the cold rolling can be expressed by the change in the thickness of cold rolled sheet as follows,

$$\varepsilon_t = \int_{t_0}^{t_1} \frac{dl}{l} = ln(\frac{t_1}{t_0}) = ln(1 + \varepsilon_n) \tag{5.1}$$

where the logarithmic strain (true strain) is ε_t, the nominal strain is ε_n, the reduced thickness of the cold rolled sheet is t_1, the initial thickness of the sheet is t_0.

It is seen from Fig. 5.2a, c and e that thickness of the grains with HAGB and its crystallite size tend to decrease with increasing strain. The cell and sub-grain formed during the plastic deformation in AM2 and AM5 specimens are hardly changed (with the lower strain, $\varepsilon_t \leq 0.69$), while the volume fraction of the grains with HAGB is increased in the AM9 specimen (Fig. 5.2e). This implies that high-angle boundaries are newly developed by further plastic deformation, which leads to the grain fragmentation due to the higher strain (Tóth et al., 2010). It is clearly seen from Fig. 5.2b, d and f, which are the higher magnification images taken from ND, dislocation microstructure is composed of sub-grain boundaries (Fig. 5.2b) and dislocation cells (Fig. 5.2b and d). On the other hand, the strain contrast of AM9 is difficult to identify the boundaries clearly, which is due to the dense dislocations introduced by heavily plastic deformation (Fig. 5.2f).

In literature(Raj et al., 1996), the cell consists of a wide and diffused boundary containing dislocation tangle, while the sub-boundary is narrow, where the misorientation angle across the sub-boundary is larger than that across the cell wall. Accounting the bright field images, distinctive differences in crystal orientations are apparent, but the dense dislocations more influence the strain contrast at the grain interior for the higher magnitude of plastic strain in Fig. 5.2f.

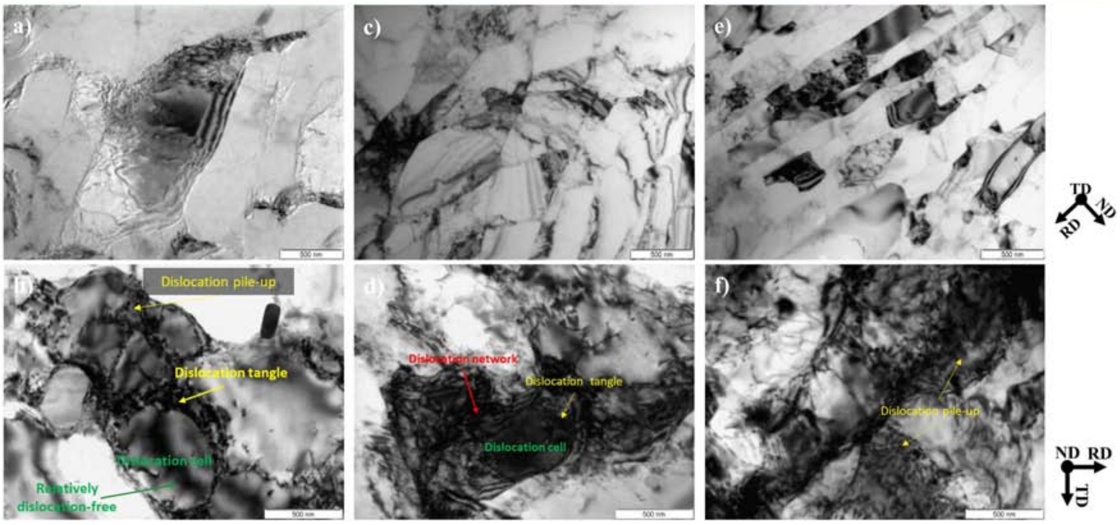

Figure 5.2: Representative TEM bright images of cold-rolled AA3003 aluminum alloy with reduction rate of (a, b) 20%, (c, d) 50% and (e, f) 90%

5.3.3 Deformation zone around the α-Al(Mn, Fe)Si precipitate with increase of strain

EBSD analysis was conducted for the deformed zones around the coarse α-Al(Mn, Fe)Si particles ($> 1\mu m$) and IPF (inverse pole figure) maps are represented in Fig. 5.3, where black regions are α-Al(Mn, Fe)Si particles. The respective IPF maps for the specimens with reduction rate of 20%, 50% and 90% demonstrate the evolution of the deformation zones with increase of the plastic strain. In particular, elongated grain morphology along the direction parallel to RD is clearly distinguished by the color coded plots, which indicates the extensive plastic flow around the undeformed α-Al(Mn, Fe)Si precipitate

(Fig. 5.3c). The deformation zone around the α-Al(Mn, Fe)Si precipitate introduced by cold rolling can be classified into two categories. The first is a characterized by the distorted zone left and right of the coarse particle, and other one is the rotated zone to the below and above the coarse particle. This rotated zone corresponds to the refined sub-grain structure and high lattice rotation, providing a high local stored energy, which is important for nucleation of recrystallization.

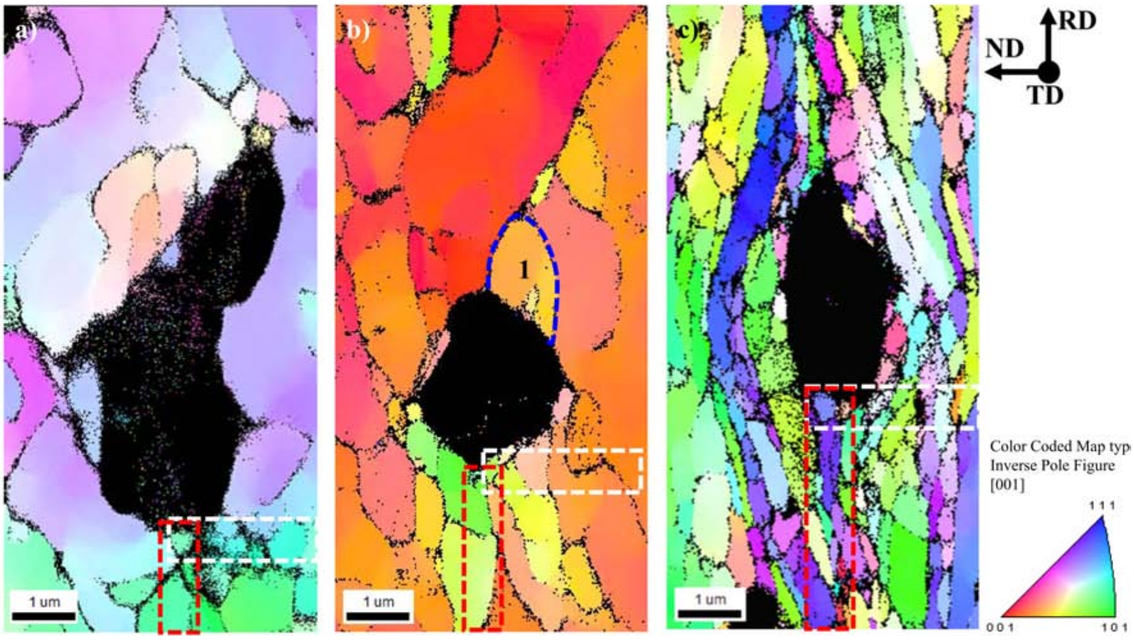

Figure 5.3: EBSD map around the α-Al(Mn, Fe)Si precipitate in the longitudinal section of the cold rolled AA3003 aluminum alloy with reduction rate of (a) 20%, (b) 50% and (c) 90%. The inverse pole figures (IPF) indicate the color key of the crystal direction parallel to the normal direction (ND)

In order to distinguish the subgrain formation in the vicinity of the α-Al(Mn, Fe)Si precipitate, the local misorientation angle observed for the EBSD map of AM5 was replotted by the Kernel average misorientation (KAM) map and its line profile in Fig. 5.4. The KAM map and the line profile of misorientation across the grain (black arrow) are obtained from the region indicated by the blue dotted line (region1 in Fig. 5.3b). It is shown in Fig. 5.4 that the misorientation profile is steeply increased to 9 degrees at a distance of 0.35 μm. After the stepwise increase and decrease of misorientation, there is no further change in the profile. This indicated that a well-developed sub-grain is formed inside the grain next to the coarse particle during plastic deformation.

Accounting the non-uniformity of the misorientation angle in Fig. 5.4b, the rotated zone consists of higher local misorientation angle reflects the existence of subgrain boundary near the coarse precipitate (Fig. 5.4a). This fact may be attributed to a exclusive lattice distortion induced at the matrix-precipitate boundary, which will be discussed in later section of inhomogeneity problem.

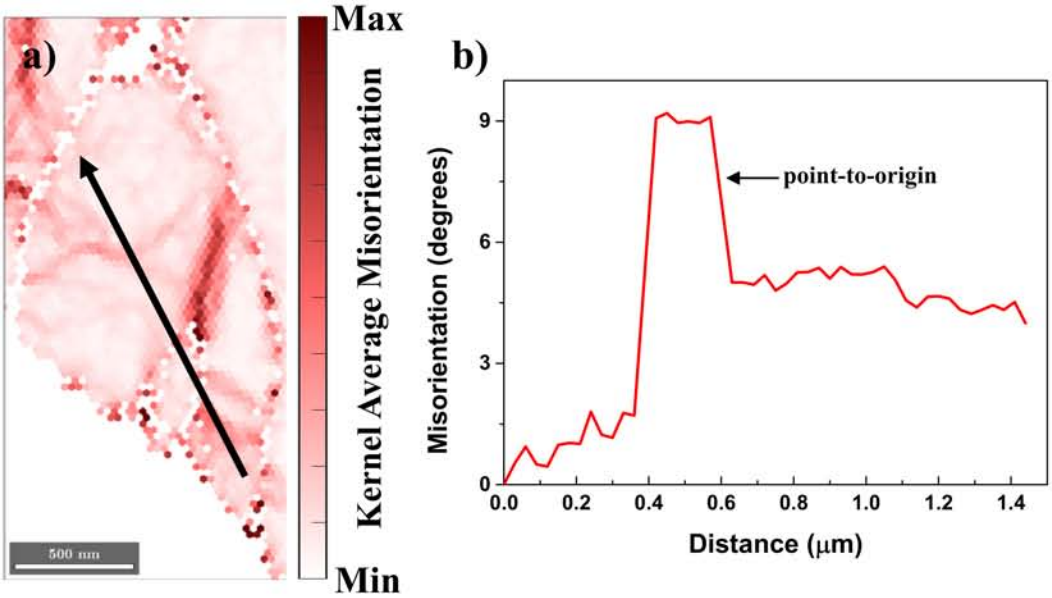

Figure 5.4: (a) Kernel average misorientation map of AM5 indicated in in Fig. 5.3b (region 1) with arrow marked (b) misorientation profile.

In order to obtain the misorientation in the vicinity of the rotated zone quantitatively, line profiles were analyzed for AM2, AM5 and AM9 on the EBSD map (Fig. 5.5). The misorientation profiles along RD and ND directions are taken from the regions indicated by dotted lines as shown in Fig. 5.3. Black line shows the difference of the misorientation angle between analysis points, while the red line shows the accumulated value of misorientation. The misorientation angle around the precipitate depends strongly on the plastic strain, where the maximum angle of AM2, AM5 and AM9 are amounted to be 17.7, 31.8 and 61.2 degrees for RD directions (Fig. 5.5a, b and c), and 29.6, 18.3 and 47.5 degrees for ND directions (Fig. 5.5d, e and f), respectively. Moreover, numbers of the misorientation boundaries can be found in both the RD and ND directions for AM9 in Fig. 5.5c and f.

Accounting the misorientation profiles of the rotated zone formed around the coarse precipitate, it is suggested that the recrystallization of the cold-rolled sheet would be easily occurred by the PSN effect under the large plastic deformation.

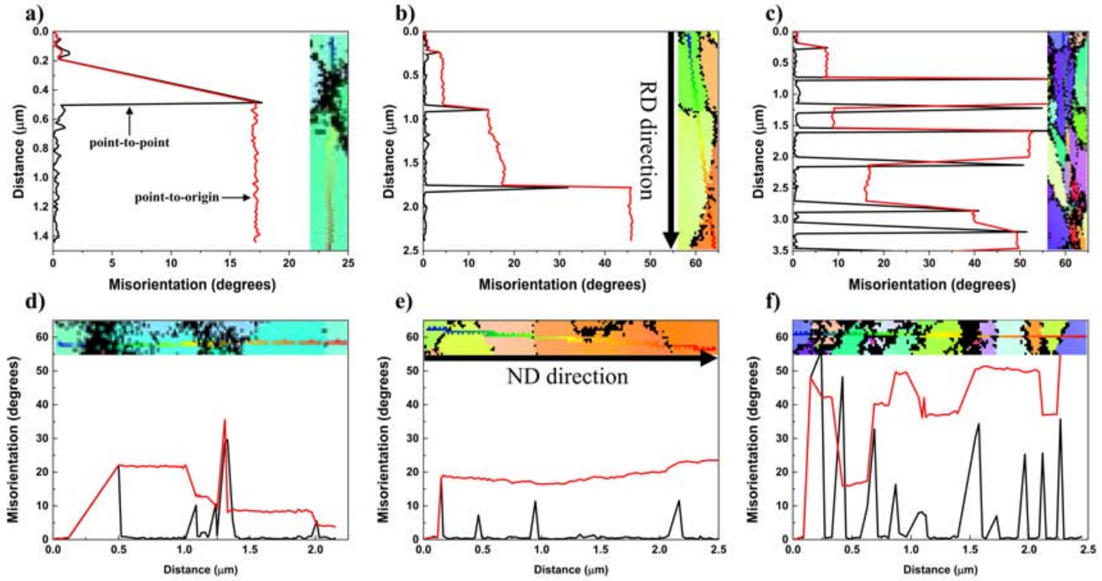

Figure 5.5: Misorientation angles profile of (a, d) AM2, (b, e) AM5 and (c, d) AM9 across the rotated zone formed around α-Al(Mn, Fe)Si precipitate. The point-to-point line (black) indicates the profile of the orientation changes between adjacent point. The point-to-origin line (red) represents the profile of the orientation changes between all point and origin point.

5.3.4 Evolution of dislocation density with increasing strain

Fig. 5.6 shows the effect of reduction rate on the (111) diffraction peaks measured by X-ray. The profile of the diffraction peaks in AM2 (logarithmic strain,$\varepsilon_t = 0.22$) is not significantly different from that of as-homo ($\varepsilon_t = 0.0$), but the diffraction angle is shifted slightly toward the lower angle. This shift of diffraction angle implies an increase of d-spacing in ND direction as a result of residual strain. The profile of AM5 ($\varepsilon_t = 0.69$) shows the broadening of diffraction peak at the similar peak position of AM2 ($\varepsilon_t = 0.22$). As the reduction rate is increased, further broadening is occurred but the diffraction peak position is not significantly changed in AM9 ($\varepsilon_t = 2.30$). Accounting the peak broadening with increase of the amount of plastic deformation, inhomogeneous strain distribution and small crystallite of cold-rolled specimen is suggested.

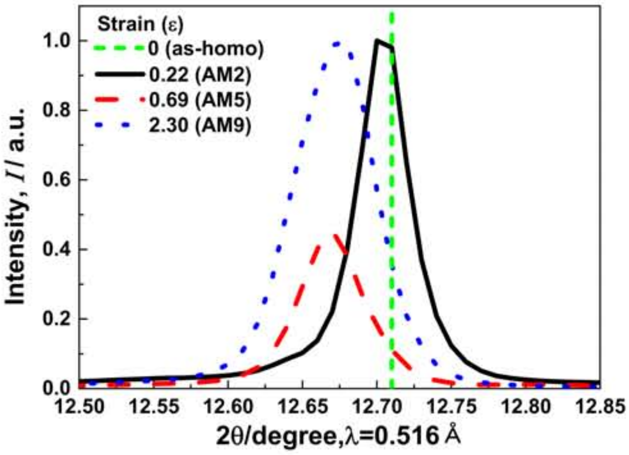

Figure 5.6: (111) diffracted peak at different reduction rate for the DC cast AA3003 aluminum alloy with homogenization

The residual strain due to the cold rolling and subsequent annealing can be quantitatively analyzed by means of Williamson-Hall plots, in which the magnitude of lattice strain and the crystallite size can be separately determined from peak shift and width (Williamson and Hall, 1953). Diffraction profiles used for this analysis were (1 1 1), (2 0 0), (2 2 0) and (3 1 1) and (2 2 2) reflections of the aluminum phase. According to Williamson-Hall equation, the effect of lattice strain, (ε_L, on the value of the full width at half maximum (FWHM) obtained from each peak can be mentioned as follows, (Williamson and Hall, 1953).

$$\Delta 2\theta \cos\theta = (0.9\lambda/D) + 2\varepsilon_L \sin\theta \tag{5.2}$$

where $\Delta 2\theta$ is the FWHM of diffraction peak, θ is the Bragg diffraction angle, λ is the wavelength of X-ray and D is the average crystallite size.

Fig.5.7a shows the FWHM values in the form of quadratic equations of the Williamson-Hall plot for each specimen. Note that, according to the first and second terms of the Williamson-Hall plot in Eq. (5.2), the crystallite size and the lattice strain can be determined from the intercept and the slope of the linear regression profiles, respectively. Apparently, the intercept for 90% cold-rolled specimens in Fig. 5.7a shows largest value, which indicates the smallest crystallite size. In the meanwhile, the slope of the profiles are similar regardless of the reduction rate. This implies that the average elastic strain is not significantly increased by further plastic strain.

The changes in crystallite size deduced from the XRD and TEM results are represented in Fig. 5.7b. It is clearly seen that the crystallite size obtained by Eq. (5.2) decreases with increase of reduction rate, which shows good consistency with those obtained by TEM observation. In literature(Ungár et al., 2001), since the crystallite size calculated from X-ray diffraction analysis by Eq. (5.2) can be regarded as the average size of sub-grains and dislocation cells due to the coherently scattered X-rays, the dislocation cell size observed in AM2, AM5 and AM9 was used for the crystallite size deduced from TEM images, which is amounted to be 510 nm, 331 nm and 214 nm, respectively.

The change in the dislocation density induced by cold rolling can be also determined from X-ray diffraction by assuming the lattice strain caused by dislocation lines. According to the relationship between the crystallite size and lattice strain obtained by Eq. (5.2), the dislocation density,ρ, is given by Williamson and Smallman as follows (Williamson and Smallman, 1956),

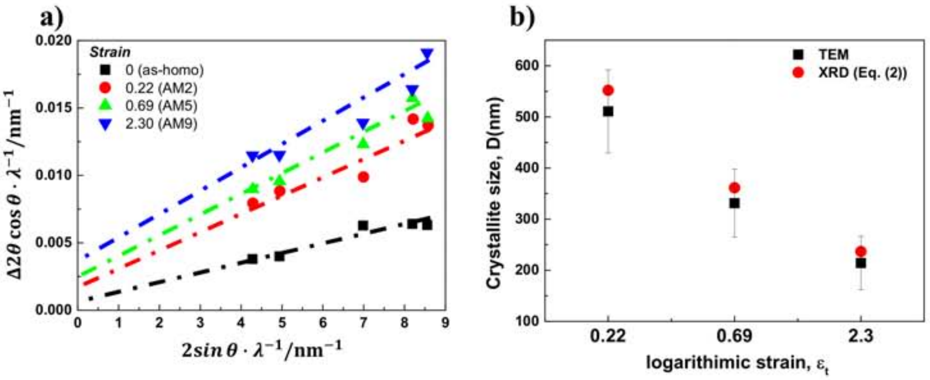

Figure 5.7: (a) Williamson-Hall plots and (b) Crystallite size of the cold-rolled AA3003 aluminum alloy measured by XRD and TEM.

$$\rho = \frac{(3nK/F)^{1/2} < \varepsilon_L^2 >^{1/2}}{Db} \tag{5.3}$$

where n is the number of dislocations on each face of matrix, K is constant depending on the strain distribution around the dislocation line, F is an interaction parameter, $< \varepsilon_L^2 >^{(1/2)}$ is root mean square strain, b is Burgers vector. In literature(Williamson and Smallman, 1954), the constant of K assumed by the Cauchy strain distribution is amounted to be $K = 25$, whereas that by Gaussian strain distribution is nearly $K = 4$. In the absence of the extensive polygonization in dislocation arrangement, the dislocation density is calculated by assuming $n \approx F$, and $K = 4$. Thus, the Eq. (5.3) can be simply given as

$$\rho = \frac{2\sqrt{3} < \varepsilon_L^2 >^{1/2}}{Db} \tag{5.4}$$

The effect of plastic deformation on the thickness of the grain for HAGB obtained by Eq. (5.1) and TEM image analysis is represented in Fig. 5.8. The thickness profiles are plotted by the black dash line for XRD analysis and the black solid line for TEM image analysis as a function of the logarithmic strains, 0.22, 0.69 and 2.30 (corresponding nominal strains, 20%, 50% and 90%). It is noted that TEM foil normal to TD direction was taken from the center part of deformed specimens. It can be seen that the HAGBs thickness in ND direction is decreased rapidly with increase of plastic strain, which is similar to the crystallite size when the plastic strain is larger than $\varepsilon_t = 1.5$. This consistency might be due to that the crystallite observed by TEM is mainly composed of the fine equi-axed grains (Fig. 5.2). It should be mentioned that the thickness of HAGBs by TEM analysis is consistent with the theoretical prediction by Eq. (5.1).

Regarding the change in the dislocation density as indicated by the blue dashed line in Fig. 5.8, the dislocation density shows parabolic increase with respect to the plastic strain, which is amounted to be $1.66\times10^{14}m^{-2}$ for AM2, $2.68\times10^{14}m^{-2}$ for AM5 and $3.87\times10^{14}m^{-2}$ for AM9. Accounting the facts of the similar slopes for lattice strains in Fig. 5.7a and the linear relationship between the crystallite size and the lattice strain in Eq. (5.4), the change in dislocation density at the larger plastic strain is attributed to the change in crystallite size D as shown in Fig. 5.7a and Fig. 5.8.

5.3.5 Recrystallization behavior in cold rolled specimen with different reduction ratio

The evolution microstructure of the AM2, AM5 and AM9 specimens annealed at 350 °C are shown in Fig. 5.9. The AM2 specimen clearly shows inhomogeneous recrystallization after 300s, where partially equi-axed grains are taken place in the vicinity of the intersection of deformed grains. By applying the longer annealing time over 600s, discontinuous recrystallization and the uni-axial grain growth parallel

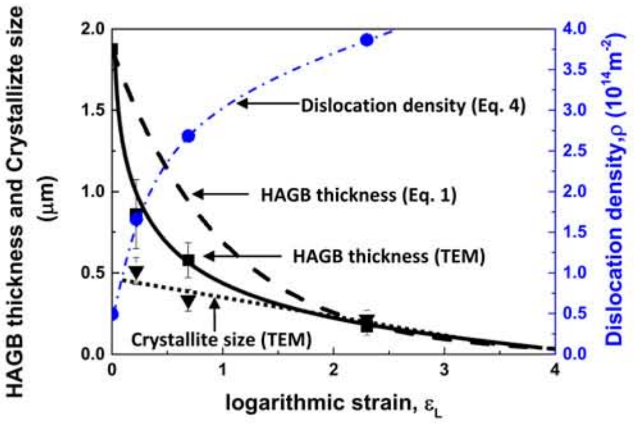

Figure 5.8: Evolution of the HAGB thickness, crystallite size and dislocation density with increasing the logarithmic strain in the AA3003 aluminum alloy

to RD has been proceeded. With increasing the reduction rate, recrystallization microstructure of AM5 specimen shows homogeneous equi-axed grains within the shorter annealing time of 30s. By further increase of the reduction rate, the recrystallization in AM9 specimen is completed within a few seconds, where recrystallized grain size is amounted to be $8\mu m$.

The change in the Vickers hardness and the dislocation density for AM2, AM5 and AM9 under the annealing temperature at 350 °C and 400 °C are represented in Fig. 5.10. The profiles of dislocation density for AM2, AM5 and AM9 are indicated by symbols with square, circle and triangle. The profiles of the Vickers hardness are represented by dotted lines. The dislocation density is computed by Eq. (5.4), in which the crystal size and the average lattice strain in Eq. (5.2) are used for the calculation. For comparisons, dislocation density of as-homogenized specimen is also plotted. It can be clearly seen that the profiles of the hardness and the dislocation density show good consistency, where the transition of the recovery to the recrystallization characterized by the rapid drop of the hardness profiles is well

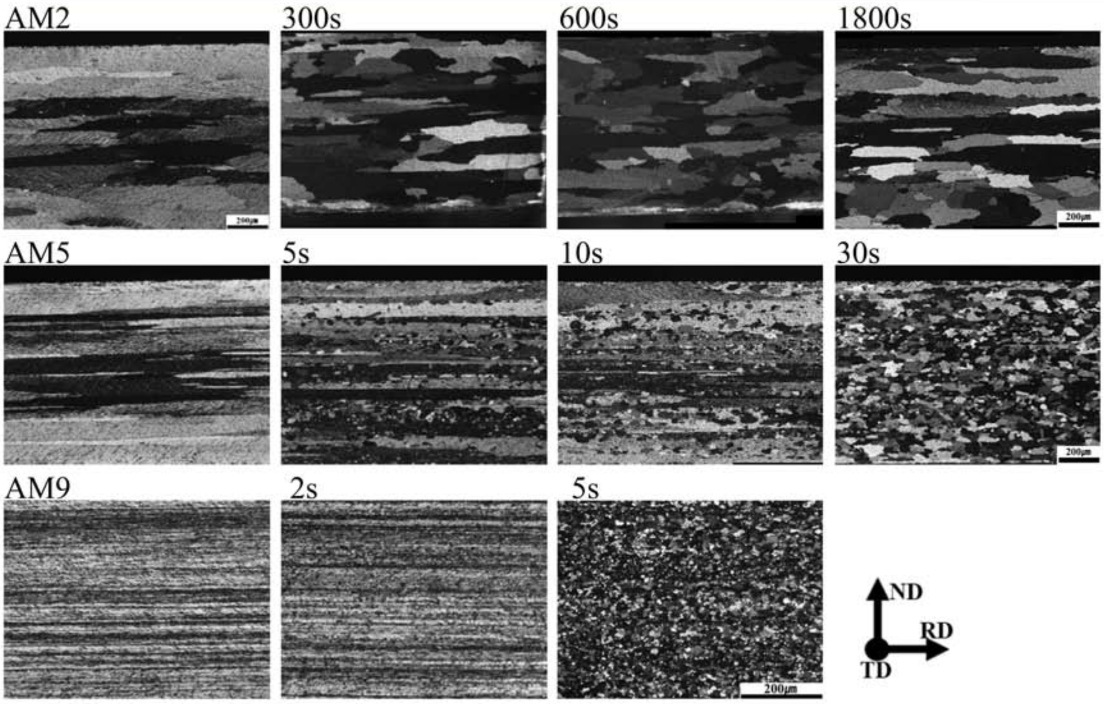

Figure 5.9: Evolution of the recrystallization microstructure for the AM2, AM5 and AM9 at 350 °C for different holding time.

explained by the change in dislocation density. These results strongly suggest that the recrystallization behavior is progressed by the dislocation absorption and relaxation of the lattice strains. When the recrystallization process is completed, the dislocation densities for the AM2, AM5 and AM9 specimens show similar values, which are amounted to be $0.71\times10^{14}m^{-2}$, $0.87\times10^{14}m^{-2}$ and $0.78\times10^{14}m^{-2}$, respectively.

As it can be seen in the Figs. 5.9 and 5.10, the recrystallization behavior proceeded by short period, especially the AM9 with large strain is completed within 5s at 350 °C. In order to observe the evolution microstructure of the dislocations during the recrystallization more clearly, TEM observation was conducted for the specimen annealed at lower temperature of 300 °C. TEM bright field images for AM5 and AM9 annealed at 300 °C are shown in Figs. 5.11 and 5.13,

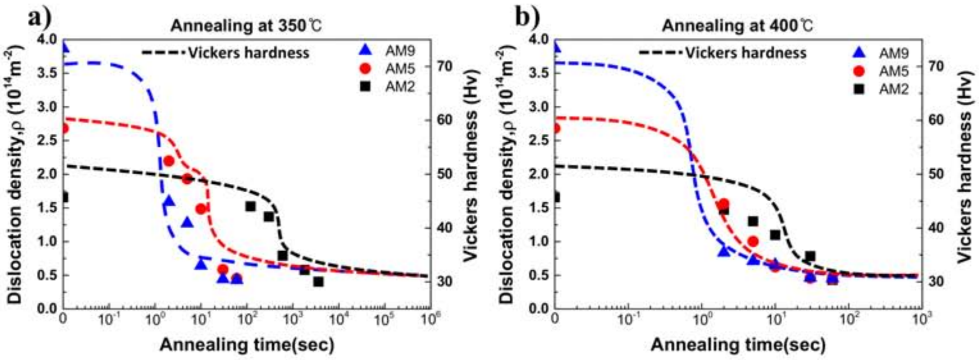

Figure 5.10: Change in the dislocation density as a function of annealing time at (a) 350 °C and (b) 400 °C in the AM2, AM5 and AM9.

respectively. As shown in Fig. 5.11a, the pinning of dislocation by fine particle inside of the grain is observed for AM5 annealed for 120s. Most of dislocations were recovered in the upper and lower part of the fine particle, while the pinned dislocation was remained due to the presence of the fine particle. After annealing for 600s, a hexagonal shaped dislocation network can be seen at the sub-boundary connected from region-I to II (Fig. 5.11b). The spacing of the dislocations in dislocation network is changed depending on the distance from the high angle boundary. For instance, the mesh size at region-I near the high angle grain boundary is amounted to be 32 *nm*, while the spacing of the mesh at region-II is 27 *nm*. Jones et al. (1979) reported that the absorption of each interior dislocation by HAGB generally results in the formation and rearrangement of different boundary dislocations, and this series of dislocation absorption processes lead to the emission of arrayed dislocation in the grain boundary by stress relaxation from the boundary edge where the low angle boundary contacts the high angle boundary.

Judging from the transmission image of dislocation arrangement in Fig. 5.11c, several boundaries consisting of the dislocation arrays are overlaid. For instance, at the area as indicated by A-B-C subdivides the lath-shaped grain into two parts, which are three dimensionally connected to the edge of the HAGB as indicated by D and E. Furthermore, several dislocations isolated from the dislocation arrays can be seen in the bottom side of the lath shaped grain. Accounting the above observation results, the region enclosed by the dislocation arrays indicates the initial stage of the sub-grain formation, where dislocation boundary is gradually developed by the subsequent annealing due to the migration of the dislocation boundary.

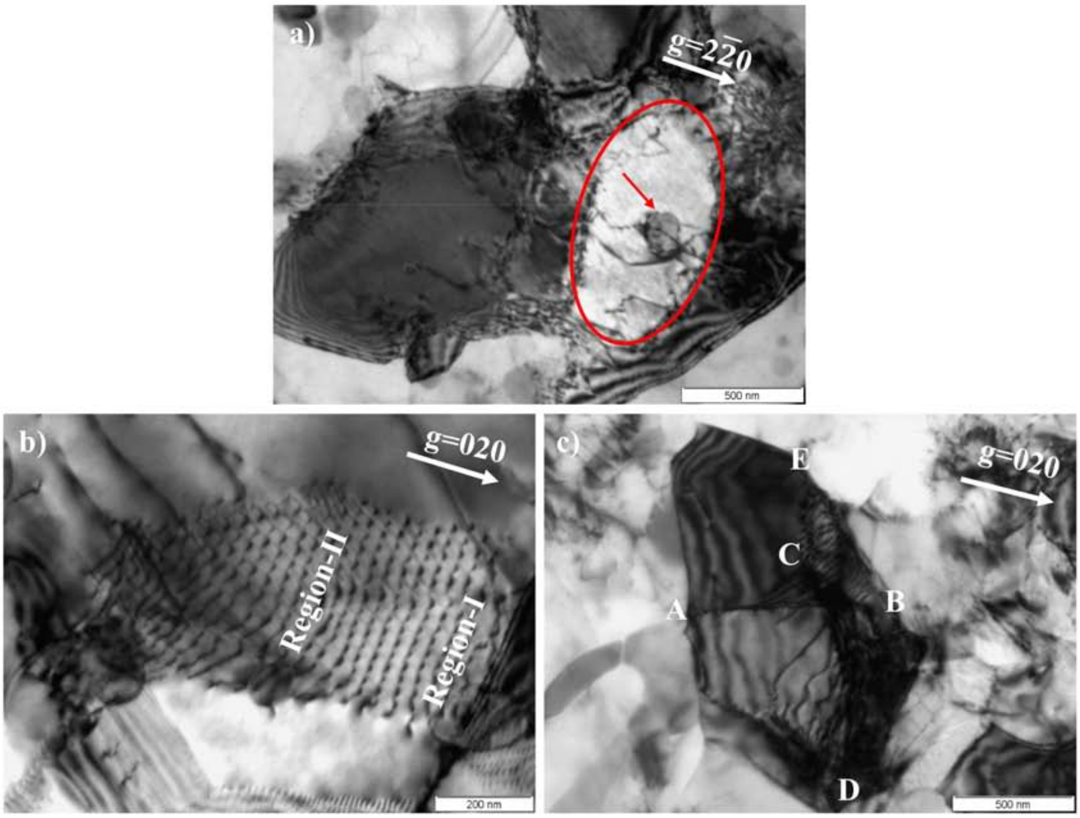

Figure 5.11: Evolution microstructure of AM5 annealed at 300 °Cfor (a) 120s and (b, c) 600s

The mechanism of subgrain growth in this specimen with low plastic deformation can be seen schematically in Fig. 5.12. The cell structure enclosed by tangled dislocations are generated inside the grains by cold rolling (Fig. 5.12a), which is changed into the subgrains by rearrangement of dislocations during the recovery stage (Fig. 5.12b). By subsequent annealing, subgrain boundaries are coalesced with adjacent subgrain, leading to larger subgrain with irregular shape of lower misorientation angle (Fig. 5.12c). This continues until the subgrains grow to a size of grain surrounded by HAGB during recrystallization, from which point the grain will begin to grow and abnormal grain growth can occur.

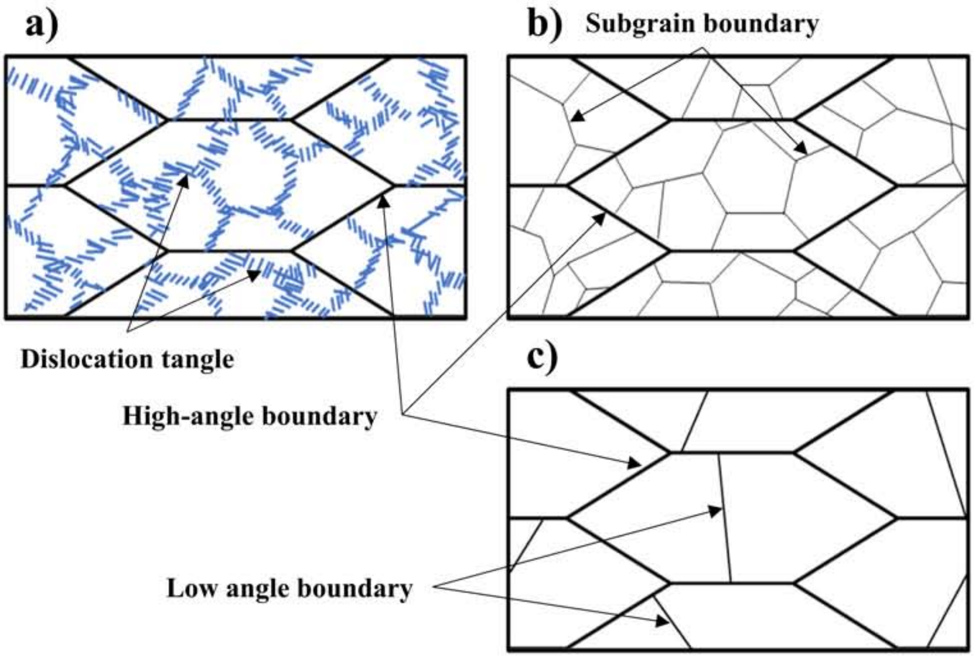

Figure 5.12: Schematic diagram for formation and coalescence of sub-grains during annealing. a) cold-rolled structure with low plastic deformation, b) formation of subgrain during recovery and c) coalescence of the subgrain by subsequent annealing

Fig. 5.13a, b and c show TEM microstructure of annealed AM9 specimen. For 5s (Fig. 5.13a and b), the recovery is delayed by the pinning effect due to the presence of a fine particle (white circle in Fig. 5.13a), thereby remaining the dislocation around the fine particle inside grain (Fig. 5.13a). In the meanwhile, preferentially recrystallized grain without interior dislocation was frequently observed next to the coarse particle by PSN effect (Fig. 5.13b).

When annealing was conducted for the 60s (Fig. 5.13c), the recrystallized grain was formed with a convex curvature and a straight boundary pinned by fine particles (white circle). It is possible to predict the direction of growth of recrystallized grains of heavily deformed specimens that naturally depend on the migration characteristics of the high-angle boundary. Since the driving pressure increases as the radius of curvature increases, the grains with concave curvature are subjected to a greater driving pressure than convex curvature toward the center of curvature. Therefore, unless the boundary is formed in a straight line, the grain growth will occur on the convex curvature side. Further details on the driving pressure are discussed in later section of thermodynamic pressure.

The recrystallized grains formed with convex curvature can be seen in both Fig. 5.13b and c, where a straight boundary pinned by particles is also observed. This implied that the recrystallized grain will grow in the direction of the convex curvature (indicated by white arrow) by further annealing, while the migration of straight boundaries will be retarded where the grain boundaries and dislocations are pinned by fine particles (white circle in Fig. 5.13a and c).

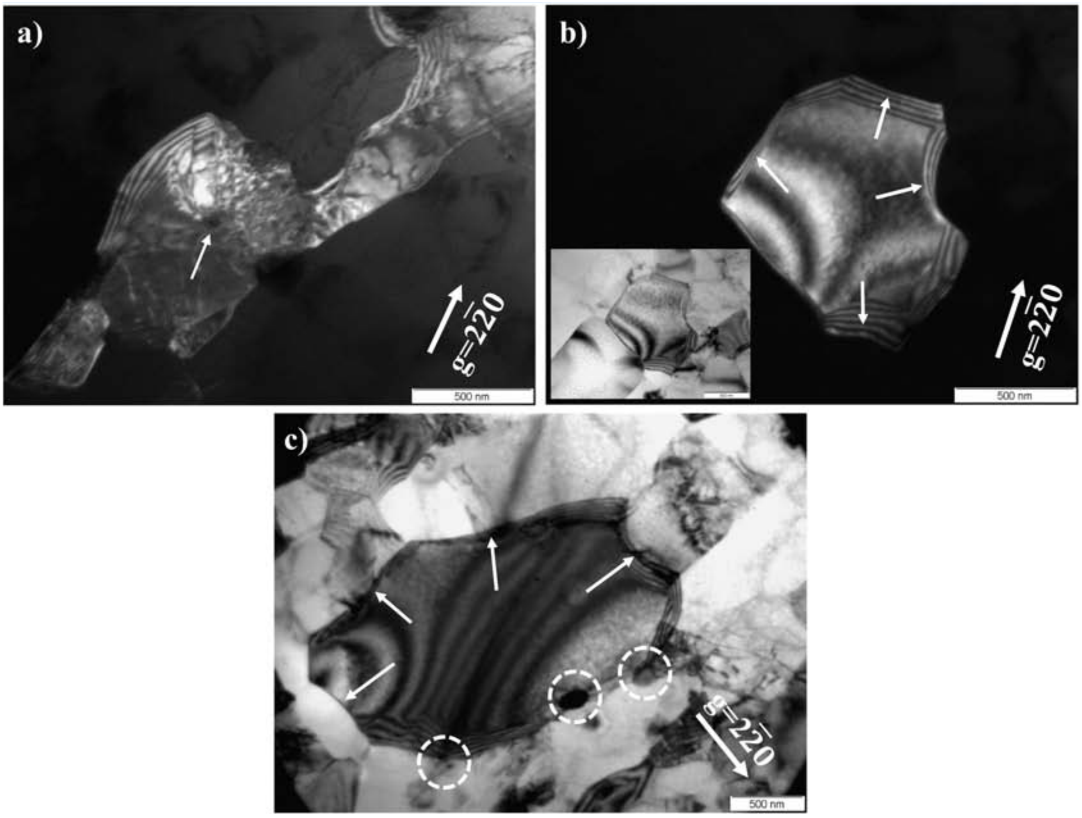

Figure 5.13: Evolution microstructure of AM9 annealed at 300 °C for (a, b) 5s, and (c) 60s

5.4 Discussions

5.4.1 Evolution of dislocation density

The dislocation density tends to increase in proportional to plastic strain, which leads to the formation of LAGBs by dislocation rearrangement. In principle, the recovery process is considered as the evolution of sub-grains which is associated with the migration of LAGBs at the region with the large strain energy differences or orientation gradients (Doherty and Cahn, 1972).

The evolution of the dislocation density and crystallite size for

AM2, AM5 and AM9 under the annealing temperature at 350 °C and 400 °C are represented in Fig. 5.14. The profiles of dislocation density and crystallite size for AM2, AM5 and AM9 are represented by solid and dotted lines, respectively, where annealing temperatures are indicated by symbols with black square for 350 °C and red triangle for 400 °C. The respective recovery and recrystallization stages during annealing were indicated as recovery and RC, where the distinction between both of the stages as a function of annealing time was obtained via the modified Johnson-Mehl-Avrami-Kolmogorov (JMAK) microhardness model in Chapter 2.

As shown in Fig. 5.14, the coarsening of crystallite occurred faster at 400 °C than low temperature at 350 °C, thereby the size of new recrystallized grains decreased in inverse proportion to annealing temperature. Therefore, a large number of nuclei for recrystallization are created by rapid migration and consumption of dislocations at high temperatures, leading to refinement of the grains by impingements between the new recrystallized grains.

The relationship between crystallites size and dislocation density during annealing could be considered in terms of the dislocation annihilation, nucleation and growth for recrystallization. Since the stored energy of the formed subgrain structure during recovery is still large, it would be further lowered by the coarsening of the subgrain during recrystallization. It can be seen in Fig. 5.14a, AM2 exhibits little change in the dislocation density and crystallite size through a relatively slow recovery at 350 °C, and rapid coarsening occurred at the beginning of recrystallization. Accounting the fact that the dislocation density is sharply dropped at recrystallization, energy dissipation by dislocation annihilation under the recovery of AM2 is not significant. Moreover, since the stored energy associated with the dislocation density in AM2 is relatively low, it takes longer annealing time for the absorbing process of the dislocations into the LAGBs and the triple junction motion of HAGBs.

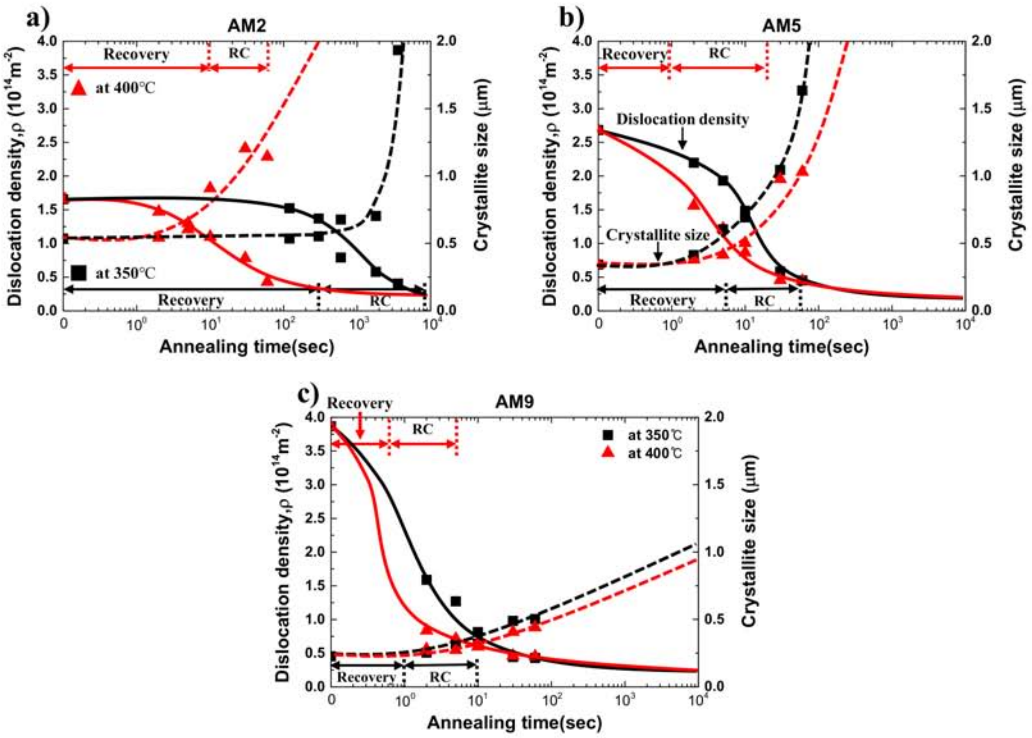

Figure 5.14: Evolution of the dislocation density and crystallite size as a function of annealing time at 350 °C and 400 °C in the (a) AM2, (b) AM5 and (c) AM9

The above facts are also supported by the change in the number fraction of LAGBs to HAGBs as mentioned in Chapter 2 (see Fig. 2.14), where the ratio of HAGBs and LAGBs in AM2 was gradually increased with increasing the annealing time, while that in AM9 exhibited almost constant value of the HAGBs and LAGBs ratio from the beginning of the annealing. This implies that the recovery is mainly due to the absorption process of dislocations into LAGBs, while the recrystallization is owing to the transition from LAGBs into HAGBs by further absorption of dislocations.

5.4.2 Driving force for recrystallization

In Chapter 2, the apparent activation energies for recrystallization were evaluated as 332KJ/mol for AM2, 239KJ/mol for AM5 and 115KJ/mol for AM9. where the apparent activation energy for recrystallization of AM9 is almost similar to the activation energy for self-diffusion in the aluminum (84 kJ/mol (Balluffi, 1970)) and AM2 and AM5 are is similar to the activation energy for lattice-diffusion of the Mn atoms (Bakker et al., 1990). The recrystallization kinetics of the cold-rolled AA3003 alloy increases the nucleation sites and grain boundary mobility due to the stored energy associated with the dislocation density, which is strongly dependent on the amount of reduction.

The changes in the number fraction of LAGBs and HAGBs associated with grain boundary energies, γ_b, under cold rolling conditions are important when discussing the mobility of grain boundaries during annealing. The energy of simple tilt boundary is given by Read-Shockley (W. T. Read, 1953).

$$\gamma_b = \gamma_{max}\frac{\theta}{\theta_{max}}(1 - ln\frac{\theta}{\theta_{max}}), \qquad (0 < \theta \leq \theta_{max}) \tag{5.5}$$

where θ_{max} is high angle boundary (commonly considered 15 degrees) and γ_{max} is the value of boundary energy when the boundary is at a high angle. γ_{max} is considered to be 0.324 J/m^2 in the aluminum (Murr, 1975).

According to Eq. (5.5), the energy of the low angle boundary increases with increasing misorientation θ, while the energy per dislocation decreases with increasing misorientation. In view of geometrically necessary dislocations (Muraishi, 2014), the contribution of the dislocation self-energy would be negligibly smaller than that of dislocation interaction energy when a certain boundary is assumed by the large numbers of dislocations.

Assuming that the energy stored by plastic deformation is dissipated by recrystallization and grain boundary migration when the towing possibility, dislocation annihilation, or dislocation absorption into the boundary is accompanied with, the stored energy, E_d, can be estimated from the dislocation density in view of self-energy of dislocations.

$$E_D = c_2 \rho G b^2 \tag{5.6}$$

where, c_2 is pre-factor for dislocation energy (0.5 is often used for self-energy of dislocation by line tension approximation). Substituting dislocation densities calculated in present study, $1.66\times10^{14} m^{-2}$ for AM2, $2.68\times10^{14} m^{-2}$ for AM5 and $3.87\times10^{14} m^{2}$ for AM9, and material constants, G=$2.6\times10^{10} Nm^2$, b = 0.286 nm, stored energy for AM2, AM5 and AM9 is amounted to be 3.1×10^5, 4.9×10^5 and $7.1\times10^5 J/m^3$, respectively. Accounting the equilibrium of thermodynamic pressure, critical radius of recrystallized grain can be predicted by following formula,

$$r_{crit} = 2\gamma_b / E_d \tag{5.7}$$

where γ_b is the grain boundary energy for 0.324 J/m^2 in the aluminum, and E_d is the stored energy (thermodynamic pressure).

By substituting thermodynamic pressure (stored energy) and grain boundary energy, critical radius of recrystallized grain yields, approximately 1.8 μm for AM2, 1.3 μm for AM5 and 0.9 μm for AM9. This result indicates that AM9 shows good consistency in prediction and observation results due to higher driving force for recrystallization (Fig. 5.14b and c), which also indicates that region of the recrystallization would not be restricted around the fine secondary particles during annealing. In the meanwhile, the values of critical radius predicted for AM2 and AM5 specimens are deviated from the observation results, which is reflected by the larger apparent activation energy for AM2 ($331kJ/mol$) and AM5 ($239kJ/mol$). Although the activation energy for recrystallization in the AM5 specimen is similar to the activation energy for Mn diffusion ($217kJ/mol$ (Bakker et al., 1990)) in aluminum, since the concurrent precipitation did not occur during recovery and recrystallization in present study, the activation energy for recrystallization of AM2 and AM5 may be influenced by pinning effect of fine secondary particles. In particular, accounting the crystallite size of AM2 is hardly changed during recovery, driving pressure for recrystallization and migration might be insufficient against the considerable pinning effect of fine particles on LAGB and HAGB. Hence, the fine secondary particle on LAGB and HAGB is responsible for the significant delay in recovery and recrystallization of AM2 and AM5.

5.4.3 Thermodynamic pressure for boundary migration

The initial thickness of grains are gradually decreased to several hundreds of nm depending on the plastic strain (Fig. 5.2e). Such decrease in thickness of high angle grain leads to the large number fraction of HAGBs. In addition, the constituent particles accompanied with the local plastic deformation of the matrix phase may act as an important factor to promote recrystallization.

In the case of lower plastic deformation (AM2 and AM5), considerable time is required for recovery and relaxation of dislocation microstructure, which is attributed to a lower driving force associated with dislocation density for recovery. Although the recovery stage for AM5 and AM9 in present study was completed in a very short time, the stored energy for AM2 in Fig. 5.15 are calculated by using Eq. (5.6), which are amounted to be $3.1{\times}10^5 J/m^3$ (as-rolled), $2.8{\times}10^5 J/m^3$ (annealed at 350 °C for 2min), $2.7{\times}10^5 J/m^3$ (annealed at 400 °C for 2s). Hence the energy consumption at 350 °C and 400 °C during the recovery stage are amounted to be 8.1% and 11.1%, respectively. These results consistent with the consumed energy as reported in (Kalu and Waryoba, 2007), where the 10% of the stored energy is consumed in the recovery process.

In literature (Humphreys et al., 2004), the tangled dislocations are changed into the dislocation wall, which is further developed into three-dimensional dislocation cell and sub-grains with increase of the plastic strain. Furthermore, thermal activation by the heat-treatment process promotes the dislocation rearrangement and boundary migration. It can be seen in Fig. 5.11c that the number of dislocations inside the grain is decreased by annealing at 300 °C for 600s, which leads to the formation of a well-developed subgrain with a size of about $1\mu m$ in the recovery stage. It is noted that, although the OM microstructure is not represented, recrystallization is not confirmed under the same annealing condition of AM5 (at 300 °C for 600s). Therefore, the transition of the dislocation microstructure from the cell wall to the subgrain boundary is supposed to be the representative behavior in the recovery process. Hence the rearrangement of dislocations for the formation of sub-grains is considered to be dominant rather than the annihilation of dislocations in the recovery process.

According to the literature (Humphreys et al., 2004), the net driving pressure, P_{net}, acted on the boundary of recrystallized grain is given as,

$$P_{net} = P_d - P_p - P_c = \frac{\alpha\rho G b^2}{2} - \frac{3 f_v \gamma_b}{d} - \frac{2\gamma_b}{r} \tag{5.8}$$

where the pressures associated with dislocation density, pinning effect by particles, boundary curvature are P_d, P_p and P_c, respectively. α is a constant of the order of 0.5, G is the shear modulus, f_v is the volume fraction of second-phase particle, γ_b is the boundary energy and d is the diameter of particle. Recalling the results of Section 5.3.2 and 5.3.4, it can be seen that the net driving pressure associated with dislocation density and curvature of boundary affecting the nucleation and growth rate of recrystallized grains in AM9 is greater than AM2 and AM5 with lower plastic deformation.

Regarding the higher magnitude of plastic strain (AM9), the large numbers of smaller recrystallized grains would be formed with the rapid recovery and nucleation rate. According to the boundary energy in Eq. (5.2), since the large magnitude of plastic strain induced the recrystallized grain with smaller radius of curvature (Fig. 5.14), the retarding pressure for the boundary migration would be increased as suggested in Eq. (5.8). Hence, the rapid recovery and nucleation rate is merely due to the higher stored energy which exceeded the retarding pressure for the boundary migration. Furthermore, as can be seen in Fig. 5.14c, the growth and migration would be delayed due to the pinning effect of particles. This indicates that, although the recrystallized grain would be firstly introduced at the rotation zone around the coarse particle, the region of the recrystallization is extended into the grain interior because of smaller retarding pressure. Eventually, the recrystallized grains are surrounded by the coarse particles.

This can be supported by the results analyzed by the EBSD and FE-SEM. The recrystallized grains are preferentially generated next to the coarse precipitate (white region, in Fig. 5.15a), where the grain orientation spread (GOS) of aluminum indicates misorientation less than 3 degrees(Sridharan et al., 2016). The convex curvature of recrystallized grain reflects the pinning effect of fine particles as can be seen in Fig. 5.15b

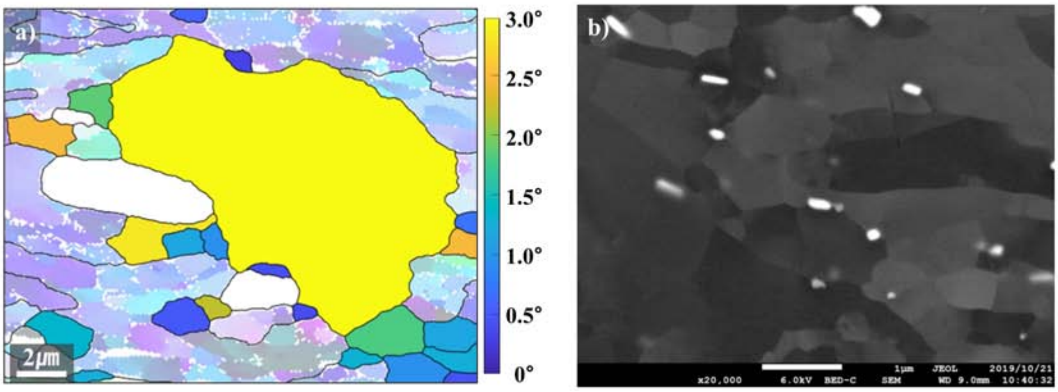

Figure 5.15: Grain orientation spread (GOS) map overlaid with IPF map in AM9 annealed at 300 °C for 30s shows growth of recrystallized grain (a) in deformation zone around a coarse particle and (b) in dispersoid zone.

5.4.4 Residual stress of α-Al(Mn, Fe)Si particle

Since the contribution of second-phase particles on the work hardening is significant, the dislocation microstructure strongly depends on the distribution microstructure of the second-phase under a certain reduction rate. This indicates that the magnitude and gradient of plastic strain are locally changed with the spatial distribution of the particles, which is commonly referred to as the particle deformation zone(Humphreys, 1977). This deformation zone provides a strong driving force for the nucleation at the local point during the initial recrystallization process. Accounting the fact that the deformation zones formed by an accumulation of dislocation around the second-phase particles are introduced by a mismatch of plastic strain between the Al matrix and the inhomogeneous precipitate, residual strain and stress around the second particle can be treated by the inhomogeneous inclusion problem under cold rolling condition (T. Mura, 1987).

According to the Eshelby theory, the stress disturbed by the inhomogeneity can be mentioned by assuming mismatch of the plastic strain, ε_{ij}^{P}, as following,

$$\sigma_{ij} = C_{ijkl}^{*}(\varepsilon_{kl}^{0} + S_{klmn}\varepsilon_{mn}^{**} - \Delta\varepsilon_{kl}^{P}) \tag{5.9}$$

$$\sigma_{ij} = C_{ijkl}(\varepsilon_{kl}^{0} + S_{klmn}\varepsilon_{mn}^{**} - \varepsilon_{kl}^{**}) \tag{5.10}$$

with

$$\varepsilon_{mn}^{**} = \varepsilon_{mn}^{*} - \Delta\varepsilon_{mn}^{P} \tag{5.11}$$

where ε_{mn}^{**} is total eigenstrain, $\Delta\varepsilon_{mn}^{P}$ is the mismatch of the plastic strain, ε_{mn}^{*} is equivalent (fictitious) eigenstrain, C_{ijkl} and C_{ijkl}^{*} are the stiffness of the matrix and the precipitate, respectively. Note that in the absence of the mismatch of the plastic strain in Eq. (5.9) ($\Delta\varepsilon_{mn}^{P}$=0), the relation of the total eigenstrain and the applied strain becomes

$$(S_{klmn} + (C_{klij}^{*} - C_{klij})^{-1}C_{ijmn})\varepsilon_{mn}^{*} = -\varepsilon_{pq}^{0} \tag{5.12}$$

The residual stress, $\Delta\sigma_{ij}$, can be simply given by substituting the applied strain, ε_{mn}^{0}=0 (T. Mura, 1987; Muraishi, 2014),

$$\Delta\sigma_{ij} = C_{ijkl}^{*}(S_{klmn}\varepsilon_{mn}^{**} - \Delta\varepsilon_{mn}^{P}) = C_{ijkl}(S_{klmn}\varepsilon_{mn}^{**} - \varepsilon_{kl}^{**}) \tag{5.13}$$

Thus, the relation of the total eigenstrain and the mismatch of the plastic strain is given as(T. Mura, 1987; Muraishi, 2014),

$$\varepsilon_{mn}^{**} = ((C_{ijkl}^{*} - C_{ijkl})S_{klmn} + C_{ijkl}I_{klmn})^{-1}C_{ijkl}^{*}\Delta\varepsilon_{kl}^{P} \tag{5.14}$$

Once the eigenstrain is solved, the stress inside the inhomogeneity can be computed by Eq. (5.9) and (5.10). The residual stress outside the α-Al(Mn, Fe)Si precipitate can be derived from the exterior point Eshelby tensor as follows,

$$\sigma_{ij}(\text{outside}) = C_{ijkl}\overline{G}_{ijmn}\varepsilon^{**}_{mn} \tag{5.15}$$

where $\overline{G}_{ijmn}$ is the exterior point Eshelby tensor.The explicit expressions of the exterior Eshelby tensors $\overline{G}$ for ellipsoidal inclusions are given by Ju and Sun (2001). Full details of all the mathematical basis associated with micromechanics are given elsewhere (T. Mura, 1987; Ju and Sun, 1999, 2001; Muraishi and Taya, 2019).

Note that, under the assumption of that the plastic deformation is dominant in the aluminum matrix, the mismatch of the plastic strain in Eq. (5.9) can be set as $\Delta\varepsilon^{P}_{kl}{=}{-}\varepsilon^{0}_{kl}$. In order to predict the shape of the deformation zone, the distribution of the residual stress around the α-Al(Mn, Fe)Si precipitate is evaluated by the equivalent stress, σ_{eqv}, as following formula,

$$\sigma_{eqv} = \sqrt{\frac{1}{2}[(\sigma_{11}-\sigma_{22})^2+(\sigma_{22}-\sigma_{33})^2+(\sigma_{33}-\sigma_{11})^2+6(\sigma_{12}^2+\sigma_{23}^2+\sigma_{31}^2)]} \tag{5.16}$$

Substituting the nominal plastic strain of present study, $\Delta\varepsilon^{P}_{33} = -\Delta\varepsilon^{P}_{11} = 0.2$ (AM2), 0.5 (AM5) and 0.9 (AM9), and $\Delta\varepsilon^{P}_{22} = 0$ into Eq. (5.9), the total eigenstrain is amounted to be $\varepsilon^{**}_{33} = -\varepsilon^{**}_{11} = 0.299$, $\varepsilon^{**}_{22} = 0$ for AM2, $\varepsilon^{**}_{33} = -\varepsilon^{**}_{11} = 0.747$, $\varepsilon^{**}_{22} = 0$ for AM5 and $\varepsilon^{**}_{33} = -\varepsilon^{**}_{11} = 1.344$, $\varepsilon^{**}_{22} = 0$ for AM9. The residual stresses and the equivalent stress computed by Eq. (5.9) and (5.16) are listed in Table 5.3. It should be noted that the computed values of stress in Table 5.3 are greatly large magnitude, even if the mismatch of plastic strain under the cold rolling condition is assumed to be, $\Delta\varepsilon^{P}_{33}{=}{-}\Delta\varepsilon^{P}_{11} = 0.2$ (reduction rate, 20%).

Note that the magnitude of the residual stress is proportional to that of eigenstrain strain within the context of linear elasticity. Accounting the stress level for plastic deformation as a yield criterion, the spatial distribution of the stress outside the inhomogeneity is important to consider the stress accumulation and relaxation phenomena under cold rolling. Assuming that the matrix phase is exclusively deformed, while the particle is completely elastic under the cold rolling, the spatial distribution of the plastic deformation is reproduced by summing the uniform plastic strain and the disturbed plastic strain in matrix phase. Accounting this fact, it is apparent that the residual stress field would be canceled by the opposite sign of uniform eigenstrain in inhomogeneity. Moreover, in view of average theory, this stress relaxation can be attained by the eigenstrain assumed outside the inhomogeneity, which is more suited for the stress relaxation by dislocations. Note that, the magnitude of the disturbed plastic strain is inversely proportional to the considering volume of the region enclosing the inhomogeneity in equivalent inclusion system though Eq. (5.10). This concept of stress relaxation is based on the Tanaka-Mori theorem (Tanaka and Mori, 1972; Muraishi and Taya, 2020), and the dislocation punching model reported by Shibata et al. (1992).

Table 5.3: Comparison of the residual stress inside the α-Al(Mn, Fe)Si precipitate with sphere computed by Eq. (5.9) under cold rolling condition ($\varepsilon^0_{11} = -\varepsilon^0_{33} = 0.2$, 0.5 and 0.9, and $\varepsilon^0_{22} = 0$). Equivalent stress σ_{eqv} is computed by Eq. (5.16).

	σ_{ij} / GPa			
ε^0_{ij}	σ_{11}	σ_{22}	σ_{33}	σ_{eqv}
0.2	8.25	$< 10^{-17}$	−8.25	14.29
0.5	20.62	$< 10^{-17}$	−20.62	35.72
0.9	37.12	$< 10^{-17}$	−37.12	64.29

Therefore, in order to realize the displacement field around the inhomogeneity, total displacement inside/outside the inhomogeneity is computed by superposing the elastic and the plastic displacements. Recalling the fact that the equilibrium shape of the inhomogeneity given from Eq. (5.9) and (5.10) is that without the uniform plastic strain in the solid, superposition of the uniform plastic strain can realize the deformed shape of the inhomogeneity in the matrix phase. Note that the displacement solutions for interior and exterior points are solved analytically by using following expressions(T. Mura, 1987; Meng et al., 2012; Muraishi, 2016),

$$u_i = 1/8\pi(1-\nu)(\varepsilon^*_{jl}\psi_{,jli} - 2\nu\varepsilon^*_{mn}\phi_{,i} - 4(1-\nu)\varepsilon^*_{il}\phi_{,l}) \tag{5.17}$$

with

$$\begin{aligned}\phi_{,i} =& -x_i I_I(\lambda) && (5.18)\\ \psi_{,ijl} =& -\delta_{ij}x_l(I_L(\lambda) - a_I^2 I_{IL}(\lambda))\\ & -x_i x_j(I_J(\lambda) - a_I^2 I_{IJ}(\lambda))_{,l}\\ & -(\delta_{il}x_j + \delta_{jl}x_i)(I_J(\lambda) - a_I^2 I_{IJ}(\lambda)) && (5.19)\end{aligned}$$

where I-integrals for spherical inhomogeneity were used for the calculation (see text book of Micromechanics, pages 84 and 92). Total eigenstrain given from Eq. (5.14) is substituted into Eq. (5.17).

Computed results of the total displacement and the residual stress solved by Eq. (5.17) and (5.9) are represented in Fig. 5.16. It can be seen from the deformed shape, the total displacement of the matrix phase is strongly constrained by the inhomogeneity, where the thickness of the region at the right and left part of inhomogeneity is hardly changed in ND direction. Moreover, judging from the signs of σ_{11} and σ_{33}, dilatational stress can be found in the vicinity of the precipitate along x_1-axis (red, positive) and x_3-axis (blue, negative). Therefore, in order to cancel and relax the large magnitude of residual stress, multiple slip system of crystal dislocations should be operated, in which the volume average of the dislocation swept area should be comparable to the equivalent eigenstrain assumed in the inhomogeneity as predicted in Eq. (5.14).

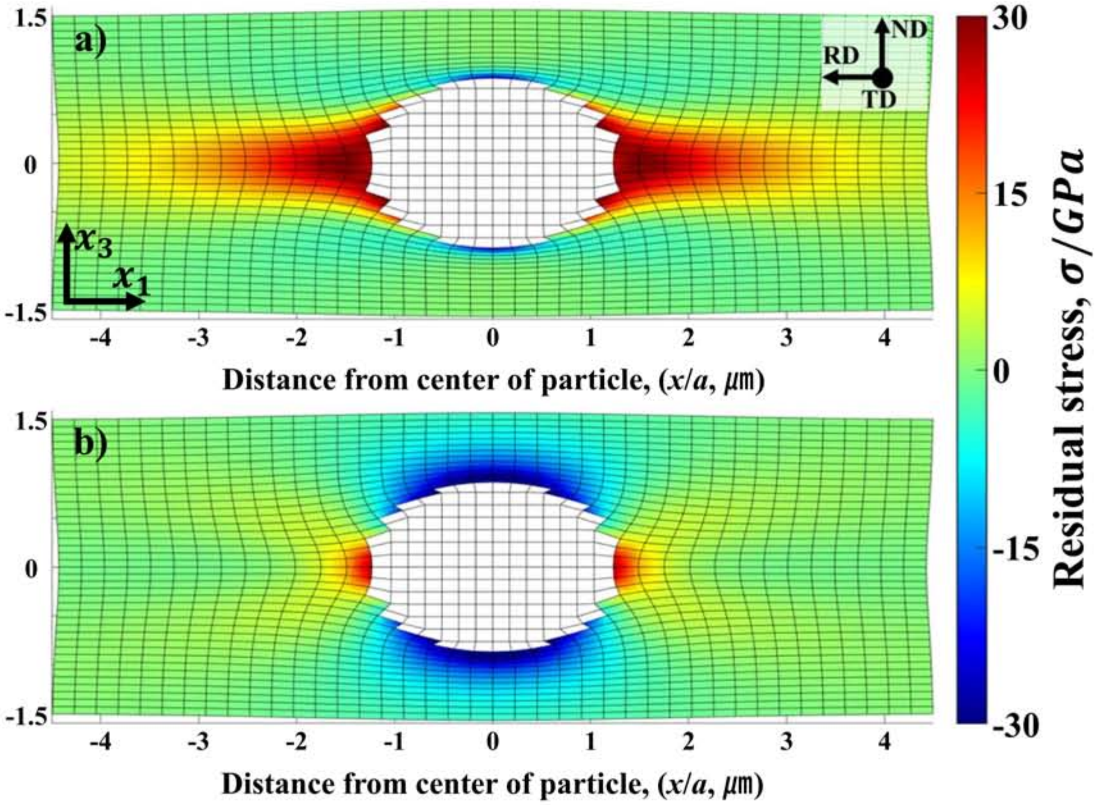

Figure 5.16: Deformed shape and residual stress around the spherical inhomogeneity (α-Al(Mn, Fe)Si precipitate) under cold rolling condition ($\Delta\varepsilon_{33}^{P} = -\Delta\varepsilon_{11}^{P} = 0.5$, and $\Delta\varepsilon_{22}^{P} = 0$) are represented in (a) σ_{11} and (b)σ_{33}. The displacement and residual stress outside the inhomogeneity is deduced from Eq. (5.16) and (5.9), respectively.

Accounting the spatial distribution of the residual stress, it is natural to consider that the misorientation of the deformed zone is accompanied with the fine equi-axed grains surrounding the inhomogeneity as shown in Fig. 5.3c. In fact, this can be supported by EBSD analysis (see Section 3.3) for the deformed microstructure and misorientation angle at the deformed zone parallel to the rolling direction near the particles. The profile of misorientation angles predicted by the displacement gradient and measured by EBSD analysis are represented in Fig. 5.17. The misorientation angles of the prediction and measurement results are indicated by the dotted and solid lines, respectively. The maximum misorientation angle at the rotated zone near the precipitate as indicated by the red solid line was amounted to be 45 degrees at a distance of 1.9 μm from the interface for AM5 (misorientation measured by point to origin in Fig. 5.5b), which is similar to the misorientation angle 45 degrees calculated from the gradient of the displacement at the same position (red dotted line in Fig. 5.17).

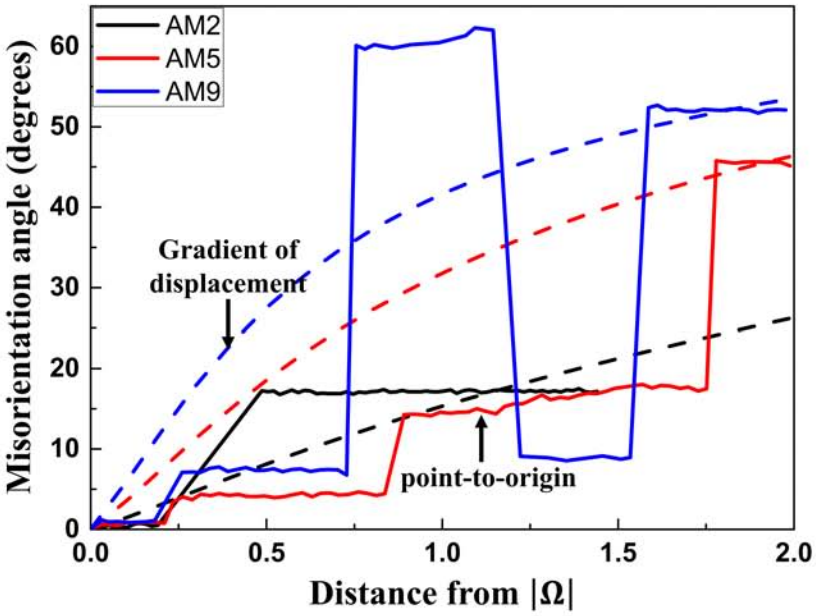

Figure 5.17: Misorientation angles profile across the rotated zone formed around the α-Al(Mn, Fe)Si precipitate measured by prediction of displacement gradient and EBSD analysis.

5.5 Conclusions

The deformation and recrystallization of cold-rolled AA3003 aluminum alloy has been investigated in terms of dislocation density, misorientation angle and residual stress around constituent particles. The dislocation density measured by X-ray was proportionally changed with the amount of reduction of the cold-rolled sheets, which shows a good consistency with the TEM observation results and microhardness profiles. In the meanwhile, the constant value of lattice strain was found in X-ray strain analysis regardless of the amount of plastic strain. These results suggest that the HAGBs would be developed by dislocation absorption into the boundaries by further plastic deformation, which, eventually leads to an increase in the driving force for the recrystallization. By subsequent annealing, the further development of the HAGBs was observed especially during the recrystallization, where the microhardness and the dislocation density are sharply decreased with an increase of the annealing time. This implies that the dislocation annihilation and dislocation absorption into the boundary were exclusively occurred during recrystallization.

The residual stress analysis based on the Micromechanics theory revealed that the region of residual stress resembles with the deformed zone around coarse particle, which is attributed to the fact that the elastic and plastic deformation of the matrix phase is strongly constrained by inhomogeneity. The prediction results of the displacement gradient along the rolling direction are consistent with the line profiles of the misorientation angle measured by EBSD analysis. These results suggest that the deformed zone composed of the fine equiaxed grains would be formed under the relaxation process of the residual stress due to local plastic deformation in the vicinity of the coarse particle, which may be responsible for the PSN effect on the recrystallization.

Chapter 6

General conclusion

6.1 Summary

Static recovery and recrystallization kinetics are essential mechanisms to achieve grain refinement for improved mechanical properties. Therefore, detailed experiments and simulation work for recovery and recrystallization have been reported during the past decades by a lot of researchers. In practice, the stored energy necessary for grain refinement is controlled under the cold rolling process with a wide range of plastic deformation because the deformed microstructure is greatly influenced by mechanical loading conditions. When secondary particles are embedded in the matrix phase, work hardening of the cold-rolled sheet and its restoration behavior under annealing treatment are changed depending on inhomogeneous distribution of constituent particles. Moreover, in case of that precipitation is simultaneously occurred during the restoration process, recovery and recrystallization kinetics become more complex ones since constituent particles have a role of an accumulation site of dislocations as well as a nucleation site for recrystallization. In this manner, dislocations and precipitates are mutually correlated in terms of stress accumulation and relaxation under the work hardening and restoration process.

Therefore, in the present thesis, the effect of the constituent particles on the plastic deformation, recovery and recrystallization behaviors in the cold-rolled Al-Mn based alloy has been studied, where the amount of plastic deformation and the number density of constituent particles have been precisely controlled by the combination of different homogenization and cold rolling conditions. Especially, in view of thermodynamics pressure for the restoration process, dislocation density and its absorption and annihilation behaviors in the plastically deformed microstructure are essential factors, which have been experimentally determined by means of TEM observation, X-ray and EBSD analysis, etc. While, in view of continuum mechanics, residual stress arisen from the mismatch of plastic strain between the matrix phase and the constituent particle should be compensated by dislocation accumulation around the constituent particles, which might be responsible for PSN (particle stimulated nucleation) effect frequently observed around the constituent particles. Based on this assumption, stress disturbance around inhomogeneity under cold rolling conditions has been formulated by micromechanics theory. The conclusions of each chapter of the present thesis are listed as follows:

In Chapter 1, the general characteristics, manufacturing methods and applications of Al-Mn based alloys are briefly introduced, and literature of the plastically deformed microstructure as well as the recovery and recrystallization behaviors during annealing has been reviewed. From the viewpoint of the recovery and recrystallization influenced by the constituent particles, the importance of the residual stress around the inhomogeneity introduced by the mismatch of the plastic strain was pointed out. The experimental methods in this study were mentioned, and the purpose and outline of this thesis were also described.

In Chapter 2, the effect of the amount of reduction on the recrystallization kinetics and microstructure evolution of cold-rolled Al-Mn based alloys with the certain volume fraction of constituent particle was investigated. The driving force for recrystallization of cold-rolled AA3003 alloys is apparently increased in proportion to the amount of reduction and the critical strain for the onset of primary recrystallization in the AA3003 aluminum alloy was obtained experimentally, where it was found that the PSN effect in the rotation zone around the coarse particle required a critical strain of about 0.5. The apparent activation energy for recrystallization of AM9 is similar to the activation energy for self-diffusion in aluminum. On the other hand, AM2 and AM5 show higher activation energies, which is due to Zener drag effect by the fine secondary particles during the restoration process. The number fraction of HAGBs increased in proportion to the amount of reduction, and the HAGBs of cold-rolled AA 3003 alloys with low strain rate increases significantly at the beginning of annealing and remains almost constant when the number ratio of HAGBs reaches 70-80%.

In Chapter 3, the correlation between the constituent particles and microstructure evolution of cold-rolled AA3003 alloys with different dispersoids distribution during annealing was investigated by applying the same magnitude of plastic strain (90% thickness reduction). The AA3003 alloy homogenized with a slow heating rate leads to precipitation of large numbers of fine secondary particles and the spheroidization and growth of coarse particles, whereas homogenized with a fast-heating rate inhibits the precipitation of fine secondary particles and the coarse particles increase the number density by breaking up during holding at high temperatures. Due to the different distribution and size of the constituent particles, the significant difference was found in the dislocation density and lamella spacing associated with the driving force even when the plastic deformation was performed under the same cold rolling conditions. In addition, the AA3003 alloy with the larger Mn supersaturation by fast-heating rate significantly retarded the recrystallization behavior due to simultaneous recrystallization and precipitation, which was significantly affecting the size and shape of the recrystallized grains. The growth of the primary recrystallized grains around the coarse particle by PSN effect was found along ND direction at the region of PFZ produced during the homogenization, which is highly dependent on the distribution of fine secondary particles produced by homogenization and concurrent precipitation. The recovery behavior of severely plastically deformed AA3003 alloy is dominated by the triple junction motion and is strongly dependent on the lamellar spacing associated with the distribution of fine secondary particles.

In Chapter 4, the analysis of residual stress around constituent particles in cold-rolled Al-Mn based alloy under cold rolling conditions was investigated by a micromechanics-based model. By assuming the mismatch of plastic strain between the matrix and the inhomogeneous precipitate, the stress disturbed by the inhomogeneity was predicted by the present model and made comparisons with the recrystallization microstructure preferentially induced around the coarse particles. The magnitude of the disturbed strain (stress) field is strongly dependent on the aspect ratio of inhomogeneity, which suggests that the region of the higher magnitude of internal stress tends to be plastically deformed to accommodate the dislocations with a higher orientation-gradient. Accounting the large magnitude of the residual stress around the coarse constituent particle, the stress predicted by this study would be lowered by the introduction of crystal dislocations, where dislocations are arranged to offset the fictitious eigenstrain at the interface of the inhomogeneity. Moreover, assuming the conservation of the Burgers vector during the plastic relaxation process, it is suggested that the deformation zone is accompanied by a large misorientation angle around the inhomogeneous precipitate. These predictions suggest that the large magnitude of plastic strain would be introduced in the vicinity of the spherical precipitate, so that the recrystallization by the PSN effect in the rotated zone effectively may acts as a site for nucleation at both ends of the spherical precipitate. To the author's best knowledge, this is the first attempt to model critical around constituent particles under cold rolling conditions.

In Chapter 5,the effect of reduction ratio and the subsequent annealing treatment on the recrystallization behavior under the certain volume fraction of primary particle in AA3003 alloy were investigated in terms of the change in dislocation density, the misorientation angle and the residual stress around the constituent particles. Although the lattice strain measured by X-ray exhibits almost a constant value with an increase of reduction ratio, the dislocation density and the micro-hardness are proportionally increased with the magnitude of plastic strain. Accounting the development of HAGBs with an increase of the dislocation density during the plastic deformation, the sharp decrease in dislocation density during the recrystallization process is attributed to the dislocation absorption into the boundaries. As the increases of reduction ratio, the commonly observed lamellar boundary evolves into an equiaxed structure within a short time by the triple junction motion. This clearly implies that the recovery and recrystallization behavior in the fine secondary particle region are dominated by the relationship between the amount of reduction and the driving pressure associated with the boundary curvature. By assuming the mismatch of the plastic strain between the matrix and constituent particle, the residual stress around the coarse precipitate was analytically solved by the interior and exterior point Eshelby tensor. Especially, the deformed shape strongly constrained by the inhomogeneity reflects the exclusive plastic deformation of the matrix phase, which shows a good agreement with the line profiles of the misorientation angle measured by EBSD.This fact implies that the area of large stress disturbance around the coarse particle is relaxed by the plastic strain of dislocation accumulation, which might be the origin of the particle stimulated nucleation around the coarse particle.

In Chapter 6, the important findings and conclusions of each chapter were briefly summarized.

As mentioned in the above conclusions, the effect of the constituent particle on the work hardening and restoration behaviors in the cold rolled Al-Mn based alloy investigated in the present thesis clearly indicates that the stored energy was locally changed in accord with the residual stress and the dislocation microstructure formed around the constituent particles. The major important findings in the present thesis are summarized as bellow,

- The increase in the size and number density of constituent particles caused an increase in the dislocation density during the plastic deformation, which enhanced the further development of the dislocation boundaries with the certain ratio of HAGBs and LAGBs. During this process, the local misorientation angle of HAGBs distributed around the constituent particle was proportionally increased with the reduction ratio.

- Under the same magnitude of plastic strain by cold rolling, the lamellar spacing was apparently decreased and the dislocation density was increased with an increase of the number density of dispersoids, which resulted in the formation of the smaller recrystallized grains within a shorter annealing time.
- The models that predict critical residual stresses to initiate recrystallization around constituent particles by micromechanical-based theory have been shown to provide a novel approach. The residual stress analysis strongly suggests that the mismatch of plastic strain should be compensated by the dislocation accumulation in accordance with the residual stress distribution. Therefore the recrystallization would be preferentially occurred around the coarse particles.

These results emphasize that the evolution of microstructures under the work hardening and annealing is highly dependent on the constituent particle characteristics (such as distribution, number density, size and shape). The level of work hardening is dominated by the size and shape of primary particles and the number density of the fine secondary particles. In addition, the restoration behavior is promoted in proportion to the size of the primary particles, while the increase in the number density of fine secondary particles suppressed the dislocation and boundary migration.

6.2 Future prospect

The experimental and computational approach in this study allows a better understanding of the recrystallization kinetics of cold-rolled Al-Mn based alloys during annealing. A code based on Micromechanics theory for predicting the residual stress occurring around constituent particles under cold rolling conditions has been successfully developed, and combining this model with the deformation zone around the constituent particles can predict the critical strain to promote recrystallization by PSN around coarse particles during annealing. However, extensive modeling of the relationship between constituent particles and cold rolling requires more experimental data on constituent particles and improvements to the code of the predictive model. Therefore, some interesting findings identified in this study are proposed for future work as follows.

1. It is well known that the quantitative analysis of HAGBs and dislocation structures by the EBSD and the TEM observations exhibits the experimental errors to some extent since the distribution, shape, and size of constituent particles locally changed depending on the observation area. Therefore, when the evolution of microstructure (such as the dislocation and boundary migration, and change in number fraction of HAGBs) is observed in a certain region using in-situ equipment (such as XRD, TEM and EBSD etc.,), the influence of constituent particles on plastic deformation and annealing can be analyzed more accurately.

2. The fine secondary particles introduced by homogenization were observed not only in spherical shape but also in long rod-shaped. In this work, the effect of particle shape on the residual stress

around the constituent particles under the residual stress was analytically computed in view of continuum elasticity, however the orientation relationship between the constituent particles and the matrix was not considered. By taking into account the effect of the crystal orientation on the nucleation and growth of recrystallization and the formation of secondary particles, a more precise discussion will be made for the dislocation accumulation and annihilation around the constituent particles.

3. The present thesis dealt with the residual stress locally distributed around a single particle with a different aspect ratio, which is due to the effectiveness of the analytical solution of the interior and exterior point Eshelby tensor. Although the stress disturbed by large numbers of particles under external loading is not considered, this problem can be simply solved by applying the Mori-Tanaka mean field theory under a specific volume fraction of the precipitate.

4. The author proposed prediction method, the residual stress around a coarse particle under cold rolling condition, can be commonly applicable for the other alloy systems. The elastic field around a coarse particle with various different shapes can be simply attained on the author developed computation code with the input values, elastic modulus, magnitude of plastic strain, external loading condition, aspect ratio of particle, etc.

Bibliography

Albert, W., 2018. Introduction to Aluminium Alloy. Introduction to Aluminium Alloy , 1–3.

Ashby, M.F., 1966. Work hardening of dispersion-hardened crystals. Philosophical Magazine 14, 1157–1178. doi:10.1080/14786436608224282.

Ashby, M.F., 1970. The deformation of plastically non-homogeneous materials. Philosophical Magazine 21, 399–424. doi:10.1080/14786437008238426.

Ashby, M.F., Johnson, L., 1969. On the generation of dislocations at misfitting particles in a ductile matrix. Philosophical Magazine 20, 1009–1022. doi:10.1080/14786436908228069.

Association, A., 2014. Aluminum Can Life-Cycle Update Report Briefing December 2014. Technical Report December. The Aluminum Association. URL: https://www.aluminum.org/sustainability/sustainability-reports.

Association, A., 2019. Aluminum Association. Technical Report. The Aluminum Association. URL: https://www.aluminum.org/.

ASTM, 1997. Standard Test Methods for Determining Average Grain

Size Using Semiautomatic and. Methods 03, 1–24. doi:10.1520/E1382-97R10.Section.

Bakker, H., Bonzel, H., Bruff, C., Dayananda, M., Gust, W., Horvath, J., Kaur, I., Kidson, G., LeClaire, A., Mehrer, H., Murch, G.E., Neumann, G., Stolica, N., Stolwijk, N., 1990. Diffusion in Solid Metals and Alloys. volume 26 of *Landolt-Börnstein - Group III Condensed Matter*. Springer-Verlag, Berlin/Heidelberg. URL: http://materials.springer.com/bp/docs/978-3-540-46109-8, doi:10.1007/b37801.

Baldwin, W.M., 1949. Residual stresses in metals.

Balluffi, R., 1970. On measurements of self-diffusion rates along dislocations in F.C.C. Metals.

Bay, B., Hansen, N., 1979. Initial stages of recrystallization in aluminum of commercial purity. Metallurgical Transactions A 10, 279–288. doi:10.1007/BF02658335.

Beck, P.A., 1954. Annealing of cold worked metals. Advances in Physics 3, 245–324. doi:10.1080/00018735400101203.

Bever, M.B., Holt, D.L., Titchener, A.L., 1973. The stored energy of cold work. Progress in Materials Science 17, 5–177. doi:10.1016/0079-6425(73)90001-7.

Bhaduri, A., 2018. Fundamentals of mechanical working. volume 264. doi:10.1007/978-981-10-7209-3_10.

Bieda, M., Sztwiertnia, K., Korneva, A., Czeppe, T., Orlicki, R., 2010. Orientation mapping study on the inhomogeneous microstructure evolution during annealing of 6013 aluminum alloy. Solid State Phenomena 163, 13–18. doi:10.4028/www.scientific.net/SSP.163.13.

Brechet, Y.J., 2010. The role of the triple line in solid-state microstructural evolutions: Interplay with interfaces and consequences on instabilities and pattern selection. Scripta Materialia 62, 910–913. doi:10.1016/j.scriptamat.2010.03.002.

Chaix, J.M., Mortensen, A., Passerone, A., 2010. Preface to the viewpoint set: Triple lines. Scripta Materialia 62, 887–888. doi:10.1016/j.scriptamat.2010.03.018.

Chen, C.L., Richter, A., Thomson, R.C., 2010. Investigation of mechanical properties of intermetallic phases in multi-component Al-Si alloys using hot-stage nanoindentation. Intermetallics 18, 499–508. doi:10.1016/j.intermet.2009.09.013.

Chen, S.P., Kuijpers, N.C., Van Der Zwaag, S., 2003. Effect of microsegregation and dislocations on the nucleation kinetics of precipitation in aluminium alloy AA3003. Materials Science and Engineering A 341, 296–306. doi:10.1016/S0921-5093(02)00245-9.

Chiang, C.R., 2007. Stress concentration around a spherical cavity in a cubic medium. Journal of Strain Analysis for Engineering Design 42, 155–162. doi:10.1243/03093247JSA226.

Christian, J., 1975. THE THEORY OF TRANSFORMATIONS IN METALS AND ALLOYS. Pergamon. doi:https://doi.org/10.1016/B978-0-08-044019-4.X5000-4.

Committee, A.H., 1990. Properties and Selection: Nonferrous Alloys and Special-Purpose Materials. ASM International. doi:10.31399/asm.hb.v02.9781627081627.

Davis, J., 2001. Aluminum and Aluminum Alloys. doi:10.1361/autb2001p351.

De Siqueira, R.P., Sandim, H.R.Z., Raabe, D., 2013. Particle stimulated nucleation in coarse-grained ferritic stainless steel. Metallurgical and Materials Transactions A: Physical Metallurgy and Materials Science 44, 469–478. doi:10.1007/s11661-012-1408-x.

De Vincentis, N.S., Avalos, M.C., Benatti, E.A., Kliauga, A., Brokmeier, H.G., Bolmaro, R.E., 2017. XRD and EBSD analysis of anisotropic microstructure development in cold rolled F138 stainless steel. Materials Characterization 123, 137–152. doi:10.1016/j.matchar.2016.11.018.

Dehmas, M., Aeby-Gautier, E., Archambault, P., Serrière, M., 2013. Interaction between eutectic intermetallic particles and dispersoids in the 3003 aluminum alloy during homogenization treatments. Metallurgical and Materials Transactions A: Physical Metallurgy and Materials Science 44, 1059–1073. doi:10.1007/s11661-012-1473-1.

Doherty, R., Cahn, R., 1972. Nucleation of New Grains in Cold Worked Metals. Journal of the Less-Common Metals 28, 279.

Donadille, C., Valle, R., Dervin, P., Penelle, R., 1989. Development of texture and microstructure during cold-rolling and annealing of F.C.C. alloys: Example of an austenitic stainless steel. Acta Metallurgica 37, 1547–1571. doi:10.1016/0001-6160(89)90123-5.

Du, Q., Jacot, A., 2005. A two-dimensional microsegregation model for the description of microstructure formation during solidification in multicomponent alloys: Formulation and behaviour of the model. Acta Materialia 53, 3479–3493. doi:10.1016/j.actamat.2005.04.004.

Eskin, D.G., 2008. Physical metallurgy of direct chill casting of aluminum alloys. CRC press.

Furu, T., Orsund, R., Nes, E., 1995. Subgrain Growth in Heavily Deformed Investigation and Modelling Treatment. Acta Metallurgica et Materialia 43, 2209–2232.

Garces, G., Bruno, G., Wanner, A., 2006. Residual stresses in deformed random-planar aluminium/Saffil® short-fibre composites. Materials Science and Engineering A 417, 73–81. doi:10.1016/j.msea.2005.10.069.

Gholinia, A., Humphreys, F.J., Prangnell, P.B., 2002. Production of ultra-fine grain microstructures in Al-Mg alloys by coventional rolling. doi:10.1016/S1359-6454(02)00253-7.

Gil Sevillano, J., van Houtte, P., Aernoudt, E., 1980. Large strain work hardening and textures. Progress in Materials Science 25, 69–134. doi:10.1016/0079-6425(80)90001-8.

Gottstein, G., Shvindlerman, L.S., 2009. Grain Boundary Migration in Metals. CRC Press. doi:10.1201/9781420054361.

Gupta, A., Lee, S.T., Wagstaff, R.B., 2007. Direct chill casting of aluminium-manganese against aluminium-silicon layer via Novelis fusion process. Materials Technology 22, 71–75. doi:10.1179/175355507X214069.

H, F.P.W., 1978. THE EFFECTS OF SEGREGATION AND PRECIPITATION ON THE ANNEALING BEHAVIOUR AND GRAIN

SIZE OF ALUMINIUM ALLOYS. ALUMINIUM, SUPPL. ENGL. 54, 135–142.

Haessner, F., Schmidt, J., 1993. Investigation of the recrystallization of low temperature deformed highly pure types of aluminium. Acta Metallurgica Et Materialia 41, 1739–1749. doi:10.1016/0956-7151(93)90193-V.

Håkonsen, A., Mortensen, D., Benum, S., Pettersen, T., Furu, T., 2002. Modelling the metallurgical reactions during homogenisation of an AA3103 alloy, in: Light Metals: Proceedings of Sessions, TMS Annual Meeting (Warrendale, Pennsylvania), Springer, Cham. pp. 793–800. doi:10.1007/978-3-319-48228-6_130.

Hansen, N., Bay, B., 1981. Initial stages of recrystallization in aluminium containing both large and small particles. Acta Metallurgica 29, 65–77. doi:10.1016/0001-6160(81)90087-0.

Harris, K., Singh, V., King, A., 1998. Grain rotation in thin films of gold. Acta Materialia 46, 2623–2633. doi:10.1016/S1359-6454(97)00467-9.

Hazzledine, P.M., Hirsch, P.B., 1974. A coplanar Orowan loops model for dispersion hardening. Philosophical Magazine 30, 1331–1351. doi:10.1080/14786437408207286.

Healy, D., Jones, R.R., Holdsworth, R.E., 2006. New insights into the development of brittle shear fractures from a 3-D numerical model of microcrack interaction. Earth and Planetary Science Letters 249, 14–28. doi:10.1016/j.epsl.2006.06.041.

Hielscher, R., Silbermann, C.B., Schmidla, E., Ihlemannb, J., 2019.

Denoising of crystal orientation maps. Journal of Applied Crystallography 52, 984–996. doi:10.1107/S1600576719009075.

Hirsch, J., 2007. Virtual fabrication of aluminum products: microstructural modeling in industrial aluminum production. Wiley-Vch.

Huang, Y., Humphreys, F.J., Ferry, M., 2000. Annealing behaviour of deformed cube-oriented aluminium single crystals. Acta Materialia 48, 2543–2556. doi:10.1016/S1359-6454(00)00068-9.

Hughes, D., Hansen, N., 2000. Microstructure and strength of nickel at large strains. Acta Materialia 48, 2985–3004. doi:10.1016/S1359-6454(00)00082-3.

Humphreys, F., 1979a. Local lattice rotations at second phase particles in deformed metals. Acta Metallurgica 27, 1801–1814. doi:10.1016/0001-6160(79)90071-3.

Humphreys, F., 1979b. Recrystallization mechanisms in two-phase alloys. Metal Science 13, 136–145. doi:10.1179/msc.1979.13.3-4.136.

Humphreys, F., 1982. Inhomogeneous Deformation of Some Aluminium Alloys at Elevated Temperature, in: Strength of Metals and Alloys (ICSMA 6). Elsevier. volume 2, pp. 625–630. doi:10.1016/B978-1-4832-8423-1.50103-6.

Humphreys, F., 1985. Dislocations and properties of real materials. London: The Institute of Metals , 175–204.

Humphreys, F., 1997. A unified theory of recovery, recrystallization and grain growth, based on the stability and growth of cellular microstructures—I. The basic model. Acta Materialia 45, 4231–4240. doi:10.1016/S1359-6454(97)00070-0.

Humphreys, F., Bate, P., 2003. Gradient plasticity and deformation structures around inclusions. Scripta Materialia 48, 173–178. doi:10.1016/S1359-6462(02)00359-7.

Humphreys, F., Rohrer, G.S., Rollett, A., 2004. Recrystallization and Related Annealing Phenomena. Elsevier. doi:10.1016/B978-0-08-044164-1.X5000-2.

Humphreys, F.J., 1977. The nucleation of recrystallization at second phase particles in deformed aluminium. Acta Metallurgica 25, 1323–1344. doi:10.1016/0001-6160(77)90109-2.

Humphreys, F.J., 1999. Quantitative metallography by electron backscattered diffraction. Journal of Microscopy 195, 170–185. doi:10.1046/j.1365-2818.1999.00578.x.

Humphreys, F.J., 2000. Particle stimulated nucleation of recrystallization at silica particles in nickel. Scripta Materialia 43, 591–596. doi:10.1016/S1359-6462(00)00442-5.

Humphreys, F.J., Ardakani, M.G., 1994. The deformation of particle-containing aluminium single crystals. Acta Metallurgica Et Materialia 42, 749–761. doi:10.1016/0956-7151(94)90272-0.

Humphreys, F.J., Hirsch, P.B., 1976. Work-hardening and recovery of dispersion hardened alloys. Philosophical Magazine 34, 373–390. doi:10.1080/14786437608222029.

Humphreys, F.J., Kalu, P.N., 1990. The plasticity of particle-containing polycrystals. Acta Metallurgica Et Materialia 38, 917–930. doi:10.1016/0956-7151(90)90164-C.

Humphreys, F.J., Martin, J.W., 1968. The effect of dispersed phases upon the annealing behaviour of plastically deformed copper crystals. Philosophical Magazine 17, 365–403. doi:10.1080/14786436808226169.

J. D. Eshelby, 1957. The determination of the elastic field of an ellipsoidal inclusion, and related problems. Proceedings of the Royal Society of London. Series A. Mathematical and Physical Sciences 241, 376–396.

J. D. Eshelby, 1959. The elastic field outside an ellipsoidal inclusion. Proceedings of the Royal Society of London. Series A. Mathematical and Physical Sciences 252, 561–569. doi:10.1098/rspa.1959.0173.

Jazaeri, H., Humphreys, J.F., 2009. The Effect of Initial Grain Size on Transition from Discontinuous to Continuous Recrystallization in a Highly Cold Rolled Al-Fe-Mn Alloy. Materials Science Forum 396-402, 551–556. doi:10.4028/www.scientific.net/msf.396-402.551.

Joffre, T., Miettinen, A., Wernersson, E.L., Isaksson, P., Gamstedt, E.K., 2014. Effects of defects on the tensile strength of short-fibre composite materials. Mechanics of Materials 75, 125–134. doi:10.1016/j.mechmat.2014.04.003.

JohnE.Hatch, 1984. Aluminum: Properties and Physical Metallurgy - ASM International. doi:10.31399/asm.hb.v02a.a0006505.

Jones, A.R., Ralph, B., Hansen, N., 1979. Subgrain Coalescence and the Nucleation of Recrystallization at Grain Boundaries in Aluminium. Proceedings of the Royal Society A: Mathematical, Physical and Engineering Sciences 368, 345–357. doi:10.1098/rspa.1979.0134.

Jordon, J.B., Horstemeyer, M.F., Solanki, K., Xue, Y., 2007. Damage and stress state influence on the Bauschinger effect in aluminum alloys. Mechanics of Materials 39, 920–931. doi:10.1016/j.mechmat.2007.03.004.

Jr, F.P., Arruda, A., Padilha, A.F., 1986. Resistance to recrystallization in Al-1% Mn alloys. Zeitschrift für Metallkunde 77, 522–528.

Ju, J.M., Sun, L.Z., 1999. A novel formulation for the exterior- point eshelby's tensor of an ellipsoidal inclusion. Journal of Applied Mechanics, Transactions ASME 66, 570–574. doi:10.1115/1.2791090.

Ju, J.W., Sun, L.Z., 2001. Effective elastoplastic behavior of metal matrix composites containing randomly located aligned spheroidal inhomogeneities. Part I: Micromechanics-based formulation. International Journal of Solids and Structures 38, 183–201. doi:10.1016/S0020-7683(00)00023-8.

Kalu, P.N., Waryoba, D.R., 2007. A JMAK-microhardness model for quantifying the kinetics of restoration mechanisms in inhomogeneous microstructure. Materials Science and Engineering A 464, 68–75. doi:10.1016/j.msea.2007.01.124.

Kaufman, J.G., 1999. Properties of aluminum alloys: tensile, creep, and fatigue data at high and low temperatures. ASM international.

Kaufman, J.G., Rooy, E.L., 2004. Aluminum alloy castings: properties, processes, and applications.

King, A.H., 1999. Geometric and thermodynamic properties of grain boundary junctions. Interface Science 7, 251–271. doi:10.1023/a:1008769209265.

Koken, E., Chandrasekaran, N., Embury, J.D., Burger, G., 1988. The role of particle distribution in recrystallization in two-phase alloys. Materials Science and Engineering 104, 163–168. doi:10.1016/0025-5416(88)90418-1.

Komatsu, S.Y., Fujikawa, S.I., 1997. Electrical resistivity of light metals and alloys - Its measurement, interpretation and application. Part 1 methodology and basic values. doi:10.2464/jilm.47.170.

Kuhlmann, D., 1948. Zur Theorie der Nachwirkungserscheinungen. Zeitschrift für Physik 124, 468–481. doi:10.1007/BF01668885.

L. M. Brown, Stobbs, W.M., 1971. The work-hardening of copper-silica. Philosophical Magazine , 1201–1233doi:https://doi.org/10.1080/14786437108217406.

Lefevre-Schlick, F., Brechet, Y., Zurob, H.S., Purdy, G., Embury, D., 2009. On the activation of recrystallization nucleation sites in Cu and Fe. Materials Science and Engineering A 502, 70–78. doi:10.1016/j.msea.2008.10.015.

Lewis, M.H., Martin, J.W., 1963. Yielding and work-hardening in internally oxidised copper alloys. Acta Metallurgica 11, 1207–1214. doi:10.1016/0001-6160(63)90109-3.

Lewis V. McCarty, Craig, N.C., 1997. Production of aluminum metal by electrochemistry. Technical Report. American Chemical Society.

Li, S., Sauer, R.A., Wang, G., 2007. The eshelby tensors in a finite spherical domain - Part I: Theoretical formulations. Journal of Applied Mechanics, Transactions ASME 74, 770–783. doi:10.1115/1.2711227.

Li, Y.J., Arnberg, L., 2002. Precipitation of Dispersoids in DC-Cast 3003 Alloy. Materials Science Forum 396-402, 875–880. doi:10.4028/www.scientific.net/MSF.396-402.875.

Li, Y.J., Arnberg, L., 2003a. Evolution of eutectic intermetallic particles in DC-cast AA3003 alloy during heating and homogenization. Materials Science and Engineering A 347, 130–135. doi:10.1016/S0921-5093(02)00555-5.

Li, Y.J., Arnberg, L., 2003b. Quantitative study on the precipitation behavior of dispersoids in DC-cast AA3003 alloy during heating and homogenization. Acta Materialia 51, 3415–3428. doi:10.1016/S1359-6454(03)00160-5.

Li, Y.J., Muggerud, A.M., Olsen, A., Furu, T., 2012. Precipitation of partially coherent α-Al(Mn,Fe)Si dispersoids and their strengthening effect in AA 3003 alloy. Acta Materialia 60, 1004–1014. doi:10.1016/j.actamat.2011.11.003.

Liu, Q., Huang, X., Lloyd, D., Hansen, N., 2002. Microstructure and strength of commercial purity aluminium (AA 1200) cold-rolled to large strains. Acta Materialia 50, 3789–3802. doi:10.1016/S1359-6454(02)00174-X.

Liu, W.C., Radhakrishnan, B., 2010. Recrystallization behavior of a supersaturated Al-Mn alloy. Materials Letters 64, 1829–

1832. URL: http://dx.doi.org/10.1016/j.matlet.2010.05.046, doi:10.1016/j.matlet.2010.05.046.

Liu, Y.L., Hansen, N., Jensen, D.J., 1989. Recrystallization microstructure in cold-rolled aluminum composites reinforced by silicon carbide whiskers. Metallurgical Transactions A 20, 1743–1753. doi:10.1007/BF02663206.

Lloyd, D.J., Kenny, D., 1980. The structure and properties of some heavily cold worked aluminum alloys. Acta Metallurgica 28, 639–649. doi:10.1016/0001-6160(80)90130-3.

Lopez-Sanchez, M.A., Tommasi, A., Barou, F., Quey, R., 2020. Dislocation-driven recrystallization in AZ31B magnesium alloy imaged by quasi-in situ EBSD in annealing experiments. Materials Characterization 165, 110382. doi:10.1016/j.matchar.2020.110382.

McAlister, A.J., Murray, J.L., 1987. The (AlMn) Aluminum-Manganese system. Journal of Phase Equilibria 8, 438–447. doi:10.1007/BF02893153.

McQueen, H.J., Spigarelli, S., Kassner, M.E., Evangelista, E., 2016. Hot deformation and processing of aluminum alloys. CRC Press. doi:10.1201/b11227.

Meng, C., Heltsley, W., Pollard, D.D., 2012. Evaluation of the Eshelby solution for the ellipsoidal inclusion and heterogeneity. Computers and Geosciences 40, 40–48. doi:10.1016/j.cageo.2011.07.008.

Muraishi, S., 2014. Formulation of Eshelby's inclusion problem by BIEM (boundary integral equation method) and PDD (parametric dislocation dynamics). Mechanics of Materials 74, 41–55. doi:10.1016/j.mechmat.2014.03.004.

Muraishi, S., 2016. Efficient interpolation algorithm of electro-elastic Green's function for boundary integral equation method and Eshelby inclusion problem. International Journal of Solids and Structures 100-101, 297–306. doi:10.1016/j.ijsolstr.2016.08.025.

Muraishi, S., Taya, M., 2019. Average Eshelby tensor and elastic field for helical inclusion problems. International Journal of Solids and Structures 180-181, 125–136. doi:10.1016/j.ijsolstr.2019.07.017.

Muraishi, S., Taya, M., 2020. Eshelby problem in continuous shape transition of helical inclusion. International Journal of Solids and Structures 199, 36–42. doi:10.1016/j.ijsolstr.2020.04.024.

Murr, L.E., 1975. Interfacial phenomena in metals and alloys.

Nadella, R., Eskin, D.G., Du, Q., Katgerman, L., 2008. Macrosegregation in direct-chill casting of aluminium alloys. Progress in Materials Science 53, 421–480. doi:10.1016/j.pmatsci.2007.10.001.

Nagahama, K., Miki, I., 1974. PRECIPITATION DURING RECRYSTALLIZATION IN Al-Mn AND Al-Cr ALLOYS. Trans Jap Inst Met 15, 185–192.

Nes, E., Embury, J.D., 1975. Influence of a Fine Particle Dispersion on the Recrystallization Behaviour of a Two Phase Aluminium Alloy. Zeitschrift fuer Metallkunde 66, 589. doi:10.1016/S0550-3213(00)00476-4, arXiv:0005026.

Nes, E., Ryum, N., Hunderi, O., 1985. On the Zener drag. Acta Metallurgica 33, 11–22. doi:10.1016/0001-6160(85)90214-7.

Paggi, A., Angella, G., Donnini, R., 2015. Strain induced grain boundary migration effects on grain growth of an austenitic stainless steel during static and metadynamic recrystallization. Materials Characterization 107, 174–181. doi:10.1016/j.matchar.2015.07.003.

Patton, G., Rinaldi, C., Bréchet, Y., Lormand, G., Fougères, R., 1998. Study of fatigue damage in 7010 aluminum alloy. Materials Science and Engineering A 254, 207–218. doi:10.1016/s0921-5093(98)00762-x.

Poole, W.J., Wells, M.A., Parson, N.C., 2012. A Through Process Model for Extruded AA3xxx Aluminum Alloys. ICAA13 Pittsburgh , 293–298doi:10.1007/978-3-319-48761-8_45.

Raj, S., Iskovitz, I., Freed, A., 1996. Modeling the Role of Dislocation Substructure during Class M and Exponential Creep. ACADEMIC PRESS, INC. doi:10.1016/b978-012425970-6/50009-6.

Rios, P.R., Siciliano, F., Sandim, H.R.Z., Plaut, R.L., Padilha, A.F., 2005. Nucleation and growth during recrystallization. Materials Research 8, 225–238. URL: http://www.scielo.br/scielo.php?script=sci{_}arttext{&}pid=S1516-14392005000300002{&}lng=en{&}tlng=en, doi:10.1590/S1516-14392005000300002.

Roberts, W.L., 1978. Cold rolling of steel. Dekker.

Robson, J.D., 2016. The effect of internal stresses due to precipitates on twin growth in magnesium. Acta Materialia 121, 277–287. doi:10.1016/j.actamat.2016.09.022.

Ryen, Ø., Nijs, O., Sjölander, E., Holmedal, B., Ekström, H.E., Nes, E., 2006. Strengthening mechanisms in solid solution aluminum alloys. Metallurgical and Materials Transactions A: Physical Metallurgy and Materials Science 37, 1999–2006. doi:10.1007/s11661-006-0142-7.

Sharma, S.C., 2000. Effect of albite particles on the coefficient of thermal expansion behavior of the Al6061 alloy composites. Metallurgical and Materials Transactions A: Physical Metallurgy and Materials Science 31, 773–780. doi:10.1007/s11661-000-0019-0.

She, H., Shu, D., Dong, A., Wang, J., Sun, B., Lai, H., 2019. Relationship of particle stimulated nucleation, recrystallization and mechanical properties responding to Fe and Si contents in hot-extruded 7055 aluminum alloys. Journal of Materials Science and Technology 35, 2570–2581. doi:10.1016/j.jmst.2019.07.014.

Shekhar, S., King, A.H., 2008. Strain fields and energies of grain boundary triple junctions. Acta Materialia 56, 5728–5736. doi:10.1016/j.actamat.2008.07.053.

Shibata, S., Taya, M., Mori, T., Mura, T., 1992. Dislocation punching from spherical inclusions in a metal matrix composite. Acta Metallurgica et Materialia 40, 3141–3148. doi:10.1016/0956-7151(92)90477-V.

Simonovic, D., Sluiter, M.H., 2009. Impurity diffusion activation energies in Al from first principles. Physical Review B - Condensed Matter and Materials Physics 79, 1–12. doi:10.1103/PhysRevB.79.054304.

Smith, C.S., 1945. Grains, phases, and interfaces: An introduction of microstructure. Trans. Metall. Soc. AIME 175, 15–51.

Somerday, M., Humphreys, F., 2003. Recrystallisation behaviour of supersaturated Al–Mn alloys Part 1 – Al–0.3 wt-%Mn. doi:10.1179/026708303225008626.

Song, R., Harada, Y., Kumai, S., 2018. Influence of Cooling Rate on Primary Particle and Solute Distribution in High-Speed Twin-Roll Cast Al-Mn Based Alloy Strip. Materials transactions 59, 110–116. doi:10.2320/matertrans.F-M2017843.

Sridharan, N., Wolcott, P., Dapino, M., Babu, S.S., 2016. Microstructure and texture evolution in aluminum and commercially pure titanium dissimilar welds fabricated using ultrasonic additive manufacturing. Scripta Materialia 117, 1–5. doi:10.1016/j.scriptamat.2016.02.013.

Sun, N., Patterson, B.R., Suni, J.P., Doherty, R.D., Weiland, H., Kadolkar, P., Blue, C.A., Thompson, G.B., 2008. Effect of heating rate on recrystallization of twin roll cast aluminum. Metallurgical and Materials Transactions A: Physical Metallurgy and Materials Science 39, 165–170. doi:10.1007/s11661-007-9367-3.

Sun, N., Patterson, B.R., Suni, J.P., Simielli, E.A., Weiland, H., Allard, L.F., 2006. Microstructural evolution in twin roll cast AA3105 during homogenization. Materials Science and Engineering A 416, 232–239. doi:10.1016/j.msea.2005.10.018.

Sztwiertnia, K., Bieda, M., Korneva, A., 2013. Continuous and discontinuous recrystallization of 6013 aluminum alloy. Materials Science Forum 753, 221–224. doi:10.4028/www.scientific.net/MSF.753.221.

T. Mura, 1987. Micromechanics of Defects in Solids, Second Edition. Springer Netherlands.

T. Mura., 1997. The determination of the elastic field of a polygonal star shaped inclusion. Mechanics Research Communications 24, 473–482. doi:10.1016/S0093-6413(97)00052-9.

Tanaka, K., Mori, T., 1972. Note on volume integrals of the elastic field around an ellipsoidal inclusion. Journal of Elasticity 2, 199–200. doi:10.1007/BF00125528.

Tangen, S., Sjølstad, K., Furu, T., Nes, E., 2010. Effect of concurrent precipitation on recrystallization and evolution of the P-texture component in a commercial Al-Mn alloy. Metallurgical and Materials Transactions A: Physical Metallurgy and Materials Science 41, 2970–2983. doi:10.1007/s11661-010-0265-8.

Thomas, S.L., Wei, C., Han, J., Xiang, Y., Srolovitz, D.J., 2019. Disconnection description of triple-junction motion. Proceedings of the National Academy of Sciences of the United States of America 116, 8756–8765. doi:10.1073/pnas.1820789116.

Tóth, L.S., Beausir, B., Gu, C.F., Estrin, Y., Scheerbaum, N., Davies, C.H., 2010. Effect of grain refinement by severe plastic deformation on the next-neighbor misorientation distribution. Acta Materialia 58, 6706–6716. doi:10.1016/j.actamat.2010.08.036.

Totten, G.E., MacKenzie, D.S., 2003. Handbook of Aluminum: Vol. 1: Physical Metallurgy and Processes - 1st. CRC Press. doi:10.1201/9780203912607.

Totten, G.E., Mackenzie, D.S., 2003. Handbook of Aluminum: Volume 2: Alloy Production and Materials Manufacturing.

Ungár, T., Gubicza, J., Ribárik, G., Borbély, A., 2001. Crystallite size distribution and dislocation structure determined by diffraction profile analysis: Principles and practical application to cubic and hexagonal crystals. Journal of Applied Crystallography 34, 298–310. doi:`10.1107/S0021889801003715`.

Ungár, T., Ott, S., Sanders, P.G., Borbély, A., Weertman, J.R., 1998. Dislocations, grain size and planar faults in nanostructured copper determined by high resolution X-ray diffraction and a new procedure of peak profile analysis. Acta Materialia 46, 3693–3699. doi:`10.1016/S1359-6454(98)00001-9`, `arXiv:arXiv:1107.6045v2`.

Vandermeer, R.A., Hansen, N., 2008. Recovery kinetics of nanostructured aluminum: Model and experiment. Acta Materialia 56, 5719–5727. doi:`10.1016/j.actamat.2008.07.038`.

Vernon-Parry, K.D., Furu, T., Jensen, D.J., Humphreys, F.J., 1996. Deformation microstructure and texture in hot worked aluminium alloys. Materials Science and Technology 12, 889–896. doi:`10.1179/mst.1996.12.11.889`.

W. T. Read, J., 1953. Dislocations in Crystals. doi:`10.1107/S0365110X54002770`.

Williamson, G., Hall, W., 1953. X-ray line broadening from filed aluminium and wolfram. Acta Metallurgica 1, 22–31. doi:`10.1016/0001-6160(53)90006-6`.

Williamson, G.K., Smallman, R.E., 1954. The use of Fourier analysis in the interpretation of X-ray line broadening from cold-worked iron and molybdenum. Acta Crystallographica 7, 574–581. doi:`10.1107/s0365110x54001879`.

Williamson, G.K., Smallman, R.E., 1956. III. Dislocation densities in some annealed and cold-worked metals from measurements on the X-ray Debye-Scherrer spectrum. Philosophical Magazine 1, 34–46. doi:10.1080/14786435608238074.

Yu, T., Hansen, N., Huang, X., 2011. Recovery by triple junction motion in aluminium deformed to ultrahigh strains. Proceedings of the Royal Society A: Mathematical, Physical and Engineering Sciences 467, 3039–3065. doi:10.1098/rspa.2011.0097.

Yu, T., Hansen, N., Huang, X., 2012. Recovery mechanisms in nanostructured aluminium. Philosophical Magazine 92, 4056–4074. doi:10.1080/14786435.2012.704418.

Yu, T., Hansen, N., Huang, X., 2013. Linking recovery and recrystallization through triple junction motion in aluminum cold rolled to a large strain. Acta Materialia 61, 6577–6586. doi:10.1016/j.actamat.2013.07.040.

Zamin, M., 1981. ROLE OF Mn IN THE CORROSION BEHAVIOR OF Al-Mn ALLOYS. Corrosion 37, 627–632. doi:10.5006/1.3577549.

Zhao, Q., Zhang, H., Qiu, F., Jiang, Q.C., 2018. Strain-induced precipitation kinetics during non-isothermal annealing of Al-Mn alloys. Journal of Alloys and Compounds 735, 2275–2280. doi:10.1016/j.jallcom.2017.11.360.

Zhou, W., Yu, J., Lin, J., Dean, T.A., 2019. Manufacturing a curved profile with fine grains and high strength by differential velocity sideways extrusion. International Journal of Machine Tools and Manufacture 140, 77–88. URL: https://

doi.org/10.1016/j.ijmachtools.2019.03.002, doi:10.1016/j.ijmachtools.2019.03.002.